NATIONAL INSTITUTE FOR FUSION SCIENCE

Collected papers at the 2019 Post-CUP Workshop & JSPS-CAS Bilateral Joint Research Projects Workshop, 24th-26th July, 2019, Nagoya, Japan

Satoshi Ohdachi, Editor of the Post-CUP Workshop proceeding

(Received - 2020/01/29)

NIFS-PROC-116

Feb. 21, 2020

Contents

Preface

Time Table

Proceedings

CFETR diagnostics design 001
HU Liqun

Recent progress of transport and confinement research on EAST 005
LIU Haiqing

Development of advanced tokamak scenarios in HL-2A plasma 009
LIU Yi

Research activities on the SUNIST spherical tokamak 020
GAO Zhe

Experimental results of disruption mitigation with SMBI and MGI on HL-2A 026
DONG Yunbo

Detection of magnetic islands using imaging diagnostics 030
OHDACHI Satoshi

Nonlinear MHD simulation of plasma termination events in stellarators 034
SUZUKI Yasuhiro

Overview of the LHD neutron diagnostics 038
ISOBE Mitsutaka

1 MeV triton orbit analysis in Experimental Advanced Superconducting Tokamak 044
OGAWA Kunihiro

Spectroscopic study of impurity behavior in the edge stochastic magnetic field layer of Large Helical Device 048
OISHI Tetsutarou

EMC3-EIRENE modeling of impurity transport in neon-seeded EAST plasma 052
LIU B.

A particular method for measuring low edge ion temperature based on VUV spectroscopy 056
MORITA Shigeru

ICRF heating experiments on EAST 061
ZHANG Xinjun

Conceptual design of CFETR ECRH system 065
WANG Xiaojie

Simulation of energetic particle driven geodesic acoustic mode channeling in LHD using MEGA code 070
WANG Hao
Evaluation method of effective ion charge in the LHD plasma 076
KAWAMOTO Yasuko
Observation of tungsten spectra from W5+ to W45+ in EAST 081
ZHANG Ling
Tungsten measurements at LHD using visible M1 lines 085
KATO Daiji
Wall recycling experiment in EAST 089
ASHIKAWA Naoko
Laser-based diagnostic of LIAS and LIBS for the plasma wall interaction on the EAST tokamak. 093
HU Zhenhua
The deuterium permeation behavior in W studied by gas driven permeation and plasma driven permeation methods 097
ZHAO Mingzhong
Current status of NIFS-SWJTU joint project for CFQS 103
SHIMIZU Akihiro
Current status of engineering aspect for CFQS 109
KINOSHITA Shigeyoshi
Finite element analysis of elctromagnetic force and stress on CFQS modular coils and support structure 118
XIONG Guozhen
Engineering analysis of vacuum vessel for CFQS 130
NAKAGAWA Sho
Micro-instabilities and turbulence transport in the CFQS 136
NAKATA Motoki

Preface:

Collected papers at the 2019 Post-CUP Workshop & JSPS-CAS Bilateral Joint Research Projects Workshop, 24th - 26th July, 2019, Nagoya, Japan

Satoshi Ohdachi, Editor of the Post-CUP Workshop proceeding

Close collaborations of scientists in the field of nuclear fusion in Japan and China have been supported by Core University Program (CUP) (2001~2010), MEXT-MOST agreement (2008~), Post-CUP program (2011~), and A3 foresight program (2012~2017). After the CUP was completed, the Post-CUP coordinator meeting was held in Guilin, China in Nov. 3rd, 2011.

To continue and to enhance close collaborations in fusion between Japan and China, the Post-CUP workshop is restarted regularly from 2019. Its main purpose is to solve several key physics issues specific to high-performance plasmas through joint experiments on advanced fully superconducting fusion devices, i.e., LHD in Japan and EAST in China, and other magnetic confinement devices to carry out multi-faceted and complementary physics researches. The workshop papers presented at the 2019 Post-CUP Workshop & JSPS-CAS Bilateral Joint Research Projects Workshop 24th - 26th July, 2019, Nagoya, Japan are collected in this volume.

All figures and some parts of sentences are in color only CD-ROM (PDF).

Program of the Workshop

24 July 2019 **(Wednesday)** 09:00 Registration open			
Session 1 (Opening & device overview) Chair: OHDACHI Satoshi	09:30	ISOBE Mitsutaka (NIFS) & HU Liqun (ASIPP)	Opening remarks
	09:40	HU Liqun (ASIPP)	CFETR diagnostics design
	10:05	LIU Haiqing (ASIPP)	Recent progress of transport and confinement research on EAST
	10:30	LIU Yi (SWIP)	Development of advanced tokamak scenarios in HL-2A plasma
Coffee Break 10:55-11:10			
Session 2 (Device overview &collaboration strategy) Chair: MORITA Shigeru	11:10	NAGASAKI Kazunobu (Kyoto Univ.)	Recent experimental results from the Heliotron J helical device
	11:35	GAO Zhe (Tsinghua Univ.)	Research activities on the SUNIST spherical tokamak
	12:00	DONG Shaohua (ASIPP)	New cooperation opportunities in the thirteenth-five-year project time
Lunch Break12:25-13:50			
Session 3 (Control & MHD) Chair: YE Minyou	13:50	DONG Yunbo (SWIP)	Experimental results of disruption mitigation with SMBI and MGI on HL-2A
	14:15	OHDACHI Satoshi (NIFS)	Detection of magnetic islands using imaging diagnostics
	14:40	SUZUKI Yasuhiro (NIFS)	Nonlinear MHD simulation of plasma termination events in stellarators
Group Photo + Coffee Break 15:05-15:30			
Session 4 (Neutron & EPs) Chair: LIU Yi	15:30	FAN Tieshuan (Peking Univ.)	Fusion neutron spectroscopy on magnetic confinement devices
	15:55	ISOBE Mitsutaka (NIFS)	Overview of the LHD neutron diagnostics
	16:20	MURAKAMI Sadayoshi (Kyoto Univ.)	Estimation of DD/DT fusion neutrons of LHD plasmas by GNET
	16:45	OGAWA Kunihiro	1 MeV triton orbit analysis in Experimental Advanced

		(NIFS)	Superconducting Tokamak

25 July (Thursday)			
Session 5 (Edge plasmas) Chair: LIU Haiqing	09:00	YE Minyou (USTC)	The influence of magnetic flux expansion on the in-out divertor asymmetry in snowflake configuration
	09:25	OISHI Tetsutarou (NIFS)	Spectroscopic study of impurity behavior in the edge stochastic magnetic field layer of Large Helical Device
	09:50	KAWAMURA Gakushi (NIFS)	EMC3-EIRENE modeling of impurity transport in neon-seeded EAST plasma
Coffee Break 10:15-10:35			
Session 6 (Heating & EPs) Chair: SUZUKI Yasuhiro	10:35	ZHANG Xinjun (ASIPP)	ICRF heating experiments on EAST
	11:00	WANG Xiaojie (ASIPP)	Status of ECRH system on EAST
	11:25	WANG Xianqu (SWJTU)	Fishbone-like modes excited by energetic particles in weak reversed shear plasmas
	11:50	WANG Hao (NIFS)	Simulation of energetic particle driven geodesic acoustic mode channeling in LHD using MEGA code
Lunch Break 12:15-13:45			
Session 7 (Diagnostics) Chair: HU Liqun	13:45	MORITA Shigeru (NIFS)	A particular method for measuring low edge ion temperature based on VUV spectroscopy
	14:10	KAWAMOTO Yasuko (NIFS)	Evaluation method of effective ion charge in the LHD plasma
	14:35	ZHANG Ling (ASIPP)	Observation of tungsten spectra from W^{5+} to W^{45+} in EAST
	15:00	KATO Daiji (NIFS)	Tungsten measurements at LHD using visible M1 lines
Coffee Break 15:25-15:45			
Session 8 (PWI)	15:45	ASHIKAWA Naoko (NIFS)	Wall recycling experiment in EAST
	16:10	DING Fang (ASIPP)	ELM-induced W source in EAST divertor

Chair: KATO Daiji	16:35	HU Zhenhua (ASIPP)	Laser-based diagnostic of LIAS and LIBS for the plasma wall interatction on the EAST tokamak
	17:00	ZHAO Mingzhong (Shizuoka Univ.)	The deuterium permeation behavior in W studied by gas driven permeation and plasma driven permeation methods

26 July (Friday)			
Session 9 (CFQS & closing) Chair: ISOBE Mitsutaka	09:00	SHIMIZU Akihiro (NIFS)	Current status of NIFS-SWJTU joint project for CFQS
	09:20	KINOSHITA Shigeyoshi (NIFS)	Current status of engineering aspect for CFQS
	09:40	XIONG Guozhen (SWJTU)	Finite element analysis of elctromagnetic force and stress on CFQS modular coils and support structure
	10:00	NAKAGAWA Sho (NIFS)	Engineering analysis of vacuum vessel for CFQS
	10:20	NAKATA Motoki (NIFS)	Micro-instabilities and turbulence transport in the CFQS
	10:40	ISOBE Mitsutaka (NIFS) & Hu Liqun (ASIPP)	Summary reports, closing and others (Proceedings with format, schedule after session etc.)
Lunch Break 11:00 - 13:00			
Session 10 Discussions on Post-CUP and JSPS-CAS Bilateral Joint Research Projects Chair: ISOBE Mitsutaka HU Liqun OHDACHI Satoshi	13:00-17:00 Discussions on next workshop plans Education of young scientists Discussion on coordinator meeting Discussion on annual report of the collaboration Discussion on web site of the collaboration Discussions on machine operation schedules Discussions on new toroidal devices Discussion on budget and administrative works "Some key issues in international cooperation among institutes" by Ms. Shaohua DONG and Prof. Mitsutaka ISOBE *et al*.		

CFETR Diagnostics Design

L.Q. Hu[1], on behalf of CFETR diagnostic team[1, 2]

[1]Institute of Plasma Physics, Chinese Academy of Sciences, P.O. Box 1126, Hefei 230031, P.R. China

[2]Southwestern Institute of Physics, P.O. Box 432, Chengdu, Sichuan 610041, P.R. China

Abstract

The China Fusion Engineering Test Reactor (CFETR) is the next generation device aiming to bridge the gaps between the fusion experimental reactor ITER and the demonstration reactor (DEMO) and help the realization of fusion energy in China. According to the roadmap of China magnetic confinement fusion development, the primary mission of CFETR is to demonstrate fusion energy production in self-sufficient burning with different-advanced operation scenarios. CFETR will be proposed to be operated in two phases [1]. Phase I emphasizes on fusion power $P_{fusion} \geqslant 200$ MW with fusion power gain Q=1-5, tritium breeding ratio (TBR)>1.0, neutron irradiation effects ~10 dpa, and steady-state operation with a duty cycle of about 0.3–0.5. Phase II focuses on DEMO validation with $P_{fusion} \geqslant 1$ GW and $Q > 10$, duty cycle $\geqslant 0.5$, neutron irradiation effects in level of 50 dpa. Auxiliary heating and current drive systems with up to 80 MW including N-NBI, ICRF, EC and LHCD will be employed to achieve steady-state advanced operation. Plasma diagnostics aiming to machine protection, plasma control and burning physics research will provide a key role in plasma performance evaluation and study to help selection of operation regime and performance optimization [2]. Due to very harsh nuclear environment in CFETR which is much worse than that in ITER, most of diagnostics adopted by ITER cannot survived. Therefore new strategy and regulation need be setup for reasonable selection of diagnostics, right development of diagnostics and relevant components to avoid unnecessary waste of budget and human resource. Engineering design progress of CFETR diagnostics and the first integration have been presented and discussed in this paper.

1. Introduction

CFETR task is to explore options for DEMO blankets and divertor solutions, and to discover a technical solution for licensing DEMO. As diagnostics in CFETR will in the severe nuclear environment with neutron irradiation effects up to 50 dpa, which is several tens of times higher than that in ITER, consequentially a range of new phenomena coming from radiation-induced performance change and resulting radiation damage must be considered and handled for physical properties intact of the material, including conductivity (RIC), electrical degradation (RIED), electromotive force (RIEMF), thermo-electric sensitivity (RITES), absorption (RIA), nuclear heating, Radioluminescence (RL or RIE). Changes in other properties such as activation, transmutation and swelling have to be dealed with as well. Those will bring new and significant challenges to diagnostic design and development, in aspects of structural metal material (physical property, mechanic strength, volume stability, electrical and thermal conductivity, dielectric loss and permittivity), signal pickup and transmission (optical properties, luminescence, coloration), electrical insulation (ceramics), signal process (electronics, cable), and maintenance. Nuclear environment sets stringent demands on the engineering of the diagnostic system: neutron shielding, tritium containment, vacuum integrity, RH

compatibility. Moreover, existence of tritium blanket module and accessibility limited by ports availability will greatly confine view and number of the diagnostics, diagnostics selection and engineering design will be a compromising result among physics requirement, engineering realizability and environment available.

2. Diagnostics selection

Five years' conceptual design of CFETR has produced fruitful results and enhanced understanding of physics design, integrated modeling of operation scenarios, advanced operation regime and engineering requirement [1,2]. Published expected plasma performance is shown in Table 1, in which machine and plasma parameters are I_p=6-14 MA, B_{t0}=6.5 T, R_0=7.2 m and a=2.2 m as top input parameters for engineering design. The machine has 16 upper ports, 16 lower inclined ports and 6 equatorial ports, and 1.2m thick tritium blanket module (TBM). Nearly 800 people from more than 30 research institutes and universities are involved in CFETR engineering design, research and development (R&D) activities. Remote handling scheme and maintenance strategy have been studied and setup. In vessel components maintenance is preferred for divertor, and divertor module will be removed through lower port during machine maintenance. TBM in multi-module segment is changed and maintained through vertical port.

Table 1 CFETR plasma performance with 0D basic operation mode

	A.1 100MW SS	A.2 200MW SS	A.2 500MW SS	A.3 1GW SS	A.4 DEMO level SS
Pf	120	229	482	974	2192
Pinternal	199	196	223	238	265
Qplant	0.46	0.70	1.14	1.98	3.79
Qplasma	1.56	3.06	5.87	11.89	28.17
Pnetelec	-107	-58	30	232	738
Pn/Awall	0.12	0.23	0.49	0.99	2.23
BetaT	0.006	0.009	0.014	0.019	0.029
BetaN	1.00	1.20	1.50	2.0	3.0
fbs	0.40	0.40	0.40	0.50	0.75
HITER98Y2	1.12	1.25	1.32	1.41	1.42
fohm	0.0	0.0	0.0	0.0	0.0
Pcd(吸收功率)	77	75	82	82	78
Ip	8.61	10.34	12.92	13.78	13.78
Bo	6.5	6.5	6.5	6.5	6.5
Ti(0)/Te(0)	18	24	32	36	32
n(0)	0.48	0.52	0.61	0.78	1.31
nbar/nGR	0.57	0.51	0.48	0.57	0.96
Zeff	2.45	2.45	2.45	2.45	2.45
P/R	8.52	9.42	11.66	15.69	30.70
q95_iter	8.87	7.39	5.91	5.54	5.54

	B.1 100MW HB	B.2 200MW HB	B.2 500MW HB	B.3 1GW HB	B.4 DEMO level HB
Pf	114	250	558	1128	2192
Pinternal	190	196	202	222	75
Qplant	0.46	0.75	1.40	2.41	12.96
Qplasma	1.54	3.35	7.65	15.30	795.16
Pnetelec	-103	-49	80	312	891
Pn/Awall	0.12	0.25	0.57	1.15	2.23
BetaT	0.006	0.009	0.014	0.019	0.029
BetaN	1.00	1.20	1.50	2.00	3.0
fbs	0.40	0.40	0.40	0.50	0.75
HITER98Y2	1.01	1.09	1.18	1.19	1.54
fohm	0.30	0.30	0.30	0.30	0.24
Pcd	74	74	73	74	3
Ip	8.61	10.34	12.92	13.78	13.78
Bo	6.5	6.5	6.5	6.5	6.5
Ti(0)/Te(0)	13	17	24	24	34
n(0)	0.67	0.74	0.82	1.16	1.23
nbar/nGR	0.79	0.72	0.64	0.85	0.90
Zeff	2.45	2.45	2.45	2.45	2.45
P/R	7.58	9.33	12.63	19.11	22.97
q95_iter	8.87	7.39	5.91	5.54	5.54

(A-Steady State operation mode; B-Hybrid operation mode)

In past decade, ITER diagnostics have got significantly progress, however they are prepared only for 0.3 dpa nuclear circumstance and are not ready to be put into about service. In the other hand, port resource for diagnostics in CFETR is relatively poor, and only two equatorial ports (EP) can be expected to diagnostics even if more upper and lower ports are available (UP, LP). Therefore, plasma diagnostics in CFETR could not be rich, and coverage range and spatial resolution would be very limited. Considering those issues, plasma diagnostics in CFETR will be developed in two phases. In Phase 1 with Pf=0.5 GW (D-Phase 1), diagnostics are designed and developed based on mature ones from ITER achievement together with a few prospective and promising technology, the target of which will be to help choose most suitable operation region/scenario from several candidates. In Phase 2 with Pf=1 GW or above (D-Phase 2), nuclear domain diagnostics plus

endurable and survival diagnostics from Phase 1 will be operated to approach target of plasma performance optimization in given operation region. The missions of those diagnostics are of priority firstly machine operation and protection, then plasma operation and control, and finally burning plasma understanding mainly on investigation of α particle behavior and performance. CFETR diagnostics should be kept in minimum but with reliable and achievable in techniques, small port resource consuming, long service time, high maintainability and nuclear radiation hardness. Individual diagnostic is better of multi-function to keep enough redundancy. List of diagnostics in D-Phase 1 is given in Table 2, in which nearly half are port dependent. They will provide plasma parameters of Te(r), Ti(r), Ne(r), V_ϕ, impurity species and flux, fusion products, etc., as much as possible from core to edge for burning control study. Nuclear techniques domain diagnostics and few in Table 2 with very limited channels for Te/Ti/Ne, impurity, etc., and with high neutron hardness and port independent could be employed for stable optimized plasma performance study in D-Phase 2.

Table 2 Diagnostics list in Phase 1

No.	Diagnostics	Objects	No.	Diagnostics	Objects
1	Magnetics (flux loop, Rogowiskis/Diamagnetic/Mirnov/Sad. coils)	Ip, Vp, W, Ψ, Δ, βp, Halo current, Dsep; MHD locking/precursor, etc.	12	Neutron Activation System (NAS)	2.45/14MeV, absolute yield
2	Polarimetry and Interferometry POINT	Ne(r), j(r) (line averaged)	13	Energy-Res. Farad Cup	Escaped α particle, T
3	MW reflectmeter	Ne(r) (physics)	14	LVIC camera	H&ELM precursor, pl.Equilibrium, REs
4	Metal Bolometer	Radiated power (total & distribution)	15	Visible survey/ imaging system	Stable operation and control, shape
5	LIDAR TS	Te(r), Ne(r)	16	IR survey/ imaging system	Wall and inner component, rs
6	CXRS	Ti edge, Rotation (NBI) nHe/n(r), Zeff	17	Divertor Erosion monitor	Vis. CCD, IR, Erosion rate
7	XICS	Ti core, rotation (non NBI), Heavy impurity	18	Thermal couple	Tmax, surface and inner components
8	Visible spectrometer	Impurity species, Zeff, H-mode&ELM, nHe/n(r)	19	Dust monitor	Collection tube HS CCD
9	Fission chamber & microfission chamber	Neutron yield, Pt, P(p&t) distribution, power loss, stability and uniformity	20	Trtium Surface concentration intensity, Hall	Contamination, n/γ dosage rate, Dosage; distribu.
10	Neutron camera (Vertical & Radial)	Neutron and α source profile, flux&emissivity, core fuel ratio and Ti(r)	21	Dosage inspection on outflow of the machine (solid, gas, liquid), T in the air	Radioactivity and Specific activity in outflow, T intensity, α/β surface contamination
11	Gamma Ray spectrometer GRS	Core fuel ratio, REs, α particle performance,			

3. Diagnostics integration

Similar to diagnostics integration scheme on ITER, the first round of integration on CFETR has been carried out and port layout is shown in Fig.1. Equatorial port (EP) in size of 3071 mm(W)×2860 mm(H)×8070 mm(L) is divided to three DSM (diagnostic sheilding module). Each DSM with size of 926 mm(W)×2860 mm(H)×8070 mm(L) is full of labyrinth to stop nuclear radiation going outside straightly. Up to now, all diagnostics in Table 2 can be settled down in the integration. Three IR and visible CCD cameras

cover most inner surface of the blanket and heating systems. Ten sets of m-NFC (micro-nuclear fission chamber) uniformly monitor the neutron yield from the divertor (toroidal 3 sets), inner blanket wall in HFS (high field side, 2 sets) and LFS (low filed side, three sets), and cryostat (2 sets). Nine poloidal channels of POINT (Polarimetry and Interferometry) will be adopted to measure electron density and current density pofile, and a single toroidal channel will be ready for density feedback control. Three sets of MW (microwave interfemeter) provide local and fast variation of elctron density (one on HFS, one on top edge, another one on the external blanket). LIDAR Thomson scattering system will be used to get electron temperature profile. Two sets of neutron camera, one in EP (RNC) and the other in UP (VNC), supply neutron and α partical source profile, and core fuel ratio. Twelve sets of Neutron Activation System (NAS) in two EPs provide absolute local 2.45 MeV or 14 MeV neutron yield. Gamma Ray spectrometers (GRS) locate after neutral camera offer confined α particle performance and runaway beam (REs) behavior. Six sets of energy-resolved farad cup (ERFC, EP1&2, each with three in vertical) give lost α particle and energetic particle message. Corresponding to two co-NBI injection beamlines, one Charge exchange recombination spectroscopy (CXRS) and one combination of CXRS and Visible spectrometer provide plasma rotation profile, edge Ti, He density and impuirty information. X-ray Imaging Crystal Spectrometer (XICS) can give core Ti, rotation profile in non –NBI case and heavy impurity information. Besides, those diagnostics will make compensation with each other to provide supplementary or backup for primary one. But, it should be noted that as detailed design of individual diagnostic moves on, much crash among them and more view space requirment from physics may come, therefor relocation of some diagnostics are probably unavoidable.

4. Summary

CFETR engineering design has been in progress well and the first integration allows detailed diagnostics design moving on. Load analyses of the structure and assessment of diagnostics function will be done and based on detailed design it will help to confirm or revise integration design. In the meantime, evaluation of redundancy and robustness, remote assembly and maintenance of the diagnostic are needed to be considered together with design. R&D activities of key components, especially common issues, are suggested to go in parallel to support the engineering design.

Acknowledgments

This work is supported by the National Magnetic Confinement Fusion Program of China under Contract No. 2017YFE0300503.

References

[1] Y.X. Wan, J.G. Li, Y. Liu, et, al., Overview of the present progress and activities on the CFETR, Nucl. Fusion, 57 (2017)102009.

[2] Y.T. Song, S.T. Wu, J.G. Li, et al., Concept Design of CFETR Tokamak Machine, IEEE Trans. Plasma Sci. 42 (2014) 503.

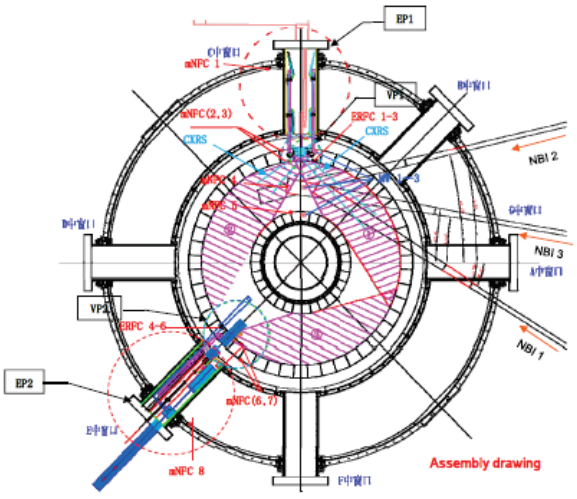

Figure 1. Port layout of the first round diagnostics integration on CFETR

Recent progress of RF heating plasma confinement research on EAST

Haiqing Liu[1], EAST team and collaborator*

1Institute of Plasma Physics, Chinese Academy of Sciences, Hefei, Anhui, China, 230031

Abstract

In tokamak plasma, a weak or reversed magnetic shear configuration is an important candidate for the future fusion reactor, it is helpful to build a hollow current profile, establish an internal transport barrier (ITB), improve the plasma confinement, and realize the long-pulse discharge. In experiments, auxiliary heating systems, including NBI (Neutral Beam Injection), ECRH (Electron cyclotron resonance heating), ICRH (Icon cyclotron resonance heating), and LHCD（Lower hybrid current drive), are used to control the plasma current as the Ohmic current driving efficiency is limited, consequently, achieving the weak or reversed magnetic shear configuration. An improved confinement plasma operation can be obtained with these heating systems. On EAST (Experimental Advanced Superconducting Tokamak), both of the four heating systems are applied to heat plasma. In recent experiments, optimized confinement plasma is obtained with the interaction between LHCD and ECRH, the simulation and experiments results are in good agreement.

1. Introduction

Advanced tokamak operation scenarios being explored for future fusion reactors must have high confinement and stability which are closely linked to the internal plasma current density distribution. Candidates scenarios can be either a weak-shear or a reversed-shear plasmas as the current profile in both plays an important role in achieving and maintaining confinement and stability[1].To obtain weak or reversed shear discharges, plasma current must be driven off-axis combining various non-inductive techniques, such as neutral beam current drive(NBCD), electron cyclotron current drive(ECCD) and lower-hybrid current drive(LHCD). LHCD has proved to be one of the most effective ways to drive the plasma current so far [2]. Numerous experiments have been conducted on the subject of LHCD in various tokamak devices like JT-60U[3, 4] and JET[2, 5, 6] and so on. The results have shown that LHCD is an effective way to achieve the current distribution required for advanced, high-performance, discharge scenarios.

Since 2015, EAST has been equipped with all ITER-relevant auxiliary heating and current drive systems, enabling the investigation of plasma profile control by coupling and integration of various sources. Table 1summarizes the designed power level of auxiliary heating systems and the recently achieved injection power on EAST. LHW(Lower Hybrid Wave) system is the steadiest and most effective way to drive plasma current. Recent experiments on EAST have demonstrated access to broad plasma current profiles by increasing the plasma density in fully non-inductive lower hybrid current-driven discharges[7].

Heating/CD scheme		Designed/projected power (MW)	Injected power and duration
LHW	2.45 GHz	4 MW/CW	2.8 MW/6 s; 1.2 MW/410 s
	4.6 GHz	6 MW/CW	3.5 MW/2 s;1.4 MW/101 s
ICRF		12 MW/CW	3.8 MW/6.0 s; 0.8 MW/60 s
NBI	Co-current	2–4 MW/10–100 s	3.2 MW/2.0 s; 0.4 MW/100 s
	Counter-current	2–4 MW/10–100 s	2.6 MW/2.0 s
ECRH		4 MW/100–1000 s	0.6 MW/5 s; 0.5 MW/101 s

Table 1 summary of heating systems on EAST

2. **RF heating optimized plasma on EAST**

1) Plasma current driven by LHCD broadens as density increases

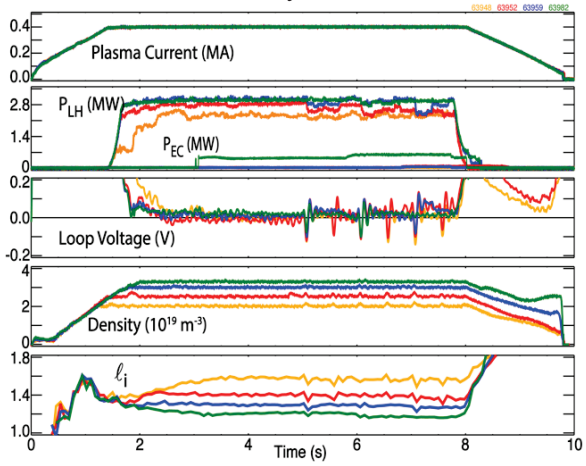

Fig.1 Discharge parameters for LHCD plasmas.

Lower hybrid wave on EAST plays a very important role in heating plasma, steady operation and high

efficiency makes it a candidate in EAST long-pulse plasma operation. In experiments, 4.6GHz lower hybrid wave was set to close heating input power, but with the different plasma density, loop voltage decreases to nearly zero as LHW inputs, implying the plasma current was driven effectively by LHCD. The LHCD profile is expected to become more off-axis with higher density, because radial penetration of the wave is reduced at higher density, thus the wave is absorbed closer to the plasma edge. Therefore, with only LHCD and bootstrap as sources of plasma current, the total current profile should become broader at higher density. Combing EFIT and POlorimeter-INTeferometer (POINT) measurement together, plasma current profile can be obtained, with LHCD current and bootstrap current only, the current driven by LHCD can be estimated with $J_{LHCD} = J_{tot} - J_{BS}$.

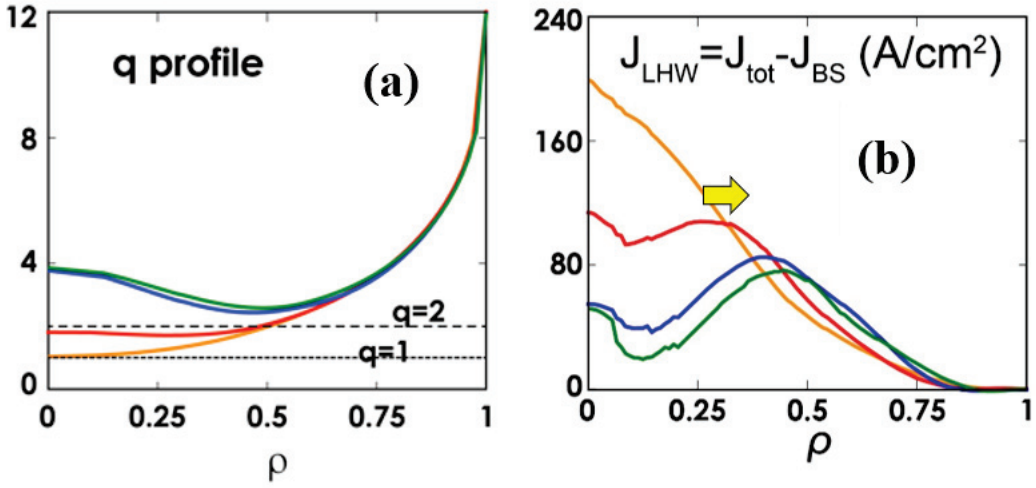

Fig.2 Selected radial profiles for the four discharges of figure 8 at t ~ 4.9 s. (a) Fit to electron density measurements, (b) reconstructed current density and calculated bootstrap current.

Results of the reconstructions are shown in figure 2, confirming that broader current profiles are obtained at higher density. Note that the q-profile goes from monotonic at lower density to negative central magnetic shear sustained in steady-state at higher density. Thus, these results show a sort of 'high performance synergy' between broad current profile and high density in LH-driven plasmas: on one hand, higher density is needed for higher performance, and on the other hand, higher density naturally gives a broader current profile, which also can improve performance.

2) **Interaction between LHW and ECH provides an approach to optimize current density profile**

LHCD is an effective way to drive plasma current in tokamak, the interaction between LHCD and other heating system is also an important topic in plasma research. On EAST, the interaction between LHW and ECH was studied, results are shown in figure 3.

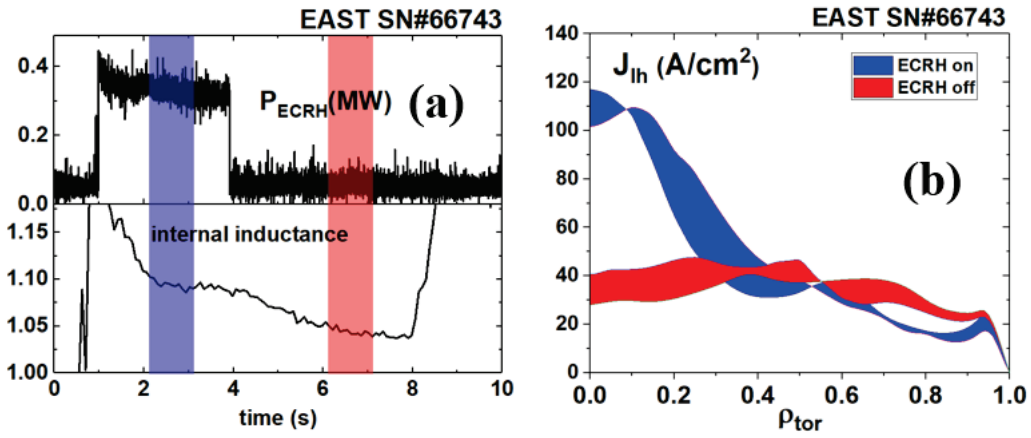

Fig.3 (a) internal inductance decreases slightly after ECRH off, (b) simulated LHCD current with by GENRAY and CQL3D codes

In the recent EAST experiment campaign, we observed a decrease in internal inductance in an electron heating dominant (LHW+ECRH+ICRF) H-mode plasma after ECRH termination. Simulations using GENRAY&CQL3D codes reproduced the flattening of LHCD profile after ECRH termination (note that LHCD is the major current drive source). Detailed analyses showed that the current profile peaking （blue color in Fig.3 b） was related to the interaction between LHW and ECRH.

Acknowledgements

This work was partly supported by the Post-CUP program. This work was supported in part by the Collaborative Research Program of the Research Institute for Applied Mechanics, Kyushu University and was also partially supported by the National Key R&D Program of China under Grant No. 2017YFE0301205.

References

[1] T. Suzuki, et al. 2008, Nuclear Fusion, 48:045002

[2] A. Ekedahl, et al.1998, Nuclear Fusion, 38:1397

[3] S. Ide, et al. 1996, Plasma Physics and Controlled Fusion, 38:1645

[4] S. Ide, et al. 2000, Nuclear Fusion, 40:445

[5] D. Mazon, et al. 2003, Plasma Physics & Controlled Fusion, 45:47

[6] D. Moreau, et al. 1991, Plasma Physics & Controlled Fusion, 33:1621

[7] A. M. Garofalo, et al. 2017, Nuclear Fusion, 57

Role of the MHD activities in triggering H-mode in HL-2A tokamak

Yi Liu[1], J. Cheng[1], M. Jiang[1], Y. G. Li[1], L. M. Yu[1], Y. B. Dong[1], D. Li[1], L. Liu[1], W. L. Zhong[1], J. Q. Xu[1], Z. H. Huang[1], X. Q. Ji[1], S. D. Song[1], D. L. Yu[1], M. Xu[1], Z. B. Shi[1], O. Pan[1], Q. W. Yang[1], X. T. Ding[1], X. R. Duan[1], Yong Liu[1] and HL-2A team

[1]*Southwestern Institute of Physics, P. O. Box 432, Chengdu, Sichuan 610041, China*

The impact of a low frequency MHD mode crash on triggering the H mode has been studied in detail on the HL-2A tokamak. The mode manifests fishbone characteristics with a procession frequency $f \approx$14-19 kHz. The abrupt mode crash evokes substantial energy release from the core to the plasma boundary and hence increases the edge pressure gradient and $E_r \times B$ flow shear, which further suppresses turbulence and leads to confinement improvement into the H-mode. Under the same NBI heating (~ 1 MW), the I-phase plasma transits into H-mode with a rapid mode crash while it returns to the L-mode without the presence of the mode in the I-phase. With increasing heating power by the ECRH added to the NBI, the kink-like mode disappears. The statistical result shows that with the MHD mode crash the heating power for accessing the H mode is significantly lower than that without the mode crash. All these facts reveal that the MHD mode crash in the I-phase plays a critical role in trigging the I→H transition at marginal heating power. In addition, it has been found that with the same NBI power heating, the magnitude of the mode (crash) increases with increasing plasma density, implying larger energy release being needed to access the H-mode for higher density plasmas. The results may have significant implication on ITER operation scenarios with tight margin of L-H threshold power.

1. Introduction

Accessing and maintaining H mode performance are of crucial importance for the ITER operation [1]. At present, the most widely used power scaling law, $P_{scale}[MW] = 0.049 \cdot \overline{n}_e [10^{20} m^{-3}]^{0.72} \cdot B_t[T]^{0.8} \cdot S[m^2]^{0.94}$, is valid for standard magnetic configuration with favorable ion ∇B drift (pointing towards X-point) [2]. This scaling law indicates that the three dominant dependences are plasma density ($\overline{n}_e$), toroidal magnetic field (B_t) and the plasma surface area (S). However, ongoing experiments from many devices discovered that other variables may also strongly affect the L-H transition threshold power. For example, the DIII-D experiments demonstrated that the plasma rotation is an important parameter affecting the L-H threshold power [3]. Investigations at ASDEX Upgrade revealed a decrease of the L-H power by about 25% for the plasmas after the transition from a full carbon wall to a full tungsten wall [4].

Findings in JET [5], DIII-D [6], MAST [7] and C-Mod [8] pointed out that the divertor magnetic geometry (e. g., the X-point height and the length of the divertor leg) has strong influence on the L-H power. Recently the key role of edge ion heat flux in the L-H transition has also been reported on AUG [9]. Up to now, the underlying physics behind theses hidden parameters has not yet been identified. Further research should be centered on identifying the key ingredients of the L-H transition in order to reduce the power threshold.

Considering the present ITER power capabilities in the range of 70 MW [1], the reduction of the L-H power threshold would have great impact on ITER plasma operation scenarios. For the tight margin of ITER L-H threshold power, an improved understanding of the L-H transition at reduced power is highly desirable. In this paper, we firstly report the favorable role of a kink-like MHD mode crash in triggering the transition into the H-mode with reduced heating power in the HL-2A tokamak.

The rest of the paper is organized as follows. The experimental setup is described in section 2. The experimental results and discussions are presented in section 3 and a summary is given in section 4.

2. Experimental setup

The H-mode experiments were performed on the HL-2A tokamak with a lower single-null divertor configuration and following parameters: R=1.65 m, a=0.4 m, B_t=1.4 T, I_p=170-180 kA, $\overline{n}_e \approx (1.4\text{-}2.8)\times10^{19}$ m^{-3}, P_{NBI}=0.8-1.0 MW and P_{ECRH} = 0.3-1.5 MW. For measuring edge equilibrium density (n_e), electron temperature (T_e) and floating potential (V_f) as well as fluctuating quantities, a four-step Langmuir probe array (connected in a triple probe model) has been employed with a sampling rate of 1 MHz [10]. The probe array was installed on a reciprocating manipulator with a scanning speed of 1.0 m/s. The radially scanned distance is about 8.0 cm, covering both the plasma edge and the scrape-off layer (SOL) [11]. The radial electric field E_r is deduced from the radial derivative of the plasma potential $V_p = V_f + 2.8T_e$ (for D plasmas). The magnetic fluctuations were detected by Mirnov coils at a sampling rate of 1 MHz. In addition, a multi-channel ECE diagnostic was used to measure the electron temperature profile and a soft x-ray (SXR) system, consisting of two pinhole cameras, to measure the soft x-ray emission intensity.

3. Experimental results

3.1 Evolution of plasma parameters across transitions

In the HL-2A tokamak, with a marginal NBI heating power ($P_{NBI} \approx$ 1.0 MW) and the plasma central line-averaged density ranged at $\overline{n}_e = (1.5\text{–}2.8)\times10^{19}$m^{-3}, an intermediate phase (I-phase) has been routinely observed during the L→H transition. The I-phase is characterized

by strong oscillations in the edge recycling (D_α emission) signal, and usually has better plasma confinement than in the L-mode. At HL-2A, in addition to a single L→I→H transition, multiple L→I→L→I→H transitions also occur frequently. Figure 1 illustrates the typical temporal evolution of plasma parameters, including D_α emission, the central line-averaged density, NBI heating power, magnetic fluctuations and its root-mean-square (RMS) level during the time period of L→I→L→I→H in shot 19380. It is clear to see that before each L→I (t_1=747ms, t_2=785 ms) or I→H (t_3=824ms) transition a strong MHD mode is developed, and it collapses rapidly just prior to the transition time. The MHD mode frequency is around 14–19 kHz. These results explicitly reveal that the MHD mode collapse plays a critical role in triggering the confinement improvement, i. e., the L→I or I→H transition. It is interesting to notice that the central line-averaged density abruptly reduces at each MHD mode crash and then gradually recovers. This reduction is associated with the variation of the density profile induced by the mode crash, as shown in figure 3 (f). The I-phase dynamics have been widely discussed in terms of turbulence-zonal flow interaction (predator-prey model) and the bifurcation model [12-20]. In the present paper, our focus is nevertheless put on investigating physical processes of the MHD mode crash and its favorable role in inducing the I→H transition at relatively low auxiliary heating power on the HL-2A tokamak.

3.2 Impact of the MHD mode crash on edge plasma parameters

In order to understand the underlying physics of the MHD mode collapse in triggering the L→I or I→H transition, we look first on the influence of the MHD mode crash on the evolution of edge plasma parameters in two types of discharges with the same NBI heating power. One is the L→I→L, while the other is the L→I→H shot. Figure 2 plots the time history of the D_α signal, the central line-averaged density, magnetic fluctuations and their RMS level, the edge radial electric field ($-E_r$), the edge pressure gradient ($-\nabla_r P_e$) and the ambient turbulence level in density fluctuations ($\tilde{n}_e^{rms}$ filtered in 20-100 kHz) during the L→I→L (#19274) and L→I→H (#19380) transitions, respectively. For the measurements of E_r, $\nabla_r P_e$ and $\tilde{n}_e^{rms}$, the probe position is located at $\Delta r \approx -8$ mm inside the last closed flux surface (LCFS). In both cases, the transition from the L to I phase is accompanied by an abrupt crash of the MHD mode, as shown in figures 2(c1, d1) and (c2, d2). However, during the I-phase, the MHD behaviors are quite different between these two type discharges. In case of L→I→L there is nearly no MHD activity in the I-phase, whereas for the L→I→H a strong MHD mode is developed during the I-period and it drastically collapses prior to the I→H transition. The impact of the abrupt MHD mode crash on edge plasma parameters can be seen in figures 2 (e1, f1, g1) and (e2, f2, g2). For the discharge of L→I→L (left column), after the quick MHD collapse (or L→I transition) the strength of edge E_r ($|-E_r|$) and $|\nabla_r P_e|$ gradually increase and then keep constant for a while during the I-period, along with

reduction in ambient turbulence level ($\tilde{n}_e^{rms}$). Finally, all of these quantities return to the L-mode level without presence of any large MHD mode. In contrast, for the I→H transition (right column) the rapid mode crash in the I-phase excites sharp increases in $|E_r|$ and $|\nabla P_e|$, and concurrently, a sudden drop in $\tilde{n}_e^{rms}$ before entering into the H-mode.

Across the I→H transition, the influence of the quick MHD mode crash on the equilibrium profile has also been surveyed and depicted in figure 3. Plotted in figures 3(a)–(d) are time evolutions of the D_α signal, the RMS level in magnetic fluctuations together with multi-chord-averaged density ($\bar{n}_{el}$) and electron temperature (T_e) measured by HCN and ECE diagnostics at different radial locations. From figures 3 (b), one can see that during the I-phase an MHD mode is developed and it grows rapidly. At about t=507.3 ms, the mode collapses and concurrently dramatic changes occur in the density and temperature signals. In the inner region of the core plasma, both $\bar{n}_{el}$ and T_e quickly reduce, as seen in green curves in figures 3(c) and (d), while in the outer area both of them increase (see brown curves). These results clearly show a release of plasma energy from the core to the edge region due to the MHD mode crash. As such, both of the density and temperature profiles are altered considerably from the peaked to flattened one (see figures 3 (e) and (f)). The change of the profiles results in a significant increase in the edge pressure gradient and the radial electric field, as shown by the sudden jump in the $|\nabla_r P_e|$ and $|E_r|$ signals in figures 2(e2) and (f2). Then, the enhanced $E_r \times B$ flow shear will suppress the micro-turbulence magnitude, as indicated in figure 2(g2). To further verify the role of the $E_r \times B$ flow shearing on the decorrelation of turbulence eddies, we have compared the time evolutions of the $E_r \times B$ flow shear rate ($\gamma_{E\times B}$) with the local turbulence decorrelation rate (γ_D) measured at $\Delta r \approx -8$ mm by probes across the I→H transition. The results are shown in figure 4. Here the $\gamma_{E\times B}$ is defined as $\gamma_{E\times B} = \partial E_r/(\partial r B_t)$ and the γ_D is calculated from the inverse of the autocorrelation time of density fluctuations. The data are taken from 10 shots with similar magnitude in the MHD mode oscillations. The time $\Delta t=0$ is defined at the time when the edge radial electric field and pressure gradient start to jump up during the I-phase. The error bars are estimated from the standard deviation about the mean over the 10 similar discharges. In the figure one can clearly see that before the MHD mode collapse ($\Delta t<0$) the γ_D is larger than $\gamma_{E\times B}$ during the I-phase, whereas after the mode crash ($\Delta t>0$) the $E_r \times B$ shear rate quickly rises up and the local turbulence decorrelation rate reduces significantly so that $\gamma_{E\times B} > \gamma_D$, resulting in turbulence suppression, and consequently, the transition from the I-phase into the H-mode. These results are generally in agreement with the turbulence decorrelation theory for the L-H transition [21]. It should be pointed out that for many years the effect of sawtooth crash on triggering the L-H transition has been widely observed [22-24]. However, the detailed physical process has not yet been reported. In this work, we provide for the first time the clear evidence showing the

physical connection between the energy release evoked by the MHD collapse and edge flow shearing on turbulence, which eventually excites an improved confinement into the H-mode.

3.3 Properties of the MHD mode

In this section, our attention focuses on exploring the nature of the MHD mode prior to the I→H transition. For this purpose, we have made an expanded time window in figures 5 (a)–(c) for the time history of the D_α and magnetic fluctuation signals drawn in figures 2(a2) and (c2), along with the time evolution of the frequency spectrum of the magnetic fluctuations. It can be seen that the MHD mode appears twice with a lifetime of 2–5 ms and a chirping frequency of 14–19 kHz before the I→H transition. The first mode grows and decays in a mild way. But for the second one the mode amplitude increases dramatically at the late stage and then crashes abruptly. The influence of the mode magnitude and decay rate on plasma parameters will be further illustrated in section 3.4. To investigate the spatial location of the mode, figure 5(d) compares the time evolution of soft x-ray (SXR) signals measured at three different radial positions. It is found that the oscillation magnitude is quite high in the core plasma and it quickly diminishes toward the edge region, suggesting that the MHD mode is localized in the plasma core area. For further identifying the spatial structure of the mode, we have made tomographical reconstruction of the SXR emission by using a Bayesian tomography method [25]. The Singular-Value-Decomposition has been implemented on these reconstructions to abstract the perturbation modes from the total emission. Figure 6(a) plots the temporal evolution of the Mirnov signal before I→H transition, The graphs below (Figs. 6(b) and (c)) show the reconstructed mode structures at the time of "t" prior to the mode crash. One can clearly see that this mode has a dominant structure of m/n=1/1 and a harmonic m/n=2/2, which rotates around the q=1 surface. Similar structures have been found for all of the perturbative MHD modes depicted in figures 1 and 2 in the L and I phases.

Further studies reveal that this mode is associated with the energetic-particle-driven fishbone, whose frequency is close to the procession frequency of trapped ions. As shown in figure 5(c), the experimentally observed mode frequency is about 14-19 kHz. The procession frequency of trapped ions is estimated by $f_{pro} = qEH(k,s)(1+0(\varepsilon))/eB_tRr$, where *q, E, ε and s* represents the safety factor, the ion energy, inverse aspect-ratio and magnetic shear, respectively. The $H(k,s)$ is the geometrical factor [26] . For the HL-2A discharge parameters, the B_t is 1.4 T and the pitch angle $\upsilon_{//}/\upsilon \approx 0.15$. Assuming that the energetic particles are attributed to the NBI energy (ion source 40 keV), the procession frequency of the energetic-particle-driven fishbone is about $f_{pro} \approx 13$ kHz near the q=1 surface, as marked by the cross symbol in figure 6 (d). Here, the effect of Doppler-shift frequency has been taken into account. Using $k_\phi \approx 1/qR \approx 0.6$ m^{-1}, V_ϕ=(30-50) km/s measured by the charge-exchange-recombination spectroscopy (CXRS) [27], the Doppler-shift frequency $f_{Dop}=k_\phi V_\phi/2\pi \approx 3$-5 kHz. Thus, the mode frequency in the lab frame is $f_{lab}=f_{pro}+f_{Dop} \approx 16$-18 kHz, in good agreement with our observations. This result indicates that the MHD mode

mentioned above is the trapped-ion-driven fishbone. In fact, at HL-2A another sort of kink-type MHD mode, the so-called long-lived mode, has also been frequently observed and it plays a similar role in triggering the I→H transition.

3.4 Influence of the mode crash rate on plasma parameters and the I→H transition.

In figures 1 and 2, one may notice that the kink-type mode of fishbone is routinely developed during the L-mode or I-phase for more than one time. However, only an abrupt crash of the MHD mode with a large amplitude and a fast decay rate can trigger the L→I or I→H transition. To understand this effect, we plot in figure 7 the time history of two fishbone modes with different decay rates in the I-phase before the I→H transition, along with the multi-channel line-averaged density and electron temperature. One can see that the first mode decays rather slowly (starting at t≈817 ms from the climax) within ~ 3 ms, while the second one collapses (starting at t≈825.5 ms) much faster in a time scale of 0.5 ms, as shown in figure 7(c) in the RMS level of the MHD modes. For the first slow crash at t≈817 ms, there is nearly no influence on the electron temperature and density at various radial locations. But for the second abrupt mode crash, both of the temperature and density are affected remarkably. These results explicitly indicate that only the fast decay of the MHD mode, i. e., a sufficiently quick release of plasma energy, can effectively modify the pressure profile, and hence, increase the edge pressure gradient and radial electric field, which further suppresses edge turbulence and leads to an improved confinement.

4. Summary

In this article, a kink-like MHD mode, routinely developing and abruptly crashing prior to the L→I and I→H transitions with low heating power in the HL-2A tokamak, has been reported. It has been found that the mode has fishbone characteristic with the procession frequency f≈14–19 kHz and spatial mode structures m/n=1/1 and 2/2 around the q=1 surface. The rapid mode crash evokes substantial energy release from the core to the plasma boundary and hence increases the edge pressure gradient and E_r×B flow shear, which further suppresses turbulence and leads to confinement improvement into the H-mode. Under the same NBI heating, the I-phase plasma transits into H-mode with a rapid mode crash while it returns to the L-mode without the presence of the mode in the I-phase. With increasing heating power by the ECRH added to the NBI, the kink-like mode disappears and the plasma enters into the H-mode with an overall rising in density and temperature profiles. Meanwhile, the lifetime and magnitude of the I-phase oscillation are both reduced. The statistical result shows that with the MHD mode crash the heating power for accessing the H mode is significantly lower than that without the mode crash. All these facts reveal that the MHD mode crash in the I-phase plays a critical role in trigging the I→H transition at marginal heating power. In addition, it has been found that with the same NBI power heating, the magnitude of the mode (crash) increases with increasing plasma density. This observation suggests that larger energy release is needed for accessing the H-mode regime for higher density plasmas, in accordance

with the empiric scaling of the L-H threshold power.

Acknowledgment

This work is partly supported by Chinese National Fusion Project for ITER under grant Nos. 2015GB104000, and the National Natural Science Foundation of China under Grant Nos. 11375054, 11575057. It was also partially supported was partly supported by the Post-CUP program.

References:

[1] Martin Y R et al 2008 J. Phys. Conf. Ser. 123 012033
[2] Doyle E J et al 2007 Nucl. Fusion 47 S18
[3] McKee G R et al 2009 Nucl. Fusion 49 115016
[4] Ryter F et al 2013 Nucl Fus 53 113003
[5] Andrew Y et al 2004 Plasma Phys. Control. Fusion 46 A87
[6] Gohil P et al 2011 Nucl. Fusion 51 103020
[7] Meyer H et al 2011 Nucl. Fusion 51 113011
[8] Ma Y et al 2012 Plasma Phys. Control. Fusion 54 082002
[9] Ryter F et al 2014 Nucl. Fusion 54 083003
[10] Cheng J et al 2014 Nucl. Fusion 54 114004
[11] Yan L W et al 2005 Rev. Sci. Instrum. 76 093506
[12] Itoh S -I et al 1991 Phys. Rev. Lett. 67 2485
[13] Kim E J et al 2003 Phys. Rev. Lett. 90, 185006
[14] Estrada T et al 2011 Phys. Rev. Lett. 107 245004
[15] Conway G D et al 2011 Phys. Rev. Lett. 106 065001
[16] Schmitz L et al 2012 Phys. Rev. Lett. 108 155002
[17] Xu G S et al 2011 Phys. Rev. Lett. 107 125001
[18] Kobayashi T et al 2013 Phys. Rev. Lett. 111 035002
[19] Cheng J et al 2013 Phys. Rev. Lett. 110 265002
[20] Shesterikov I et al 2013 Phys. Rev. Lett. 111 055006
[21] Burrell K H et al 1997 Phys. Plasma 4 1499
[22] Tynan G R et al 1994 Phys. Plasma 1 3301
[23] Ido T et al 2002 Phys. Rev. Lett. 88 055006
[24] Martin Y R et al 2004 Plasma Phys. Control. Fusion 46 A77
[25] Li D et al et al 2013 Rev. Sci. Instrum. 84 083506
[26] Yu L M et al 2013 Nucl. Fusion 53 053002
[27] Wei Y L et al 2014 Rev. Sci. Instrum. 85 103503

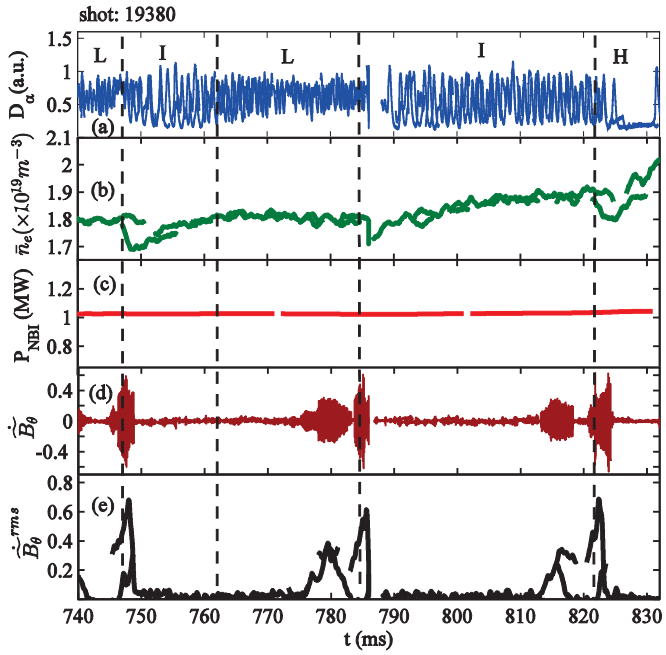

Fig. 1 Temporal evolutions of (a) D_α emission; (b) the central line-averaged density; (c) NBI heating power; (d) the magnetic fluctuation signal and (e) the RMS level of magnetic fluctuations across the time period of L→I→L→I→H mode transitions.

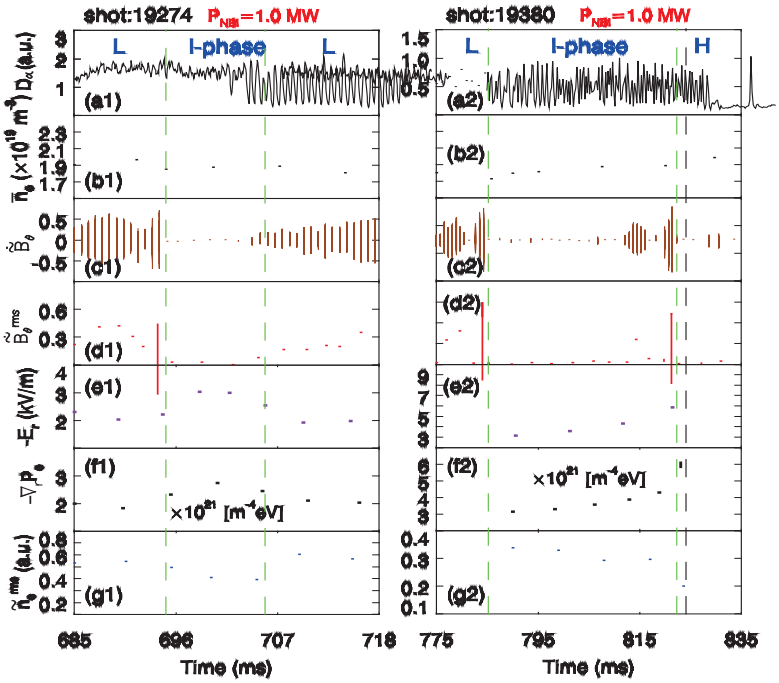

Fig. 2 Temporal evolutions of D_α emission (a1, a2); the central line-averaged density (b1, b2); the magnetic fluctuation signal (c1, c2); the RMS level of magnetic fluctuations (d1, d2); the radial electric field (e1, e2); edge electron pressure gradient (f1, f2) and the RMS level of density fluctuations (g1, g2) in the L→I→L (left column) and L→I→H (right column) discharges under

the same NBI heating power.

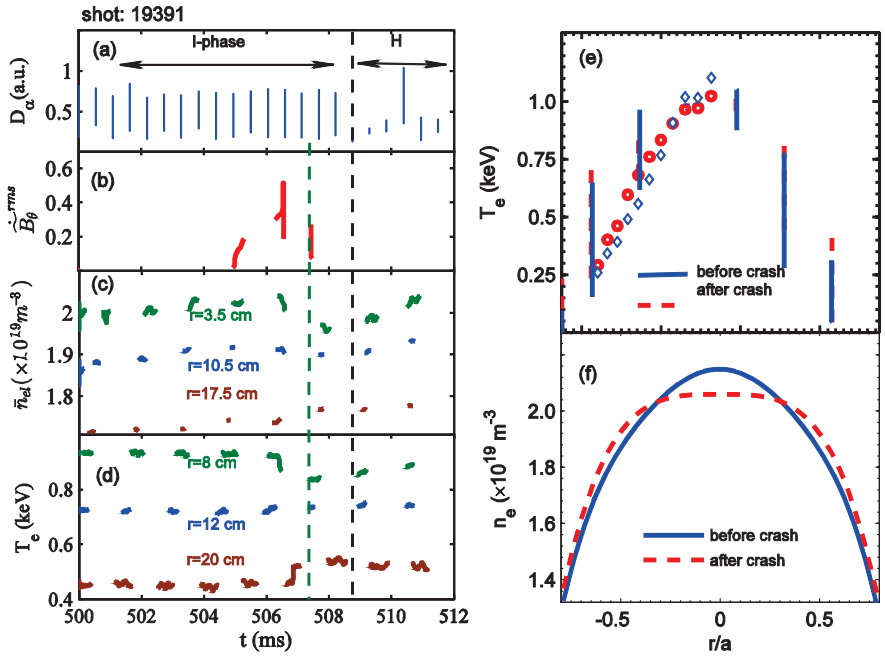

Fig. 3 Left: time evolutions of (a) D_α emission; (b) the RMS level of magnetic fluctuations; (c) the chord-averaged density detected by different HCN channels and (d) the electron temperature detected by multi-channel ECE diagnostic at various radial locations across the I→H transition. Right: comparison of radial profiles of (e) electron temperature and (f) plasma density estimated by Abel inversion from multi-channel HCN signals before (blue curves) and after (red curves) the kink-like mode crash during the I-phase.

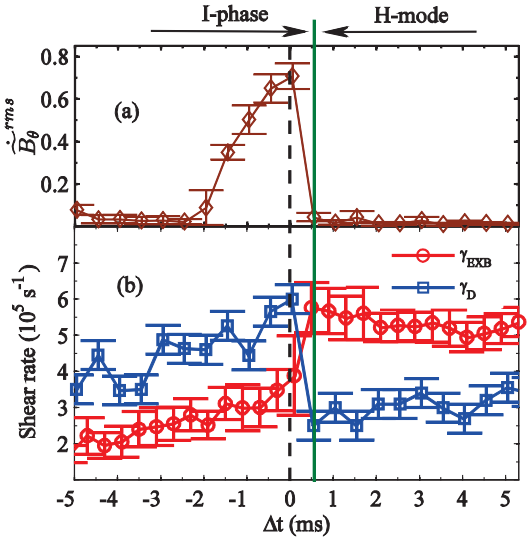

Fig. 4 Time-resolved evolutions of (a) the MHD mode magnitude indicated by the RMS level of magnetic fluctuations and (b) the E_r×B flow shear rate (red symbols) and turbulence decorrelation rate (blue symbols) measured at $\Delta r \approx -8$ mm by probes across the I→H transition. The $\Delta t=0$ is defined as the starting time of the MHD mode collapse. The data are averaged over 10 similar shots.

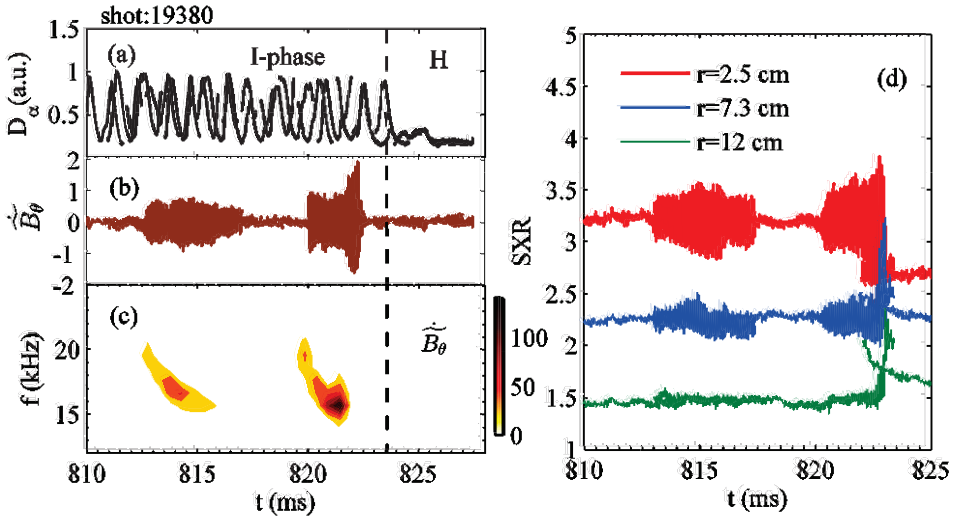

Fig. 5 Temporal evolutions of (a) D_α emission; (b) magnetic fluctuation signal and (c) the frequency spectrum of magnetic fluctuations during the I→H transition. Shown in (d) is the comparison of SXR signals measured at three different radial locations.

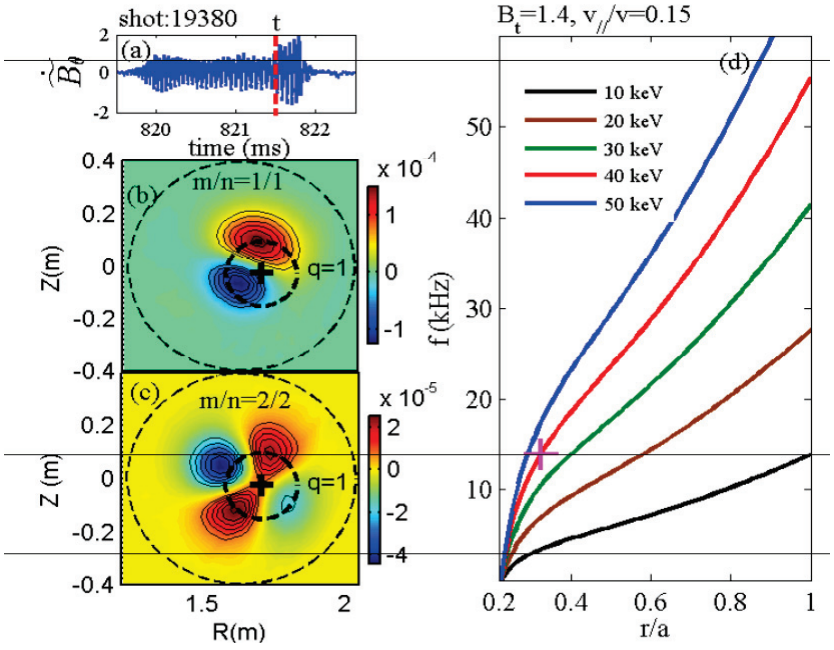

Fig. 6 (a) Temporal evolutions of the Mirnov signal along with contour-plots of the tomographically reconstructed SXR emission around the time of "t" before the mode collapse; (b) estimation of procession frequencies of trapped ions with different NBI energies at B_t =1.4T and the pitch angle =0.15.

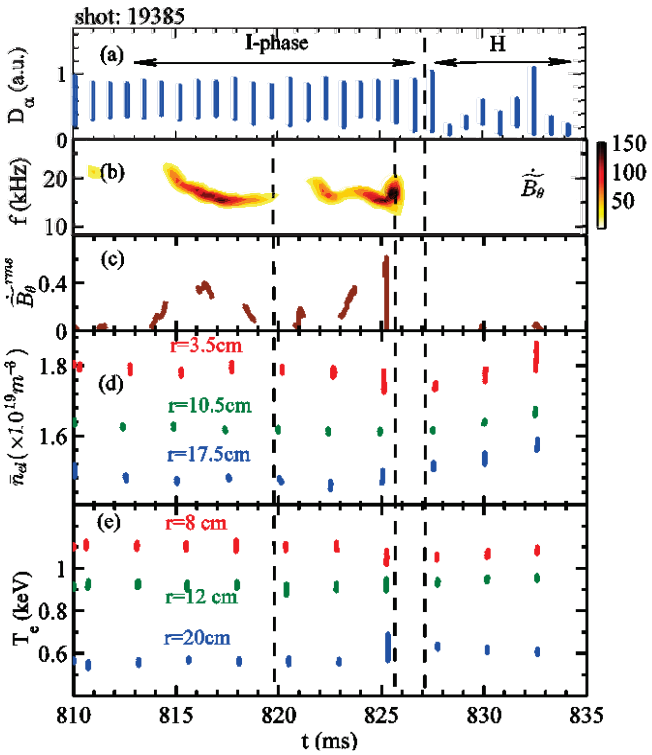

Fig. 7 Temporal evolutions of (a) D_α emission; (b) the frequency spectrum of magnetic fluctuations; (c) the RMS level of magnetic fluctuations; (d) chord-averaged density detected by HCN channels and (e) and electron temperature detected by multi-channel ECE at different radial locations across the I→H transition.

Recent Research Activities on the SUNIST Spherical Tokamak

Z. Gao[1], and the SUNIST group[1, 2]

[1]Department of Engineering Physics, Tsinghua University, Beijing 100084, China

[2]Institute of Physics, Chinese Academy of Sciences, Beijing, China

Abstract

Recent research activities on the SUNIST spherical tokamak are introduced. Experimental researches are focused on MHD behaviors during plasma current (Ip) ramp up /down phases of ohmic discharges, including toroidal Alfven eigenmodes (TAEs) during minor disruption, internal reconnection events (IREs) in Ip ramp-down phase, and tearing mode(TM) instabilities in Ip ramp-up phase.

1. Introduction

In tokamak discharges, the magneto-hydrodynamic (MHD) stability strongly relays on the profile of the plasma current and pressure. Therefore, various MHD activities appears in the ramp-up and ramp-down stage of plasma current.

During the ramp-down stage, the MHD activities have strong impacts on the operation safety of fusion plasma device. The avoidance of major disruption and/or the emigration/suppression of runaway electrons during disruption is of great importance in tokamak plasmas. However, major disruption seldom occurs in spherical tokamak (ST), instead of minor disruptions or IRE relaxation. Therefore, ST provides a unique platform for studying MHDs during Ip ramp-down phase. On the other hand, since the current torus in a spherical tokamak has a smaller inductance than that of traditional tokamaks due to small major radius as well as the low aspect ratio of the torus, the plasma current in a spherical tokamak will generally exhibit a faster current rise speed, which is accompanied with heavier skin effect and increases the potential for detrimental MHD activities. Although the inherent MHD stability of spherical tokamaks reduces the tendency of disruptions, fast confinement deteriorations have been experimentally observed during the fast current rise, which deters the plasma from reaching the high beta regime.

The SUNIST device is a typical university-scale spherical tokamak. Its typical parameters are as follows: major radius/minor radius ~ 0.3m/0.23m; magnetic field at the axis < 0.3T, plasma current < 80kA; plasma density ~ $1*10^{19}$m-3; pulse durations ~ 10~20ms. Recently, SUNIST focuses on MHD behaviors during IP ramp up /down phases of ohmic discharges, including toroidal Alfven eigenmodes (TAEs) identification during minor disruption and internal reconnection events (IREs) in Ip ramp-down phase, and tearing mode(TM) instabilities in Ip ramp-up phase.

2. Toroidal Alfven eigenmode during minor disruption in Ip ramp-down phase

Toroidal Alfven eigenmodes (TAEs) excited in purely ohmically heated plasmas without any auxiliary heating have been identified for the first time in the SUNIST spherical tokamak. [1] The experiments were

performed in purely ohmic plasmas with Ip ~ 40 kA, toroidal magnetic field Bt ~ 0.15 T. The line-averaged density was measured by a 94 GHz microwave interfer- ometer within the range of 0.2–6 *10^{18} m^3. The hard x-ray (HXR) was detected by CdZnTe with a narrow collimating aperture, which was used to estimate the energy of REs.

Typical discharge is shown in figure 1. A series of minor disruption was displayed in the Ip ramp-down phase. The MHD activities were observed during minor disruptions with a frequency range of 150–500 kHz. Figure 2 shows that the mode structure analysis indicated the existence of both m/n~-3/-1 and -4/-1 harmonics, propagating in the electron diamagnetic direction in the laboratory frame of reference. When the density or magnetic field varied, the frequency also changed. Figure 3 shows that the observed mode frequency scales linearly with the calculated TAE frequency. Also, TAE calculated by the GTAW code [2] agrees with experimental results. These TAEs appear simultaneously with the generation of runaway electrons in the current quench phase, accompanying with the density sweeping during the minor disruption. Recent in the MAST, J-TEXT and HL-2A,[3] there were also observed some high-frequency Alfven-like MHD oscillations during minor or major disruptions. All of these indicate that be some stories between Alfven instabilities and disruption/RE. However, the driving mechanisms of these TAEs are still open.

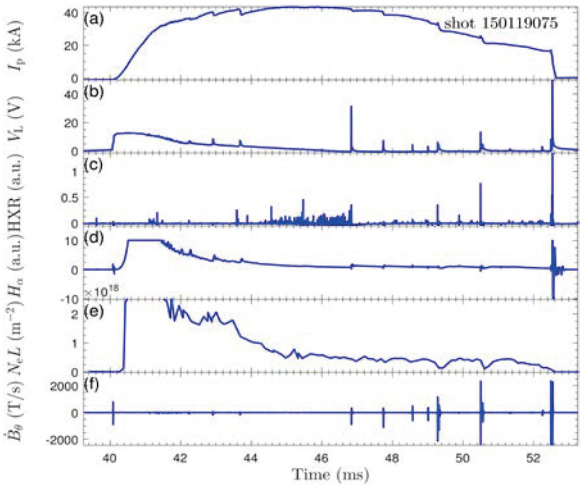

Figure 1. Typical discharge with minor disruptions in the SUNIST

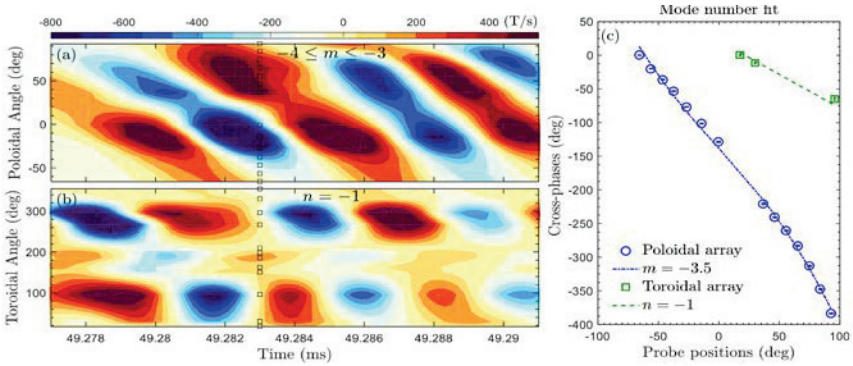

Figure 2. Toroidal and poloidal mode structure analysis

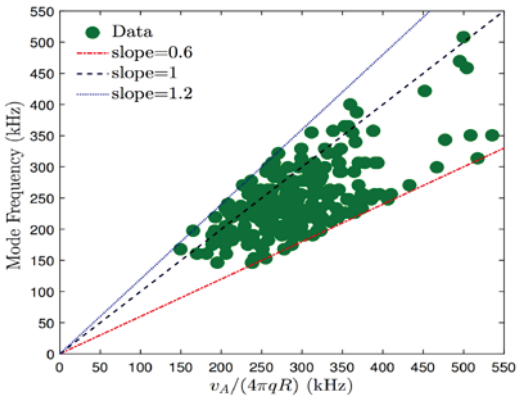

Figure 3. Observed mode frequency scales linearly with the calculated TAE frequency

3. Internal reconnection events (IREs) in Ip ramp-down phase

In SUNIST, two typical phenomena were observed in Ip ramp-down phase. One is the minor disruption described in last section. The other is so-called IREs, which is frequently observed in STs, and the IREs can be observed as a collection of various MHD activities in different phases, which is shown in figure 4.[4] The cross-bispectrum during the TQ phase shown in figure 5 indicated that the multi-field energy transfer from electrostatic to magnetic fluctuations. This behavior can also be seen in figure 6 as the time history of the wavelet spectra. In the CI phase, it results in mode coupling in magnetic fluctuations, growing to a large scale with a broad frequency spectrum, finally leading to the reconnection of local field lines, which is just the so-called IREs. However, in the CQ phase the magnetic fluctuations returns energy to electrostatic one and the system gradually comes back to a stationary state.

The mechanism displayed in the excitation of IREs in the SUNIST is different to the Hayashi's simulation picture.[5] Although the IREs was due to the mode coupling, the mode with high f magnetic fluctuation grew due to nonlinear coupling in the SUNIST experiment rather than the linear instability simulated in Hayashi's simulation.

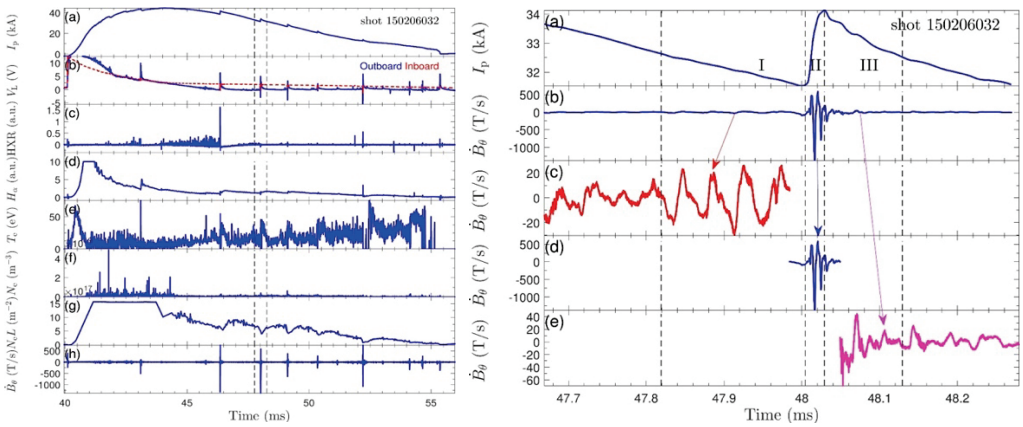

Figure 4. (left) typical discharge with IREs in the SUNIST; (right) three phases of IRE evolution: thermal quench (TQ), current increment (CI) and current quench (CQ)

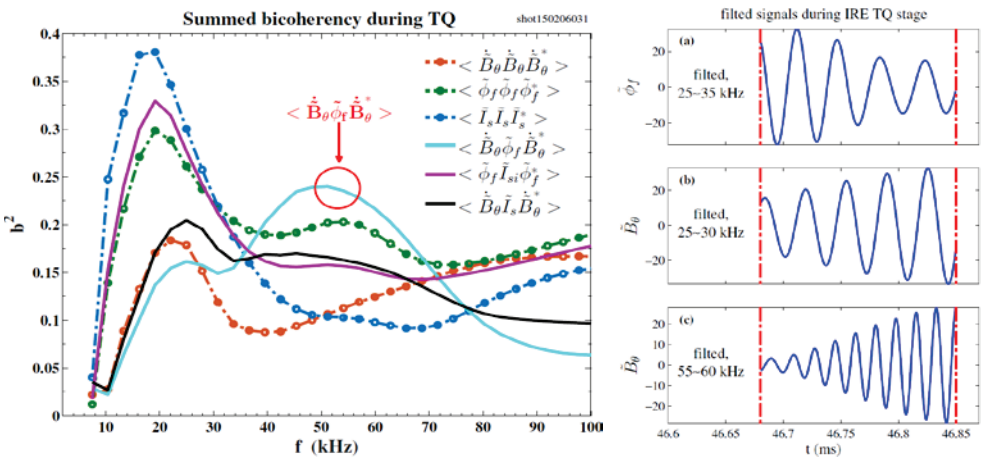

Figure 5. (left) Cross-bispectrum during the TQ phase of IREs; (right) Time history of the wavelet spectra.

4. Tearing mode(TM) instabilities in Ip ramp-up phase.

Figure 6 displayed a typical plasma discharge with strong TM activities in the current ramp up stage. [6]The TM activities started at 40.5 ms and weakened spontaneously at 43 ms with the measured MHD frequency from ~10 kHz rising to ~20 kHz. Although the TM activities disappeared finally after the ramp up, it is clearly shown that it caused a significant loss of plasma confinement. Consequently, the plasma exist with a rather low density.

The TM instabilities was carefully measured with the magnetic diagnostic system, which includes a 12-channel toroidal probe array, a 14-channel poloidal probe array at the low field side, and a 30-channel radial probe array with high spatial resolution. It is easily found that, the $n = -1$ mode was dominant throughout the MHD stage for most of the discharges. the poloidal mode number appeared to be decreasing throughout the MHD evolution, from $|m| \approx 6$ to $|m| \approx 3$. The radial mode structure is also of particular interest when considering the position and size of the magnetic island. The radial distribution of B □$_\theta$ as measured by the radial probe array is illustrated in figure 7, where a conspicuous phase reversal layer could be observed. Such a phase reversal layer extracts the approximate position of the magnetic island chain. Figure 7 also indicated that as I_p was rising, the rational q surfaces generally shifted outward, which agree with the observation of the poloidal mode number to decrease during the current rise.

Figure 8 shows the correlation of density confinement, indicated by □$n_{emax,}$ to the radial position of the magnetic island chain, $R_{inv,}$ and the amplitude of TM, $\langle \delta B_\theta \triangleleft B_\theta \rangle_{max}$. Although the variation in $\langle \delta B_\theta \triangleleft B_\theta \rangle_{max}$ could explain some observations, it failed to explain the results when R_{inv} was close to the edge. When R_{inv} approached the edge, $\langle \delta B_\theta \triangleleft B_\theta \rangle_{max}$ became weak while n_{emax} still decreased. In fact, figure 8(b) shows the relation between n_{emax} and R_{inv}, neglecting the variation in the perturbation level. It can be found that the confinement deterioration effect could be approximately described by R_{inv} alone in both OF control and VF control. It indicated that R_{inv} plays a dominant role in the confinement deterioration effect rather than the magnetic perturbation amplitude. Therefore, during the current rise, the confinement deterioration effect of the TM activity might be reduced effectively by controlling the magnetic island chain position.

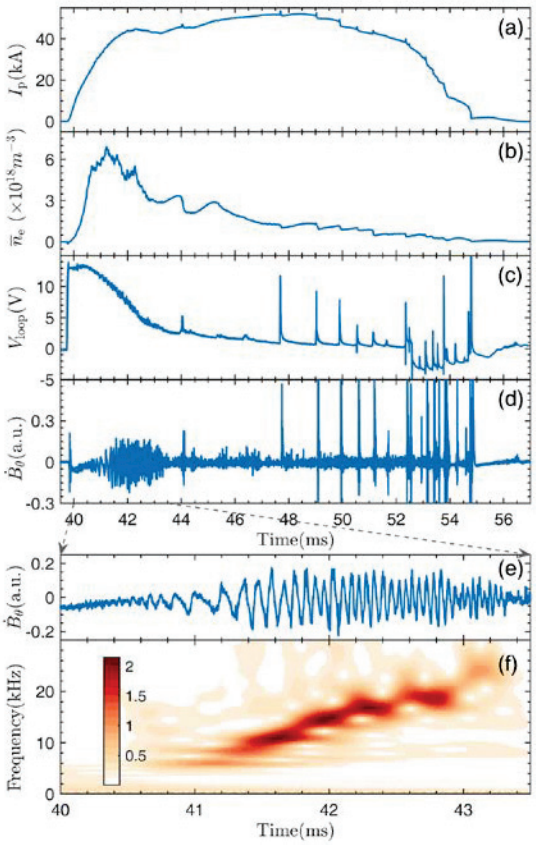

Figure 6. Typical discharges with TM instabilities

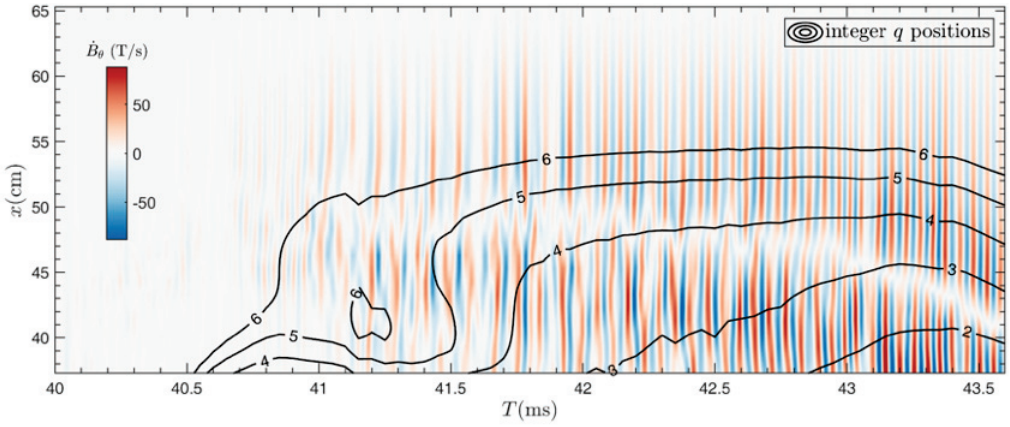

Figure 7. The radial distribution of B $\dot{\theta}$ during current rise. Calculated q positions also labelled.

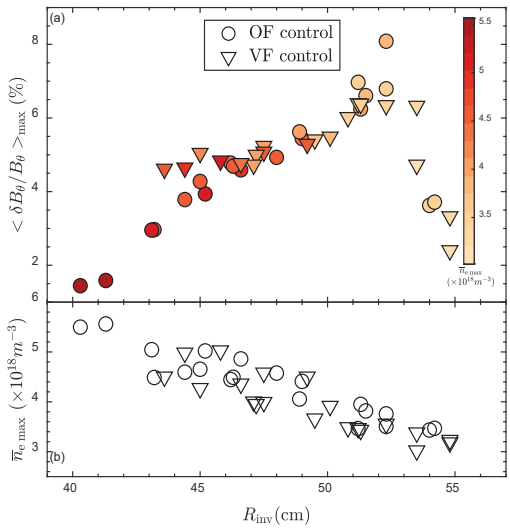

Figure 8. The corelation of density confinement to the amptitute of TM and the radial position of the magnetic island chain

5. Summary

MHD activities during the startup, ramp-up and ramp-down of plasma current have important impacts on plasma performances as well as the operation safety of plasma device. Here the MHD behaviors in the SUNIST spherical tokamak, including tearing modes during ramp-up phase, REs and TAEs during ramp-down phase were investigated preliminary. It is hoped to explore an effective way to control the MHD activity during plasma startup by multiple methods and following fast current ramp-up, and, meanwhile, to find a ramp-down senarios to increase the resilence of plasma and to decrease the energy and percentage of runaway electrons. Further understanding of these MHD behaviors are still necessary. The development of advanced diagnostics with high spatial and temporal resolutions are needed as well.

Acknowledgements

This work was supported by NSFC under Grant Nos. 11827810 and 11875177, Science Challenge Project with No. TZ2016005, and National Ten Thousand Talent Program. This work was also partly supported by the Post-CUP program.

References

[1] Yangqing Liu, Yi Tan, Zhe Gao, et al, Phys. Plasmas 23, 120706 (2016)

[2] Y. J. Hu, G. Q. Li, N. N. Gorelenkov, et al, Phys. Plasmas 21, 052510 (2014).

[3] M. Gryaznevich, private communication (2016); Z. Y. Chen, private communication (2016); Y Liu, IAEA FEC 2016 EX9-3

[4] Song Chai, Yuhong Xu, Zhe Gao, et al, Phys. Plasmas 24, 032503 (2017).

[5] T. Hayashi, N. Mizuguchi, T. H. Watanabe, Y. TOdo, and T. Sato, Nucl. Fusion 40, 721 (2000).

[6] Zhong, H., Tan, Y., Gao, Z.,Nucl. Fusion 58, 126013 (2018)

Experimental study of disruption mitigation by shattered pellet injector on HL-2A

Y.B. Dong, H. B. Xu, C.Y. Chen, J.M. Gao, Y.P. Zhang, X. Q. Ji, Yi Liu

Southwestern Institute of Physics, Chengdu, China

Abstract

A shattered pellet injector (SPI) based on in situ technology was developed in the HL-2A tokamak. In this paper, the basic principle of pellet formation is introduced, t the mechanism of a SPI is described in detail, and test results are presented. Bench test experimental results show that reliable formation and acceleration of a large nitrogen pellet (diameter of ~3.5 × 4 mm) were obtained. A double-impact tube was developed and tested for effective and reliable shattering of the pellet.

1. Introduction

Plasma disruptions cannot be avoided during tokamak operations. Plasma disruptions damage the tokamak by heat loads deposited on plasma-facing components (PFCs). Additionally, large electromagnetic faces acting on the device and runaway electrons will also impact and damage PFCs. So, it is necessary to look for some effective method to mitigate plasma disruptions.[1–4]

Usually, pellet injection and massive gas injection (MGI) are used to mitigate damage caused by the plasma disruptions. Experimental results from fusion devices indicate that MGI can mitigate the heat load and Halo current. But, the critical Rosenbluth density for the suppression of runaway electrons cannot be obtained. However, shattered pellet injection as an effective strategy for mitigating plasma disruptions has been investigated in DIII-D (Ref. 5). The experimental results show that shattered pellet injection can improve penetration depth, enhance assimilation, and lead to higher plasma density when compared with MGI with the same quantity of injection atoms. The results also show that thermal quench (TQ) and current quench (CQ) are controlled in mitigated disruptions.[6] This cools the plasma to reduce the TQ heat load, speed up the current decay, and reduce the halo currents. A shattered pellet injector (SPI) technique has been shown to have several advantages relative to MGI. This observation indicates that a SPI should be a good candidate to mitigate plasma disruption in ITER.

In order to verify the effects of shattered pellet injection for plasma disruption mitigation, a SPI based on in situ pellet formation technology has been developed in the HL-2A tokamak.

2. HL-2A Shattered Pellet Injector

A shattered pellet injector based on the in-situ technology was developed for HL-2A. Pellet is produced by in-situ technology in cryogenic vacuum chamber. The technology is very mature. Compared with the extruder, it has a simpler structure and lower cost. Fig.1. is the shattered pellet injector (SPI) on the HL-2A tokamak. The size of the shattered pellet injector is 2700mm by 945mm by1300mm.

The pellet injector is composed of two-stage vacuum differential pumping system, cryostat, gas vacuum system, diagnostic system, etc. An advanced 2-stage GM-cycle refrigerator (Sumitomo Heavy Industries, Model RDK-415D) is used. This concept has demonstrated a high reliability, an easy maintenance, a

facilitated control of temperature and the turn-around time of an operation and a standstill time are shortened. It is easier to meet the condition for the formation of a pellet.

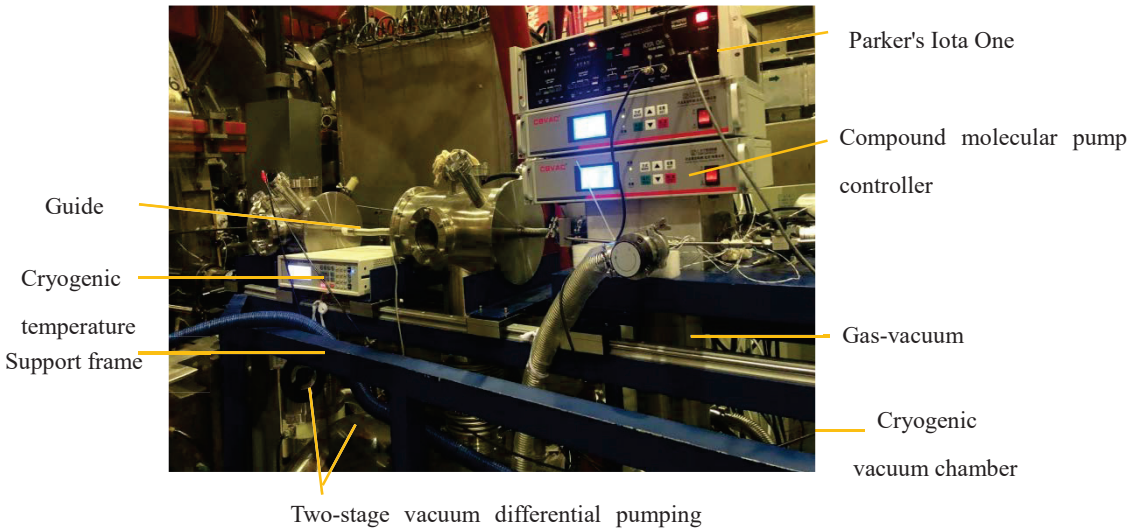

Fig. 1. The shattered pellet injector on the HL-2A Tokamak

The pellet injector can provide frozen pellets of different species, such as, N2, Ar or Ne, etc. The diameter and the length of pellet are 3.5mm and 4mm respectively. The pellet is accelerated by high-pressure helium gas (0.5MPa-6MPa, pure 99.999 %).The pellet injector can supply one shattered pellet during plasma disruption. The pellet velocity can be changed from 150 to 400 m/s under different propellant gas pressures. The injection reliability is required to be greater than 90%.

The pellet will be shattered before entering the plasma by Double-Impact-Tube at the entrance to the tokamak vacuum chamber. The basic design of the double impact tube is shown in Fig.2. Shattered pellets can achieve good effect by Double-Impact-Tube through the experiment. Normally, the time interval between injection cycles is about8 min.

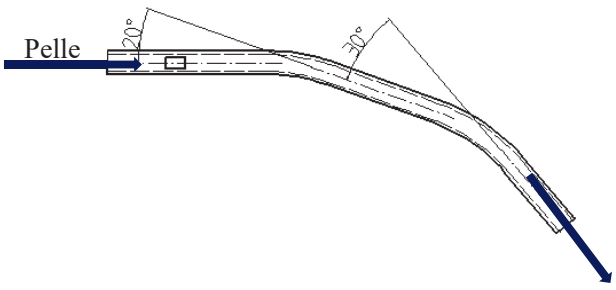

Fig.2. Schematic of double-impact tube

3. Experimental setup

HL-2A is a middle-size tokamak (major radius R =1.65 m and minor radius r = 0.4 m) with a closed divertor[7, 8]. The current direction in deuterium plasma discharges is counter-clockwise, but the toroidal magnetic field is clockwise.

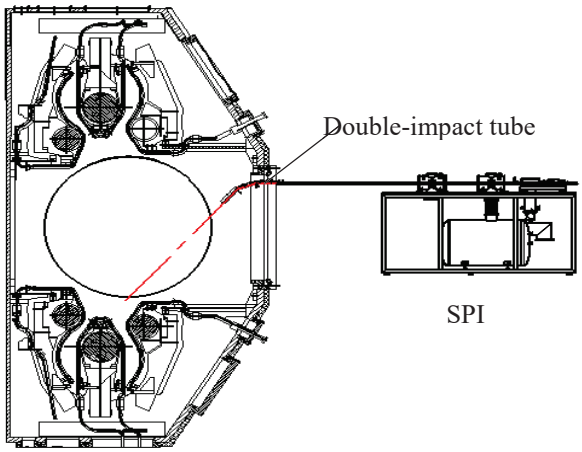

Fig. 3. Schematic view of the shattered pellet injector installed on HL-2A(major radius R =1.65 m, minor radius a = 0.4 m)

The pellet injection system is installed in a horizontal position. A series of diagnostics have been employed on HL-2A for SPI experiments in order to evaluate the effectiveness of the SPI system. Being constrained by the around space of HL-2A, the installation position of SPI is not reasonable, as shown in Fig.3. Shattered pellet is tangent injected. It is expected that particle numbers of shattered pellet will be reduced into plasma. Next, we will readjust the SPI installation location and implementing core injection.

4. **Experimental results**

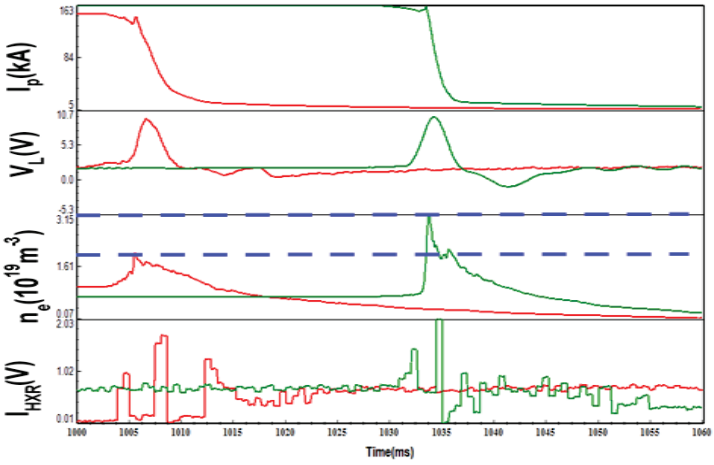

Fig. 4 The comparison of disruption mitigation for SPI versus MGI with 1.0×1021 atoms of Ar injection.

Disruption mitigation with MGI and SPI is designed to rapidly inject a large amount of material into the plasma in order to radiate the thermal energy of the plasma. A typical example of such comparison on identical scenarios with identical quantities of argon is shown in Fig.4. The typical plasma parameters during these experiments were a toroidal field of 1.6T, plasma current of 160kA, line-averaged electron density ne = 0.8×10^{19} m^{-3}, safety factor qa = 3.5.

The line-averaged electron density is on average about 1.4 times as large for SPI (3.15×10^{19} m^{-3}) than it

is for MGI (2.29×10^{19} m^{-3}). We think that since SPI injects material in the form of small cryogenic fragments, the resulting deposition is expected to be deeper by analogy with fueling pellets that have been observed to have a deeper deposition than gas puffing thanks to shielding effects from the cold gas and plasma surrounding the pellet that regulate the ablation process. The rate of current quench is about 80 MA/s by SPI, but the rate of current quench is about 52 MA/s by MGI. The difference between these two methods is about 50%. The plasma current decay time is about 7.6ms. The plasma current decay time is about 7.2ms. The results of the evaluation show that they have similar effects on current decay time. This indicates more efficient particle assimilation for SPI, which could result in better thermal energy dissipation.

5. Discussion

A SPI based on in situ technology was developed in HL-2A. Reliable formation and acceleration of a large nitrogen pellet (diameter of ~3.5 × 4 mm) were demonstrated in laboratory testing. In addition, a double-impact tube was developed and tested for effective and reliable shattering of the pellets. A SPI will be installed in HL-2A to carry out related disruption mitigation research.

During the commissioning of the injector, we found that the given temperature of the heat sink was much lower than the triple-point temperature of the nitrogen for producing a good pellet. Maybe this results from the large thermal resistance between the barrel and the heat sinks. To solve this problem, we will modify the connection structure between the barrel and the heat sinks. Meanwhile, a thin-walled steel barrel (diameter of 3.5 × 0.7 mm) replaces the existing barrel. It was also found that the shattered pellet through the double-impact tube was better at the speed of more than 300 m/s than that at the speed of less than 200 m/s. In addition, more tests should be done to study the performance of the Parker's pulse valve.

Acknowledgements

This work was partly supported by the Post-CUP program. It was also supported by National Key Research and Development Program of China (No. 2017YFE0301300), and was also partially supported by the National Key Research and Development Program of China (No. 2017YFE0300405, 2017YFE0300504).

References

[1]. M. SHIMADA et al., "Progress in the ITER Physics Basis—Chapter 1: Overview and Summary," Nucl. Fusion, 47, S1 (2007).

[2]. V. RICCARDO and JET EFDA CONTRIBUTORS, "Disruptions and Disruption Mitigation," Plasma Phys. Control. Fusion, 45, 12A (2003): A269.

[3]. S. K. COMBS et al., "Development and Testing of Plasma Disruption Mitigation Systems Applicable for ITER," International Atomic Energy Agency (IAEA) (IAEA-CN–197) (2012).

[4]. M. BAKHTIARI et al., "Fast Plasma Shutdown Scenarios in the JT-60U Tokamak Using Intense Mixed Gas Puffing," Nucl. Fusion, 42, 1197 (2002).

[5]. L. R. BAYLOR et al., "Disruption Mitigation Technology Concepts and Implications for ITER," IEEE Trans. Plasma Sci., 38, 419 (2010).

[6]. D. SHIRAKI et al., "Thermal Quench Mitigation and Current Quench Control by Injection of Mixed Species Shattered Pellets in DIII-D," Phys. Plasmas, 23, S128 (2016).

Detection of Magnetic Islands Using Imaging Diagnostics

S. Ohdachi[1], Y. Suzuki[1, 2]

[1]National Institute for Fusion Science, Toki 509-5292, Gifu, Japan

[2]Graduate University for Advanced Studies, Toki 509-5292, Gifu, Japan

Abstract

Plasma response to the externally applied magnetic field is fairly complicated issue. The physics of the shielding and penetration of the external field has not been fully understood. A new kind of diagnostics using two tangentially viewing SX camera system is proposed. Island detection from the reconstruction of 3D emission profile related to the magnetic field structure with L1 regularization is discussed in this study [1].

1. Introduction

In order to sustain the high-performance plasma having an edge transport barrier, instabilities related to the steep pressure gradient in the edge region is a critical issue. For example, the heat flux released by the excitation of the edge localized mode (ELM) is hazardous for the divertor of the next-generation Tokamak devices, such as the ITER. It is thus urgent to find a way to control the edge MHD activities. Though the resonant magnetic perturbation (RMP) is the most promising candidate to control the ELMs, the detailed mechanism how the RMP affects the MHD activities, has not been fully understood. In order to study the change of the behavior of the MHD instabilities, the determination of the equilibrium field is required.

If the externally applied magnetic field penetrate the plasma, the toroidal symmetry of the torus plasma is broken as shown in Fig. 1. From the difference of the two images, we can evaluate the wave number and the location of the magnetic island induced by the RMP [2]. However, it is not always possible to perform the forward modelling assuming a theoretical profile. If the direct reconstruction of the two camera data can be made, many physical phenomena can be studied. In this article reconstruction using orthogonal basis patterns and L1 regularization is discussed in detail.

2. Regression with orthogonal pattern and L1 / L2 regularization

Consider the problem that the local emission profile $\boldsymbol{g}$ is reconstructed from the line-integrated signals $\boldsymbol{f}$. With column vectors $\boldsymbol{f}$ and $\boldsymbol{g}$, $\boldsymbol{f}$ can be represented as, $\boldsymbol{f} = H\ \boldsymbol{g} + noise.$, using the geometrical relationship expressed as the matrix H. If the least square fitting method is used to solve, the following minimization may give the solution $\boldsymbol{g}$,

$$\boldsymbol{g} = \underset{(\boldsymbol{g})}{Argmin} \left| \ (f_i - \sum_i h_i \cdot \boldsymbol{g})^2 \right. \qquad (1)$$

where h_i is the i-th row vector of the geometrical matrix H. If this solution is ill-behaved and unstable to the noise, an additional penalty function is often introduced. When the penalty function is concerned with the total magnitude of the local emission, the function to be minimized becomes Eq. (2).

$$\boldsymbol{g} = \underset{(\boldsymbol{g})}{Argmin} \left| \; (f_i - \sum_i h_i \cdot \boldsymbol{g})^2 + \lambda \sum_i |g_i|^{\alpha} \quad (2) \right.$$

When $\alpha = 2$, the penalty function is the squared Euclid norm of the vector $\boldsymbol{g}$. This regularization scheme is called the L2 regularization (Ridge regression). When $\alpha = 1$, the scheme is called the L1 regularization (least absolute shrinkage and selection operator (Lasso) regression). Recently the algorithm for L1 regularization is significantly improved and widely used for the regression problems in various fields research.

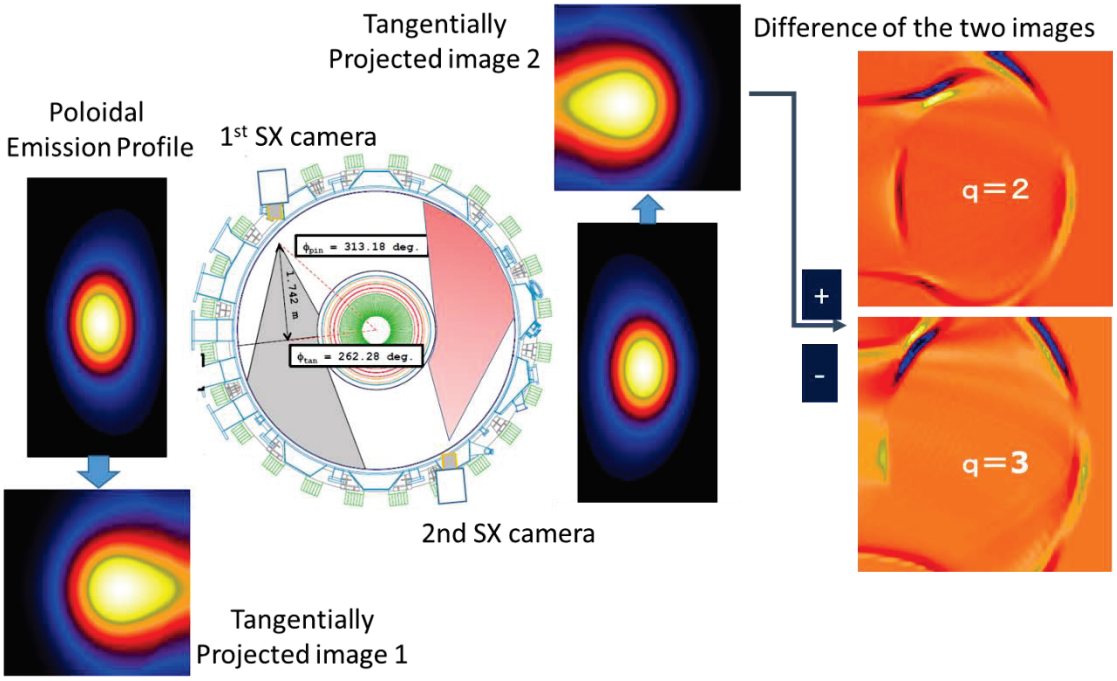

Fig. 1 Schematic view of the concept of the dual tangentially viewing SX camera system.

On the other hands, the series expansion method using global orthogonal basis patterns was a method proposed in the early stage of fusion research [3]. This method was quite effective for reconstructing the emission profile, especially, of the Tokamak plasmas in circular cross section. Since this method is based on the global patterns, it might be possible to reconstruct the emission profile from the information that is acquired by the measurements of much limited coverage of the entire objective region.

In the series expansion methods, the emission profile $\boldsymbol{g}$ is expanded by a series of patterns $\boldsymbol{b_i}$ as

$$\boldsymbol{g} = \sum_i \beta_i \boldsymbol{b_i} \qquad (3)$$

that is, we have a series expansion of $\boldsymbol{f}$ with basis patterns $\boldsymbol{x_i} = H\boldsymbol{b_i}$

$$\boldsymbol{f} = \sum_i \beta_i \boldsymbol{x_i} \qquad (4)$$

The relation can be written as $\boldsymbol{f} = \beta \cdot \boldsymbol{x}$, where $\boldsymbol{x} = \mathrm{H}\boldsymbol{b}$ .When the coefficients β_i are determined by the measurement, by minimizing the $\boldsymbol{\beta} = \underset{(\boldsymbol{\beta})}{Argmin} \left| \; \sum_i (f_i - \boldsymbol{\beta} \cdot \boldsymbol{x_i})^2 + \lambda \; \sum_i \beta_i^{\alpha} \right.$ (5)

L1 regularization is used for solving Eq. (5). After the coefficients β_i is determined, the local emission

profile $\boldsymbol{g}$ can be easily composed using Eq. (4).

3. Reconstruction of the tangentially viewing camera data

In this numerical test of reconstruction of the dual tangentially viewing camera system, Fourier-Bessel type basis patterns having $n = 0$ components and $n = 1$ components are used as,

$$\begin{aligned} \Psi_l^m(\rho,\theta,\phi) &= exp(im\theta)\ J_m(\lambda_m^l\rho)\ \ (n=0) \\ \Psi_l^m(\rho,\theta,\phi) &= exp(im\theta)\ J_m(\lambda_m^l\rho)\exp(i\phi)\ \ (n=1) \end{aligned} \tag{5}$$

Here, $J_m$is the m-th Bessel function of the first kind where λ_m^l is the l-th zero location of the m-th Bessel function. θ and ρ are the coordinate in poloidal direction and the averaged minor radius, respectively. ϕ is the toroidal angle. Schematic image of this 3D basis patterns are shown in Fig. 2.

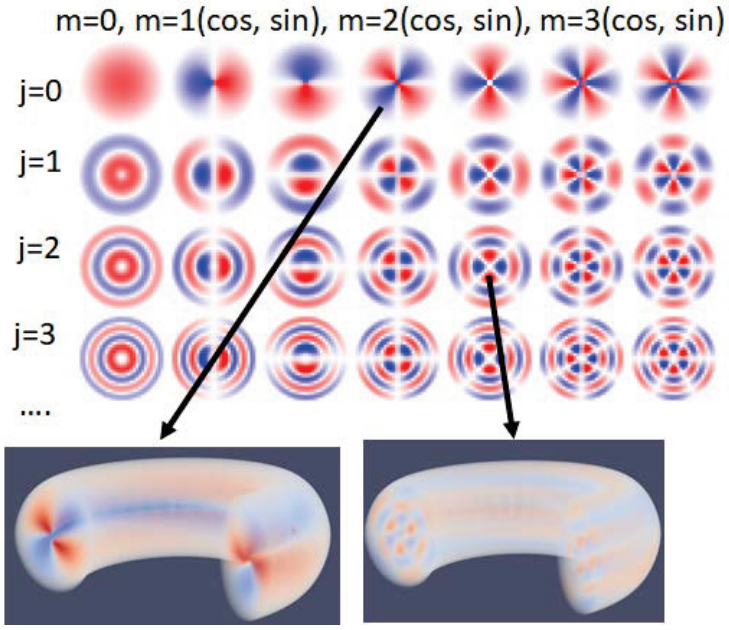

Fig. 2 Schematic image of the 3D basis patterns. n=0 example is shown in the left figure and n=1 in the right.

First, reconstruction having n=0 type emission profile are tested with one camera system [1]. The reconstructed pattern is quite similar to the assumed profile when the peaked emission profile and hollow emission profile are assumed. For the reconstruction, the Scikit-learn (https://scikit-learn.org/) library using the LARS algorithm [4] is used for solution. The hyper parameter is optimized by the cross validation method. In the case in which only the part (1/2~ 1/4) of the tangential image is used, reconstruction is still fairly good. It is a great advantage of this type of method using global patterns since the viewing field in the fusion experiment is often limited severely.

When the emission profile is superposition of the n=0 component and n=1 component, which is closer to the real experiments, the performance of this reconstruction method is examined. Fig. 3(b) is the tangential emission image where both the toroidally constant (n=0) peaked emission profile of Fig. 3 (a1) and the magnetic island like structure of the Fig. 3 (a2) (m/n =

2/1 type) are assumed. Here, m and n are the poloidal and toroidal mode number, respectively.

Reconstruction of the n=0 and n=1 component are shown in Fig. 3 (c1) and Fig. 3 (c2). Though the low amplitude noises can be seen in Fig. 3 (c2), fundamental characteristics of the n=1 mode is adequately reconstructed. L1 regularization is a key of this kind of reconstruction. The noise of the reconstruction image using L2 regularization is much larger especially in the core region of the image. One of the reasons of the merit of the L1 regularization is that less contributed components are neglected and not used. Most of the coefficient for L1 regularization is zero and only the coefficients for m=2 patterns are not zero and sufficiently large.

In summary, it is shown that dual SX camera system can detect asymmetric component of the SX emission. Penetration of the RMP or the locked-islands can be studied by using the reconstruction of the emission profile using L1 regularization.

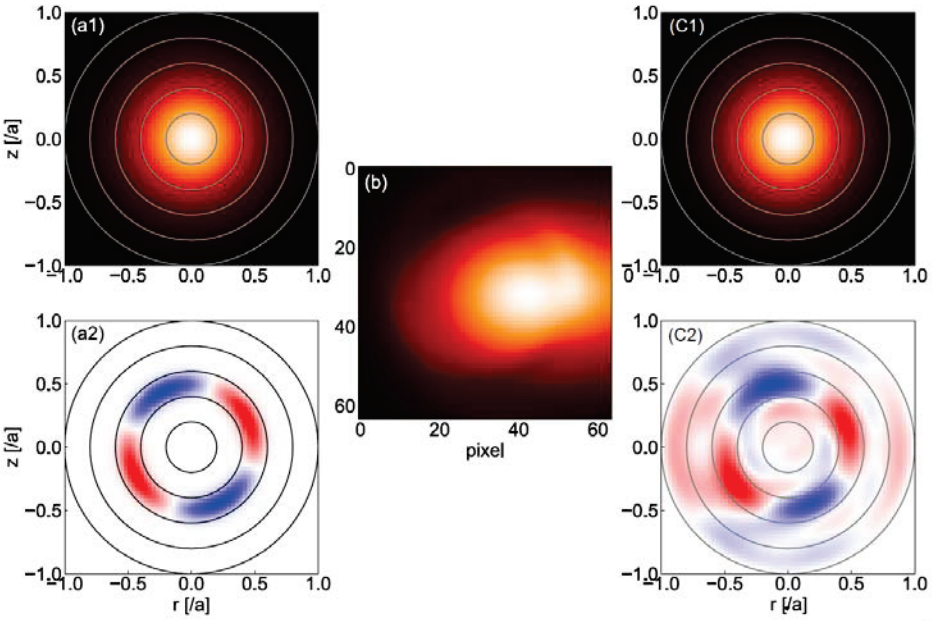

Fig.3 Assumed profile (a) and tangentially projected synthetic image(b) and reconstructed image(c) are shown.

Acknowledgements

This work was partly supported by the Post-CUP program. It is also supported by Japan / U. S. Cooperation in Fusion Research and Development.

References

[1] S. Ohdachi, Plasma Fusion Res., **14** (2019) 3402087

[2] X. D. Du, et. al., Phys. Plasmas, **26** (2019) 042505

[3] Y. Nagayama, Journal of Applied Physics, **62** (1987) 2702

[4] B. Efron, J. Am. Statist. Assoc., **99** (2004) 619

Nonlinear MHD simulation of plasma termination events in stellarators

Y. Suzuki[1,2], S. Futatani[3], and J. Geiger[4]

[1]National Institute for Fusion Science, Toki 509-5292, Gifu, Japan

[2]Graduate University for Advanced Studies, Toki 509-5292, Gifu, Japan

[3] Polytechnic University of Catalonia, Barcelona 08034, Spain

[4] Max-Planck Institute for Plasma Physics, Greifswald D-17491, Germany

Abstract

two types of plasma termination events, which are MHD instabilities driven by the pressure gradient and plasma current, are studied, respectively. In the Large Helical Device (LHD) experiment, many MHD instabilities are observed. Especially, if the peaked pressure profile was sustained by the pellet injection, a collapse event, so-called the core density collapse (CDC), was happen. In nonlinear MHD simulations, it is expected the CDC is driven by the resistive ballooning mode. On the other hand, in Wendelstein 7-X (W7-X) experiment, collapse events simultaneously happened in the plasma core, if the strongly localized plasma current, which is ECCD for an example, is driven in the plasma core. If the rotational transform, ι, increases by ECCD and crosses the rational of $\iota = 1$, the magnetic island opens on $\iota = 1$ rational surface. However, in nonlinear simulations, MHD event does not happen on $\iota = 1$ rational surface. At the outer region of $\iota = 1$ rational surface, where is the negative shear region corresponding to the positive shear region in tokamaks, the ballooning mode appears and destroys the flux surfaces completely. That is a mechanism to terminate the plasma.

1. Introduction

Nonlinear dynamics of plasma termination events in stellarators are studied using a 3D nonlinear MHD simulation code. In this study, two types of plasma termination events, which are MHD instabilities driven by the pressure gradient and plasma current, are studied, respectively. In the Large Helical Device (LHD) experiment, many MHD instabilities are observed. Especially, if the peaked pressure profile was sustained by the pellet injection, a collapse event, so-called the core density collapse (CDC), was happen. In nonlinear MHD simulations, it is expected the CDC is driven by the resistive ballooning mode [1]. Recently, a new imaging diagnostic of the two-dimensional soft-X ray arrays is installed in the LHD. Using the new diagnostics, perturbations localized at the outward of the torus. That is a characteristic of the ballooning mode. So, it seems the ballooning mode is observed in the LHD experiments. However, to interpret the experimental observation, we need to know what kind mode patterns should be observed.

On the other hand, in Wendelstein 7-X (W7-X) experiment, collapse events simultaneously happened in the plasma core, if the strongly localized plasma current is driven in the plasma core. That expects an MHD event driven by the plasma current. However, we did not identify what kind mode makes the collapse event in such a case.

In this study, we study 3D MHD equilibria with reconstructed pressure profile using a 3D MHD

equilibrium code, which does not assume nested flux surfaces [2]. And then, we will study nonlinear MHD simulations based on the 3D MHD equilibrium with the magnetic island [3]. In this study, we note nonlinear saturation to compare with the experimental observation.

2. Numerical Model

Nonlinear MHD simulation is carried out by using the MIPS code (MHD Infrastructure for Plasma Simulation) which solves the following full MHD equations in the cylindrical coordinates $(\mathrm{R}, \phi, \mathrm{Z})$,

$$\frac{\partial \rho}{\partial t} + \nabla \cdot (\rho (\mathbf{v} + \delta_i \mathbf{v}_i^*)) = \nabla \cdot (D_\perp \rho) + S_\rho, \tag{1}$$

$$\rho \left(\frac{\partial \mathbf{v}}{\partial t} + \mathbf{v} \cdot \nabla \mathbf{v} + \delta_i \mathbf{v}_i \cdot \nabla \mathbf{v}_i \right) = -\nabla p + \mathbf{j} \times \mathbf{B} + \frac{4}{3} [\nu \rho \nabla \cdot \mathbf{v}] - \nabla \times [\nu \rho \nabla \times \mathbf{v}], \tag{2}$$

$$\frac{\partial p}{\partial t} + \nabla \cdot (\rho \mathbf{v}) + (\Gamma - 1) p \nabla \cdot \mathbf{v} = \nabla \cdot (\chi_\perp \nabla p) + \nabla \cdot \left[\mathbf{B} \left(\frac{\chi_\parallel}{B^2} (\mathbf{B} \cdot \nabla) p \right) \right] + S_p, \tag{3}$$

$$\frac{\partial \mathbf{B}}{\partial t} = -\nabla \times \mathbf{E}, \tag{4}$$

$$\mathbf{E} + \mathbf{v} \times \mathbf{B} = \eta \mathbf{j} \tag{5}$$

The ρ is the mass density, v is the plasma velocity, p is the pressure, B is the magnetic field, η is the resistivity, ν is the viscosity, $D_\perp$ is the particle diffusion coefficient, $\chi_\parallel$ and $\chi_\perp$? are parallel and perpendicular thermal diffusion coefficients respectively, and Γ is the adiabatic constant. In these equations, the variable $\mathrm{v} = \mathrm{E} \times \mathrm{B}/B^2 + v_\parallel \mathrm{B}/\mathrm{B}$ represents the MHD velocity, and $v_i^* = \mathrm{B} \times \nabla p_i / \rho B^2$ is the normalized ion diamagnetic velocity.

The quantities $S_\rho = -\nabla \cdot \chi_\perp \rho_{eq}$ and $S_p = -\nabla \cdot \chi_\perp \nabla p_{eq}$ are the sources of density and pressure, where ρ_{eq} and p_{eq} are the equilibrium density and pressure respectively. The normalization is as follows: the magnetic field is normalized to the field magnitude on the magnetic axis B_0, the density to the density on the magnetic axis ρ_0, the velocity to the Alfven velocity $v_A = B_0/\sqrt{\mu_0 \rho_0}$, and the pressure to ρv_A^2. The time is normalized to the Alfven time $\tau_A = x_0/v_A$, where x_0 is the distance normalization. As a result of this normalization, all the diamagnetic terms are multiplied by the parameter $\delta_i = 1/(\omega_i \tau_A) = d_i/x_0 = K/(x_0\sqrt{n_0})$, where $\omega_{ci} = eB/m_i$ is the cyclotron frequency, d_i is the ion skin depth and $\mathrm{K} = \sqrt{m_i/(\mu_0 e^2)}$ is a constant. In these studies, all extended MHD terms were switched off. That means all simulations are resistive MHD simulations.

The original MIPS code uses the fourth-order finite difference scheme to approximate the spatial difference. The fourth order Runge-Kutta method is used for the time integration.

3. Core Density Collapse (CDC) in LHD

In LHD experiment, high performance confinement with a superdense core (SDC) inside the internal diffusion barrier (IDB) has been achieved using the pellet injection scheme. In the re-heating stage in such a discharge, where the plasma beta increases gradually after ceasing the pellet injection, an abrupt flushing of the central density occurs in some cases. Such a collapse phenomenon, which is named “core density collapse” (CDC), should be avoided since it often limits the density increase. Although the physical mechanism of CDCs remains unclear, several models based on the magnetohydrodynamics (MHD) instability or the

equilibrium limit have been proposed. Revealing the mechanism of CDC is one of the key issues in further development of the confinement toward the high-density branch. This article reports the first attempt to conduct a nonlinear MHD simulation in helical plasma with a large pressure gradient, which corresponds to the IDB-SDC state of LHD [58, 59]. The result obtained by the simulation would provide us with basic understandings for the collapse phenomena, including the CDC, from the viewpoint of MHD.

4. Collapse event in core by ECCD current drive in W7-X

Figure 1 shows the time history of two shots with co- and counter-ECCD. For the counter-ECCD case, small crashes of the electron temperature appeared but crashes are not huge. However, for the case of co-ECCD case, crashes frequently appeared and drops of the electron temperature are huge. Since co-ECCD increases the rotational transform, it is expected the rotational transform reached $\iota = 1$ rational surface or crossed the rational surface.

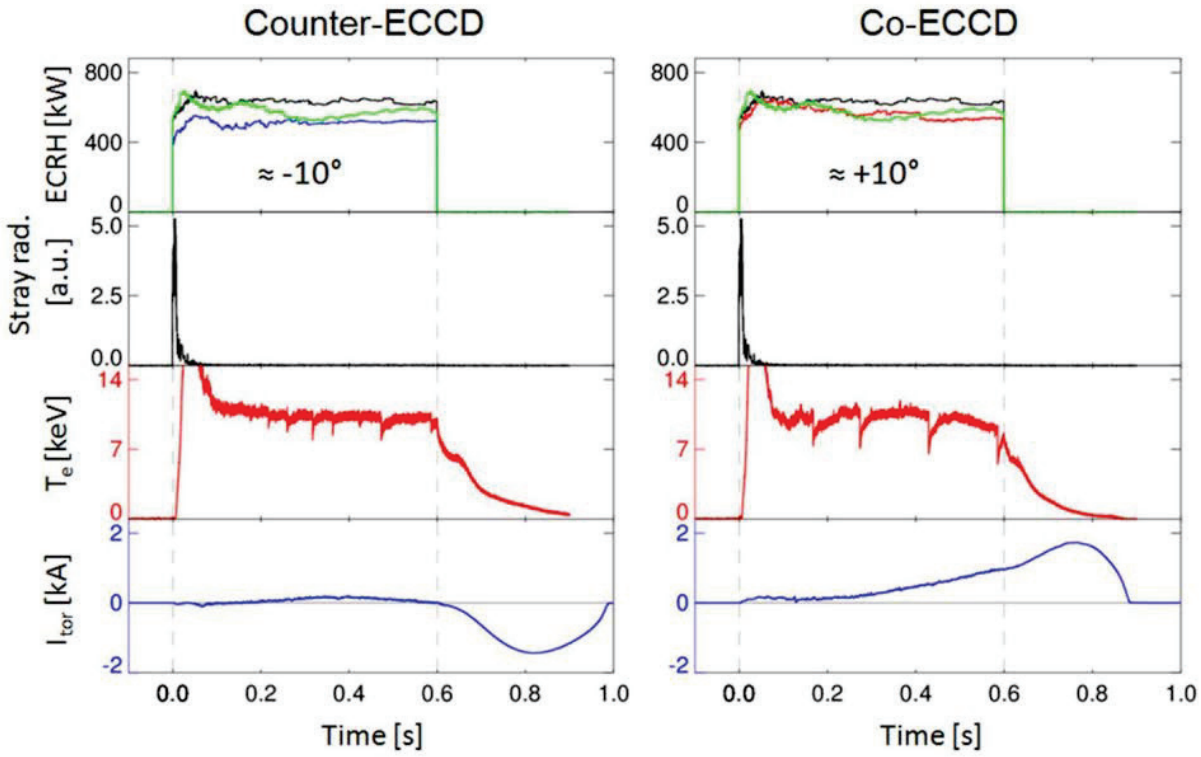

Fig.1 Time histories of discharges with co-ECCD and counter-ECCD. Temperature crashes happed when ECCD is evolved.

The 3D equilibrium is studied by HINT code, which does not assume perfectly nested flux surfaces. The target configuration is the low-iota configuration, which is used in OP1.1. This configuration has 5/6 islands in the plasma edge, but those islands are limited by the material limiter. For co-ECCD of 43kA, the rotational transform reached $\iota = 1$ rational surface at $\rho = 0.4$. And, flux surfaces strongly deviated by the natural resonances. In addition, if the beta effect is induced, the magnetic island is opened. However, clear flux surfaces are keeping and crashes from the equilibrium effects cannot be expected. Thus, these crash events will be caused by nonlinear MHD behavior.

To confirm that hypothesis, nonlinear MHD simulations are studied by MIPS code. nonlinear MHD

simulations are initialized by HINT equilibrium in above mentioned. From MIPS simulations, linear and nonlinear behaviors are observed. In linear phase, the ballooning mode clearly appears in the outside of $\iota = 1$ rational surface, where the magnetic shear is negative corresponding to the positive shear in tokamak, in spite of the magnetic well. However, flux surfaces are keeping clearly. For the beginning of the nonlinear phase, the ballooning mode destroys the flux surface. Only flux surfaces on the ballooning mode are destroyed and then the region in the outside of the ballooning mode keeps nested flux surfaces. In the later phase of nonlinear simulation, flux surfaces are completely destroyed and then the plasma pressure diffuses along the stochastic field line. That is a reason the electron temperature drops by nonlinear MHD.

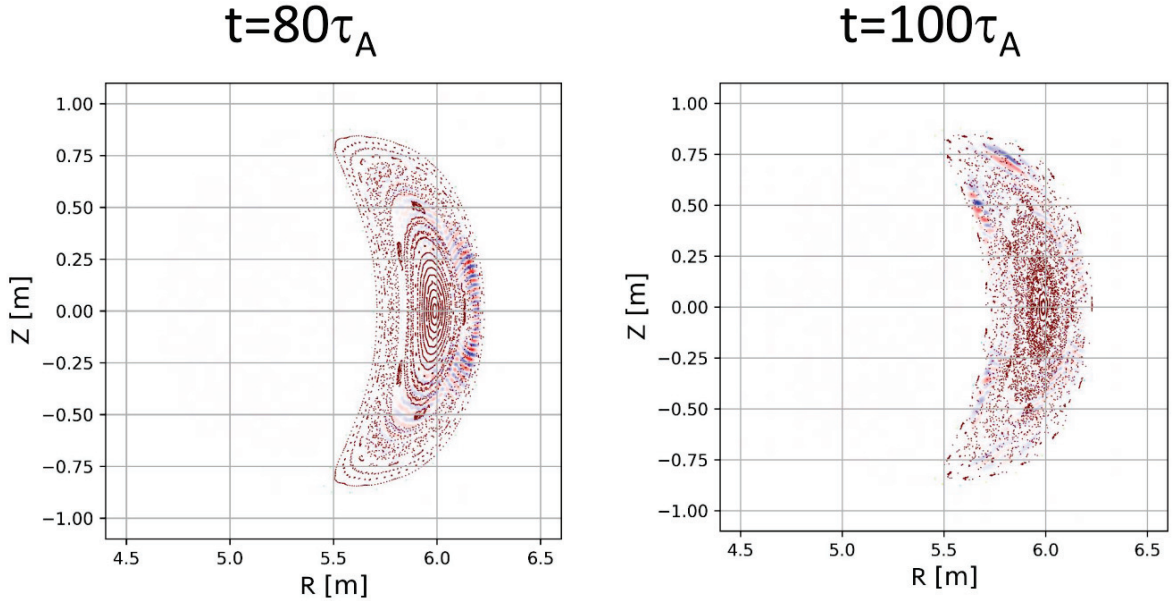

Fig.2 magnetic fields and perturbed pressure distributions in nonlinear simulations. The bolloning strucutre of the perturbation appeared in the outside of ι=1 rational surface. In the later phase of the nolinear state, flux surfaces are completeley broken.

5. Summary

In this study, two types of the plasma collapse events observed in LHD and W7-X are studied by nonlinear MHD simulation code, MIPS.

Acknowledgements

This work was partly supported by the Post-CUP program. It was also supported by NIFS budget code KEJC001 and was also partially supported by JSPS (the Japan Society for the Promotion of Science) Grant-in-aid for Scientific Research (B) 18H01202.

References

[1] N. Mizuguchi, Y. Suzuki and N. Ohyabu, Nucl. Fusion **49** (2009) 095023.

[2] Y. Todo, N. Nakajima, M. Sato and H. Miura, Plasma Fusion Res. **5** (2010) S2062.

[3] Yasuhiro Suzuki, et al., Nucl. Fusion **46** (2006) L19.

Overview of the LHD Neutron Diagnostics

M. Isobe[1,2], K. Ogawa[1,2], E. Takada[3], T.S. Fan[4], M. Kobayashi[1,2],
S. Yoshihashi[5], T. Nishitani[1], M. Osakabe[1,2], and the LHD Experiment Group[1]

[1]National Institute for Fusion Science, National Institutes of Natural Sciences, Toki 509-5292, Japan
[2]SOKENDAI (The Graduate University for Advanced Studies), Toki 509-5292, Japan
[3]National Institute of Technology, Toyama college, Toyama 939-8630, Japan
[4]Peking University, Beijing 100871, People's Republic of China
[5]Nagoya University, Nagoya 464-8603, Japan

Abstract

A comprehensive set of neutron diagnostics has been successfully operated in the Large Helical Device (LHD) deuterium discharges, playing an important role in assessing fusion gain (Q), confinement property of energetic particles, and/or radiation safety. So far, maximum neutron emission rate (S_n) of 3.3×10^{15} n/s, maximum shot-integrated neutron yield of 5.0×10^{15} n/shot, Q_{DD} of 4×10^{-4}, and equivalent Q^{DT} assumed for deuterium-tritium reaction of 0.11 have been recorded. In addition, energetic-particle confinement studies have been significantly enhanced through measurements of S_n, DD neutron emission profile, and secondary triton burnup 14 MeV neutron emission rate. The triton burnup ratio defined as the ratio of DD neutron yield to secondary DT neutron yield has reached 0.45%.

1. Introduction

The Large Helical Device (LHD) has been operated with deuterium gas since March, 2017 [1-3]. The LHD deuterium operation began with a comprehensive set of neutron diagnostics [4]. Since the LHD is equipped with five intensive neutral beam (NB) injectors, most of neutrons are generated by so-called beam-plasma reactions [5]. Therefore, neutron measurement can work as a new tool of energetic-particle (EP) diagnostics in the LHD. Neutron diagnostics have been playing an important role in the LHD deuterium experiments in enhancement of confinement study of EPs [6-10], assessment of fusion gain (Q) [11], and strict observance of neutron yield management [12].

2. Neutron diagnostics in LHD

Conceptual design of neutron diagnostics in the LHD was initiated in the late 1990's [13,14]. After long-term preparation, a comprehensive set of neutron diagnostics was established before the start of the deuterium operation. The LHD is now equipped with (1) three sets of ex-vessel neutron flux monitor (NFM) with wide dynamic range capability [15-17], providing time evolution of total neutron emission rate (S_n) and/or shot-integrated neutron yield (Y_n), (2) neutron activation system (NAS) having two irradiation ends at horizontal and vertical ports for Y_n measurement with indium disk and/or triton burnup study by use of silicon disk [4,18], (3) two vertical neutron cameras (VNCs) for radial profile of neutron, i.e., beam ion [19-21], (4) three scintillating-fiber (Sci-Fi) detectors developed by Los Alamos National Laboratory (LANL) in United States

of America [22, 23], National Institute for Fusion Science (NIFS) in Japan [24], and National Institute of Technology, Toyama College (TOYAMA) in Japan [25, 26] for time-resolved measurement for triton burnup 14 MeV neutron emission rate, (5) neutron fluctuation detector (NFD) for observation of rapid change of neutron flux due to unusual events such as magnetohydrodynamics (MHD) instabilities [27], and (6) single crystal chemical vapor deposition (CVD) diamond detector [28] for evaluation of neutron field and/or development of neutron field suitable for boron neutron capture therapy called BNCT. These have been successfully working and have provided plenty of new information for EP's behaviors in LHD plasmas.

To increase understanding of confinement property of EPs, the LHD neutron diagnostics will be largely enhanced in 2019. Third VNC characterized by high-detection efficiency will be installed at the basement beneath the 1.5-L port, having a vertical line of sight (LOS) at vertically elongated poloidal cross section. To increase performance of neutron fluctuation measurement, an EJ-200 plastic scintillator characterized by fast-response capability will be also installed as the second NFD. In addition, three different neutron energy spectrometers (NESs) will be operated from the 2019 campaign. The first one is time-of-flight enhanced diagnostics called TOFED developed in Peking University in People's Republic of China [29]. This task is undertaken as an international collaboration between NIFS and Peking University. The overview of TOFED on the LHD is schematically depicted in Fig. 1a). The TOFED in the LHD will have a vertical LOS. Fig. 1b) shows expected DD neutron energy spectrum at the end of collimator embedded in the concrete floor [16]. The second one is a fast-neutron scintillation detector based on ^{7}Li-enriched Cs_2LiYCl_6:Ce (CLYC) crystal [30]. The ^{7}Li-enriched CLYC is a recently developed scintillation crystal and can provide an opportunity for direct observation of neutron energy spectrum without unfolding technique. The third one is a conventional detector based on liquid fast-neutron scintillator designated as EJ-301. Existing neutron diagnostics together with future detectors in the LHD are listed in Table 1.

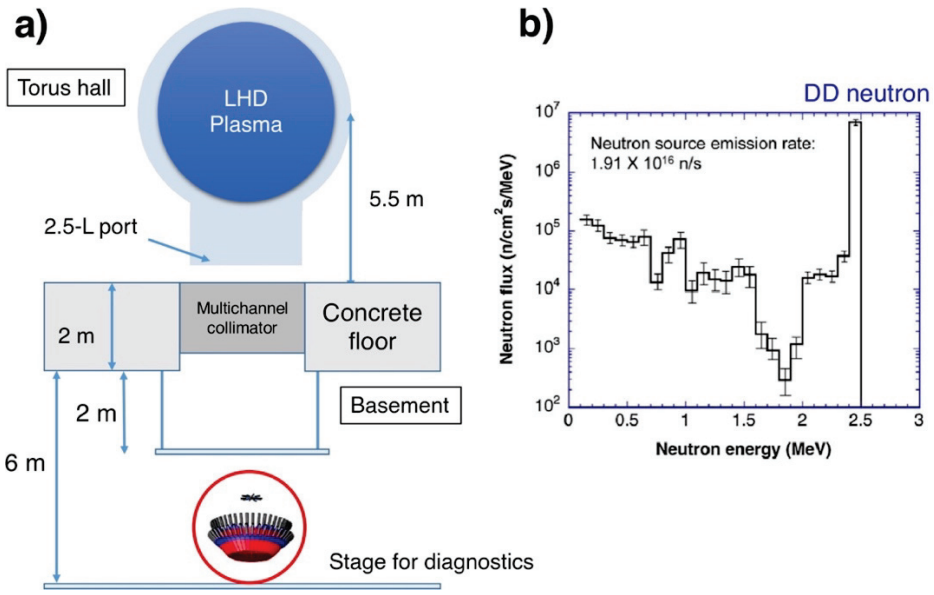

Fig. 1a) Overview of TOFED in the LHD, b) DD neutron energy spectrum at the collimator end. The DD neutron spectrum is calculated by the MCNP6 code [16].

Table 1. Neutron diagnostics in LHD

System	Ch.	Detector	Location	Primary purposes	Status
NFM [15-17]	1	^{235}U FC, ^{10}B counter	Top of LHD	· Fusion output and Q_{DD} · Time-resolved S_n	2017~
	2	^{235}U FC, ^{3}He counter	10-O port		
	3	^{235}U FC, ^{3}He counter	4-O port		
NAS [4,18]	1	In, Al, and Si foils	2.5-L port	· Shot-integrated Y_n for DD and secondary DT neutrons	2017~
	2	In, Al, and Si foils	8-O port		
VNC	1	Stilbene [19-21]	2.5-L port/ vertical LOS	· Time-resolved DD neutron emission profile	2017~
	2-1	EJ-410 (ZnS:Ag + Plastic)	1.5-L port/ Diagonal LOS		2018~
	2-2	EJ-410 (ZnS:Ag + Plastic)	1.5-L port/ vertical LOS		2019~
Sci-Fi	1	LANL Sci-Fi detector [22, 23]	8-O port	· Time-resolved DT neutron emission rate	2017~
	2	NIFS Sci-Fi detector [24]	2.5-L port		
	3	TOYAMA Sci-Fi detector [25, 26]	2.5-L port		
NFD	1	EJ-410 (ZnS:Ag + Plastic) [27]	2.5-L port	· Neutron fluctuation	2017~
	2	EJ-200 (Plastic)	2.5-L port		2019~
NES	1	TOFED [29]	Basement beneath 2.5-L port	· DD and DT neutron spectrometry	2019~
	2	^{7}Li enriched CLYC [30]	6-T port	· DD neutron spectrometry	2019~
	3	EJ-301 (Liquid)	6-T port		2019~
CVD-D	1	Single crystal CVD diamond [28]	9.5-L port	· Evaluation of neutron field	2018~

3. Representative results in the FY2017 and FY2018 campaign

3.1 Neutron emission rate and yield

Dependences of S_n on electron density (n_e), magnetic axis position (R_{ax}), and toroidal magetic field strength (B_t) were systematically investigated in NB-heated plasmas in the early phase of deuterium experiment. S_n in high-B_t plasmas is higher than in low-B_t plasmas as expected. Also, it increases as R_{ax} is shifted inwardly, and vice versa as expected. The measurement indicated that S_n increases in low-n_e regime ($<2\times10^{19}$ m^{-3}), reaches the peak around n_e of (2-3)$\times10^{19}$ m^{-3}, and decreases as n_e increases [6, 11]. This tendency matches that predicted by calculation in advance based on steady-state Fokker-Planck equation [5]. So far, the maximum S_n has reached 3.3×10^{15} (n/s) in R_{ax}/B_t of 3.55 m/2.89 T in the FY2017 campaign with full power NB heating [6].

Fig. 2 shows waveforms of maximum Y_n shot obtained in the FY2018 campaign in R_{ax}/B_t of 3.55 m/2.89 T. Full power NB heating with five NB injectors lasts for 2 s and electron cyclotron resonance heating (ECRH) is superposed in this shot. n_e increases gradually from 2×10^{19} m^{-3} to 3×10^{19} m^{-3} in time. S_n almost keeps constant

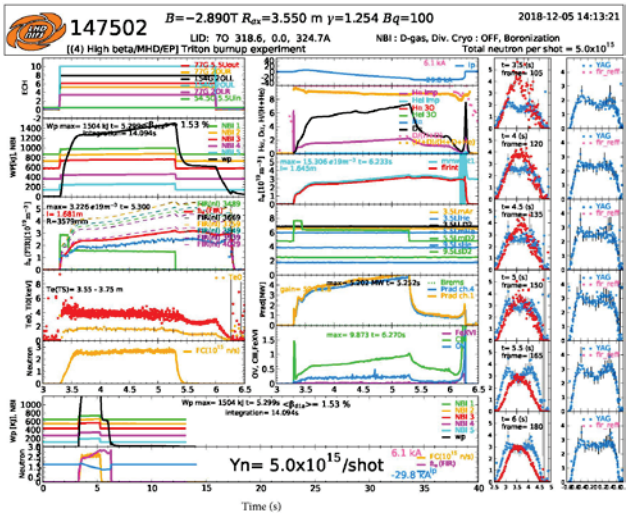

Fig. 2 Maximum neutron yield shot obtained in the FY2018 campaign of the LHD.

during NB injection. In this shot, Y_n reached 5.0×10^{15} n/shot which is the maximum record value in the LHD.

3.2 Fusion gain

The fusion gain (Q) is an intrinsic interest in nuclear fusion experiments. The Q value defined as the ratio of fusion output divided by heating power has been systematically investigated with negative-ion-source-based NBs (N-NBs) characterized by high injection energy of 180 keV. Note that positive-ion-source-based NBs (P-NBs) injected with relatively low energy of 60-80 keV and ECRH are not used in this study because these are inefficient in terms of neutron production compared with N-NBs. Q_{DD} and equivalent Q_{DT} as a function of $P_{N\text{-}NB\_dep}$ are shown in Fig. 3. Here, $P_{N\text{-}NB\_dep}$ stands for deposition power of the N-NBs. The Q value increases as $P_{N\text{-}NB\_dep}$ increases up to ~3 MW, and saturates when $P_{N\text{-}NB\_dep}$ is over ~3 MW. The maximum Q_{DD} value has reached 4×10^{-4} with $P_{N\text{-}NB\_dep}$ of ~3.5 MW. The equivalent Q_{DT} value is assessed with a help of the FBURN code [10], assuming the classical slowing down of beam ion without loss. The maximum equivalent Q_{DT} value is obtained in the FY2017 campaign and is evaluated to be ~0.11. Note that this value is quite similar to that obtained in large tokamaks with NB power of 5 MW [31].

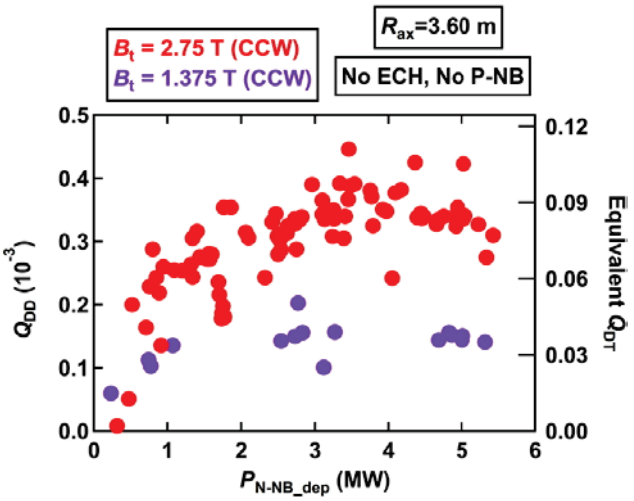

Fig. 3 Fusion gain Q_{DD} and equivalent Q_{DT} as a function of deposition power of negative-ion-source-based neutron beam [11].

3.3 Extension of energetic-particle confinement study

Here, the result of triton burnup experiment is described. 1 MeV tritons are produced in deuterium plasmas. 1 MeV tritons undergo secondary DT reaction through nuclear fusion reaction with background plasma deuterons. Because kinetic parameters such as Larmor radius and precessional drift frequency of 1 MeV triton are quite similar to those of DT-born 3.5 MeV alpha particles, 1 MeV triton can be recognized as a simulation particle of 3.5 MeV alphas. We investigated the triton burnup ratio defined as the ratio of DD neutron yield to secondary DT neutron yield measured with NAS and Sci-Fi detector calibrated with NAS. Fig.4 shows triton burnup ratios as a function of R_{ax} obtained in LHD deuterium plasmas with n_e of $(1\sim4)\times10^{19}$ m^{-3}. The triton burnup ratio becomes higher as R_{ax} is shifted inwardly as expected since helically trapped energetic-ion orbits tend to match magnetic flux surfaces in the inward shifted configuration.

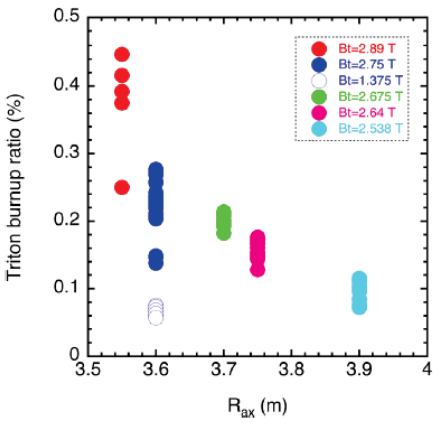

Fig. 4 Triton burnup ratio as a function of R_{ax} [6].

The maximum triton burnup ratio has reached 0.45% in B_t/R_{ax} of 3.55 m/2.89 T in the FY2017 campaign. In addition to triton burnup, understanding of beam ion transport and/or loss due to MHD instabilities has been largely increased through measurements of DD neutron emission profile [8, 9].

4. Summary

A highly integrated fusion neutron diagnostics has been established in the LHD, including ex-vessel NFMs with wide dynamic range capability, a NAS having two irradiation end, two VNCs, three Sci-Fi detectors, a NFD. To enhance EP physics studies, third VNC and three different types of neutron energy spectrometers will be installed before the start of FY2019 campaign. So far, maximum S_n of 3.3×10^{15} n/s, maximum Y_n of 5.0×10^{15} n/shot, Q_{DD} of 4×10^{-4}, and equivalent Q_{DT} assumed for deuterium-tritium reaction of 0.11 have been achieved. In addition, the triton burnup ratio defined as the ratio of DD neutron yield to secondary DT neutron yield has reached 0.45%.

Acknowledgements

This work was partly supported by the Japan-China Post-Core-University-Program called Post-CUP. It was also supported by the LHD project budget (ULHH003, ULHH034, ULHH802 and ULGG801) and NIFS collaboration research programs (KOAH033 and KOAH037).

References

[1] Y. Takeiri, IEEE Trans. Plasma Sci., **46** (2018) 1141.

[2] Y. Takeiri, IEEE Trans. Plasma Sci., **46** (2018) 2348.

[3] M. Osakabe *et al*., IEEE Trans. Plasma Sci., **46** (2018) 2324.

[4] M. Isobe *et al*., IEEE Trans. Plasma Sci., **46** (2018) 2050.

[5] M. Osakabe *et al*., Fus. Sci. Technol. **72** (2017) 199.

[6] M. Isobe *et al*., Nucl. Fusion **58** (2018) 082004.

[7] K. Ogawa *et al*., Nucl. Fusion **58** (2018) 034002.

[8] K. Ogawa *et al*., Nucl. Fusion **58** (2018) 044001.

[9] K. Ogawa *et al*., Plasma Phys. Control. Fusion **60** (2018) 044005.

[10] K. Ogawa *et al*., Plasma Phys. Control. Fusion **60** (2018) 095010.

[11] K. Ogawa *et al*. Nucl. Fusion **59** (2019) 076017.

[12] M. Kobayashi *et al*., Fus. Eng. Des. **143** (2019) 180.

[13] M. Sasao *et al*., Fus. Eng. Des. **34-35** (1997) 595.

[14] M. Sasao *et al*. Diagnostics for Experimental Thermonuclear Fusion Reactor 2, edited by Stott et al., Plenum Press, New York, 1998, pp.583.

[15] M. Isobe *et al*., Rev. Sci. Instrum. **85** (2014) 11E114.

[16] T. Nishitani *et al*., Fus. Eng. Des. **123** (2017) 1020.

[17] T. Nishitani *et al*., Fus. Eng. Des. **136** (2018) 210.

[18] N. Pu *et al*., Rev. Sci. Instrum. **88** (2017) 113302.

[19] K. Ogawa *et al*., Rev. Sci. Instrum. **85** (2014) 11E110.

[20] K. Ogawa *et al*. Rev. Sci. Instrum. **89** (2018) 113509.

[21] H. Kawase *et al*., IEEE Trans. Plasma Sci. **47** (2019) 462.

[22] G.A. Wurden *et al*., Rev. Sci. Instrum. **66** (1995) 901.

[23] W.C. Sailor *et al*., Rev. Sci. Instrum. **66** (1995) 898.

[24] N. Pu *et al*., Rev. Sci. Instrum. **89** (2018) 10I105.

[25] E. Takada *et al*., Plasma Fus. Res. **11** (2016) 2405020.

[26] E. Takada *et al*., Rev. Sci. Instrum. **90** (2019) 043503.

[27] K. Ogawa *et al*., Plasma Fus. Res. **13** (2018) 3402068.

[28] M. Kobayashi *et al*., submitted to Journal of Instrumentations.

[29] X. Zhang *et al*., Rev. Sci. Instrum. **85** (2014) 043503.

[30] A. Giaz *et al*., Nucl. Instrum. Meth. A **825** (2016) 51.

[31] D.L. Jassby *et al*., Phys. Fluids B **3** (1991) 2308.

1 MeV triton orbit analysis in EAST

K. Ogawa[1,2], G. Q. Zhong[3], R. Zhou[3], K. Li[3], M. Isobe[1,2], and L. Hu[3]

1) National Institute for Fusion Science, National Institutes of Natural Sciences, Toki-city, Gifu, Japan
2) SOKENDAI, Toki-city, Gifu, Japan
3) Institute of Plasma Physics, Chinese Academy of Sciences, Hefei, Anhui, China

1 MeV triton orbit analysis is performed in order to understand the triton confinement property in EAST. Collisionless Lorentz orbit of 10^6 1 MeV triton having random velocity is followed from the birth position calculated by NUBEAM code. Prompt loss is dominant when the orbit following time is set to be 10^{-3} s. 1 MeV tritons existing in a wider pitch angle range are confined in the case of high plasma current conditions.

1. Introduction

Confinement of energetic particles has been intensively studied in magnetic confinement fusion machine because a fusion burning plasma is sustained by deuterium (D)-tritium (T) born alpha particles. Therefore, energetic alpha particles must be confined well for realizing a fusion reactor. In a deuterium plasma experiment, following two reactions are mainly occurred: D(d,n)^{3}He and D(d,p)T. By former reaction, 2.45 MeV neutrons are created, whereas 1 MeV tritons are created by latter reaction. It is worth noting that the number of two reactions is almost the same. DD-created 1 MeV triton can undergo secondary reaction with bulk deuteron if the triton slows down in the plasma. Confinement property of 1 MeV tritons is intensively studied as DT born alpha particles because kinetic parameters such as Larmor radius and precession frequency of the tritons are almost the same as that of the alpha particles. In those studies, triton burnup ratio, which is DT neutron yield divided by DD neutron yield, is one of the common index.

In EAST, integrated neutron diagnostics such as neutron flux monitor, radial neutron camera, and neutron spectrometers are installed and working successfully [1]. From 2018 experimental campaign, the neutron activation system (NAS) was newly installed in order to evaluate shot-integrated neutron yield. Triton burnup measurement was initiated with the NAS. Secondary DT neutron was measured using 10 g silicon foil. Initial measurements showed that DT neutron yield was around 10^{11} n/shot. The measurement has been continued in order to obtain neutron yield on various configurations. In this paper, 1 MeV triton orbit analysis is reported in order to understand 1 MeV triton

confinement in EAST.

2. Experimental Setups

In this calculation, collisionless Lorentz orbit of 1 MeV tritons is followed by LORBIT code [2] in various plasma current (I_p) conditions. The orbit following time is set to be 1 ms, which is quite shorter than the Spritzer slowing down time. Toroidal field ripple is not considered. Velocity of triton is randomly distributed using random numbers. We randomly launched 10^6 1 MeV triton according to the birth profile of 1 MeV tritons calculated using NUBEAM code [3] as shown in Figure 1. Here, only co-inject neutral beam injector is considered. The equilibrium is given by EFIT result. Electron temperature, and electron density in the plasma center are 1.64 keV, and 3.2×10^{19} m^{-3}, respectively. Radial profiles of electron temperature and electron density are assumed to be parabolic profile.

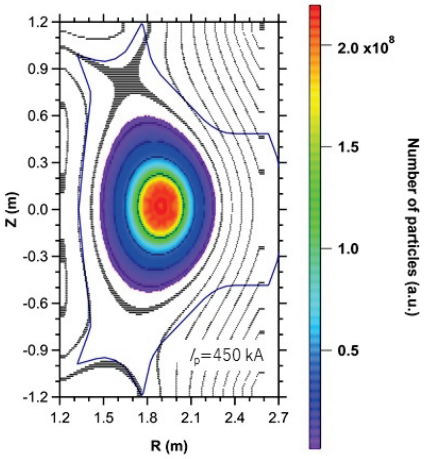

Fig.1 Emissivity profile of 1 MeV triton calculated by NUBEAM code.

3. Calculation Results

Figure 2 shows the typical 1 MeV triton orbit in I_p of 300 kA, 450 kA, and 1 MA cases. Here, toroidal magnetic field strength is around 2.3 T, and ion grad-B drift is directed to

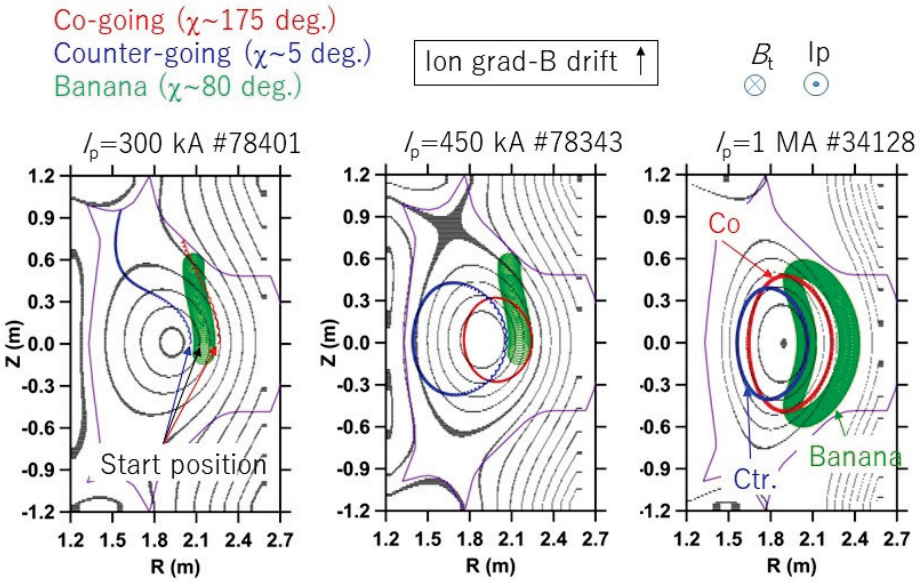

Fig.2 Typical 1 MeV triton orbit calculated by LORBIT code.

be upward. Co-going transit 1 MeV triton having pitch angle of 175 degrees is launched at (R, Z) of (2.25 m, 0.0 m). The triton is lost at I_p of 300 kA, whereas the triton is confined at I_p of 450 kA and 1 MA. Counter-going transit 1 MeV tritons having a pitch angle of 5 degrees is launched at (R, Z) of (2.05 m, 0.0 m). The triton is confined at I_p of 450 kA and 1 MA. Banana 1 MeV triton having the pitch angle of 80 degrees is launched at (R, Z) of (2.15 m, 0.0 m). The triton is only confined at I_p of 1 MA. Although the deviation of orbit from the magnetic flux surface becomes smaller as the increase of I_p, the deviation is relatively large even in 1 MA case because of the high energy.

Confinement of 1 MeV triton is surveyed at I_p of 300 kA, 450 kA, 600 kA, 800 kA, and 1 MA cases. Figure 3 shows the time evolution of 1 MeV triton loss. Number of lost 1 MeV tritons increases rapidly at 10^{-6} s, then almost saturated at 10^{-5} s in all the cases. This time evolution shows that prompt loss is dominant up to 10^{-3} s. The loss ratio at I_p of 300 kA, 450 kA, 600 kA, 800 kA and 1 MA reached 85%, 73%, 56%, 48%, and 33%, respectively. Number of lost ions at 10^{-3} s decreased with the increase of I_p. Pitch angle distribution of confined 1 MeV tritons are plotted on Figure 4. Black line shows the pitch angle distribution of launched particles. Confinement of co-going transit particles are better than that of counter-going transit and banana particles. 1 MeV tritons existing in wider pitch angle range can be confined in higher I_p cases. Some of co-going particles are confined even if I_p of 300 kA. Most of banana particles are lost even in I_p of 1 MA case because the banana width is comparable with a minor radius of a plasma.

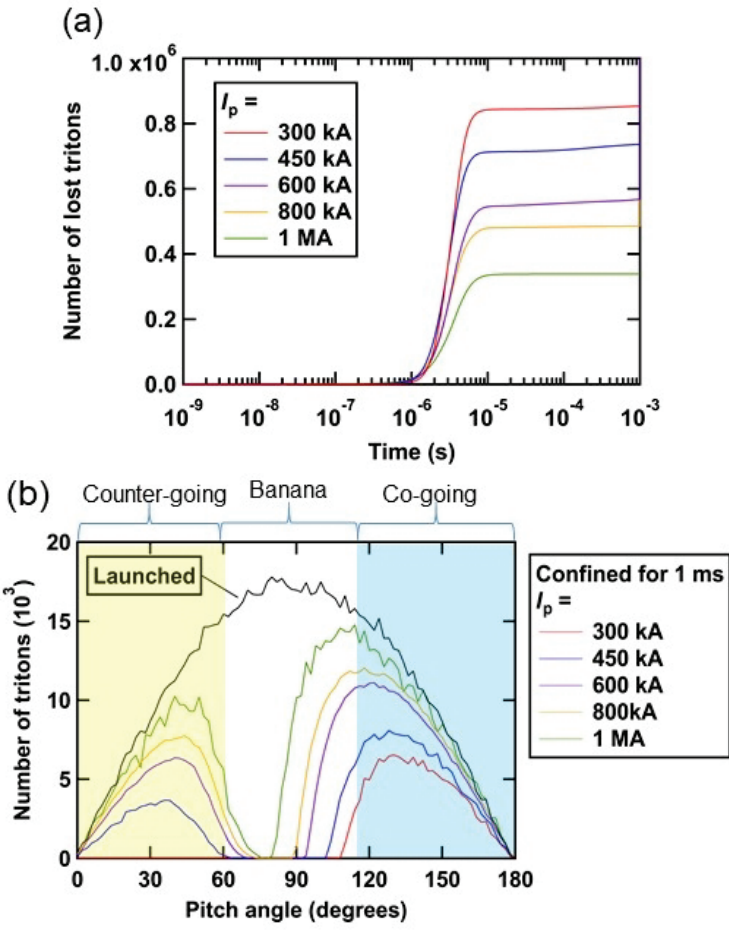

Fig.3 (a) Time evolution of number of lost 1 MeV tritons. (b) Pitch angle distribution of confined 1 MeV tritons.

Strike points of 1 MeV tritons in I_p of 300 kA, 600 kA, and 1 MA cases are plotted in Figure 5. Although number of particles decrease with the increase of I_p, strike points of 1 MeV tritons are not so changed. Note that the strike points of 1 MeV tritons are mainly located at the upper panel of the vessel because the ion grad-B drift is directed to be upward. Strike points of 1 MeV triton are located at the lower panel if we changed direction of toroidal magnetic field. The location of strike points are consistent with the direction of ion grad-B drift, as expected.

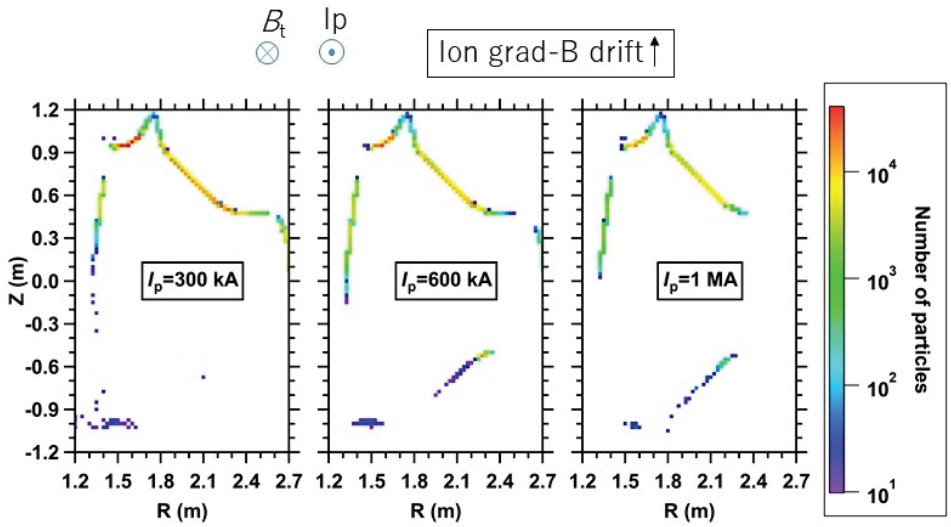

Fig.4 Distribution of strike point of 1 MeV tritons.

4. Summary

Study of 1 MeV triton confinement is performed using Lorentz orbit code LORBIT in order to understand 1 MeV triton confinement characteristics in EAST. Typical 1 MeV triton orbit shows that the deviation of orbit from the flux surface decrease with the increase of I_p, as expected. The deviation is comparable with minor radius of a plasma even in 1 MA case because of high-energy of tritons. Time evolution of 1 MeV triton loss shows that the prompt loss of the triton occurs at $t<10^{-5}$ s in all I_p cases. 1 MeV tritons existing wider pitch angle region are confined in higher I_p cases compared with lower I_p cases. Strike points of 1 MeV triton shows that most of the particles are lost on the upper wall which is consistent with the direction of ion grad-B drift.

References

[1] G. Q. Zhong et al 2016 Plasma Phys. Control. Fusion **58** 75013.
[2] M. Isobe et al 2009 J. Plasma Fusion Res. SERIES **8** 330.
[3] A. Pankin et al 2004 Comput. Phys. Commun. **159** 157.

Spectroscopic study of impurity behavior in the edge stochastic magnetic field layer of Large Helical Device

T. Oishi[1,2], S. Morita[1], M. Kobayashi[1,2], G. Kawamura[1,2], Y. Kawamoto[1], M. Goto[1,2], and the LHD Experiment Group[1]

[1]National Institute for Fusion Science, National Institutes of Natural Sciences, 322-6, Oroshi-cho, Toki, Gifu 509-5292, Japan

[2]Department of Fusion Science, SOKENDAI (Graduate University for Advanced Studies), 322-6, Oroshi-cho, Toki, Gifu 509-5292, Japan

Abstract

Carbon impurity transport in a thick stochastic magnetic field layer called "ergodic layer" located at the edge plasma of LHD was studied for both deuterium (D) and hydrogen (H) discharges by EUV and VUV spectroscopy, and EMC3-EIRENE simulation. By comparing emission intensities from carbon impurity ions in high- and low- charge states, impurity screening is found to be more effective in D plasmas rather than H plasmas. Enhancement of the bulk-impurity collision frequency in D plasmas might be one of the reasons of the effective impurity screening. In high density discharges, the carbon impurity flow in the ergodic layer is directed toward the same direction of the friction force, indicating the presence of the impurity screening. The carbon flow velocity measured by the VUV spectroscopy is smaller in the deuterium plasmas. The difference of the flow velocity was reproduced by the simulation qualitatively.

1. Introduction

Stochastization of edge magnetic fields is extensively studied not only for the ELM mitigation but also for the plasma detachment and the impurity transport. A thick stochastic magnetic field layer called "ergodic layer" of the large helical device (LHD) consists of stochastic magnetic fields with three-dimensional structure intrinsically formed by helical coils, while well-defined magnetic surfaces exist inside the last closed flux surface [1]. It is therefore extremely important to study the impurity behavior and transport in the ergodic layer and to compare with those in the scrape-off layer of tokamaks. In LHD, it is found that carbon impurities are screened by the presence of the ergodic layer [2] and iron impurities are more effectively screened. As a result, the iron density in core plasmas of LHD is found to be extremely low despite the stainless steel vacuum vessel [3]. A transport model for the impurity behavior in the ergodic layer has been proposed considering the parallel momentum balance on impurity ions along a magnetic field line connecting the core plasma and the divertor plate based on the following equation;

$$m_Z \frac{\partial V_{Z//}}{\partial t} = -\frac{1}{n_Z}\frac{\partial T_Z n_Z}{\partial s} + ZeE_{//} + m_Z \frac{V_{i//} - V_{Z//}^{imp}}{\tau_s} + 0.71Z^2 \frac{\partial T_e}{\partial s} + 2.6Z^2 \frac{\partial T_i}{\partial s}, \quad (1)$$

where five terms in the right-hand side are contributions of impurity ion pressure gradient, parallel electric field, friction force between bulk ions and impurity ions, electron thermal force, and ion thermal force, in the order [4]. Among these terms, the friction force term and the ion thermal force term are the dominant terms.

When the ion density gradient increases, the friction force increase resulting the impurity flow is directed toward divertor plates, which means the impurity screening. On the other hand, when the ion temperature gradient increases, the ion thermal force increases resulting that the impurity flow is directed toward the core plasmas, which means the impurity accumulation. Based on the model, the parallel flow of the impurity ions is considered to be a key mechanism to determine impurity distributions in the ergodic layer.

2. Impurity screening phenomena observed by spectroscopy

In the present study, spectroscopic diagnostics has been performed in discharges with a magnetic configuration with the position of the magnetic axis, R_{ax}, of 3.6 m and the toroidal magnetic field, B_t, of 2.75 T. The discharge initiated by the electron cyclotron heating (ECH) is grown by three neutral beam injections based on the negative ion sources (n-NBI) beams with total port-through power of 10 MW and maintained with a flat-top phase for 1 s. We performed similar operations for the working gas of H_2 and the beam particle of the neutral beam of hydrogen (denoted as "H plasma"), and the working gas of D_2 and the beam particle of the neutral beam of hydrogen (denoted as "D plasma").

Intensities of carbon line emissions are monitored as an indicator of the impurity screening. CIII (977.03 Å, $2s^2$-$2s2p$) and CIV (1548.02 Å, 2s-2p) are measured using a 20 cm normal incidence VUV spectrometer [5], while CV (40.27 Å, $1s^2$-$1s2p$) and CVI (33.73 Å, 1s-2p) are measured using a grazing incidence EUV spectrometer [6]. The ionization potential, Ei, for C^{2+}, C^{3+}, C^{4+}, and C^{5+} is 48 eV, 65 eV, 392 eV, and 490 eV, respectively. Therefore, CIII and CIV radiation is emitted by carbon ions with low Ei located at the outer region of the ergodic layer, while CV and CVI radiation is emitted by carbon ions with high Ei located at inner region of the ergodic layer. Figure 1 shows the electron density dependence of line intensity of (a) CIII, (b) CIV, (c) CV, and (d) CVI normalized by the line-averaged electron density and (e) a line ratio of CV / CIV as an indicator of the impurity screening effect. Smaller values of the ratio leads to enhancement of the impurity screening effect. The line ratio decreases with the electron density, because carbon lines emitted from the outer region of the ergodic layer (CIII, CIV) increase, while those from inner

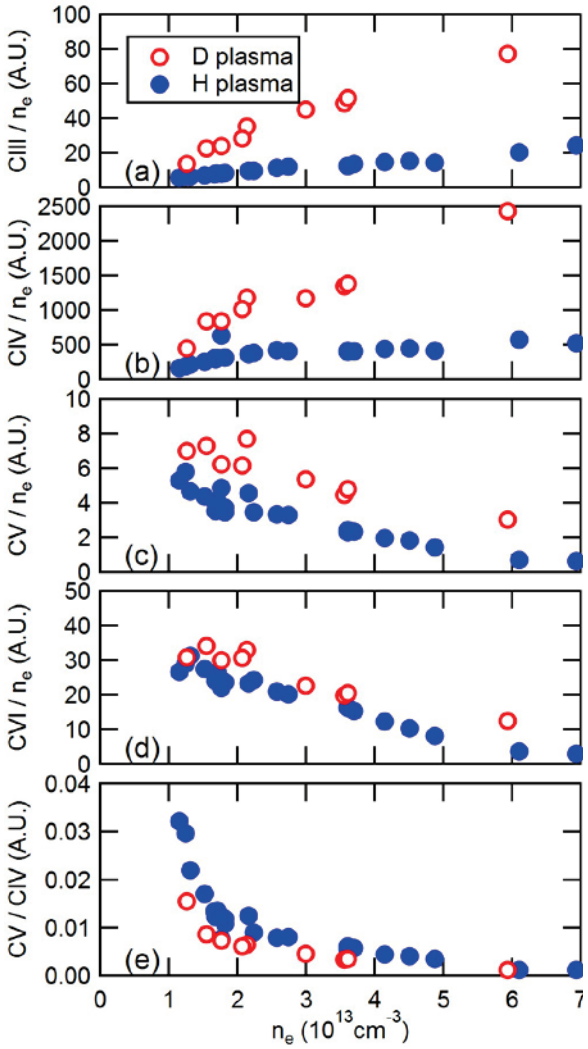

Fig. 1 Electron density dependence of line intensity of (a) CIII, (b) CIV, (c) CV, (d) CVI normalized by the electron density and (e) line ratio CV / CIV for deuterium and hydrogen discharges.

region (CV, CVI) decrease. It indicates enhancement of the impurity screening in the high density regime. Figure 1(e) also shows a comparison of the line ratio between the D plasmas compared to the H plasmas. The impurity screening effect is more obvious in the D plasmas. Enhancement of the friction force in D plasmas might be one of the reasons of the effective impurity screening.

3. Relationship between the impurity screening and the impurity flow

Figure 2 shows vertical profiles at the bottom edge of the ergodic layer of the flow velocity derived from the CIV line emission measured by VUV spectroscopy for an H plasma and a D plasma with a magnetic configuration with R_{ax} = 3.6 m and B_t = 2.75 T. The observation range of the edge profile measurement of the VUV spectroscopy is shown in Fig. 2 [7]. The flow velocity along the sightline, v_R, is given by $v_R = c\ (\Delta\lambda\ /\ \lambda)$, where c is the light speed, $\Delta\lambda$ the Doppler-shift and λ the wavelength of line emission. The measured flow velocity is projection of the flow along the observation chord which can be approximately considered to be the direction of the plasma major radius. Therefore, a variable of v_R is used to indicate the measured flow value. Positive and negative sign in the vertical axis of Fig. 2 corresponds to the outboard an inboard direction along the plasma major radius, respectively. As shown in the figure, the flow velocity toward the outboard direction develops clearly with the maximum value at Z = -480 mm, which is a location close to the outermost region of the ergodic layer in the H plasma. This direction is same as the friction force in the parallel momentum balance calculated with a three-dimensional simulation code, EMC3-EIRENE [8]. On the other hand, the maximum value of the flow velocity in the D plasma is clearly smaller than that in the H plasma.

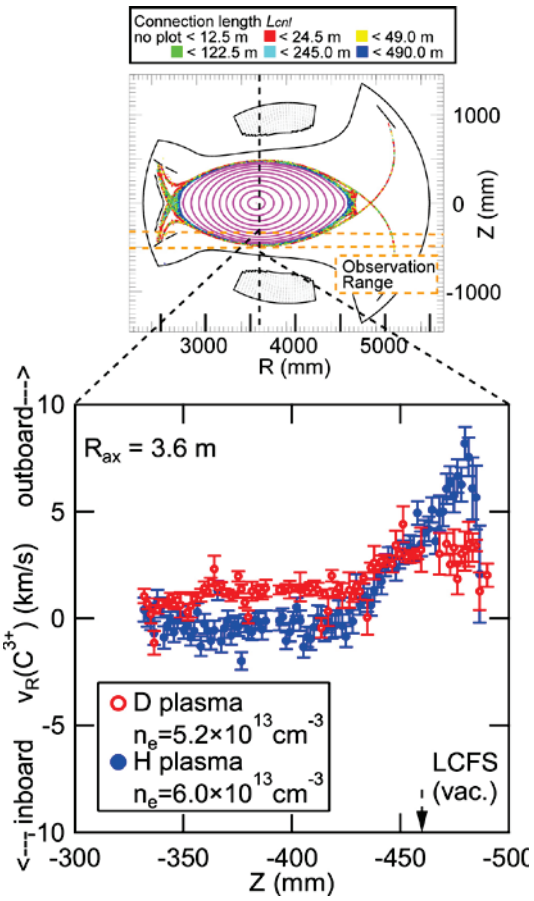

Fig. 2 Vertical profile at the bottom edge of the ergodic layer of impurity flow velocity derived from the Doppler profile of the CIV line emission measured by VUV spectroscopy in a D plasma (red open circle) and a H plasma (blue closed circle). The observation range of the VUV spectroscopy is illustrated together.

The electron density dependence of the maximum value of the observed flow is summarized in Fig. 3. All plots in the figure have directions same as the friction force. In the case of the H-discharge, the flow increases with the electron density. The result supports a prediction by the simulation that the friction force becomes more dominant in the force balance in higher density regime, which results in the increase of impurity flow causing the impurity screening. In the case of the D-discharge, the flow has a smaller value. In the friction force term in the equation of the momentum balance, $m_Z\ (V_{i//} - V_{Z//}^{imp})\ /\ \tau_s$, the parallel

velocity of the bulk ion, $V_{i//}$, and the collision time between the bulk ion and the impurity ion, τ_s, might be changed between the H-discharge and the D-discharge. Further experiments and simulations for the H-D comparison are needed to clarify the difference.

4. Summary

Carbon impurity transport in a thick stochastic magnetic field layer called "ergodic layer" located at the edge plasma of LHD was studied for both deuterium (D) and hydrogen (H) discharges by EUV and VUV spectroscopy, and EMC3-EIRENE simulation. By comparing emission intensities from carbon impurity ions in high- and low- charge states, impurity screening is found to be more effective in D plasmas rather than H plasmas. Enhancement of the bulk-impurity collision frequency in D plasmas might be one of the reasons of the effective impurity screening. In high density discharges, the carbon impurity flow in the ergodic layer is directed toward the same direction of the friction force, indicating the presence of the impurity screening. The carbon flow velocity measured by the VUV spectroscopy is smaller in the deuterium plasmas. The difference of the flow velocity was reproduced by the simulation qualitatively.

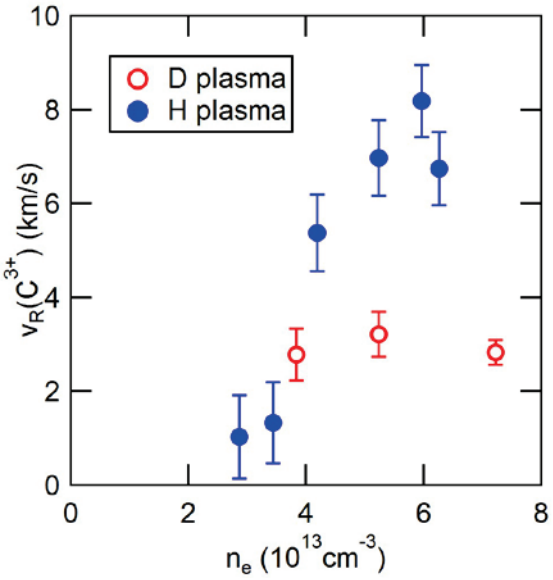

Fig. 3 Observed C^{3+} flow at the bottom edge of the ergodic layer in the H and D plasmas as a function of density for inward-shifted magnetic configuration with R_{ax} = 3.6 m.

Acknowledgements

This work was partly supported by the Post-CUP program. It was also supported by NIFS budget code ULPP010 and was also partially supported by the Ministry of Education, Science, Sports and Culture Grant-in-Aid for Scientific Research for Young Scientists (B) (17K14426).

References

[1] T. Morisaki *et al.*, J. Nucl. Mater. **313-316** (2003) 548.

[2] M. B. Chowdhuri et *al.*, Phys. Plasmas **16** (2009) 062502.

[3] S. Morita *et al.*, Nucl. Fusion **53** (2013) 093017.

[4] M. Kobayashi *et al.*, Nucl. Fusion **53** (2013) 033011.

[5] T. Oishi *et al.*, Plasma Fus. Res. **10** (2015) 3402031.

[6] M. B. Chowdhuri *et al.*, Appl. Opt. **47** (2008) 135.

[7] T. Oishi *et al.*, Appl. Opt. **53** (2014) 6900.

[8] T. Oishi *et al.*, Nucl. Fusion **58** (2018) 016040.

3D effects of neon injection position on the toroidally symmetric/asymmetric heat flux distribution on EAST

B. Liu[1], S.Y. Dai[1], G. Kawamura[2,3*], L. Zhang[4], Y. Feng[5] and D.Z. Wang[1]

[1]Key Laboratory of Materials Modification by Laser, Ion and Electron Beams (Ministry of Education), School of Physics, Dalian University of Technology, Dalian 116024, China

[2]National Institute for Fusion Science, National Institutes of Natural Sciences, Toki 509-5292, Japan

[3]Department of Fusion Science, SOKENDAI (the Graduate University for Advanced Studies), Toki 509-5292, Japan

[4]Institute of Plasma Physics, Chinese Academy of Sciences, Hefei 230031, China

[5]Max-Planck-Institut für Plasmaphysik, D-17491 Greifswald, Germany

[*]presentation at the Post-CUP workshop

Abstract

The heat flux deposition on the divertor targets with neon impurity injection on EAST has been investigated by the three-dimensional (3D) edge transport code EMC3-EIRENE. Impacts of the poloidal neon injection position on heat flux deposition have been studied. It is found that neon impurity injected around the separatrix at the divertor (i.e. strike point) can lead to a toroidal asymmetric distribution of heat loads on the same-side targets as the injection position.

1. Introduction

One of the most critical issues in fusion devices is mitigation of the heat flux deposition on the plasma-facing components (PFCs) [1,2]. The extrinsic impurity seeding is usually utilized to achieve the power dissipation and heat loads reduction in fusion facilities. The gas puffing such as neon, nitrogen, argon has been investigated on Alcator C-Mod [3], JET [4], LHD [5] and EAST [6]. Spatial localization of impurity seeding may result in the toroidal asymmetry of heat flux distribution on the divertor targets. The previous experimental results on EAST show that the argon impurity injection at the divertor region can lead to suppression in the divertor heat loads [6]. However, the toroidal symmetric/asymmetric characteristics of heat flux deposition under the toroidally-localized gas injection are not well understood on EAST due to diagnostic limitations. Hence, modelling predictions of symmetric/asymmetric heat flux distribution are important to obtain a better understanding of the underlying mechanisms involved and to be able to optimize impurity puffing position to minimize heat loads on EAST.

2. Construction of EMC3-EIRENE simulations

The EMC3-EIRENE code [7,8] can deal with arbitrary magnetic confinement configurations and has

been applied to many fusion devices. The EMC3 code solves a set of time-independent Braginskii's fluid equations for the mass, momentum and energy for electrons and ions using a Monte Carlo (MC) method [7] and is iteratively coupled with EIRENE [8], which solves the kinetic Boltzmann equation for neutral atoms or molecules and gives the particle momentum and energy source terms due to plasma-neutral interactions. In this work, the computational grid used in the simulation is constructed based on shot number #74209 at 4.0s of EAST, which is the upper single null magnetic configuration. A two-dimensional poloidal cross section of the computational grid is shown in figure 1. Deuterium is used as the main plasma species and neon is considered as the extrinsic impurity to be injected into the torus. The arrows in figure 1 indicate the neon impurity seeding directions and positions (named I1~I5). The red points named corner 1 and corner 2 indicate the corner of each divertor target. The purple dashed line is used to indicate the boundary between the inboard and outboard sides of the torus for the discussion in section 3. The toroidal location of the neon impurity injection position is defined as the toroidal angle of φ=0° in this study. The injected neon flux with an initial energy of 0.03 eV is 100 A for all neon injected cases. The input power is 2.66 MW, which is equally divided into the power of electrons and ions in the simulation. The upstream density is set to $1.0\times 10^{19}\ m^{-3}$, which is regarded as boundary condition for particle transport. The cross-field transport of particle and heat modelled by diffusive transport coefficients are assumed as $D_{\perp}$=0.4 m^2s^{-1} and $\chi_{\perp}$ =3$D_{\perp}$. The impurity perpendicular diffusivity D_{imp} is assumed to be same as the background plasma, i.e. 0.4 m^2s^{-1}.

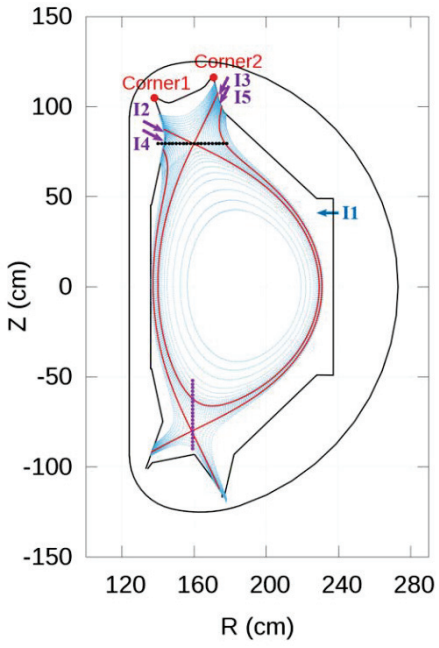

Figure 1. The poloidal cross section of the computational grid used in EMC3-EIRENE for EAST modelling. The red balls mark the corner of each divertor target. Five neon impurity injection positions are indicated by arrows. The purple dashed line indicates the boundary between the inboard and outboard of the torus. The black dashed line indication the vertical positions across the X-point.

3. Results and discussion

Figure 2 shows the 2D distributions of heat flux deposition on the upper inboard divertor targets with neon impurity injected at the positions of I1, I2 and I3. The horizontal and vertical coordinates indicate the toroidal angle and the distance from the position on the target plates to the corner 1, respectively. It is seen

that the downstream injections at I2 and I3 can result in a lower heat flux deposition on the upper inboard divertor targets compared with the upstream injection at I1. The most effective suppression of heat loads on the upper inboard divertor targets is achieved at I2 with the peak value of about $1.2\ \mathrm{MW/m^2}$. Moreover, a toroidal asymmetric distribution of heat loads on the upper inboard targets is obtained with neon impurity injected at I2. From the toroidal injection angle of 0°, the heat flux reduces gradually as the toroidal angle increases. The heat loads in the range from about 40° to 120° is much lower than other toroidal locations as shown in figure 2 (b).

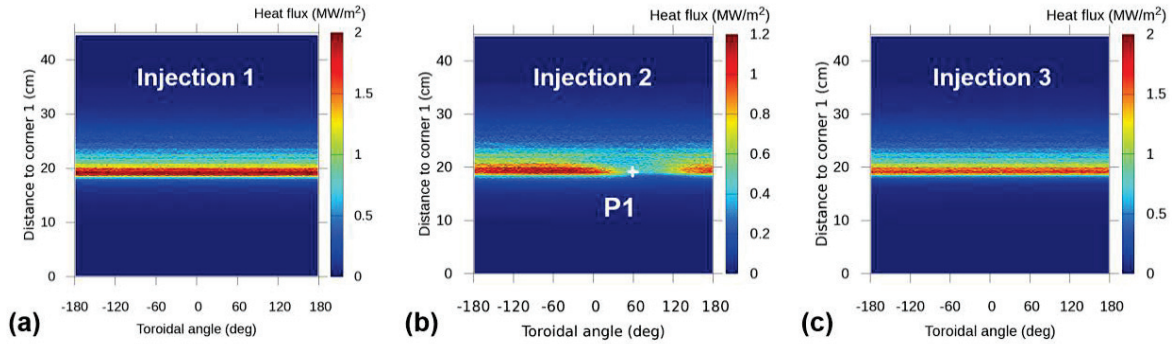

Figure 2. The 2D distributions of heat flux deposition on the upper inboard divertor targets with neon impurity injected at I1 (a), I2 (b) and I3 (c), respectively. The horizontal and vertical axis indicate the toroidal angle and the distance between the corner 1 and the positions on target plates.

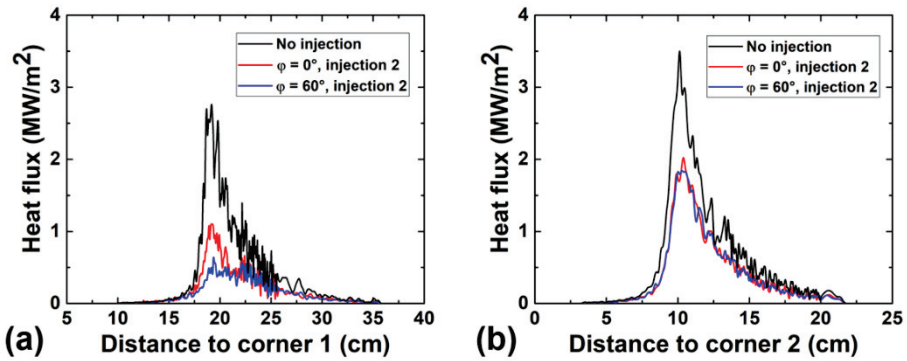

Figure 3. The heat flux distributions on the upper inboard (a) and upper outboard (b) divertor targets at toroidal angles of φ=0° and 60° with impurity seeded at I2 and without neon injection.

Figure 3 shows the heat flux distributions along the divertor targets poloidally for the upper inboard and outboard divertor targets at toroidal angles of φ=0° and 60°. The horizontal axis is the distance from the location on target plates to each corner of divertor target. The peak heat loads on the upper inboard targets in figure 3 (a) are about $1.1\ \mathrm{MW/m^2}$ and $0.6\ \mathrm{MW/m^2}$ at φ=0° and 60°, respectively. However, the heat flux distributions for the upper outboard targets with injection I2 are similar at φ=0° and 60° in figure 3 (b), which does not show an asymmetric property of the heat flux distribution. This indicates that the neon impurity injected around the strike point at the divertor can lead to a toroidal asymmetric distribution of heat loads on the same-side targets as the injection position. In addition, the heat flux

distribution without neon impurity injection is also presented in figure 3. The heat loads on the upper inboard and outboard without neon impurity seeded are about 2.8 MW/m^2 and 3.7 MW/m^2, respectively. In comparison with no neon injection, the neon impurity injected at I2 results in the suppression of heat loads by about 61% and 48% on the upper inboard and outboard targets, respectively.

4. Summary

The heat flux deposition on the divertor targets with different poloidal neon impurity injection positions has been investigated by EMC3-EIRENE code. The neon impurity is seeded at upstream and targets plate to study the 3D impacts of spatial impurity transport and radiation on the divertor heat flux distribution. It is found that a lower heat flux deposition is obtained with neon impurity injection position at the downstream divertor compared with that at the upstream. Moreover, neon impurity injected near the strike point can lead to not only the larger reduction in heat loads but also the asymmetric distribution of heat flux on the same-side targets as injection positions. The neon impurity injected near the strike point leads to a larger neon ions density and radiation power at the same-side of the torus as the injection position, which results in the lower heat loads on the same-side divertor targets in comparison with the upstream neon injection.

Acknowledgments

This work was supported by National MCF Energy R&D Program of China Nos: 2018YFE0311100, 2018YFE0303105, 2017YFE0301206, 2017YFE0300501 and 2017YFE0300402, National Natural Science Foundation of China under Grant Nos. 11405021, 11675037, 11575244 and 11775269, High-level talent innovation support program of Dalian No. 2017RQ052, and the Fundamental Research Funds for the Central Universities No. DUT18LK03, and was supported partly by Japan-China Collaboration for Fusion Research (Post-CUP Collaboration) and JSPS KAKENHI Grant Number 16K18340.

References

[1] Federici G *et al.* 2001 Nucl. Fusion **41** 1967.
[2] Loarte A *et al.* 2007 Nucl. Fusion **47** S203.
[3] Loarte A *et al.* 2011 Phys. Plasmas **18** 056105.
[4] Oberkofler M *et al.* 2013 J. Nucl. Mater. **438** S258-261.
[5] Tanaka M *et al.* 2017 Nucl. Mater. Energy **12** 241.
[6] Chen J B *et al.* 2017 Chin. Phys. B **26** 095205.
[7] Feng Y *et al.* 2004 Contrib. to Plasma Phys. **44** 57.
[8] Reiter D *et al.* 2005 Fusion Sci. Technol. **47** 172.

A particular method for measuring low edge ion temperature based on VUV spectroscopy

S. Morita

National Institute for Fusion Science, Toki 509-5292, Gifu, Japan

Abstract

Ion temperatures have been measured with high accuracy in Compact Helical System (CHS) using a 1m normal incidence VUV monochromator by carefully checking a slit function, which was obtained from Lyα spectral profile by changing an entrance slit width in steady state ECR discharges for wall conditioning. As a result, low ion temperatures could be successfully measured at T_i<10eV from VUV lines located in the edge region of CHS plasmas, e.g. CIV at 1548.2Å, while high ion temperatures (T_i<400eV) were observed in plasma central region using OVII at 1623.3 Å. Hopefully, the present method will be helpful for development of edge ion temperature profile measurement.

1. Introduction

Recently, impurity/particle transport in edge plasmas including stochastic magnetic field layer has been well studied experimentally and theoretically through 1-D and 2-D spectroscopy and EMC3-EIRENE code calculation. However, the study of energy/heat transport in edge plasmas is entirely insufficient due to a lack of experimental data, in particular, ion temperature distribution. Sufficient energy relaxation between electrons and ions cannot be expected in the plasma edge, i.e. $T_e \neq T_i$. Then, the edge ion temperature profile measurement is important for evident progress of the edge energy/heat transport study. Results of ion temperature measurement using VUV monochromator in Compact Helical System (CHS) are presented, which were mainly carried during 1990-1992.

2. Spectral resolution

Spectral resolution of spectrometers is given by

$$\lambda/\Delta\lambda \sim mN, \qquad (1)$$

where m is the diffraction order, and the value of N (=1/d) is the number of grating grooves per unit length, is usually used for indicating the grating specification. Then, d means distance between two adjacent grating grooves. Typical value of N is 10^3/mm for grating and 10^7/mm for crystal. Wavelength ranges are roughly given as follows;

Visible range: 4000-7000Å

Vacuum ultraviolet (VUV) range: 300-3000Å

Extreme ultraviolet (EUV) range: 10-500Å

X-ray range: 1-10Å

Since the angle of incidence of EUV spectrometers is very large, e.g. 89°, the spectral resolution is not high. In general the ion temperature measurement in EUV range is difficult. On the other hand, visible and x-ray spectrometers have an advantage for the ion temperature measurement due to the long wavelength and high N value, respectively. However, disadvantages also exist in the two spectrometers, i.e. edge visible lines are affected by Zeeman Effect and kind of noble gases useful for the central ion temperature measurement is very limited in X-ray spectroscopy. Although Ar gas is usually used for the X-ray diagnostic, He- and H-like Ar ions do not exist in the plasma center at T_e>2-3keV. The x-ray spectroscopy using Ar gas may work well in ITER as the edge ion temperature diagnostic.

3. Zeeman Effect

Zeeman separation, ΔE, at magnetic field strength, B, is given by

$$\Delta E = g_e \cdot \mu_B \cdot B, \qquad (2)$$

where μ_B and g_e are the Bohr magneton and g value (~2.0), respectively. Therefore, the Zeeman splitting is large with increasing magnetic field strength. The visible spectrum basically arises at a transition between two excited levels because the transition energy is very small. Since the total number of sublevels is described by $|2J+1|$ (J=S+L at LS coupling), the excited level intrinsically involves many sublevels, while those are degenerated at B=0. When B increases, the degeneracy is disappeared and the Zeeman splitting is appeared. Typical examples are shown in Fig.1 (a) and (b) for Hα and HeI visible lines, respectively. The spectral line can be clearly resolved in π (parallel to B field) and σ (perpendicular to B field) components. As a result, the ion temperature cannot be obtained straightforwardly from the measured visible spectra. On the contrary, VUV lines are not practically affected by the Zeeman Effect because the transition energy is relatively large and the transition is connected to the grand level of electric configuration.

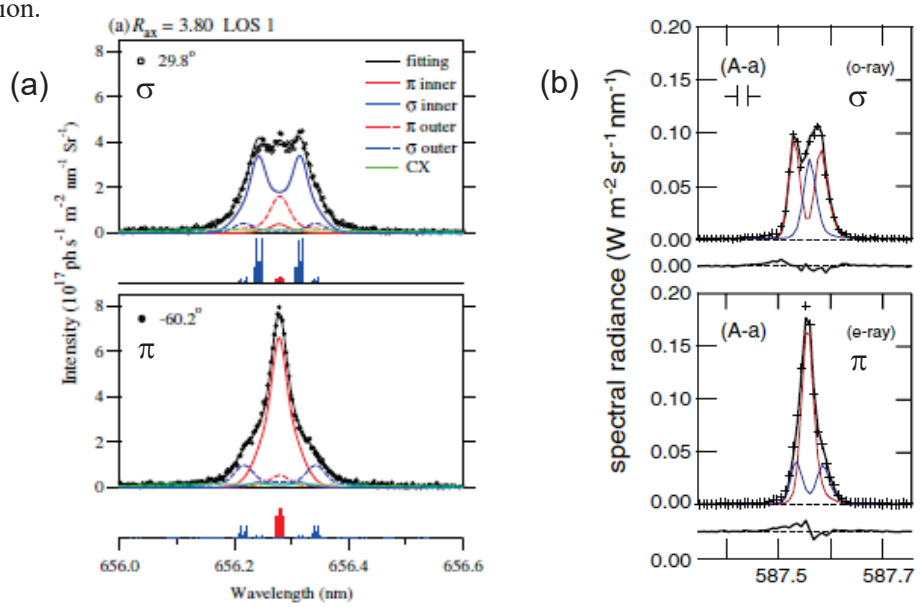

Fig. 1 Zeeman Effect of (a) Hα (6563Å) [1] and (b) HeI (5876Å) [2] spectra. When polarizer is not used, measured spectral profiles are broadened by a mixture of π and σ components.

4. Entrance slit function of 1m normal incidence VUV monochromator

In order to measure the ion temperature using a 1m VUV normal incidence monochromator, an entrance slit function has to be accurately determined because the monochromator has a large spectral aberration due to a simple focal system without use of mirror. At first the entrance slit must be carefully checked with laser light and simple microscope. Two sharp knife edges have to be set accurately parallel to the grating axis and zero position of the entrance slit has to be determined after checking an exact parallel position of the two knife edges along the slit height.

The slit function was obtained by scanning the wavelength in steady ECR and He-glow discharges for wall cleaning in CHS. Lyα (1215.67Å) and HeI (584.3Å) lines were measured for checking the slit function. Mercury lamp was also used in N_2 flow condition to avoid air attenuation of VUV lines at HgI 2536.5Å, HgI 3125.66Å and HgI 3131.83Å. The results from Lyα spectral profile measurement are shown in Figs.2 (a), (b) and (c) at entrance slit width of 10, 20 and 30μm, respectively. The exit slit width is identical to the entrance slit width. A secondary electron multiplier (R595: Hamamatsu co. ltd.) is used for detecting the VUV line. The detector possesses sufficient quantum efficiency in most VUV wavelength ranges, i.e. 300-1800Å.

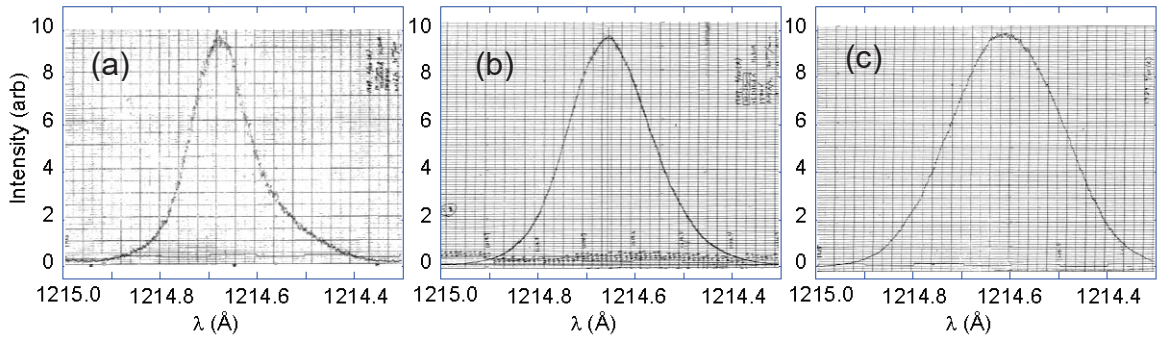

Fig. 2 Slit function of 1m normal incidence VUV monochromator obtained through Lyα spectral profile measurement at entrance slit width of (a) 10μm, (b) 20μm and (c) 30μm.

When the entrance slit width is narrower, the slit function is asymmetric, e.g. 10μm case in Fig. 2(a). It indicates the spectral aberration in focusing mechanism of the present VUV monochromator. The slit function is further checked for different wavelength ranges using several lines mentioned above. We found the slit function hardly changes against the wavelength.

The spectral resolution is also examined as a function of entrance slit width. The result is compared between Lyα and HeI lines, as shown in Fig.3. It is clear from the figure that the spectral resolution is identical between two lines. We understand the spectral resolution is almost constant against the wavelength.

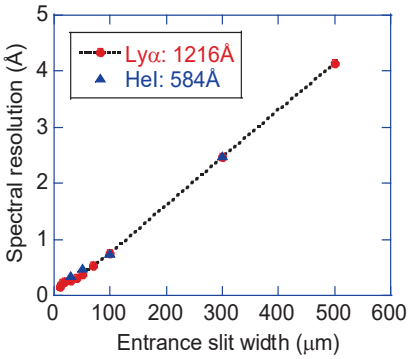

Fig. 3 Spectral resolution as a function of entrance slit width at Ly (solid circles) and HeI (solid triangles) lines.

5. Results of edge ion temperature measurement

5-1 Ion temperature from OVI

Spectral profiles of OVI (1031.9Å) were observed from ECH plasmas (B_t=0.9T, P_{ECH}~100kW, $T_e(0)$~0.4keV, n_e=0.6x10^{13}cm^{-3}) in CHS. Since the density of ECH plasmas is very low, the ion temperature is entirely low due to less equipartition between ions and electrons. Of course the OVI emission is not located in the central plasma region, but the ion temperature of OVI is not so different from $T_i(o)$ because the ion temperature profile seems to be flat along the plasma radius direction. The ion temperature analyzed from OVI spectral profiles is plotted in Fig.4 as a function of discharge time. The electron density shows a gradual increase during the ECH pulse of 35ms, then the electron and ion temperatures begin to decrease during the discharge.

The ion temperature is analyzed by

$$I(\lambda) = \int [+\infty \rightarrow -\infty] G(\lambda') S(\lambda-\lambda') d\lambda', \quad (3)$$

where $I(\lambda)$ and $G(\lambda')$ are the measured spectral profile and the Gauss profile, respectively. $S(\lambda-\lambda')$ is the slit function obtained from Fig. 2(a). As $G(\lambda')$ and $S(\lambda-\lambda')$ are normalized, $I(\lambda)$ is also normalized as

$$\int [+\infty \rightarrow -\infty] I(\lambda) d\lambda = 1. \quad (4)$$

The ion temperature can be obtained from analyzed $G(\lambda')$ profile, as shown in Fig. 5. A very low OVI ion temperature can be obtained with small error bar at the end of ECH pulse, T_i(OVI) = 19±3eV at t=35ms.

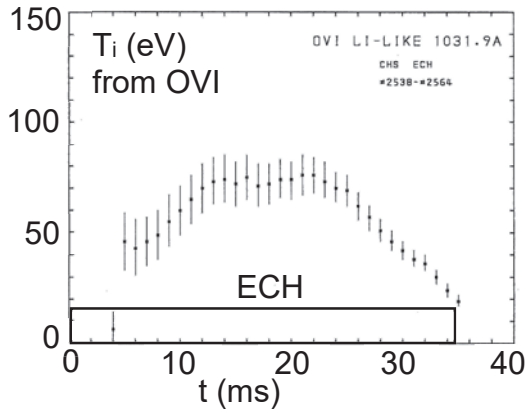

Fig. 4 Temporal ion temperature behavior analyzed from OVI profile during ECH discharge.

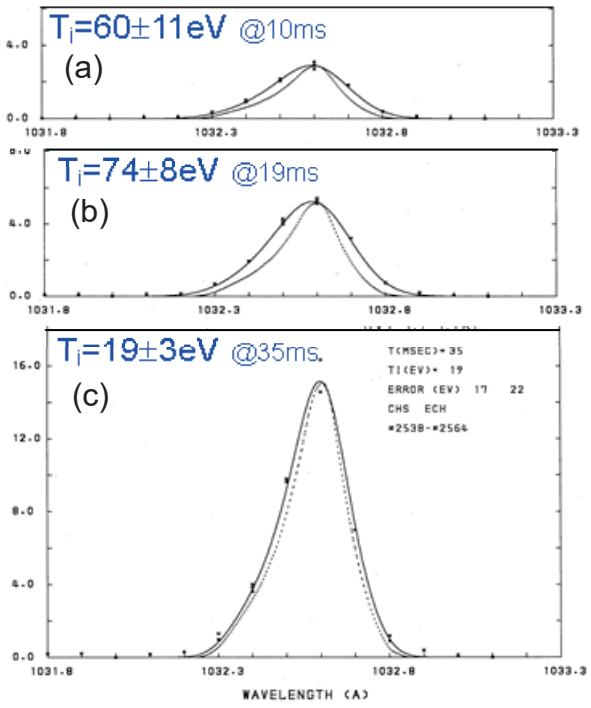

Fig. 5 Measured OVI profile $I(\lambda)$ (solid line) and slit function $S(\lambda-\lambda')$ at (a) t=10ms, (b) t=19ms and (c) t=35ms.

5-2 Ion temperature from CIV

Ion temperature was also measured from CIV (1548.2Å) spectral profile during NBI discharges in CHS. The ion temperature decay after switching off the NBI pulse is plotted in Fig.6. The edge ion temperature measured from CIV keeps a constant value of T_i(CIV)~40eV during 2ms after switching off the NBI pulse. After switching off the NBI beam the heat input to the edge plasma is a function of plasma confinement time, τE, and beam slowing down time, τ_s. Since the energy exchange time between ions and electrons, τ_{ei}, has a similar value to the τ_E in the discharge, i.e. $\tau_{ei} \sim \tau_E = 3$ms, the ion temperature is probably identical to the electron temperature. In the NBI discharge of CHS the electron temperature immediately starts to decrease after switching off the NBI beam, while the NBI fast ions mainly heat electrons and the value of τ_s (~5ms) is longer than τ_E. Therefore, the constant edge ion temperature phase of 2ms after switching off the NBI beam may be reasonable because it simply reflects τ_E.

Based on the present method an extremely low edge ion temperature is successfully observed, e.g. T_i(CIV)=9eV at t=136.6ms, as shown in Fig.7. A small temperature increase during t=135-136ms may reflect an effect of recombination from C^{4+} ions to C^{3+} ions.

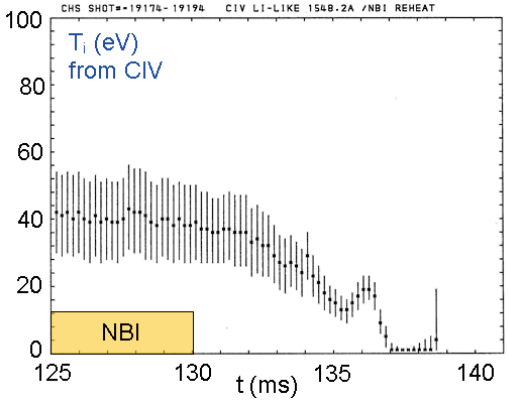

Fig. 6 Temporal ion temperature behavior analyzed from CIV profile at the end of NBI discharge.

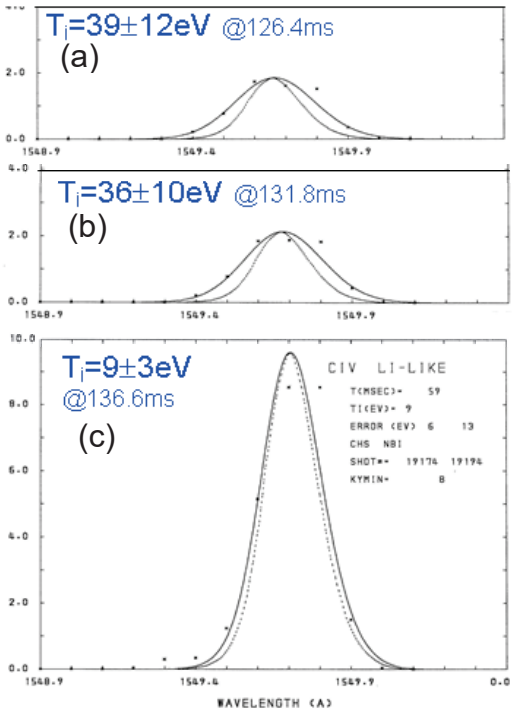

Fig. 7 Measured CIV profile I(λ) (solid line) and slit function S(λ-λ') at (a) t=126.4ms, (b) t=131.8ms and (c) t=136.6ms.

6. Summary

The present method based on accurate determination of slit function enabled to observe low edge ion temperature in VUV region. If a VUV spectrometer is combined with concave mirror system [3], a spatial profile measurement of edge ion temperature may be possible.

References

[1] A. Iwamae, A. Sakaue, N. Neshi et al., J. Phys. B **43** (2010) 144019.

[2] K. Mizushiri, K. Fujii, T. Shikama et al., PPCF **53** (2011) 105012.

[3] S.Morita, S.Muto and M.Sakurai, Fusion Eng. Des. **34-35** (1997) 211

ICRF Heating on EAST

Xinjun Zhang[1,a)] , C.M. Qin[1)], L.N. Liu[1)], Y.P. Zhao[1)], H. Yang[1)] ,B. Lyu[1)],J.F. Chang[1)],J. Huang[1)], M.H. Li[1)], B.J. Ding[1)], X.Z. Gong[1)], B.N. Wan[1)], Y.T. Song[1)], J.G. Li [1)] , L. Ai[1)] , L.L. Ping[1)] , and EAST Team

[1]Chinese Academy of Sciences, Hefei 230031, China

Abstract

Radio frequency (RF) power in the ion cyclotron range of frequencies (ICRF) is one of the primary auxiliary heating techniques for Experimental Advanced Superconducting Tokamak (EAST). This paper summarizes effects of ICRF power on LH coupling and modification of heat loads on EAST. Different rotation behavior are observed in the LHCD discharges. ICRF can also be induced counter-current rotation in the LHCD L-modes discharges. In Hydrogen minority in Deuterium plasma, the interaction of fast wave and fast D-NBI ions are detected on EAST. Acceleration of fast D ions are confirmed by neutron yield.

1. Introduction

The research objectives of EAST are to perform advanced tokamak research in high performance regime and to explore methods for achieving a steady-state operation for a tokamak fusion reactor[1,2]. RF power in the ICRF is one of the primary auxiliary heating techniques for EAST. The ICRF system[3] on EAST provides plasma heating and current drive through various scenarios over a range of magnetic fields. A 12MW ion cyclotron resonance heating (ICRH) system has been designed and constructed on ASIPP for EAST. The system consists of eight independent power lines. each designed to generate and launch 1.5 MW of RF power into the machine during a 1000-s period in the 25 to 70 MHz frequency range. In this paper, we will present an overview of the main experimental results from recent campaign on EAST.

2. Challenges for ICRF Coupling and Heating on EAST

The performance of ICRF heating has progressed steadily in the EAST [4-11]. For the present EAST antennas, the coupled power has been limited often by arcing in the antenna and transmission lines and by larger reflected power due to ELMs and others. This is thought to be a result of light loading at the low densities typically used for long pulse operation. Thus, EAST has identified increasing the coupled power and improving the core heating effectiveness as high priority. The coupling experiments were focus on antenna phasing and gas puffing. The coupling performance was better under lower wave number. By fueling the plasma from antenna local gas injectors, as shown in fig.1, placed as uniformly spaced array from top to bottom at each side limiter of the B-port antenna, which works in dipole phasing, the coupling resistance of the B-port antenna increased obviously. Furthermore, the coupling resistance of the I-port antenna was insensitive to a smaller rate of gas puffing but a sharp increase in the coupling resistance of the I-port antenna occurred when the gas injection rate was higher. which was mainly caused by the toroidal asymmetric boundary density arising from gas puffing.

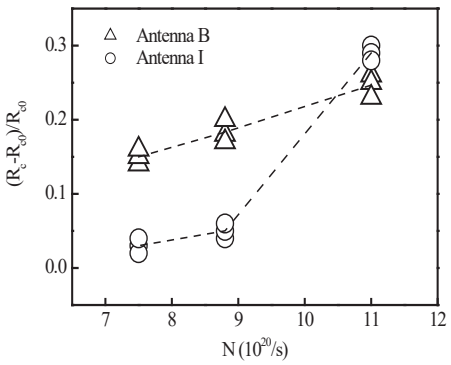

Figure 1. Relative improvement of antenna resistance with gas puff

3. Observations of impurities behavior and Modification of LH coupling and heat load

As shown in Fig. 2(a) the application of ICRF power can reduce LH coupling efficiency. Previous experiments on Tore Supra[12], EAST[13], Alcator C-Mod [14] and JET[15] have demonstrated ICRF power can depletes the density in front of the LH antenna when the active ICRF antenna is magnetically connected or adjacent to the LH antenna. As shown in Fig.2., spectroscopic observations revealed significant increases in metal impurity concentrations during the RF pulse, with tungsten levels increasing by as much as a factor of four at the RF powers about 1.0MW. This indicates that the tungsten limiters of LH are the major impurity sources in the ICRF heating phases.

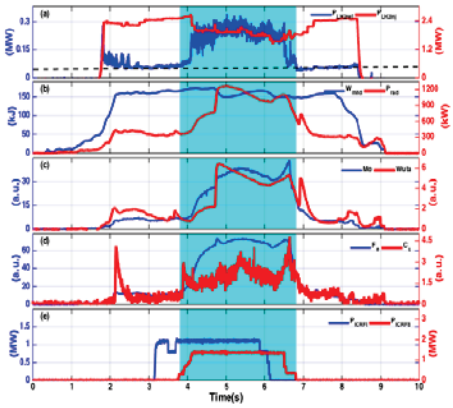

Figure 2 Observations of impurities behaviour are presented from ICRF heating experiments on the EAST, using graphite limiters and stainless steel antenna Faraday shields.

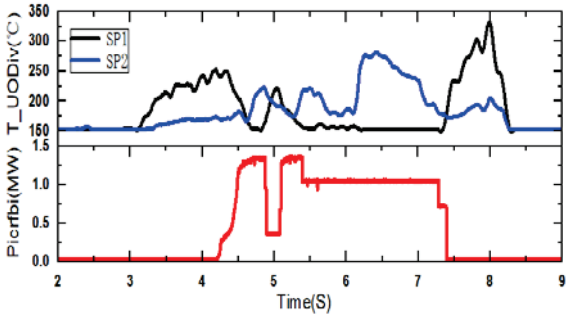

Figure 3 Surface temperature evolution on the right side limiter

The surface temperature elevation on the actively cooled side limiters of the LH launcher

is monitored by infrared cameras. When the 4.6GHz LH launcher was powered alone. Hot spots appeared in front of the waveguide rows on the left and right side limiter. When ICRH was added from B-port antenna next to the LH launcher, both LH coupling and heat loads were modified. The total power reflected coefficient averaged over all the LH modules increase from 3% to 14%. Furthermore, as shown in Fig.3, the LH coupling and heat loads showed different evolutions on the top and bottom parts of the launcher.

4. Interaction of fast wave and fast ions

On EAST, NBI and ICRF are usually combined in experiments requiring a large amount of heating power. The interaction between fast waves and the fast particles has been observed in two different types of experiments. The first type is the second harmonic of deuterium with higher hydrogen concentration. The second type of experiments is third harmonic heating of a D plasma. As shown in figure 4, when adding the ICRF in NBI heated plasma, the increase of neutron can reach 150. But operating ICRH only, the increase in neutron is less than 30. A possible candidate explanation would be that the beam ions are absorbing the RF power.

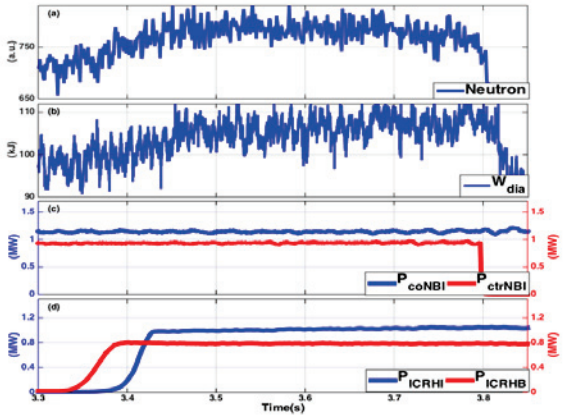

Figure 4 Examples of the EAST shots with combined NBI and second harmonic RF Heating

5. Plasma Rotation driven by ICRF in LHCD target plasma

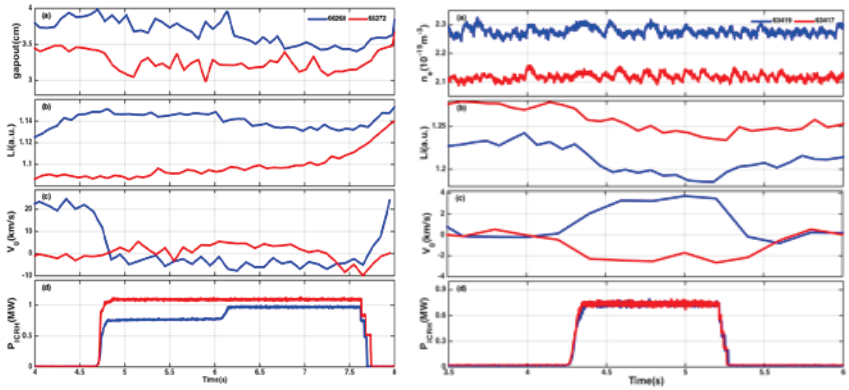

Figure 5 Counter Rotation driven by ICRH in the LHCD target plasma: small change in outer gap(left) and in the core plasma density(right).

Toroidal plasma rotation in a tokamak has attracted a great interest due to its effects on plasma stability and confinement. On EAST, toroidal rotation changes due to ICRH have been measured using a high resolution X-ray imaging crystal spectrometer[16]. Core toroidal

rotation behavior with ICRF minority heating have been examined in the plasmas with and without Lower Hybrid Current Drive (LHCD) on EAST[17,18]. ICRH induced rotation changes in both the co- and counter-current direction have been observed on EAST L-mode LHCD plasmas. Here, we show an example of two discharges with very similar parameters. As shown in Fig.5, small outer gap change(left) and small density change(right) may lead to totally different rotation behavior. The reason for this is still not clear. We found that the changes in the profiles are almost the same both before and during ICRF phase. It seems to have correlation with current profiles.

Acknowledgements

This work was supported by: 1) National key research and development program (grant No. 2016YFA0400600 and 2016YFA0400601); 2) National Natural Science Foundation of China under grant No. 11675213 and 111628509; 3) National Magnetic confinement Fusion Science Programme (grant No. 2015GB101001, 2015GB103002 and 2013GB106001B).

References

[1] B.N. Wan, International Collaborators, Nucl. Fusion 49 (2009) 104011.

[2] J. Li, B. Wan, for the EAST Team and International Collaborators, Nucl. Fusion 51 (2011) 094007.

[3] Y.P. Zhao, X.J. Zhang, et al Fusion Engineering and Design 89 (2014) 2642–2646

[4] L.N. Liu, X.J. Zhang, et al J. Plasma Phys. 85, 101017 (2019).

[5] N. Liu, X. J. Zhang, Y. B. Zhu et al., Rev. Sci. Instrum. 90, 101063 (2019).

[6] X.J.Zhao, L.N. Liu et al Nucl. Fusion 59 (2019) 044004

[7] G. Urbanczyk, X.J. Zhang, et al Nucl. Fusion 59 (2019) 066023

[8] X.J. Zhang, B.N. Wan, Y.P. Zhao, L. Hu, B.J. Ding, X.Z. Gong, et al., Invited Talk, 20th Topical Conference on RF Power in Plasmas, Sorrento, Italy, June, 2013.

[9] X.J. Zhang, Y.P. Zhao, Y.Z. Mao, S. Yuan, D.Y. Xue, L. Wang, et al., Plasma Sci. Technol. 13 (2011) 172.

[10] X.J. Zhang, Y.P. Zhao, B.N. Wan, X.Z. Gong, Y.Z. Mao, S. Yuan, et al., Nucl. Fusion 52 (2012) 032002.

[11] X.J. Zhang, Y.P. Zhao, B.N. Wan, X.Z. Gong, J.G. Li, Y. Lin, et al., Nucl. Fusion 53 (2013) 023004.

[12] A Ekedahl et al. AIP Conference Proceedings, pages 259–262, 2003.

[13] E H Kong et al. Plasma physics and controlled fusion, 54(10), 2012.

[14] G Wallace. Behavior of Lower Hybrid Waves in the Scrape Off Layer of a Diverted Tokamak. PhD thesis, Massachusetts Institute of Technology, December 2009.

[15] K K Kirov et al. Effects of icrf induced density modifications on lh wave coupling at jet. Plasma physics and controlled fusion, 51(4), 2009.

[16] Lyu, et al., Rev. Sci. Instrum. 87 (2016) 11E326

[17] Pan, et al., Plasma Sci. Technol. 18 (2016) 114

[18] Lyu, et al, 25th IAEA FEC, EX/P3-5

[19] Rice J.E., Greenwald M.J., Hutchinson I.H. et al., ‘‘Observations of central toroidal rotation in ICRF heated Alcator C-Mod plasmas’’, Nuclear Fusion 38 (1998) 75.

Conceptual design of CFETR ECRH system

X.J. Wang[1], F.K. Liu[1], Y.Y. Tang[1], L.Y. Zhang[1], D.J. Wu[1], H.L. Wang[1], W. Wei[2], J.G. Li[1]

[1]Institute of Plasma Physics Chinese Academy of Sciences, No.350 Shushan lake Road, 230031, Hefei, China

[2] Hefei University of Technology, No.193 Tunxi Road, 230009, Hefei, China

Abstract

The China Fusion Engineering Test Reactor (CFETR) is the proposed next-generation fusion facility in China, during its two operational phases, a large fraction of externally driven current is foreseen to meet the scientific goals of the two operating scenarios for CFETR. The design of electron cyclotron resonance heating and current drive (ECRH/ECCD) will be carried out with the requirements of physical objectives, as a key design activity of auxiliary heating mix for CFETR. Based on the physical requirements and the technical availability, the frequency is chosen to be 170GHz in order to benefit from the technologies development for ITER, the consideration and the preliminary design of the EC system will be presented in this paper.

1. Introduction

The China Fusion Engineering Test Reactor (CFETR) is the next device for China magnetic controlled fusion (CN-MCF) program which aims to demonstrate fusion energy production up to 200 MW initially and to eventually reach DEMO relevant power level 1 GW, to manifest a high duty factor of 0.3–0.5, and to realize the tritium self-breeding with tritium breeding ratio (TBR) >1. For meeting both phase I and II targets with achievable technical solutions, a new design has been made by choosing a larger machine with major radius R = 7.2 m, minor radius a = 2.2 m, the toroidal magnetic field BT at major radius of 6.5 T for both the physics and engineering designs [1-3].

Two operating scenarios which are self-consistent steady-state and hybrid mode scenarios for CFETR have been developed by using a multi-dimensional code suite with physics-based models [4, 5]. A large fraction of externally driven current is foreseen for achieving the two operating scenarios of CFETR, which calls for optimization of both plasma CD efficiency as well as the engineering integration design of the CD systems. The design of electron cyclotron resonance heating (ECRH) is a key activity in order to achieve the operational scenarios by mixing with other auxiliary heating systems (neutral beam injection (NBI) and lower hybrid current drive (LHCD)).

The main tasks assigned to the EC system are assisted start-up, plasma heating, current drive and MHD instability suppression. The consequent requirements are used for the conceptual design of the EC system. According to the physical integrated simulation, the ECW power is about 30 MW operating at fundamental O mode with the frequency of 250 GHz, applied to drive ~0.88 MA to maintain the magnetic shear in the core and to control $q_{min} > 2$ to avoid any low n MHD mode. In the frame of the present design phase, the conceptual design of ECRH system is undertaking in order to comply with the engineering integration requirement of CFETR as well as to exploit the key technologies for the critical components.

The preliminary design progress along with the considerations of ECRH system are demonstrated in this paper.

2. Overview of ECRH system design

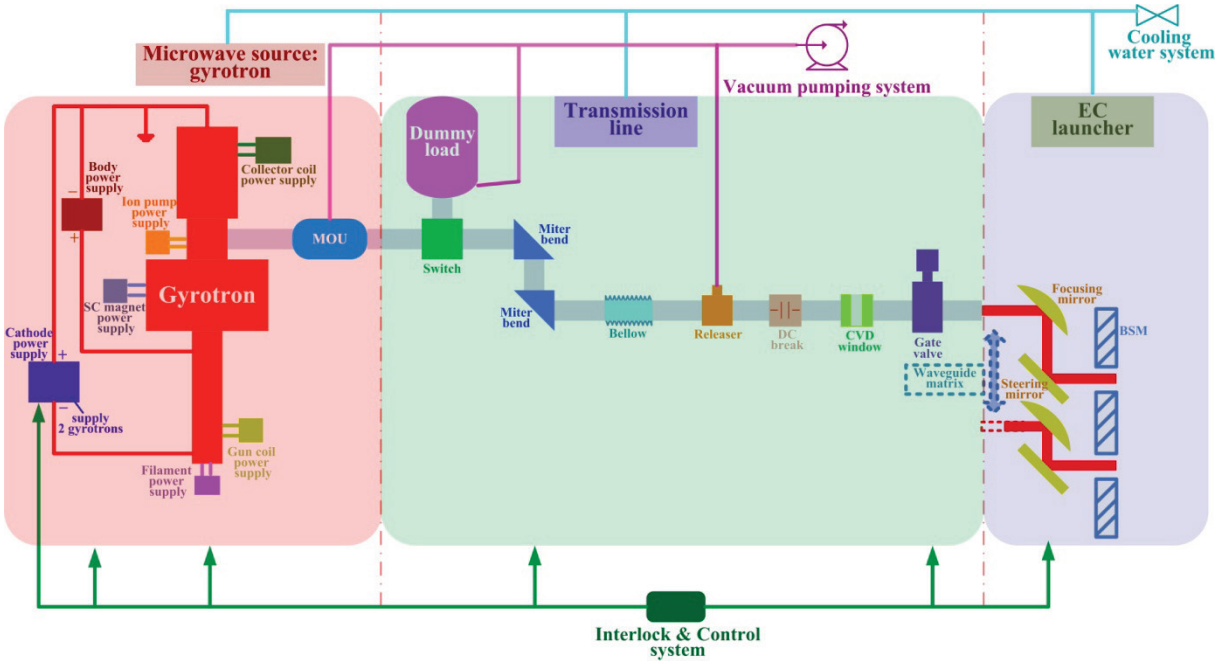

Fig.1 The schematic layout of EC system.

The ECH system, as shown in Fig.1, is composed of gyrotrons, transmission lines, launcher and auxiliary subsystems, such as high voltage power supply, interlock & control, water cooling. In 2015, a version of conceptual design of 170 GHz / 20MW ECRH system was made based on the small size CFETR, in which the total 20MW power was injected through an equatorial window [6]. The challenges that ECRH design encounter are both in technology and physics, advanced design will be foreseen due to the increased Bt, particularly in the development of high frequency gyrotron (~250GHz), the physical needs for each function are not fully defined. From the point of view of the integration machine design, the present approach is to perform a feasible, integrated concept design with parameters of 30 MW /170GHz, which will contribute to the interfaces iteration and engineering integration to comply with CFETR design specifications and assessment the impact on the Tritium Breeding Ratio (TBR), safety and so on.

In this compromise, the selection of the RF source could benefit from the state of art of the megawatt gyrotron for ITER. The arrangement of gyrotrons should be modular to satisfy design criteria on reliability, availability, safety and maintenance. For the target 30MW injection power, 36 gyrotrons with the parameters of 1MW output power at 170GHz are proposed based on the evaluation of appropriate redundancy. The RF source is split into 5 +1 backup clusters delivering power to the launchers.

3. R&D activities of transmission line

The generated power will be transmitted by the evacuated corrugated waveguide transmission lines. Transmission lines should satisfy a series of technical requirements, therefore there are different microwave components distributed along the line, such as MOU, corrugated waveguide, miter bends and some

auxiliary devices. For the sake of vacuum maintaining, Chemical Vapor Deposition (CVD) diamond window together with fast gate valve will be equipped in each line. The external site allocation of CFETR is not yet defined, some R & D activities are implemented for microwave components design (seen in Fig.2), based on the EAST 140GHz /1000s ECRH system [7,8]. The performances of TL components will be evaluated on the new test-bench at the frequencies of 140GHz and 170GHz.

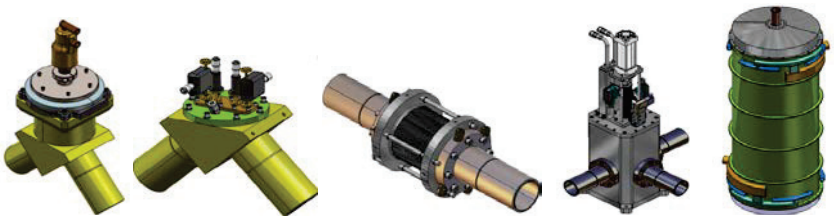

Fig.2　R&D of some key transimission components.

4. Launcher

For the sake of meeting the engineering integration requirement of CFETR, the launcher design is in high priority. The front of the launcher is exposed to the plasma with harsh neutron damage. The launcher configuration should be compact and robust in order to realize reliable continuous operation. Movable parts are not preferred in facing of plasma. However, for the purpose of current profile control, the capability of beam steering is needed. Any launcher structure in CFETR needs to be compliant with other systems, of most importance are the breeding blankets (BB) and remote handling procedures. In order to facilitate the iteration with other engineering tasks, the launcher is currently design based on the front steering concept, which is extensively used in current fusion devices.

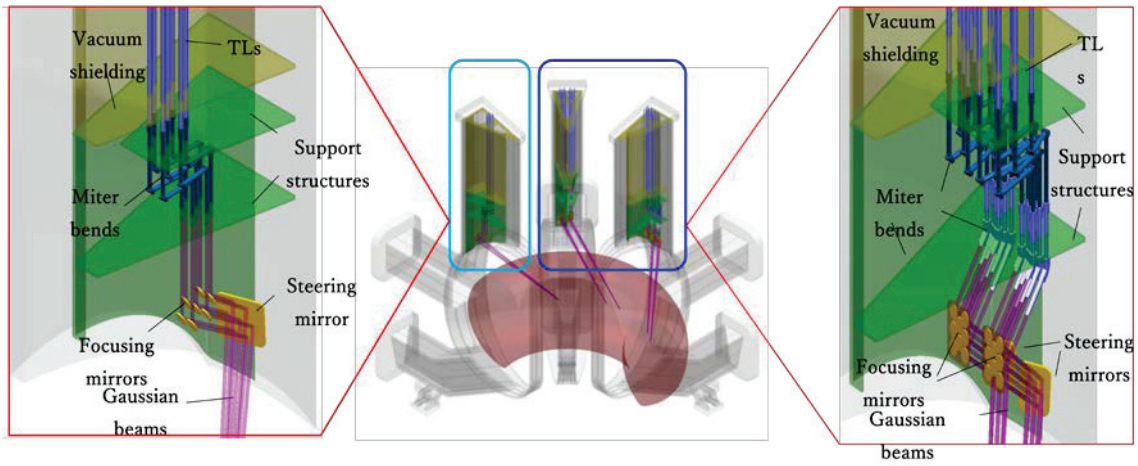

Fig.3　Schematics of launcher concepts.

With regards to the limited equatorial ports, ECW power is anticipated to be top injected. The view of launchers installed in three top ports is shown in Fig.3. Two of the vertical launchers are used for current drive with the maximum power of 16MW, two bunches with 8 beams each are accommodated. Another launcher that emits a bunch of 7MW is considered for NTM control with wide-angle range. To investigate the performance and optimize schemes of power injection for the design of the launcher, ray tracing

simulation needs to be performed based on new plasma equilibrium for optimization launching parameters and EC operational regime [9].

As is shown in Fig.3, in this case, four breeding blanket modules are affected by the required openings for beam penetrations of each launcher. The first estimate of the decrease in Tritium Breeding Ratio(ΔTBR) and the induced neutron heat flux on launcher components and toroidal field coils is under calculating. The impacts are depending on the design of the launcher and its integration in the blanket, for saving TBR, the optical routes of beam-line are further optimized to minimize the openings area of blankets. Fig.4 demonstrates the modified transmitting routes of Gaussian beam which results in embedding the last reflecting mirror into the blankets. The occupied area can be slightly reduced by modification in the launched beam.

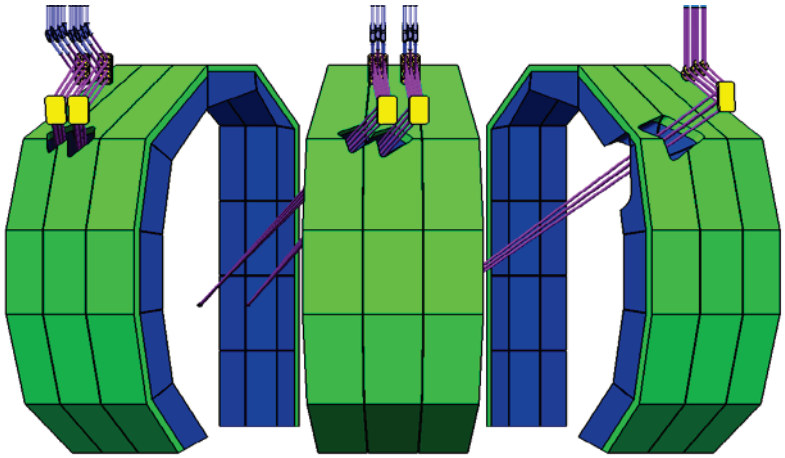

Fig.3　EC Launchers integration in breeding blankets .

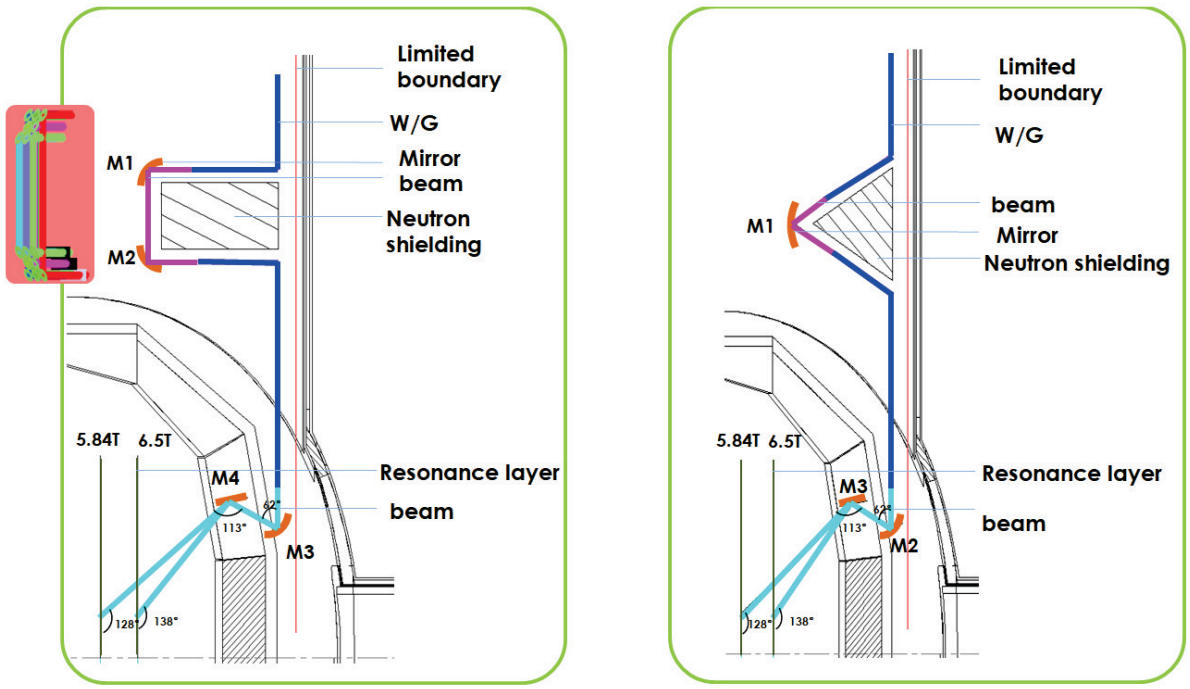

Fig.4　Alternative optical routes for top launcher to reduce the opening area on BB .

5. Summary

The conceptual design of 30MW 170GHz ECH system for CFETR is presented, mainly concerned with the technical feasibility assessment to comply with the integration requirement of CFETR as well as to pursue technical solutions for critical components. As the project is in the initial stage, efforts are focus on the design of launcher, several beam injection options for front steering top launcher are under assessment taking into account the guidelines for the integration with other systems. The crucial issues of multi-beam launcher will be addressed further. Detailed design is anticipated to be conducted which could provide a baseline design with maximal achievable reliability and availability in the near future.

Acknowledgements

This work was partly supported by the Post-CUP Program. It was also supported by National Key R&D Program of China (grant nos. 2017YFE0300500 and 2017YFE0300503).

References

[1] G. Zhuang, et al., Nucl. Fusion **59** (2019) 112010.
[2] Y.X. Wan, et al., Nucl. Fusion **57** (2017) 102009.
[3] J. Li, et al., J. Fusion Energy **38** (2018) 113-24.
[4] X. Jian, et al., Nucl. Fusion **57** (2017) 046012.
[5] J. Chen et al., Plasma Phys. Control. Fusion **59** (2017) 075005.
[6] Y.Y. Tang, et al., Fusion Engineering and Design **94** (2015) 48–53.
[7] D. J. Wu, PHD dissertation, University of Science and Technology of China (2019).
[8] D. J. Wu, et al., IEEE Access **5** (2017) 6187-6191.
[9] W. Wei, et al., Plasma Sci. Technol. **21** (2019) 065101.

Simulation of energetic particle driven geodesic acoustic mode channeling in LHD using MEGA code

Hao WANG[1], Yasushi TODO[1], Masaki OSAKABE[1], Takeshi IDO[1], and Yasuhiro SUZUKI[1,2]

[1]National Institute for Fusion Science, Toki 509-5292, Gifu, Japan

[2]Graduate University for Advanced Studies, Toki 509-5292, Gifu, Japan

Abstract

Energetic particle driven geodesic acoustic modes (EGAMs) in the Large Helical Device (LHD) plasmas are investigated using MEGA code. MEGA is a hybrid simulation code for energetic particles (EPs) interacting with a magnetohydrodynamic (MHD) fluid. The low frequency EGAMs are reproduced. Also, the energy transfer is analysed and the bulk ion heating during the EGAM activity is observed. The ions obtain energy when the EPs lose energy, and this indicates that an energy channel is established by EGAM. The EGAM channelling is reproduced by simulation for the first time. The heating power of bulk ions is 3.4 kW/m^3 which is close to the value 4 kW/m^3 evaluated from the experiments. It is found that the sideband resonance is dominant during the energy transfer from EGAM to the bulk ions, and the transit frequencies of resonant bulk ions are half EGAM frequency.

1. Introduction

Geodesic acoustic mode (GAM) is an oscillatory zonal flow coupled with density and pressure perturbations in toroidal plasmas[1-2]. In the past years, energetic particle driven GAM (EGAM) has been observed in JET, DIII-D, Large Helical Device (LHD), ASDEX-Upgrade, and HL-2A[3-9]. In the DIII-D experiment, the drops in neutron emission during the EGAM bursts suggest beam ion losses. Also, in the LHD experiment, anomalous bulk ion heating during the EGAM activity suggests an energy channel created by EGAM. In addition, EGAMs interact with turbulence and affect the plasma confinement. Then, the understanding of the EGAMs is important for magnetic confinement fusion, because the energetic particles (EPs) need to be well confined and the bulk plasma heating needs to be improved. At present, the existence of EGAM energy channel has not been demonstrated by simulation. Also, it is quite conceivable that the bulk ions obtain energy from EGAM via Landau damping, but it is not clear which resonant bulk ions are the dominant. The present proceeding solves the above problems and gives clear evidence in the following sections.

2. Simulation model and parameters

The simulation of the EGAM channelling is conducted with MEGA code[10-11], and the simulation model is the same as Ref. [12]. In the extended model, both the bulk ions and EPs are described kinetically. The following equations in the extended model are different from that in the conventional model:

$$\rho\frac{\partial}{\partial t}\mathbf{u}_{\mathbf{E}\perp} = -(\mathbf{M}\cdot\nabla)\mathbf{u}_{\mathbf{E}\perp} - \nabla p_e + (\mathbf{j} - \frac{Z_i e}{m_i}\rho_i\mathbf{v}_{\mathbf{pi}} - \frac{Z_h e}{m_h}\rho_h\mathbf{v}_{\mathbf{ph}})\times\mathbf{B}, \quad (1)$$

$$\mathbf{E} = -\mathbf{u}_{\mathbf{E}}\perp\times\mathbf{B} + \frac{\nabla_{\parallel}p_e}{(-e)n_e} + \eta(\mathbf{j} - \mathbf{j}_{\mathbf{eq}}), \quad (2)$$

$$\rho = \rho_i + \rho_h, \quad (3)$$

$$\mathbf{M} = \rho\mathbf{u}_{\mathbf{E}\perp} + (\rho_i v_{i\parallel} + \rho_h v_{h\parallel})\mathbf{b} + \rho_i\mathbf{v}_{\mathbf{pi}} + \rho_h\mathbf{v}_{\mathbf{ph}}, \quad (4)$$

$$\rho_i\mathbf{v}_{\mathbf{pi}} = \frac{m_i}{Z_i e}(-\frac{\nabla p_{i\perp}\times\mathbf{B}}{B^2} + (p_{i\parallel} - p_{i\perp})\frac{\nabla\times\mathbf{b}}{B}). \quad (5)$$

A realistic 3-dimensional equilibrium generated by HINT code is used for the simulation[13]. This equilibrium data is based on the LHD shot #109031 at time t = 4.94 s. At this moment, the EGAM activity is very strong, thus it is good to reproduce the EGAM phenomenon. The parameters for the EGAM simulation are based on an LHD experiment[5-6]. The injected neutral beam energy is E_{NBI} = 170 keV. For simplicity, a slowing-down EP distribution is assumed in the proceeding. The bulk ion distribution is considered as Maxwellian.

3. Simulation results

MEGA code was applied to the LHD experiment. Figure 1(a) shows the spatial profile of the simulated mode. This mode peaks around r/a = 0.2, the mode width is about 0.4a. The simulated mode is identified as a global mode, which is consistent with the global structure of EGAM. The dominant mode number is m/n = 0/0 for poloidal velocity as represented by the red curve in Fig. 1(a). Also, the dominant mode number is m/n = 1/0 for pressure perturbation. These mode numbers are also consistent with the nature of EGAM. Finally, the magnetic perturbation is much weaker than the poloidal velocity perturbation, and this indicates that it is an electrostatic mode. This is also consistent with the nature of EGAM. Thus, based on the above 3 properties, the simulated global electrostatic mode is identified as an EGAM. This the first time to reproduce an EGAM using the extended model of MEGA code. In addition, the simulated EGAMs' linear frequencies are between 40 kHz to 50 kHz as shown in Fig. 1(b), lower than the theoretically predicted conventional GAM frequency 54 kHz, thus these are low frequency branches of EGAM. The mode frequency decreases with the increasing of EP pressure, and this is consistent with the EGAM property.

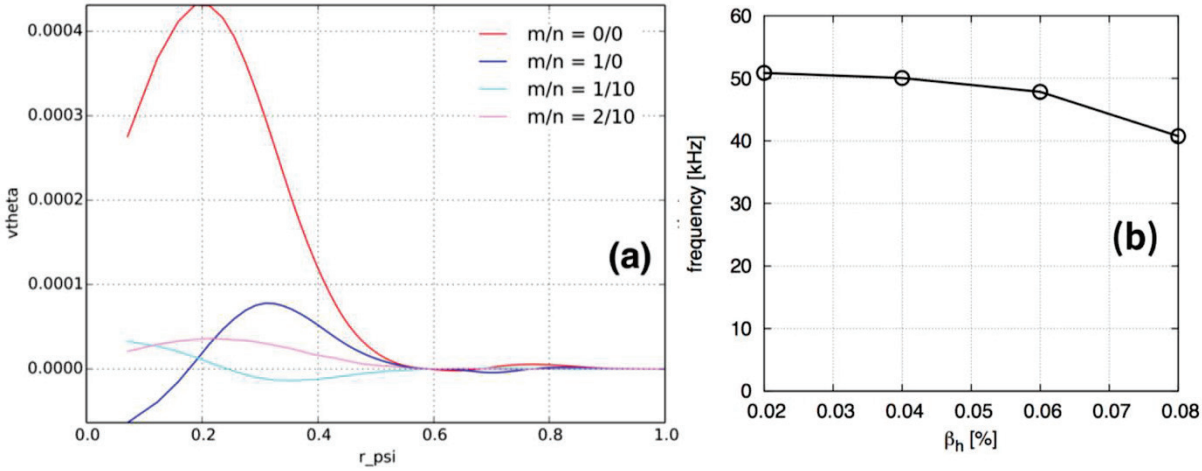

Fig. 1 (a) Poloidal velocity profile of the EGAM. (b) The EP pressure dependence of EGAM frequency in the linear growth phase.

A typical case is simulated to demonstrate the EGAM channelling phenomenon as shown in Fig. 2. Figure 2(a) shows the frequency spectrum of simulated EGAM. The mode frequency in linear stage is 50 kHz, and then, frequency chirps up in the nonlinear phase with time evolution. At t = 0.5 ms, the frequency has already exceeded 60 kHz. Fig. 2(b) shows the time evolution of EGAM amplitude vθ. The linear stage is from t = 0 to about t = 0.1 ms. At t = 0.1 ms, the mode amplitude reaches the maximum value, and then, steps into the nonlinear phase. Fig. 2(c) shows the energy transfer of various species. The product of the perpendicular current of each species and the electric field is integrated in space and time. The perpendicular current consists of grad-B and curvature drift current, and magnetization current. The bulk ion heating during the EGAM activity is observed. The ions obtain energy when the EPs lose energy, and this indicates that an energy channel is established by EGAM. The EGAM channelling is reproduced by simulation for the first time. From t = 0 to t = 0.36 ms, the energy transferred from EP is 63 J. About half of this energy (51%) is transferred to bulk ions (34%) and electrons (17%), while another half is dissipated. The heating power of bulk ions around t = 0.1 ms is 3.4 kW/m^3 which is close to the value 4 kW/m^3 evaluated from the experiments[5].

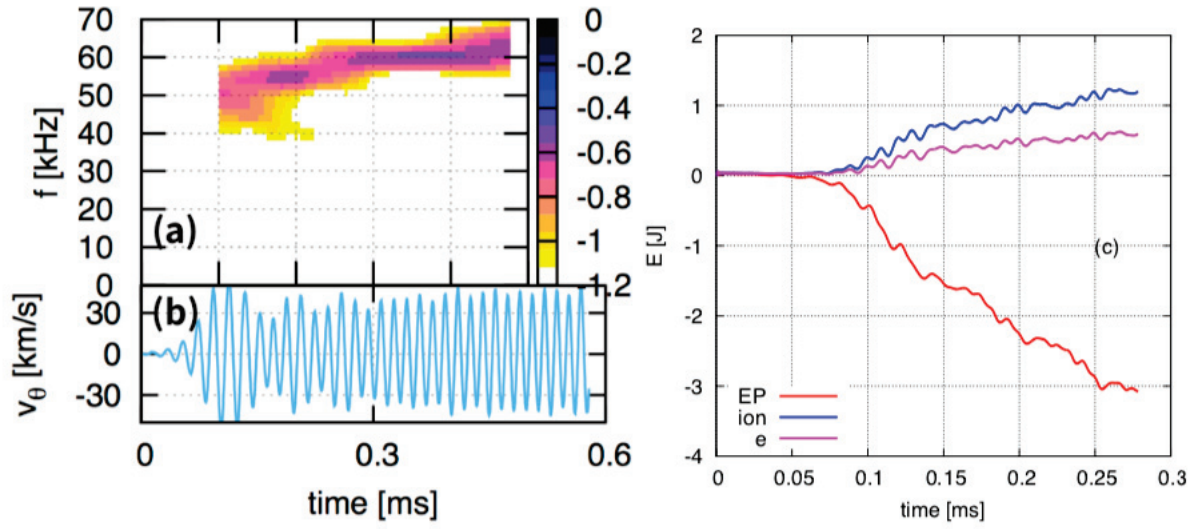

Fig. 2 (a) The frequency spectrum of EGAM. (b) The time evolution of EGAM amplitude vθ. (c) Energy transfer of various species during EGAM activity.

In order to investigate the resonant particles, the δf distribution of both EPs and bulk ions at different times are analysed in the particle transit frequency space, as shown in Fig. 5. The particle transit frequency f_{tr} is defined by $f_{tr} = v_{||}/(2\pi qR0)$, where $v_{||}$ is particle parallel velocity, q is the safety factor value, and R0 = 3.75 m is plasma major radius. For simplicity of f_{tr} calculation, q = 2.8 is a constant for all the particles in the above f_{tr} equation, although q value has a normal shear profile in the equilibrium of simulation. The EGAM obtains energy from EPs via inverse Landau damping, and EGAM transfer energy to bulk ions via Landau damping. These processes modify the distribution function of both EPs and bulk ions, and thus, δf values change with mode evolution. The negative δf value forms the hole structure in phase space, and the positive δf value forms the clump structure. Large absolute δf values indicate strong interactions between EGAM and resonant particles. Fig. 5(a) shows the resonant EPs. A hole around f_{tr} = 50 kHz is formed. The transit frequencies of particles in the hole increase with time evolution, and this increase of frequency is kept consistent with the chirping up of EGAM frequency. The resonance condition between EGAM and EPs is given by $f_{EGAM} = f_{tr,EP}$. Fig. 5(b) shows the resonant bulk ions. Two groups of clumps around f_{tr} = 25 kHz and f_{tr} = 5 kHz are formed. The transit frequencies of bulk ions in these clumps increase with time evolution, and these transit frequencies are kept at half the EGAM frequency (and one-tenth of EGAM frequency). The resonance condition between EGAM and bulk ions is given by

$$f_{EGAM} = l \cdot f_{tr,bulk} \quad , \tag{6}$$

and dominant l values are l = 2 and l = 10. This is the first time to quantitatively reveal the resonance condition between EGAM and bulk ions during the establishment of EGAM channelling.

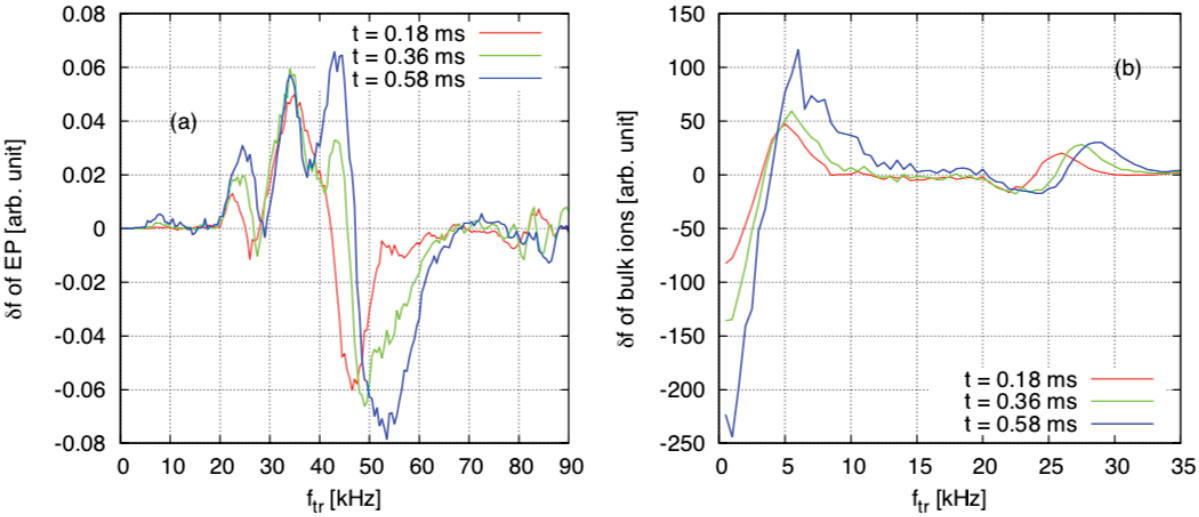

Fig. 3 The δf distribution of (a) EPs and (b) bulk ions in f_{tr} phase space at t = 0.18 ms (red), t = 0.36 ms (green), and t = 0.58 ms (blue).

In Eq. (6), l = 2 is important because l = 2 sideband resonance condition is much easier to be satisfied than higher l value cases. However, l = 10 corresponds to very low transit frequency ions, and these low transit

frequency ions should be difficult to obtain energy from EGAM. In order to confirm that, the energy transfer rate of bulk ions in f_{tr} phase space is analysed as shown in Fig. 4. There is a peak around f_{tr} = 25 kHz, and this peak gradually moves rightward. Similar to Fig. 3(b), this rightward moving indicates that the bulk ions with half mode frequency are kept resonant with the mode. The energy transfer rate is positive, and this indicates that the bulk ions absorb energy from EGAM. In Fig. 4, the red curve at t = 0.109 ms represents a transition between linear growth phase and nonlinear frequency chirping phase, this can also be confirmed from Fig. 2(b). From t = 0.145 ms in the fully nonlinear phase, another peak appears around f_{tr} = 15 kHz. In this simulation, the bulk ion temperature is 4.85 keV, and this thermal velocity corresponds to a transit frequency 14.7 kHz. The peak around f_{tr} = 15 kHz appears in Fig. 6 because most bulk ions' transit frequencies are around 15 kHz. In Fig. 3(b), there is a peak around 5 kHz, but this peak is very weak and difficult to identify in Fig. 4, because the particles around 5 kHz do not absorb too much energy. The bulk ions mainly absorb energy via the particles whose transit frequencies are half the EGAM frequency. In Eq. (6), l = 2 is more important than l = 10 for the establishment of EGAM channeling.

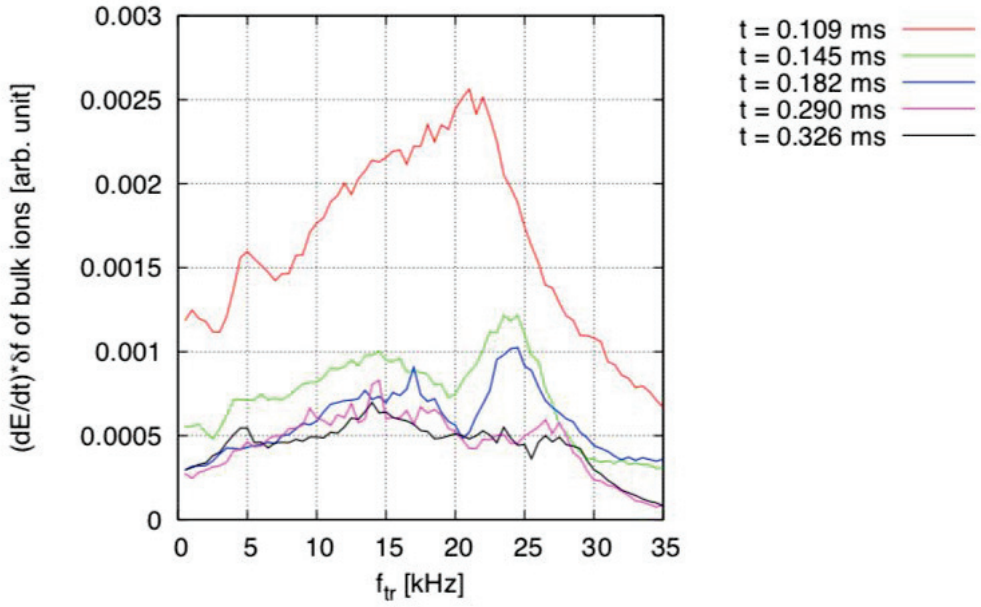

Fig. 6. Energy transfer rate of bulk ions in f_{tr} phase space at different times.

4. Summary and conclusions

A global electrostatic mode is reproduced using extended model, and the mode is identified as an EGAM. Both the mode number and the mode frequency are consistent with the theoretical prediction. The ions obtain energy when the EPs lose energy during the EGAM activity, and this indicates that an energy channel is established by EGAM. The EGAM channelling is reproduced by simulation for the first time. The heating power of bulk ions is 3.4 kW/m^3 which is close to the value 4 kW/m^3 evaluated from the experiments. The δf distribution of both EPs and bulk ions at different times are investigated, and the transit frequencies of resonant particles are analysed. Also, the energy transfer rate of bulk ions at different times are investigated and compared with δf distribution. The resonance condition $f_{EGAM} = l \cdot f_{tr,bulk}$ is satisfied where the dominant l values is l = 2. Another resonance with l = 10 was also found. The resonance condition between EGAM and

bulk ions during the establishment of EGAM channelling is quantitatively revealed for the first time.

Acknowledgements

This work was partly supported by the Post-CUP program. Numerical computations were performed on the 'Plasma Simulator' (FUJITSU FX100) of the National Institute for Fusion Science (NIFS) with the support and under the auspices of the NIFS Collaboration Research program (NIFS17KNST111, NIFS18KNST136, NIFS18KNXN365, and NIFS19KNXN397), and the 'K Computer' of the RIKEN Advanced Institute for Computational Science (Project ID: hp170260 and hp180200). This work was partly supported by MEXT as a 'Priority Issue on Post-K Computer' (Accelerated Development of Innovative Clean Energy Systems), JSPS KAKENHI Grant Nos. JP15K06652, JP18K13529, and JP18H01202. The authors thank Professor H. Sugama, Professor K. Toi, Dr K. Shinohara, and Professor D. Zarzoso for fruitful discussions.

References

[1] DIAMOND, P. et al., Zonal flows in plasma—a review, Plasma Phys. Control. Fusion **47** (2005) R35-R161.

[2] SUGAMA, H. and WATANABE, T., Collisionless damping of zonal flows in helical systems, Phys. Plasmas, **13** (2006) 012501.

[3] BOSWELL, C. et al., Observation and explanation of the JET n = 0 chirping mode, Phys. Lett. A **358** (2006) 154-158.

[4] NAZIKIAN, R. et al., Intense Geodesic Acousticlike Modes Driven by Suprathermal Ions in a Tokamak Plasma, Phys. Rev. Lett. **101** (2008) 185001.

[5] OSAKABE, M. et al., "Indication of bulk-ion heating by energetic particle driven Geodesic Acoustic Modes on LHD", Paper No. EX/10-3, IAEA Fusion Energy Conf., St. Pertersburg (2014).

[6] IDO, T. et al., Identification of the energetic-particle driven GAM in the LHD, Nucl. Fusion **55** (2015) 083024.

[7] IDO, T. et al., Strong Destabilization of Stable Modes with a Half-Frequency Associated with Chirping Geodesic Acoustic Modes in the Large Helical Device, Phys. Rev. Lett. **116** (2017) 015002.

[8] HORVATH, L. et al., Experimental investigation of the radial structure of energetic particle driven modes, Nucl. Fusion **56** (2016) 112003.

[9] CHEN, W. et al., Observation of energetic-particle-induced GAM and nonlinear interactions between EGAM, BAEs and tearing modes on the HL-2A tokamak, Nucl. Fusion **53** (2013) 113010.

[10] TODO, Y., Properties of energetic-particle continuum modes destabilized by energetic ions with beam-like velocity distributions, Phys. Plasmas, **13** (2006) 082503.

[11] TODO, Y. et al., Comprehensive magnetohydrodynamic hybrid simulations of fast ion driven instabilities in a Large Helical Device experiment, Phys. Plasmas, **24** (2017) 081203.

[12] TODO, Y., "A new magnetohydrodynamic hybrid simulation model with thermal and energetic ions", Paper No. O9, Int. Toki Conf. and Asia Plasma Fusion Association Conf., Toki (2017).

[13] SUZUKI, Y. et al., Development and application of HINT2 to helical system plasmas, Nucl. Fusion, **46** (2006) L19-L24.

Evaluation method of effective ion charge (Z_{eff}) in LHD plasma

Y. Kawamoto[1], M. Goto[1,2], T. Oishi[1,2], M. Osakabe[1,2] and T. Morisaki[1,2]

[1]National Institute for Fusion Science, Toki 509-5292, Gifu, Japan

[2]Department of Fusion Science, Graduate University of Advanced Studies, SOKENDAI, Toki 509-5292, Gifu, Japan

Abstract

The measurement of effective ion charge Z_{eff} in LHD is reconsidered. The plasma equilibrium database, the so-called TSMAP, recently made available is used for mapping of locations on the line-of-sight on the effective minor radius r_{eff} so that accuracy of the electron temperature and density profiles for evaluating the Bremsstrahlung intensity has been improved. The influence of impurity lines is also estimated from other diagnostic data, and it is demonstrated that unrealistically large Z_{eff} values derived with the conventional method for low density plasmas are avoidable.

1. Introduction

The effective ion charge Z_{eff} is a fundamental parameter for the plasma confinement study. Although efforts have been made for providing accurate Z_{eff} for all the discharges in the Large Helical Device (LHD) [1, 2], it has been always a concern that magnetic surface structures are changed when the plasma pressure becomes high which causes inconsistency in deriving Z_{eff}.

Z_{eff} is evaluated from the Bremsstrahlung intensity, which is in many cases measured by a line-integrated observation. Evaluation of Z_{eff} therefore needs profiles of the electron temperature T_{e} and electron density n_{e} along the line-of-sight of the Bremsstrahlung measurement. In LHD, the T_{e} and n_{e} profiles are obtained by the Thomson scattering measurement along the major radial direction on the horizontally elongated plasma cross section. For obtaining the T_{e} and n_{e} values on an arbitrary line-of-sight, mapping of locations on the line-of-sight to the locations on the axis of the Thomson scattering measurement is necessary, and this mapping requires information on the plasma equilibrium state. Recently, the TSMAP project has started to provide the plasma equilibrium data for all the discharges in LHD [3], and they can be used for the Z_{eff} measurement.

Another problem in deriving Z_{eff} from the Bremsstrahlung intensity is contamination of impurity lines in the signals. In the evaluation of Z_{eff} in LHD to date, Z_{eff} shows a skyrocketing behavior when plasma density is decreasing, which is believed to be due to the influence of a collection of small impurity lines. We have attempted to exclude such impurity lines in the evaluation of Z_{eff} by quantifying the influence of such impurity lines with the help of other diagnostic data. This paper reports our efforts for such improvements in evaluation of Z_{eff} for LHD.

2. Experimental setup

The measurement of Bremsstrahlung intensity is being made for all the LHD discharges. The radiation is observed by an optical fiber having a core diameter of 300 μm with a collimator lens. The line-of-sight

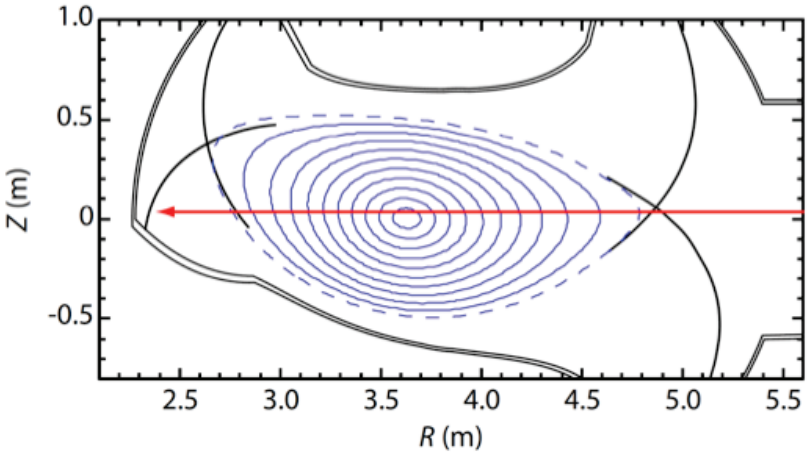

Fig. 1: Vertical cross section of the plasma which includes line-of-sight of the present measurement.

is shown with the plasma cross section in Fig. 1. The collected light passes through an interference filter which limits the transmittable wavelength range in a narrow band width, and is guided to a photomultiplier tube (PMT, HAMAMATSU H5784-01MOD). The central wavelength and FWHM (full width at half maximum) of the transmittance profile of the filter are 536.5 nm and 6 nm, respectively, and the profile is shown with the black dashed line in Fig. 2. The signal from the PMT is digitized with 12 bit dynamic range and recorded with a 10 kHz sampling rate. The measurement with this observation system is referred to as the "intensity measurement" in later discussions.

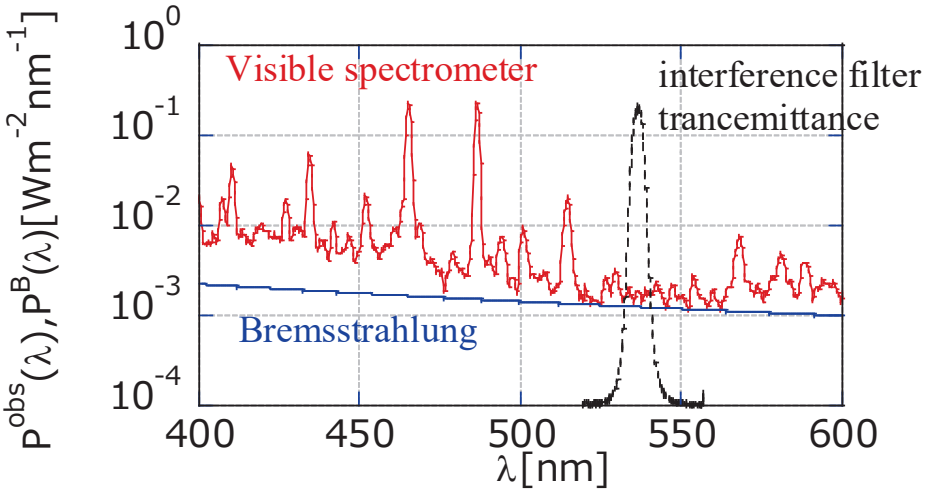

Fig. 2: Example of spectra by the spectral measurement (red dots and solid line), transmittance profile of the interference filter (black dashed line), and synthetic Bremsstrahlung spectrum (blue solid line).

For a supplementary purpose, we sometimes made observation of the Bremsstrahlung spectrum with the system composed of a UV-visible spectrometer and a CCD (charge coupled device) detector. An almost

identical line-of-sight to that for the intensity measurement is used for this observation. The spectrometer, Chromex 500is, has a focal length of 0.5 m and is equipped with three gratings. A grating of 100 grooves/mm out of three is used for the present measurement. The reciprocal linear dispersion is 20.0 nm/mm. The CCD detector (Andor DV-420) has 1024×255 pixels with pixel size of 26 μm^2.

The optical fiber image on the detector is extended over several pixels in the vertical direction, which is perpendicular to the wavelength dispersion. All the signals within such extended fiber image are accumulated and recorded as an intensity signal at the corresponding wavelength position. The time resolution of this measurement is 200 ms. The absolute sensitivity has been calibrated for this system with an integrating sphere (USS-600C). The measurement with this system is hereafter called the "spectral measurement."

3. Theoretical Bremsstrahlung intensity

In the present study, Z_{eff} is assumed to be constant and has no spatial profile in the plasma. In that case, Z_{eff} is evaluated as a ratio of the observed and synthetic Bremsstrahlung intensities, for the latter a pure hydrogen plasma is considered. The synthetic Bremsstrahlung spectrum $P^{\mathrm{B}}(\lambda)$, where λ is the wavelength, is given as

$$P^{\mathrm{B}}(\lambda) = Z_{\mathrm{eff}} \int^{\mathrm{LOS}} \rho^{\mathrm{B}}(\lambda)\, ds \qquad [\mathrm{W\ m^{-3}}], \tag{1}$$

Here, $\int^{\mathrm{LOS}}$ indicates that the integration is conducted along the line-of-sight, and the local quantity $\rho^{\mathrm{B}}(\lambda)$ is explicitly written as

$$\rho^{\mathrm{B}}(\lambda) = \frac{2^6\sqrt{2}}{3\sqrt{3}} \frac{\pi^{1/2}\alpha h a_0^2 R^2}{m^{3/2}c} \sqrt{\frac{1}{kT_{\mathrm{e}}}} \exp\left(-\frac{hc/\lambda}{kT_{\mathrm{e}}}\right) \langle g_{\mathrm{ff}}(T_{\mathrm{e}}, \lambda)\rangle\ n_{\mathrm{e}}^2 \frac{1}{\lambda^2} \qquad [\mathrm{W\ m^{-4}}], \tag{2}$$

where α, h, a_0, and R are the fine structure constant, Planck constant, Bohr radius, and Rydberg constant, respectively, m and c are the electron mass and the light speed, respectively, and $\langle g_{\mathrm{ff}}(T_{\mathrm{e}}, \lambda)\rangle$ is the thermally averaged Gaunt factor for free-free transitions.

For local T_{e} and n_{e} values which are necessary to evaluate Eq. (2), the data measured by the Thomson scattering diagnosis are used. Any location along the line-of-sight can be mapped onto the effective minor radius r_{eff} by the TSMAP database, and T_{e} and n_{e} values at arbitrary r_{eff} can be obtained by interpolation. The values of $\langle g_{\mathrm{ff}}(T_{\mathrm{e}}, \lambda)\rangle$ are calculated with the method of Ref. [4]. Numerical integration is made for Eq. (1) with these parameters.

4. Results and discussion

Although for the intensity measurement we have chosen the wavelength range by the interference filter in which no noticeable line radiation is found, it is known that the signal always contains influence of small impurity lines, and their fraction becomes noticeably large when n_{e} is low so that the Bremsstrahlung intensity is relatively weak.

For a quantitative evaluation of such impurity lines fraction, we use the data obtained by the spectral measurement. An example of the measured spectra is shown with the red dots in Fig. 2. This spectrum contains the Bremsstrahlung and impurity lines. We try to distinguish the Bremsstrahlung part from the

impurity lines by comparing a synthetic spectrum evaluated by Eq. (1) with the measured spectrum.

In this comparison, Z_{eff} in Eq. (1) is increased from unity so long as no experimental value lies below the corresponding synthetic value, and the finally obtained maximum value is here regarded as Z_{eff} of the corresponding plasma. The Bremsstrahlung spectrum evaluated with Z_{eff} obtained this way is drawn with the blue solid line in Fig. 2. It is noted that Z_{eff} derived here should be therefore regarded as the upper limit rather than the best estimate.

Because the spectral measurement can be made only for a limited number of discharges, the method of Z_{eff} evaluation described above is inappropriate to be used as a routine plasma diagnosis in LHD. Instead, we consider to make corrections for the intensity measurement data with the help of other diagnostic data.

The black dotted line in Fig. 2 shows the transmittance profile of the interference filter $T(\lambda)$ as mentioned above. What we obtain by the intensity measurement I_{obs} can be understood as the measured spectrum $P^{\mathrm{obs}}(\lambda)$ multiplied with $T(\lambda)$ and integrated over the wavelength, i.e.,

$$I_{\mathrm{obs}} = \int P^{\mathrm{obs}}(\lambda)T(\lambda)\,d\lambda. \tag{3}$$

The Bremsstrahlung intensity I_{B} can be similarly evaluated from the synthetic Bremsstrahlung spectrum $P^{\mathrm{B}}(\lambda)$ as

$$I_{\mathrm{B}} = \int P^{\mathrm{B}}(\lambda)T(\lambda)\,d\lambda = Z_{\mathrm{eff}}\int \left(\int^{\mathrm{LOS}} \rho^{\mathrm{B}}(\lambda)\ ds\right) T(\lambda)\,d\lambda, \tag{4}$$

where Z_{eff} value derived in the above analysis is used. The difference between I_{obs} and I_{B} would be the contribution of the impurity lines I_{imp}. In LHD, the impurity monitoring system measures several impurity line intensities for watching impurity contaminations in the plasma. Figure 3 shows I_{imp} against the carbon ion line (CIII, 97.7 nm) intensity I_{CIII} from the impurity monitoring system for various discharges used in the present study. It is clearly seen that I_{imp} has a strong correlation with I_{CIII}, and I_{imp} is well expressed

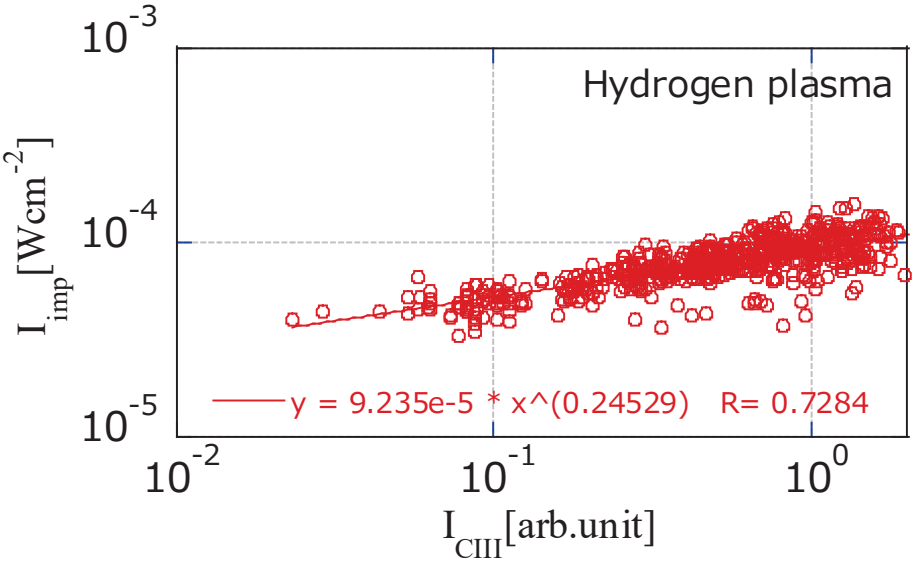

Fig. 3: Correlation between I_{imp} and I_{CIII}.

with I_{CIII} as

$$I_{\mathrm{imp}} = 9.235\times10^{-5}\ (I_{\mathrm{CIII}})^{0.24529}, \tag{5}$$

and this relationship is expected to be valid for all the LHD discharges. Because I_{CIII} is always measured by the impurity monitoring system, I_{imp} can be also evaluated from Eq. (5) without the spectral measurement. I_{B} is then obtained as $I_{\mathrm{obs}} - I_{\mathrm{imp}}$ and Z_{eff} is evaluated with Eq. (4). Figure 4 shows an example of the results which shows the temporal variation of Z_{eff} for a discharge with increasing n_{e}. In this figure, the result without correction of impurity lines is also shown, and it is confirmed that the correction by the present method works effectively. Finally, we conclude that the evaluation method of Z_{eff} has been significantly improved and the reliability is high enough for being used for the various LHD plasma analyses.

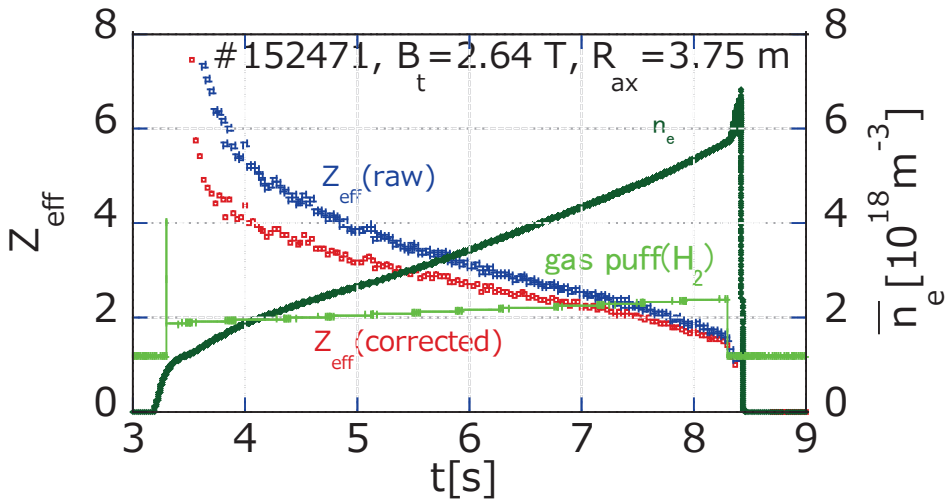

Fig. 4: Example of derived Z_{eff} for a discharge with increasing n_{e}. The result without impurity lines correction is also shown.

Acknowledgements

This work was partly supported by the Post-CUP program. It was also supported by NIFS budget code UPLL010. The help of LHD experiment group for conducting the experiment is also acknowledged.

References

[1] H. Y. Zhou et al., Jpn. J. Appl. Phys. **49** (2010) 106103.

[2] X. L. Huang et al., Plasma and Fusion Research **10** (2015) 3402036.

[3] M. Emoto et al., Fus. Eng. Des. **87** (2012) 2076.

[4] P. J. Storey and D. G. Hummer, Comp. Phys. Comm. **66** (1991) 129.

Observation of tungsten spectra from W^{5+}-W^{45+} in EAST

L. Zhang[1], S. Morita[2], Z. Xu[3], Y. X. Cheng[1,4], X. D. Yang[1,4], L. Li[1,4], Z. W. Wu[1], Y. Yang[5], X. B. Ding[6], T. Oishi[2]

[1] Institute of Plasma Physics Chinese Academy of Sciences, Hefei 230026, China

[2] National Institute for Fusion Science, Toki 509-5292,Gifu, Japan

[3] Advanced Energy Research Center, Shenzhen University, Shenzhen 518060, China

[4] Science Island Branch of Graduate School, University of Science and Technology of China, Hefei 230026, China

[5] Institute of Modern Physics, Fudan University, 220 Handan Road, Shanghai 200433, China

[6] Key Laboratory of Atomic and Molecular Physics and Functional Materials of Gansu Province, Northwest Normal University, Lanzhou 730070, China

Abstract

In the present work, the tungsten spectra at 20-150Å from W^{24+}-W^{45+}ions are analyzed for L-mode plasmas (T_{e0}=1.4keV), typical H-mode plasmas (T_{e0}=2.6-3.0keV) with RF-heating and with NBI heating. The analysis is also done for plasmas with tungsten accumulation (T_{e0}~3.0keV). Recently, identifications of EUV spectra from weakly ionized tungsten ions of W^{4+}-W^{7+} are being newly attempted based on EAST plasmas with extremely low temperature, e.g. T_{e0}<=0.2keV. Preliminary results are presented in the proceeding.

1. Introduction

In order to improve the capability of mitigating heat load of the divertor target, graphite divertor plates at upper divertor in the EAST tokamak were replaced by tungsten monoblock plates [1]. Since then, in the EAST experiment, studies on tungsten behavior and its effect on the plasma performance are crucially important for maintaining high-performance plasmas for a long period. For the purpose fast-time-response and space-resolved extreme ultraviolet (EUV) spectrometers [2-4], which are workable at 10-130Å, 20-500Å and 30-520Å, respectively, have been developed to observe line emissions from tungsten ions and to study the tungsten behavior in the EAST plasma.

2. Tungsten spectra at 40-140Å

Tungsten spectra at 40-140Å are observed in many different plasma scenarios in EAST. In this session, the typical tungsten spectra at 40-140Å observed in five different cases are compared, i.e., L-mode phase with tungsten dust dropping (#80565), NBI and LHW dominant H-mode phase (#80575 and #80093), and

the NBI and LHW dominant H-mode phase with tungsten accumulation (#70769 and #83880). The electron temperature in central plasma, T_{e0}, plasma density, n_e, heating method, and plasma condition and tungsten source for the plasma in these five discharges are listed in Table 1.

Figure 1(a)-(e) shows the tungsten spectra in wavelength range of 40-140Å measured in five different plasma scenarios described in Table 1. As shown in Figure 1 that there are several W-UTA (Tungsten Unresolved Transition Array) existing in this wavelength range, i.e., 45-55Å, 55-72Å, 78-82Å. Additionally serval isolated tungsten lines at the wavelength range of 120-140Å could be observed. It could be found that W-UTA near 50 Å composed of W^{24+} to W^{34+} ions is always observed with strongest intensity, even in high T_e plasmas with T_{e0}≥4.0keV. And the highest ionization stage of tungsten ions depends on T_{e0}. for example, the highly ionized tungsten ions of W^{37+} - W^{45+} are absent in low T_e case of T_{e0}=1.4keV. In general, in the NBI dominant H-mode discharges the observed signal noise in the spectra (see Figure 1(b)) is much larger than that in RF heated H-mode discharges (see Figure 1(c)) due to the existence of energetic particles, which will reduce the certainty of identification of weak tungsten lines. And it is obvious that strong or saturated tungsten spectra are observed during tungsten accumulation phase in Figure 1(d) and Figure 1(e).

Table 1. Comparison of plasma scenarios for observation of the tungsten spectra

Shot No.	T_{e0} (keV) / n_e ($10^{19}m^{-3}$)	Heating method	Discharge condition	W source
80565	1.4 / 3.6 @t=4.9s*	NBI+ECRH	L-mode	Dust dropping
80575	2.6 / 3.0 @t=4.2s	NBI+ECRH	H-mode	with ELMs
80093	3.0 / 2.1 @t=6.6s	LHW+ECRH	H-mode	with ELMs
70769	2.7 / 2.9 @t=3.4s	NBI+ECRH	H-mode, W accumulation	with ELMs
83880	3.0 / 4.4 @t=3.5s	LHW+ECRH	H-mode, W accumulation	with ELMs

*Data are taken at t=4.9s during a discharge

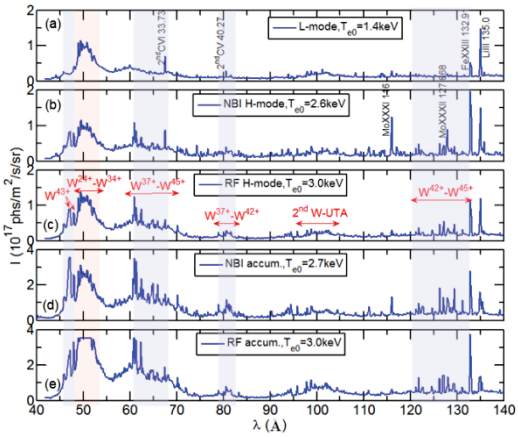

Figure 1. Comparison of W spectra in 40-140 Å for five plasma scenarios

Figure 2 presents the detailed line identification in the spectra at wavelength range of 40-140Å observed in typical RF-heated H-mode based on the NIST database. It could be noted that the W^{43+}-W^{45+} lines with strong intensity are identified from W-UTA at 55-72Å. And W^{40+}-W^{45+} lines with weak intensity is identified at longer wavelength range of 120-137 Å. There are six lines with 4p-4s transition which are very important for quantitative analysis [4], i.e., W^{43+} (E_i=2.210keV) at 61.334 Å and 126.29Å with transition of $4s^24p$-$4s^24s$, W^{44+} (E_i=2.354keV) at 60.93 Å and 132.88Å with transition of 4s4p-$4s^2$, W^{45+} (E_i=2.414keV) at 62.336 Å and 126.998Å with transition of 4p-4s. Unfortunately, the line of 132.88 Å is blended with Fe XXIII at 132.91 Å as shown in Figure 2(c).

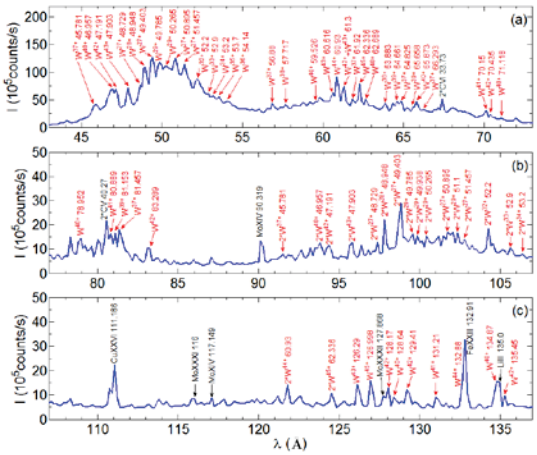

Figure 2. Identification of W spectra in 40-140 Å

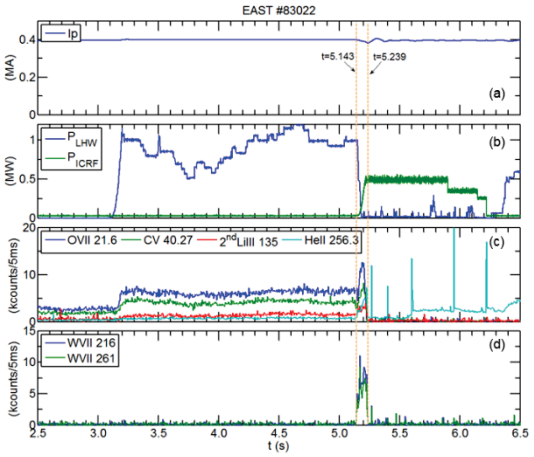

Figure 3. Waveform of EAST discharge #83022

3. Observation of EUV spectra from weakly ionized tungsten ions

Observation of lines from weakly ionized W ions in normal discharges is important because the intensity can suggest tungsten influx rate. Figure 3 shows the waveform of the discharge (#83022). During this discharge minor disruption occurred at t=5.143s when LHW heating is switched to ICRF heating, and tungsten sputtering may be enhanced at tungsten guard limiter of LHW antenna. Strong line intensity of WVII lines (216.219 and 261.35 Å) was observed during 5.143-5.239s (20 CCD frames in total) indicating increased tungsten influx. Plasma was cooled down quickly with large reduction of T_{e0} from 1.5keV to about 0.2keV. And run-away electrons were triggered at t≥5.239s.

Figure 4 shows the time-developed EUV spectra at longer wavelength range of 195-425 Å during t=5.143-5.239s. Several lines from W^{5+} and W^{6+} ions are identified and indicated based on previous experiments in SSPX spheromak [5] and HL-2A tokamak [6]. Identification of more emission lines from W^{7+}, W^{6+}, W^{5+} and W^{4+} ions based on NIST database is indicated with red, pink, orange and light green arrows in Figure 5(c).

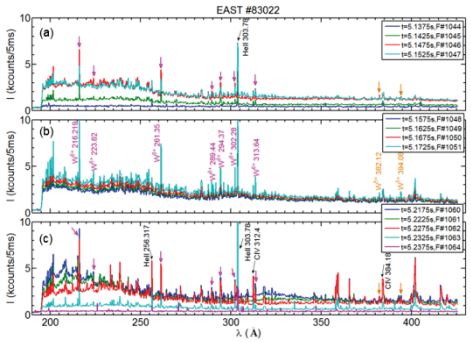

Figure 4. Time-developed EUV spectra at 195-425 Å

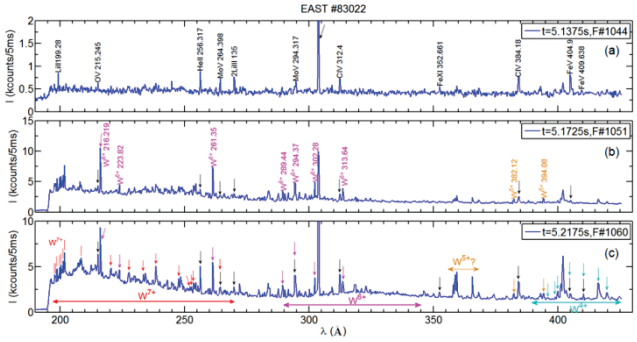

Figure 5. Identification of lines from W^{4+}-W^{7+}

4. Summary and future work

In this work, tungsten spectra at 40-140Å from W^{24+}-W^{45+} ions are analyzed for L-mode plasmas, H-mode plasmas with RF- and NBI heating, and plasmas with tungsten accumulation. Observations of

EUV spectra from weakly ionized tungsten ions of W^{4+}-W^{7+} are being newly attempted, based on EAST plasmas with extremely low temperatures.

In the near future the second fast EUV spectrometer working at wavelength range of 20-500 Å will be installed with observation chords passing through edge plasma and the simultaneous observation of EUV spectra at full range of 10-420Å will be realized. And the accuracy of tungsten line identification at longer wavelength range of 195-425 Å will be increased with the assistance of experimental results from EBIT device.

Acknowledgements

This work was partly supported by the Post-CUP program. It was also supported by Users with Excellence Program of Hefei Science Center CAS (No. 2019HSC-UE014), National Natural Science Foundation of China (Grant Nos. 11575244, 11775269) and National Key Research and Development Program of China (No. 2018YFE0311100).

References

[1] B. N. Wan et al., Nucl. Fusion **55** (2015) 104015

[2] L. Zhang et al., Nucl. Mater. Energy **12** (2017) 774-778

[3] L. Zhang et al., Rev. Sci. Instrum. **86** (2015) 123509

[4] L. Zhang et al., Nucl. Instrum. Meth. **A916** (2019) 169

[5]J. Clementson et al., J Phys B **43**(2010)14409

[6] C. F. Dong et al., Nucl. Fusion **59**(2019)016020

Tungsten Measurements at LHD using Visible M1 Lines

D. Kato[1,2], S. Era[2], H.A. Sakaue[1], I. Murakami[1,3], M. Goto[1,3], T. Oishi[1,3], S. Morita[1,3], N. Nakamura[4], K. Fujii[5], F. Koike[6], X.-B. Ding[7], C.-Z. Dong[7]

[1]National Institute for Fusion Science, Toki 509-5292, Gifu, Japan

[2]Dept. Advanced Energy Engineering Sciences, Kyushu University, Kasuga 816-8580, Fukuoka, Japan

[3]Graduate University for Advanced Studies, Toki 509-5292, Gifu, Japan

[4]Inst. for Laser Science, The Univ. of Electro-Communications, Chofu 182-8585, Tokyo, Japan

[5]Graduate School of Engineering, Kyoto University, Kyoto Nishikyo-ku 615-8246, Kyoto, Japan

[6]Faculty of Science and Technology, Sophia University, Chiyoda-ku 102-8554, Tokyo, Japan

[7]Key laboratory of Atomic and Molecular Physics & Functional Materials of Gansu Province, College of Physics and Electronic Engineering, Northwest Normal University, Lanzhou, 730070, China

Abstract

Visible emission lines of tungsten ions have a potential usefulness for tungsten measurements at ITER and future DEMO reactors. Near ultra-violet (UV) and visible lines of highly charged tungsten ions have been reported at Large Helical Device (LHD). In the last LHD campaign, we experimentally observed local intensity change of the near-UV magnetic-dipole (M1) line emission from the ground state W^{27+} ions corresponding to local electron temperature change by superimposing electron cyclotron heating (ECH) on neutral beam injection heating. At elevated temperatures (about 3 keV) obtained by the ECH, we found a new near-UV emission line of a higher charge state of tungsten ions.

1. Introduction

Tungsten, which is used for divertor materials in ITER, has good properties as a plasma facing component such as high thermal conductivity, small thermal expansion, low erosion yield, and less tritium retention [1]. However, once tungsten accumulates in the core plasma, large radiative power losses of tungsten highly charged ions will limit the plasma performance [2,3]. Tungsten concentration in the core plasma of ITER is a key issue for sustainable operation of high-performance operation with tungsten in-vessel components.

Visible emission lines from the tungsten ions provide useful diagnostics means for ITER and future DEMO reactors because the radiation shielding of detectors is not necessary by using optical fibers. However, spectroscopic observations of tungsten highly charged ions in the core plasmas of existing large devices [4-8] have been limited in soft X-ray, Extreme-Ultra-Violet (EUV) and Vacuum-Ultra-Violet (VUV) regions. Since visible magnetic-dipole (M1) lines of iron highly charged ions in the ground states are observed in solar flares, its potential usefulness for fusion plasma diagnostics has been pointed out [9]. Such visible M1 line emission of highly charged tungsten ions in high-temperature magnetically confined plasmas was observed for the first time by tungsten pellet injection experiments at Large Helical Device (LHD) [10]. However, the highest charge state definitely identified with the visible M1 lines at LHD has been W^{28+} which

is abundant at electron temperatures of about 1 keV [11]. In the present work, near-UV and visible emission lines of higher charge states of tungsten ions are investigated at elevated electron temperatures by superimposing 154 GHz electron cyclotron heating (ECH) on neutral beam injection (NBI) heating.

2. Tungsten pellet injection and visible spectroscopy at LHD

Tungsten is introduced into the LHD plasmas by injecting a carbon pellet containing a tungsten wire. Size of the tungsten wire in the carbon tube is 0.1 mm in diameter and 0.7 mm in length. The pellet is accelerated by pressurized He gas of 10 – 20 atm and injected at 10-O port with the angle of 12˚ to a radial axis on the equatorial plane. Photon emission of injected tungsten was measured at 7.5-L port along 44 lines of sight on a vertically elongated poloidal cross section. Time-resolved (sampling times for 41.55 ms at every 100 ms) emission spectra are obtained using a Czerny-Turner visible-UV spectrometer (grating of 1200 gr/mm and slit width of 50 μm) equipped with a CCD detector.

3. Effects of ECH on local M1 line intensities

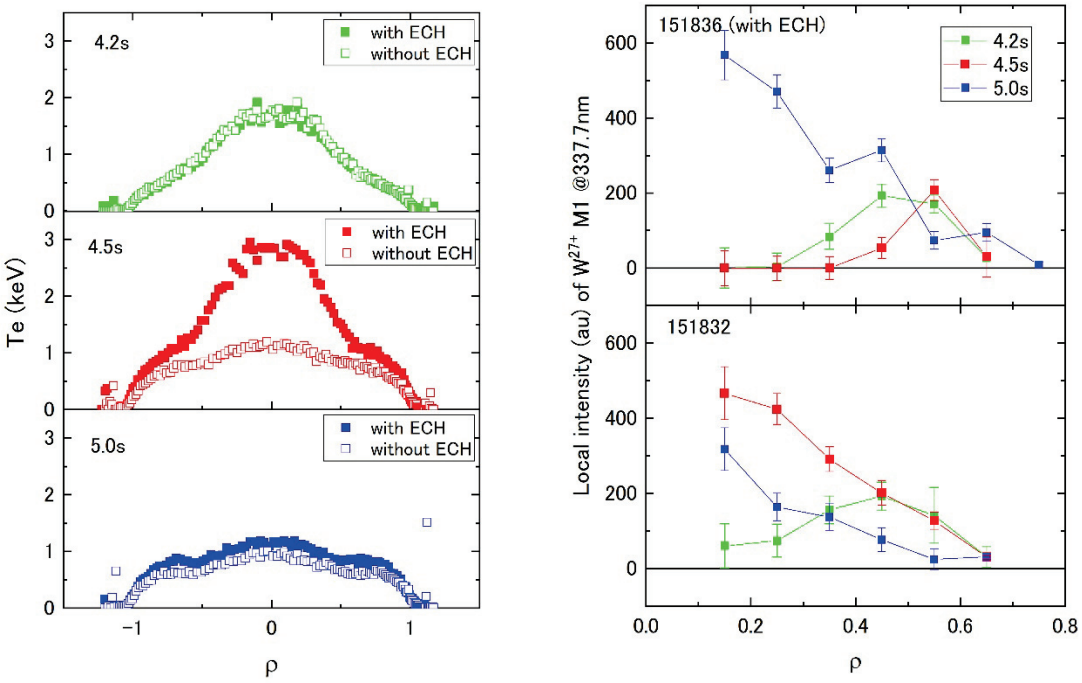

Left: Fig. 1 Radial profiles of electron temperatures by Thomson scattering. Solid squares stand for the discharge with 154 GHz ECH, and open square for without the ECH.
Right: Fig. 2 Local line intensities of the W^{27+} M1 line at 337.7 nm for each discharge with (151836) and without (151832) the ECH.

Figure 1 shows evolutions in radial profiles of electron temperatures after tungsten pellet injection at 4.1 s for each discharge without and with superimposing 154 GHz ECH (about 2MW from 4.2 s until 4.7 s). The NBI heating of about 10 MW was being applied during the both discharges. Without the ECH the central

electron temperature decreases down to about 1 keV due to a strong radiation of tungsten, whereas superimposing ECH recovers that up to about 3 keV. A near-UV line emission due to an M1 transition of W^{27+} in the ground state was observed at 337.7 nm [12] in the both discharges. Line integrated intensities of the M1 line along each line of sight were measured, and local intensities of the M1 line on the poloidal cross section were obtained by Able inversion. Figure 2 shows the local intensities as a function of normalized minor radius, ρ. At 4.2 s (before superimposing ECH), the both discharges show the similar local intensity profiles for the M1 line peaking at $\rho = 0.4 - 0.5$ where the electron temperature is about 1 keV (see Fig. 1). Without the ECH, the peak position moves toward the center ($\rho = 0$) following the decrease of the central electron temperature. In contrast, the M1 line emission at 4.5 s with the ECH which gives a high central electron temperature of about 3 keV, has a vanishing intensity at the center, and has a peak intensity at $\rho = 0.5 - 0.6$.

Photon emissivity coefficients of the M1 line become almost constant at electron densities above 10^{18} m^{-3}. Average electron densities of the both discharges were $3 - 4 \times 10^{19}$ m^{-3}. Therefore, the evolutions in the local line intensities reflect those in the ion abundance of W^{27+} on the poloidal cross section.

4. A near-UV line emission of a higher charge state formed by superimposing ECH

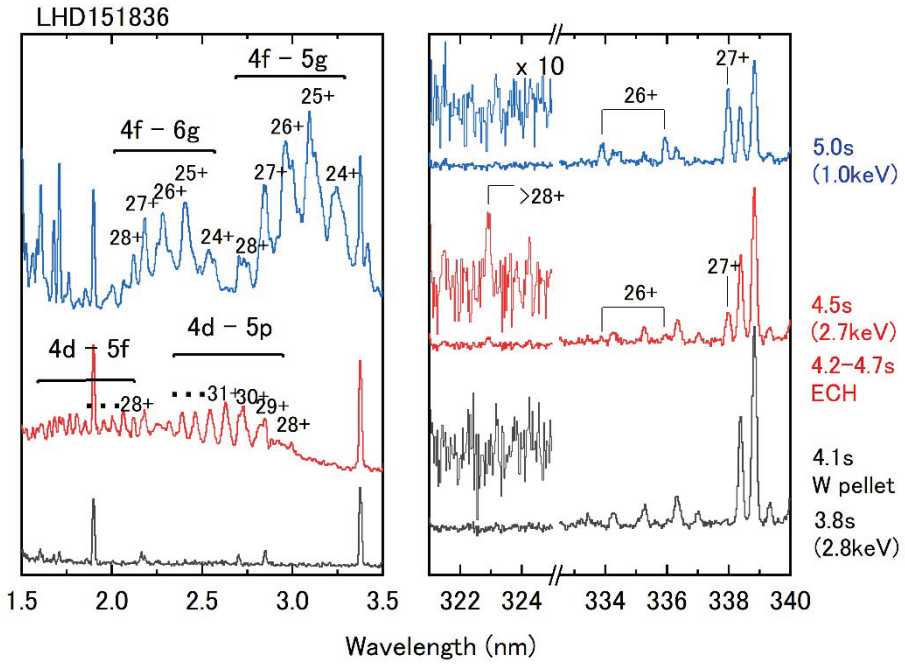

Fig. 3 Extreme-ultra-violet (EUV) and near-UV spectra of the discharge 151836. The spectra before tungsten pellet injection at 4.1 s (black) are also shown as a reference. The ECH was being superimposed for 4.2 – 4.7 s.

Figure 3 shows extreme-ultra-violet (EUV) and near-UV spectra of the discharge with the ECH superimposed for 4.2 – 4.7 s. It is noted that each peak in the EUV spectra is formed by many emission lines. The EUV spectrum at 4.5 s (during the ECH) consists of peaks of W^{28+} or higher charge states, and the EUV

spectrum at 5.0 s (after ECH is turned off) consists of W^{24+} - W^{28+}. The charge state assignment of each peak in the EUV spectra has been done by experiments with a compact electron beam ion trap (CoBIT) [13]. The near-UV spectrum at 4.5 s has a weak emission line at about 323 nm which is absent in the spectrum at 5.0 s. This emission line must be assigned to W^{28+} or higher charge states according to the corresponding EUV spectra. Further investigations are necessary for a definite identification of the emission line.

Acknowledgements

This work was partly supported by the Post-CUP program. It was also supported by NIFS budget code NIFS18KLPF063 and was also partially supported by KAKENHI 18H01201.

References

[1] N. Noda, V. Philipps and R. Neu, J. Nucl. Mater. 214-243 (1997) 227.
[2] R. Neu et al., Fusion Eng. Des. 65 (2003) 367.
[3] T. Pütterich et al., Nucl. Fusion 50 (2010) 025012.
[4] K. Asmussen et al., Nucl. Fusion 38 (1998) 967.
[5] T. Pütterich et al., Plasma Phys. Control. Fusion 50 (2008) 085016.
[6] T. Nakano et al., Nucl. Fusion 49 (2009) 115024.
[7] C.S. Harte et al., J. Phys. B: At. Mol. Opt. Phys. 43 (2010) 205004.
[8] S. Morita et al., AIP Conf. Proc. 1545 (2013) 143.
[9] G.A. Doschek and U. Feldman, J. Apll. Phys. 47 (1976) 3083.
[10] D. Kato et al., Phys. Scr. T156 (2013) 014081.
[11] K. Fujii, D. Kato et al., J. Phys. B: At. Mol. Opt. Phys. 50 (2017) 055004.
[12] Z. Fei et al., Phys. Rev. A 86 (2012) 062501.
[13] H.A. Sakaue, D. Kato et al., Phys. Rev. A 92 (2015) 012504.

Wall recycling experiment in EAST

N. Ashikawa[1,2], K. Nojiri[3], A. Terakado[3], Y.W. Yu[4], Z.H. Hu[4], L. Wang[4], Y. Suzuki[1,2], J. Huang[1], F. Ding[4], H.M. Zhang[4], Y.J. Chen[4], L. Zhang[4], L. Meng[4], M. Sakamoto[3], J.S. Hu[4], G.N. Luo[4], S. Ohdachi[1]

[1]National Institute for Fusion Science, Toki 509-5292, Gifu, Japan

[2]Graduate University for Advanced Studies, Toki 509-5292, Gifu, Japan

[3]University of Tsukuba, Tsukuba 305-8577, Ibaraki, Japan

[4]Institute of plasma physics, Chinese academy of science, Hefei 230031, Anfui, China

Abstract

Hydrogen isotope recycling on metal plasma facing wall is one of the most critical issues in ITER and DEMO. EAST has tungsten upper single null configurations and lithium coatings as wall conditioning methods are used. In this work, divertor plasma parameters at different magnetic configurations are compared for understandings of wall recycling on n tungsten with coated lithium wall. From divertor flux measured by Langmuir probes, differences of spatial distributions at three magnetic configurations and wetting areas are shown. In a previous work, wall recycling related to divertor pumping efficiency at different configurations was discussed. But, it can be seen that the difference in plasma characteristics in different configurations is not only due to pumping efficiencies but also to spatial distributions and wetting areas. In future work, a comparison between experimental and numerical results related to magnetic configurations is planned.

1. Introduction

Understanding of hydrogen recycling on metal plasma facing wall is one of critical issues for achieving the steady state operation in fusion devices, toward ITER and DEMO. Hence a comparison of wall recycling on tungsten divertor targets after lithium wall conditions is planned.

Remained lithium coating was about 1.5 microns after one-day plasma discharges at the first wall position in EAST [1]. But divertor targets have higher erosion rate by attached plasma and facing tungsten might be occurred after few plasma discharges, due to different density decay at morning and night on the day. In this research, wall recycling at different coated lithium on tungsten divertor is compared at different positions of divertor attachments. In addition, diverter parameters at different positions are normalized using numerical calculations for divertor configurations, and compared with tungsten divertor targets. And then wall recycling characterizations on tungsten wall are shown in EAST.

2. Experimental

Figure 1 shows divertor structure of upper single null configurations at plasma experiment on May 19 in EAST. We requested three kinds of different configurations and standard configuration is a position of #84817 and 84815.

An experimental time was selected at morning session in EAST [2-3]. At just morning, Ohmic

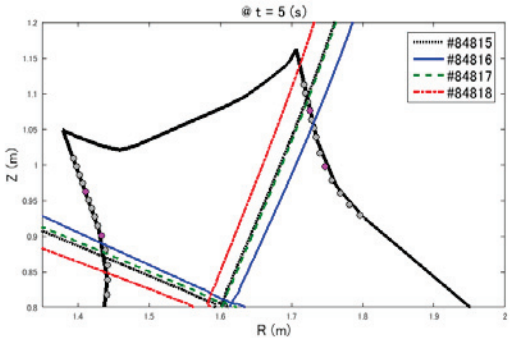

Figure 1. Divertor configurations at 5 seconds at four plasma discharges in EAST, on May 17, 2019.

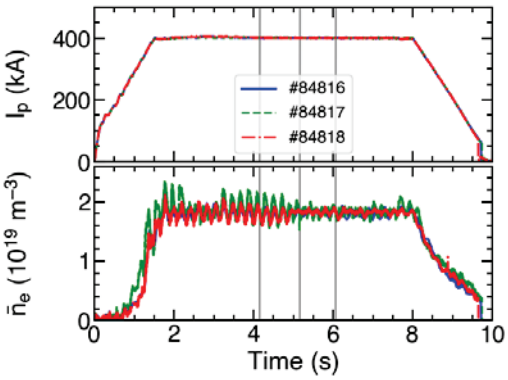

Figure 2. Time evaluations of a plasma current and an electron density.

discharges were operated and then tokamak discharges were started. We had done about 5 plasma discharges at three different configurations.

Data of spectroscopes at mid-plane and Langmuir probe measurement around upper divertor regions were obtained. Electron density of 1.8 E19 during 6 seconds is sustained as shown in Fig.2. Electron densities were modulated that might be done by density feedback control. For different divertor configurations, electron densities are similar to each other as shown in Fig.2.

3. Results and Discussions

Spatial profiles of divertor flux by divertor probes at upper single null as shown in Fig.3 Distances from a corner edge of the divertor to probe positions are shown at Y –axis in Fig.3. Divertor configurations at each discharge are already shown in Fig.1 A white dashed line shows peak position of divertor profiles at #84815 and #84817 discharges, which is the same configuration.

A comparison between #84818, 384817 and #84816 shows similar peak positions, but profiles are different. Based on these results in Fig.3, it is shown that different wet areas and configurations of divertor plasmas in EAST. In ref.4, wall recycling related to divertor pumping efficiency at different configurations was discussed. In Fig.3, it can be seen that the difference in plasma characteristics in different configurations is not only due to pumping efficiencies but also to spatial distributions and wetting areas. In Fig.3, details of the divertor configurations have not yet been shown due to limitations on detection limits, such as positions of diverter probes.

Figure 4 shows spatial profiles of tungsten and deuterium intensities measured by spectroscopies [5], which observed upper single null configurations. Due to problems of diagnostics, data at some plasma discharges was not obtained. At least, we did not obtain differences at different configurations as shown in Fig.4, and we require additional plasma experiments.

Numerical analyses of magnetic field at edge plasmas for divertor configurations are useful tools and it was

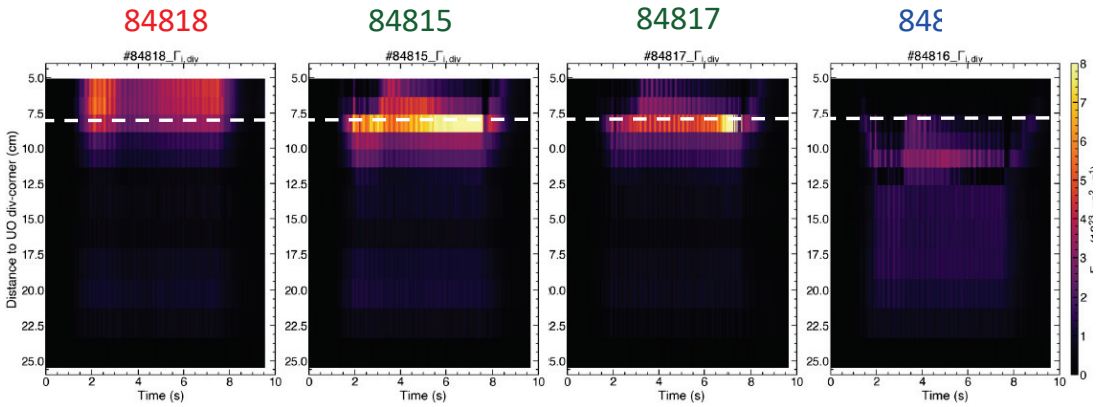

Figure.3 Spatial profiles of divertor flux at upper single null. Each divertor configurations are shown in Fig.1 Distances from a corner edge of the divertor to probe positions are shown at Y – axis. A white dashed line shows peak position of divertor profiles at #84815 and #84817 discharges.

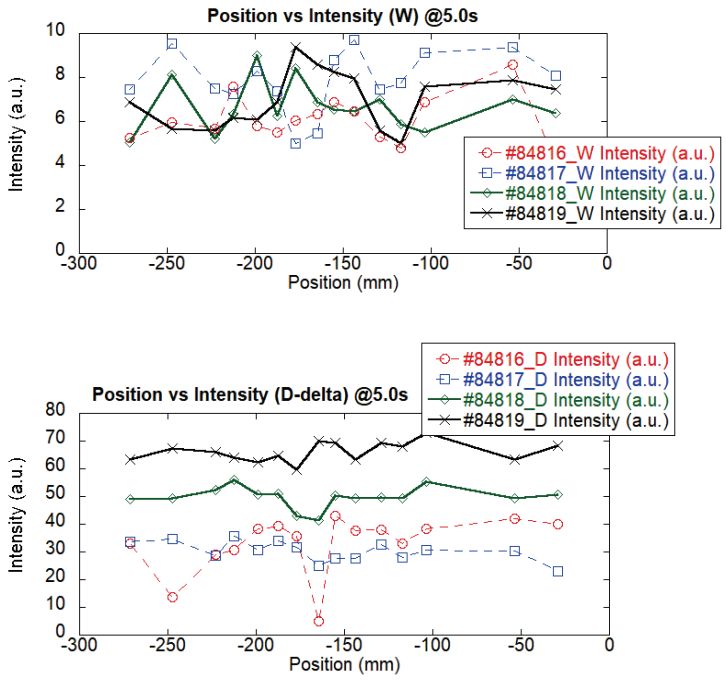

Figure 4. Spatial profiles of deuterium and tungsten intensities, measured by spectroscopies measurement from mid-plane port.

started to support diagnostics issues for EAST. In future works, experimental and numerical results are compared.

4. Results

We had plasma experiments at different magnetic configurations for understandings of wall recycling in EAST. From divertor probe measurement, different spatial distributions at three kinds of magnetic configurations were obtained, we considered that these spatial profiles and wetted areas on divertor targets are also important parameters for understanding of wall recycling in EAST. But it is also clearly understanding that it is not sufficient to show spatial distributions, because space channel intervals are required due to installation location issues in actual probe measurements at fixed plasma discharges.

Based on this experiment, we plan to do scanned divertor configuration experiments at next time, and then more details about relationships between wall recycling related and spatial distributions on divertor targets are discussed.

Acknowledgements

This work was partly supported by the Post-CUP program, and the bilateral collaboration, JSPS-CAS, "Control of wall recycling on metallic plasma facing materials in fusion reactor". It was also supported by NIFS budget code NIFS11UFFF028-2.

References

[1] N. Ashikawa, Y.W.Yu, J. Wu, E. Bang, S. Son, K. Katayama, et al., ITC-26/APFA-11 conference, Oral-1, December 2017, Toki, Japan.

[2] Y.W. Yu, et al., Phys. Scr T70 (2017) 014070

[3] G.Z. Zuo, J.S.Hu, et al., J. Nucl. Mater. 438 (2013) S90.

[4] L. Wang et al., Nucl. Fusion 59 (2019) 086036.

[5] F. Ding, et al., J. Nucl. Mater. 455 (2014) 710.

Laser-based wall diagnostics of LIAS and LIBS for the plasma wall interaction study on the EAST tokamak

Z. Hu[1], J. Oelmann[2], C. Li[3], F. Ding[1], J. Wu[1], L. Sun[3], J. Liu[3], N. Ashikawa[4], S. Brezinsek[2], H. Ding[3], G. Luo[1]

[1]Institute of Plasma Physics, Chinese Academy of Sciences, Hefei 230031, Anhui, China
[2]Institute of Energy and Climate Research, Forschungszentrum Jülich, AssocEURATOM-FZJ, Jülich 52425, Germany
[3]Dalian University of Technology, Dalian 116024, Liaoning, China
[4]National Institute for Fusion Science, Toki 509-5292, Gifu, Japan

Abstract

The PWI at the first wall in fusion reactors is critical for the life time of plasma-facing components (PFC) and tokamak safety. There is an urgent need to measure PWI processes in situ. Two laser-based diagnostics of laser-induced breakdown/ablation spectroscopy (LIBS and LIAS) were successfully developed for the plasma wall interaction of fuel retention, material deposition and transport study on EAST tokamak. The LIBS was applied for the daily routinely monitoring the first wall compositions. The dedicated LIAS experiment on graphite and tungsten during limited and divertor discharge indicate that LIAS is suitable for the dynamic measurements of first wall condition in EAST tokamak.

1. Introduction

Plasma–wall interaction (PWI) plays a key role in future fusion reactors[1-3]. The post-mortem analysis cannot meet the requirements of in situ characterization of fuel retention and impurity deposition in the future fusion device with the active cooled plasma-facing components (PFCs). To ensure the safety operation of the fusion device, there is an urgent need to develop in situ diagnostics to characterize the material deposition and fuel retention on the first wall and to further understand the PWI processes for plasma performance. Laser-based methods are promising candidates and highly important for ITER and future fusion devices[4,5], as they are required to monitor the tritium inventory without the break of vacuum and allow the monitoring of PWI processes in real-time, compared to campaign-integrated results based on post mortem material analysis. Here we report on the development of LIBS and LIAS diagnostics for the plasma wall interaction study on the EAST tokamak.

2. LIBS results in EAST campaign

During the EAST experimental campaign of 2016 and spring 2017, LIBS measurements were carried out in vacuum conditions after the plasma discharge finished on a routine daily basis[6]. Experiments were carried out after wall conditioning (lithium coating, boron coating, etc.) finished. LIBS measurements were conducted on the Mo substrate with lithium coating. To highlight the depth profiling capabilities of LIBS, a number of subsequent laser shots were repeatedly focused at a fixed position on the sample surface and the

LIBS spectra as a function of the laser shot number were recorded for each measurement position. Since LIBS can well detect the hydrogen isotope from the co-deposition layers, it was routinely used on daily basis for monitoring the isotope ratio of the first wall in EAST. The isotope ratio measured under different conditions in the 2016 EAST campaign is presented. The LIBS results showed that the isotope ratio was of 64% in the boron film because of the carborane was used for the boronization. The isotope ratio after lithium conditioning decrease to about 20% because the lithium condition would effectively remove hydrogen by Li/H co-deposition processes. After the water leakage in the vacuum chamber, the isotope ratio increases to 70% because of the water. The first wall was saturated after long-pulse and high-performance discharge. As shown in Fig.1, Isotope ratio change daily on the first wall measured by LIBS, when the vacuum chamber was opened, the H/(H+D) was increased due to the wall absorbed the water vapor. The results in different conditions indicated that LIBS could be a useful method for predicting the wall condition of EAST tokamak.

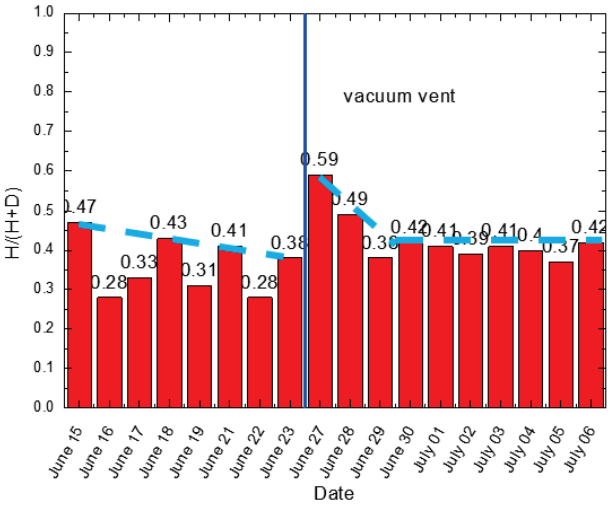

Fig.1 Isotope ratio on the first wall measured by LIBS

3. LIAS results in EAST campaign

Dedicate LIAS experiments were carried out on graphite and tungsten during the limiter and divertor discharges to study the dynamic retention in situ, separately. A schematic illustrating the measurement strategy is shown in Fig.2(A) and Fig.3(A).

In the dedicate experiments of the limiter shape of the plasma, due to the location which was measured by LIAS is lower than the midplane, so the plasma was actively moved down 5cm to increase the particle flux which is shown in Fig.2(A). Two groups of triple probes were installed near the samples. From the signal of the probe, the saturation ions of the probe gradually increased. During the discharges, multiple laser pulses were shotted on the first wall to measure the dynamic retention. As shown in Fig.2(B), the signal of LIAS was plotted with the plasma position. The LIAS signal on both of graphite material and tungsten material have a good linear relationship with the ion saturation. The retention on graphite material is high than that of tungsten material because the retention on the metallic material is low.

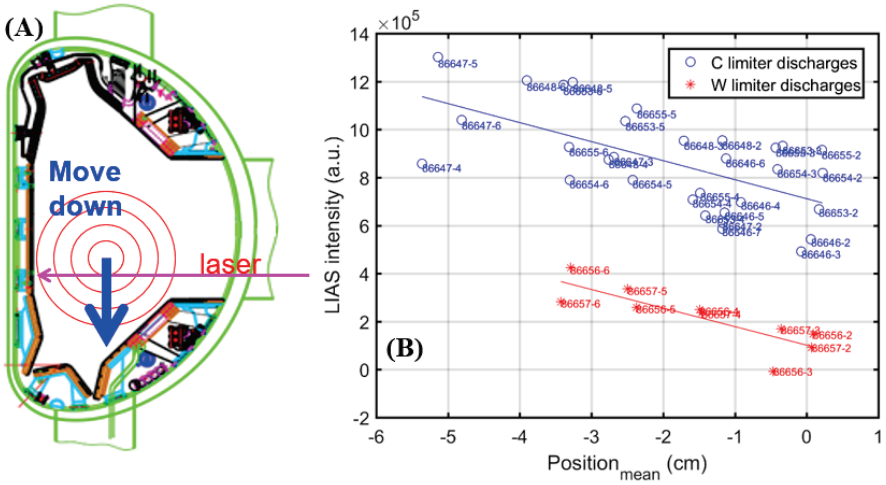

Fig.2 (A) Measurement strategy for dynamic retention with LIAS during limiter discharges. Shifting the plasma position downwards to increase the LIAS signal. (B)Dynamic deuterium retention on graphite and tungsten during limiter discharges

In the dedicate experiments of the divertor shape of the plasma, the plasma was actively moved out from the high field side from 3.5 cm to 6.5 cm to decrease the particle flux which is shown in Fig.3(A). From the signal of the probe, the saturation ions of the probe gradually decreased. During the discharges, multiple laser pulses were shotted on the first wall to measure the dynamic retention. As shown in Fig.3(B), the signal of LIAS was plotted with the distance between the plasma and first wall. The LIAS signal on graphite material has a good linear relationship with the ion saturation. For the tungsten material, there is no clear trend, more detailed analysis is necessary.

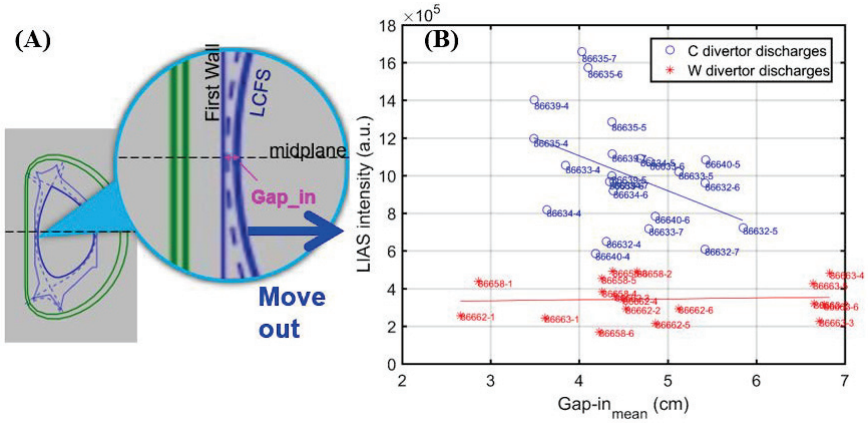

Fig.3 (A) Measurement strategy for dynamic retention with LIAS during divertor discharges. Shifting the plasma position out of the high field side to decrease the LIAS signal. (B)Dynamic deuterium retention on graphite and tungsten during divertor discharges

4. Conclusion

Laser-based diagnostics of LIAS/LIBS was successfully developed and applied for the plasma wall

interaction study in EAST tokamak. The results indicate that the LIBS is a useful method to predict the wall condition for the operation and wall conditioning. The dedicated LIAS experiments performed on graphite and tungsten indicates LIAS could be suited for dynamic retention measurements. With the upgrade of the lower tungsten divertor, the LIAS/LIBS will upgrade to measure the divertor region in the future.

Acknowledgements

This work was supported by supported by JSPS-CAS Bilateral Joint Research Projects (No. GJHZ201984) and National Natural Science Foundation of China (Nos. 11605238, 11575243, 11605023).

References

[1] C. Linsmeier, et al., 442 (2013) J. Nucl. Mater. S834

[2] A. Möslang, et al., 45 (2005) Nucl. Fusion 649

[3] H. Zohm, et al., 53 (2013) Nucl. Fusion 073019

[4] A. Huber, et al., 86 (2011) Fusion Eng. Des. 1336–1340

[5] V. Philipps, et al., 53 (2013) Nucl. Fusion 093002

[6] Z. Hu, et al., 19 (2017) Plasma Science and Technology 025502

The deuterium permeation behavior in W studied by gas driven permeation and plasma driven permeation methods

Mingzhong Zhao[1], Shota Yamazaki[2], Moeko Nakata[2], Fei Sun[3], Takuro Wada[2], Ayaka Koike[2], Yasuhisa Oya[2]

[1]Graduate School of Science and Technology, Shizuoka University, Shizuoka, 422-8529 Japan

[2]Graduate School of Integrated Science and Technology, Shizuoka University, Shizuoka, 422-8529 Japan

[3]Faculty of Science, Shizuoka University, Shizuoka, 422-8529 Japan

Abstract

Well understanding of tritium (T) permeation and retention behavior in tungsten (W) requires the knowledge of hydrogen isotopes transport parameters. In the present study, the deuterium (D) permeation behavior in tungsten (W) are studied by gas driven permeation (GDP) and plasma driven permeation (PDP) methods. The D-GDP process in W agrees with the Sieverts's law that the steady state permeation flux under different temperature are proportional to the square root of pressure. According to the Siverts' law and Fick's first law, the D permeability and effective diffusivity in W are obtained from the GDP results. To study the hydrogen isotopes plasma driven permeation (PDP) behavior in plasma facing materials, a linear Radio Frequency (RF) plasma device has been constructed in the radiation controlled area at Shizuoka University. In the PDP experiment, the steady state permeation flux is approximate proportional to the square root of the ion flux indicating that D-PDP process takes place in the RD regime. The D recombination coefficient on upstream surface of W is obtained by the PDP results.

1. Introduction

Tungsten (W), is the most attractive plasma facing material (PFMs) for fusion device attribute to its favorable properties, such as high melting point, low physical sputtering yield and low T retention [1]. As the plasma facing material, W will be exposed to deuterium and tritium plasma under elevated temperature leading to the concern on the tritium (T) retention and permeation in W. To realize the T self-sustaining and safety operation, the evaluation of T retention and permeation behavior in W is important. Well understanding of T retention and permeation behavior in W requires the knowledge of hydrogen isotopes transport parameters.

The hydrogen isotopes permeability and effective diffusivity in W material obtained by thermal desorption method [2, 3] and gas driven permeation (GDP) method [4-10] have been reported. The hydrogen isotopes recombination coefficient in W are given in [11, 12]. However, the available data on hydrogen isotopes permeation parameters in W are very limited at present. In addition, there is discrepancy in the extrapolation of the data. Hence, it is necessary to enrich the basic hydrogen permeation parameters in W.

In the present study, the D permeation behavior in W are studied by GDP and PDP methods. A linear Radio Frequency (RF) plasma device for PDP study has been constructed in the radiation controlled area of Shizuoka University.

2. Experimental

W wafers cut from W rod, which is supplied by A.L.M.T. Corp. Ltd., are used in the present study. The sample disc size for GDP experiment is 6 mm in diameter and 0.5 mm in thickness. For

PDP experiment, the sample size is 10 mm in diameter and 0.5 mm in thickness. Both side of W wafers used in the experiment are mirror finished with the surface roughness of ~50 nm. To release the internal stress, annealing treatment in high vacuum is performed under the temperature of 1173 K for 30 min.

The D permeation behavior in W material are studied by GDP and PDP methods where the grain elongated orientation is parallel to the D diffusion direction. In the present work, the GDP experiments are performed at temperature from 627 to 965 K. The PDP experiments are conducted in the temperature range from 749 K to 813 K. The permeation signals, mass 4 (D2) and mass 3 (HD), are measured by a quadrupole mass spectrometer (QMS). The mass 4 signal measured by QMS is calibrated by two standard D_2 leak bottles with different leak rate. The sensitivity of HD is taken as an average of the H_2 and D_2 sensitivities. Both of HD and D_2 signal are considered in the GDP and PDP experiments.

3. The deuterium gas driven permeation behavior in W

The D permeation flux as a function of gas loading time is given in Fig. 1. The D_2 gas loading was stared at time 0 s. In the present study, the permeation curves were obtained under the D_2 pressure of 83 kPa. The permeation parameters, effect diffusivity (D_{eff}) and permeability (Φ), can be hardly effected by the hydrogen isotopes gas loading pressure, unless the pressure is pretty high [13]. The effective diffusivity is calculated by time lag method [14].

$$D_{eff}=\frac{L^2}{6t} \quad (1)$$

, where, t is the lag time, which is obtained by the time-integrated method. L is the thickness of the sample. The temperature dependence of effective diffusivity from the present experiments can be given by:

$$D_{eff}=3.0\times10^{-6}\exp\left(-\frac{0.64\ (eV)}{kT}\right),\ m^2\ s^{-1} \quad (2)$$

The measured steady state permeation flux under various gas loading pressure are given in Fig. 2(a). As shown in Fig. 2(b), the steady state permeation flux has a linear relationship with the square root of gas loading pressure, meaning that the gas driven permeation process agrees with Siverts' law. According to the Siverts' law and Fick's first law, the steady state permeation flux (J_∞) can be expressed as:

$$J_\infty=\frac{\emptyset\sqrt{P}}{L} \quad (3)$$

, where P is the upstream pressure, L is the thickness of sample, Φ is permeability.
In the present study, the D permeability in W is given as follows,

$$\emptyset=3.2\times10^{-8}\exp\left(-\frac{0.81\ (eV)}{kT}\right),\ mol\ m^{-1}\ s^{-1}\ Pa^{-0.5} \quad (4)$$

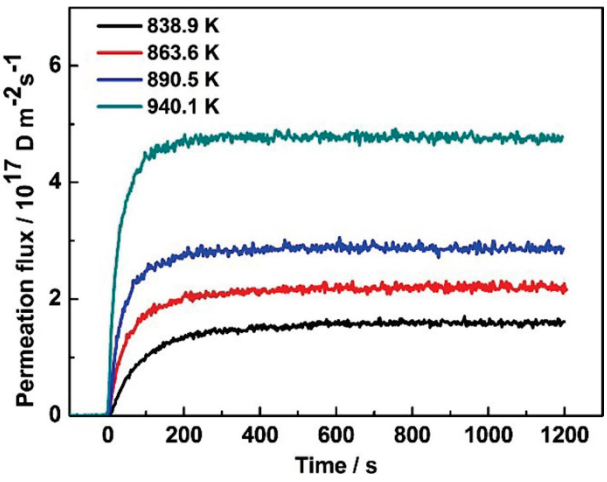

Fig. 1. The D permeation flux as a function of gas loading time under various temperature.

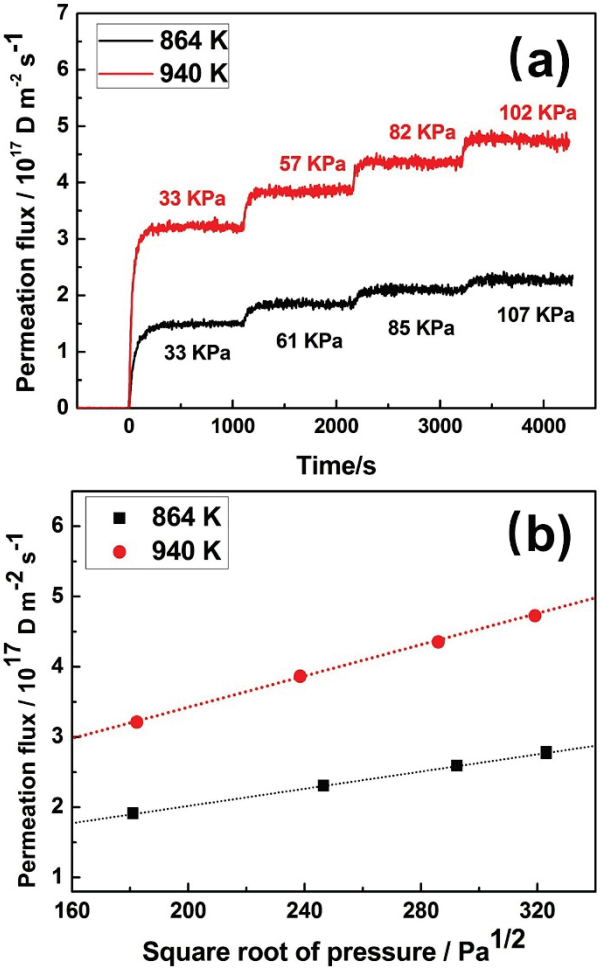

Fig. 2. (a) pressure dependence of steady state permeation flux, (b) steady state permeation flux as a function of square root of pressure.

4. The deuterium plasma driven permeation behavior in W

Plasma experiments are performed with two different input powers of 500 W and 700 W. In the case of 500 W, D_2 pressure in the upstream chamber is maintained to be 0.16 Pa. For 700 W, D_2 pressure of 0.05 Pa is used. The plasma parameters at the center of D plasma are measured by a

Langmuir probe. The plasma parameters, namely electron temperature (Te), electron density (n_e) and ion flux, under different discharge conditions are summarized in Table 1., where the ion flux is calculated by applying the Bohm criterion [15].

Table 1. Plasma parameters under various discharge condition.

	T_e (eV)	n_e (m^{-3})	Ion flux (m^{-2} s^{-1})
500 W	12.4	4.4×10^{14}	1.1×10^{19}
700 W	7.5	1.2×10^{16}	2.3×10^{20}

The permeation curves under different discharge conditions are shown in Fig. 3. As shown in Fig. 3(b), the influence of temperature on the D permeation behavior in W is studied with the discharge power 700 W. Under the temperature of 803 K, the steady state permeation flux for the discharge power 700 W and 500 W are 1.5×10^{18} D m^{-2} s^{-1} and 2.6×10^{17} D m^{-2} s^{-1}, respectively. As shown in Table 1., the ion flux of discharge power 700 W is about 20 times as high as that of 500 W.

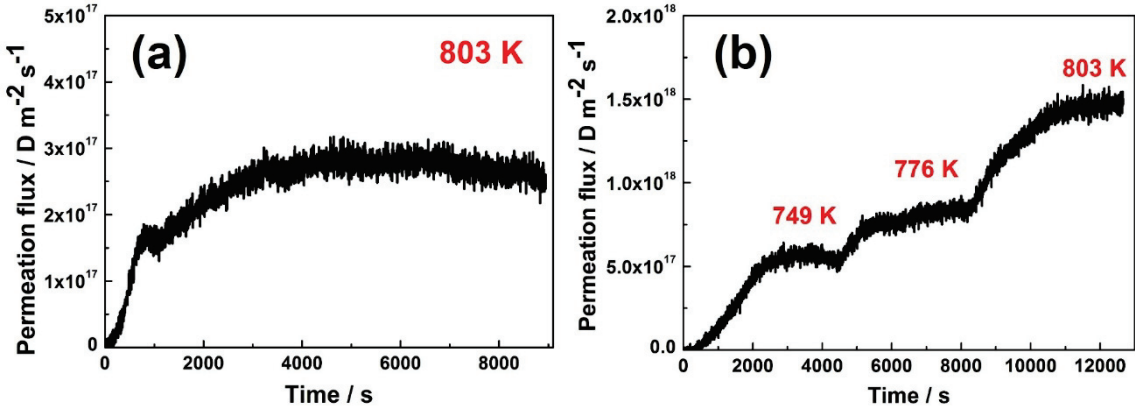

Fig. 3. The D permeation curves in W under different discharge conditions, (a) 500 W, (b) 700 W.

There are three regimes for the steady state plasma driven permeation process [14]: (1) the release of hydrogen isotopes from the upstream and downstream surfaces are limited by diffusion process, named as DD-regime, (2) release of hydrogen isotopes from the upstream surface and downstream surface are limited by the recombination of hydrogen isotopes and diffusion of hydrogen isotopes, named as RD-regime, (3) the release of hydrogen isotopes from both surfaces are limited by the recombination process, named as RR-regime. The relationship of steady state permeation flux (J_p) and the implantation flux (J_i) in different regime can be expressed as:

$$J_p = \frac{R}{L} J_i \quad \text{(DD-regime)} \tag{5}$$

$$J_P = \frac{D}{L}\sqrt{\frac{J_i}{K_U}} \quad \text{(RD-regime)} \tag{6}$$

$$J_P = \frac{K_U}{K_U + K_D} J_i \quad \text{(RR-regime)} \tag{7}$$

, where, R, L and D represent the ion projected range, sample thickness and the bulk diffusion coefficient. K_U and K_D are the recombination coefficient on upstream surface and downstream surface. In the present experiment, the steady state permeation flux is approximate proportional to

the square root of the ion flux indicating that permeation takes place in the RD regime.

For the RD regime, the D recombination coefficient (K_U) at the upstream surface can be obtained by the equation (6). The diffusivity measured by Frauenfelder [2] is used as the bulk diffusion coefficient. Because the diffusivity in Ref. [2] is measured at elevated temperature and less likely to be effected by defects. The calculated K_U as a function of inverse temperature is shown in Fig. 4 in which the literature data from I. Takagi [11] and R. A. Anderl [12] are also plotted. The available hydrogen isotopes recombination coefficient in W material is real scarce at present. The possible reasons for the difference in recombination coefficient are that (1) the recombination coefficient is obtained by different experiment method, (2) the recombination coefficient is sensitive to the sample surface condition. In Ref. [11], the recombination coefficient is obtained according to the D concentration which is measured by nuclear reaction analysis (NRA). In Ref. [12], the recombination coefficient is determined by the IDP experiment with 3 keV D_3^+ ions.

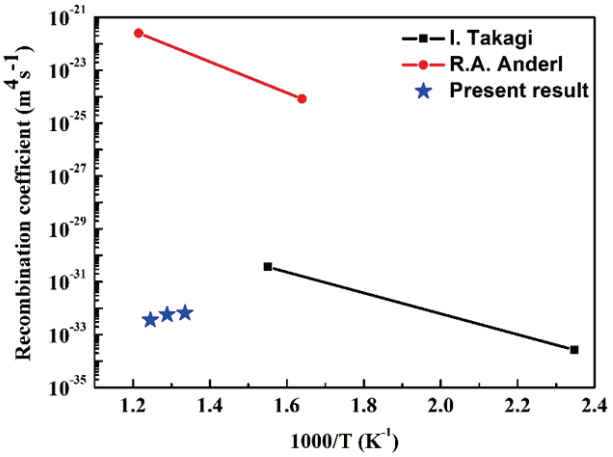

Fig. 4. The recombination coefficient of D for W sample.

5. Conclusion

The deuterium (D) permeation behavior in W are studied by gas driven permeation (GDP) and plasma driven permeation (PDP) methods. The D permeability and effective diffusivity in W are obtained by GDP method. A linear Radio Frequency (RF) plasma device for the PDP study is constructed in the radiation controlled area at Shizuoka University. The PDP results under different discharge power show that the D permeation process in W agrees with the RD regime. The recombination coefficient, which is an important parameter for the estimation of the hydrogen isotopes permeation behavior in fusion reactor, is obtained by the RD regime.

Acknowledgements

This work was partly supported by the Post-CUP program. It was also supported by NIFS budget code 19KOBF042.

References

[1] X. D. Du., et al., Phys. Rev. Lett. **114** (2015) 155003, Nucl. Fusion **56** (2016) 016002.

[2] T. Bando, S. Ohdachi, et. al., Nucl. Fusion **58** (2018) 082025.

[3] X. D. Du., et al., Phys. Rev. Lett. **118** (2017) 125001.

[1] V. Philipps, J. Nucl. Mater., 415 (2011) S2-S9.
[2] R. Frauenfelder, J. Vac. Sci. Technol., 6 (1969) 388-397.
[3] G. Esteban, A. Perujo, L. Sedano, et. al., J. Nucl. Mater., 295 (2001) 49-56.
[4] R. Frauenfelder, J. Chem. Phys., 48 (1968) 3955-3965.
[5] A. Zakharov, V. Sharapov, E. Evko, Materials Science, 9 (1975) 149-153.
[6] F. Liu, H. Zhou, X.-C. Li, et al., J. Nucl. Mater., 455 (2014) 248-252.
[7] F. Liu, H. Zhou, Y. Xu, et al., Fusion Eng. Des., 113 (2016) 216-220.
[8] Y. Uemura, S. Sakurada, H. Fujita, et al., J. Nucl. Mater., 490 (2017) 242-246.
[9] G. Benamati, E. Serra, C. Wu, J. Nucl. Mater., 283 (2000) 1033-1037.
[10] D.A. Buchenauer, R.A. Karnesky, Z.Z. Fang, et al., Fusion Eng. Des., 109 (2016) 104-108.
[11] I. Takagi, R. Imade, Y. Ikegami, et al., J. Nucl. Mater., 417 (2011) 564-567.
[12] R. Anderl, D. Holland, G. Longhurst, et al., Fusion Technol., 21 (1992) 745-752.
[13] T. Oda, Fusion Eng. Des., 112 (2016) 102-116.
[14] H. Zhou, Y. Hirooka, N. Ashikawa, et al., J. Nucl. Mater., 455 (2014) 470-474.
[15] H. Amemiya, J. Phys. Soc. Jpn, 66 (1997) 1335-1338.

Current status of NIFS-SWJTU joint project for CFQS

Akihiro Shimizu[1], Haifeng Liu[2], Shigeyoshi Kinoshita[1], Mitsutaka Isobe[1,3], Shoichi Okamura[1], Kunihiro Ogawa[1,3], Motoki Nakata[1,3], Yasuo Yoshimura[1], Takanori Murase[1], Sho Nakagawa[1], Hiroyuki Tanoue[1], Yuhong Xu[2], Guozhen Xiong[2], Hai Liu[2], Junren Shao[2], Yangbo Li[2], Xianqu Wang[2], Jie Huang[2], Xin Zhang[2], Changjian Tang[2,4], Dapeng Yin[5], Yi Wan[5] and CFQS team[1,2,5]

[1]National Institute for Fusion Science, National Institutes of Natural Sciences, Toki 509-5292, Japan
[2]Institute of Fusion Science, School of Physical Science and Technology, Southwest Jiaotong University, Chengdu 610031, People's Republic of China
[3]SOKENDAI (The Graduate University for Advanced Studies), Toki 509-5292, Japan
[4]School of Physical Science and Technology Sichuan University, Chengdu 610041, People's Republic of China
[5]Hefei Keye Electro Physical Equipment Manufacturing Co. Ltd, Hefei 230000, People's Republic of China

Abstract

The Chinese First Quasi-axisymmetric Stellarator (CFQS) is a new quasi-axisymmetric experimental device planned for construction at Southwest Jiaotong University (SWJTU), China. This is a joint project of the National Institute for Fusion Science (NIFS) and the SWJTU. The present paper discusses the equilibrium configuration of the CFQS with a major radius of 1.0 m, a toroidal magnetic field strength of 1.0 T, and an aspect ratio of 4.0. As the CFQS is a quasi-axisymmetric stellarator, a tokamak-like substantial bootstrap current is expected. The magnitude of the bootstrap current was estimated by BOOTSJ code. Next, the effects of the bootstrap current on the quasi-axisymmetric property and the neoclassical diffusion coefficient were estimated. Effect of the bootstrap current on the quasi-axisymmetric property is not significant, and a good neoclassical transport property is maintained.

1. Introduction

Helical devices are advantageous over tokamak in terms of steady-state operation capability as a future nuclear fusion reactor because their magnetic configurations are produced by external magnetic field coils, thus, no inductive plasma current is intrinsically required. Recently, plasma experiments conducted by a large-sized helical device, *e. g.* the large helical device (LHD) [1] and Wendelstein 7-X (W7-X) [2], presented remarkable results, by which the possibilities of a future helical reactor can be anticipated. The neoclassical transport of a helical device was considered to be not good basically in the collisionless

regime, so called in the $1/\nu$ (ν is the collision frequency) regime. In recent decades, various optimized stellarator configurations, which have improved the neoclassical transport property, have been proposed and experimental devices have been constructed. A quasi-axisymmetric stellarator (QAS) [3] is one of those stellarators, of which magnetic configuration is axisymmetric in magnetic coordinates, i.e., the Boozer coordinates [4,5]. The neoclassical transport property of QAS is similar to that of tokamak; however, the current drive is not required and the advantage of the steady-state operation capability is retained. The Chinese first quasi-axisymmetric stellarator (CFQS) is the first experimental device of the QAS, which will be constructed in China, under the international joint project of National Institute for Fusion Science (NIFS) in Japan and Southwest Jiaotong University (SWJTU) in China [6,7,8]. The physical design for the CFQS has been almost completed, and the engineering is underway. The proposed parameters of the device are as follows: toroidal magnetic field B_t = 1.0 T, major radius R = 1.0 m, and aspect ratio A_p = 4.0. This paper presents the equilibrium configuration of the CFQS, then examines the neoclassical bootstrap current and its effect on the quasi-axisymmetric configuration. After that, we describe about construction of mockup coil briefly.

2. Equilibrium and modular coil system of the CFQS

The present equilibrium configuration of CFQS is based on the CHS-qa, 2b32 configuration [9] having A_p of 3.2 and the toroidal periodic number N_p of 2, which was previously considered for a post-Compact Helical System (CHS) project. Based on this configuration, the geometry of the outermost magnetic surface of the CFQS was determined, therefore, the N_p of the CFQS was chosen as 2. Fabricating the modular coil system of a compact machine (e.g., R = 1.0 m) with a low aspect ratio is challenging issue, therefore, the A_p of the CFQS was enlarged to 4.0. The free-boundary VMEC [10] equilibrium results

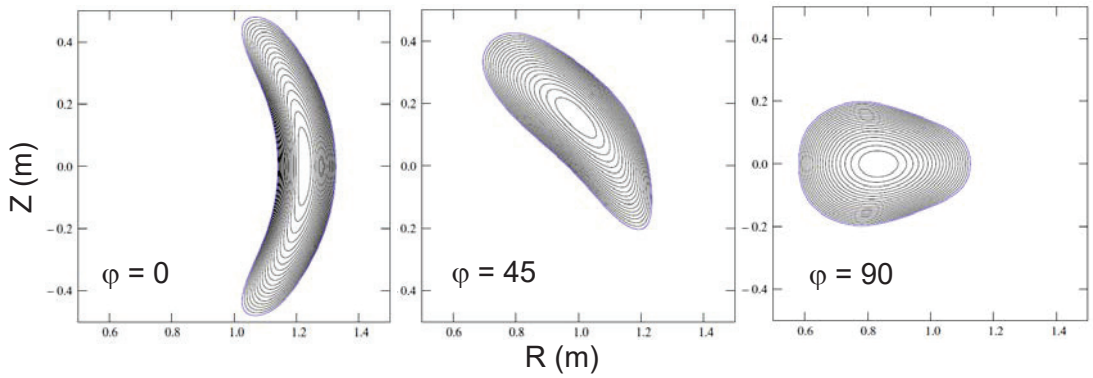

Fig.1 Poloidal cross sections of the CFQS equilibrium calculated by the VMEC code in free-boundary condition at three toroidal angles.

for the 0 % volume-averaged beta, $<\beta>$, at different toroidal angles (0°, 45°, and 90°) are shown in Fig. 1. Fig. 2 shows the radial profiles of the rotational transform and magnetic well depth. The typical rotational transform was around 0.4, and it has a weak shear profile as obtained in other optimized stellarators. The magnetic well property was achieved throughout all radial region.

As in other optimized stellarators, the modular coil system was optimized to realize the target geometry of the outermost magnetic surface, which was determined before designing the magnetic coil system. The modular coil system produces an average normalized normal component of the magnetic field, $\boldsymbol{B}\cdot\boldsymbol{n}/|\boldsymbol{B}|$, on the target outermost magnetic surface. The coil optimization process reduces this component to zero, while simultaneously engineering the properties of the filament coils, such as the minimum distance between the coils and the minimum curvature radius of the coils are also evaluated and optimized. The modular coil system was optimized by the NESCOIL code [11,12]. In total, the CFQS consists of 16 modular coils, which is shown in Fig.3. The minimum coil-to-coil distance and radius of curvature of the coils are 18.5 cm and 21.5 cm, respectively. Note that these values are estimated for filament structure coils [6]. This coil system is used to obtain the free-boundary VMEC equilibrium results as shown in Fig.1 and Fig.2.

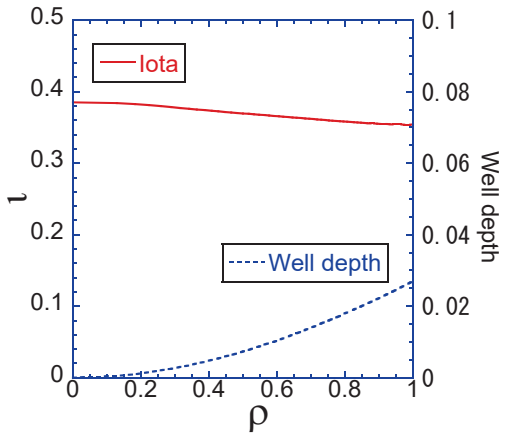

Fig. 2 Radial profiles of the rotational transform and well depth of the CFQS at $\beta = 0.0\%$.

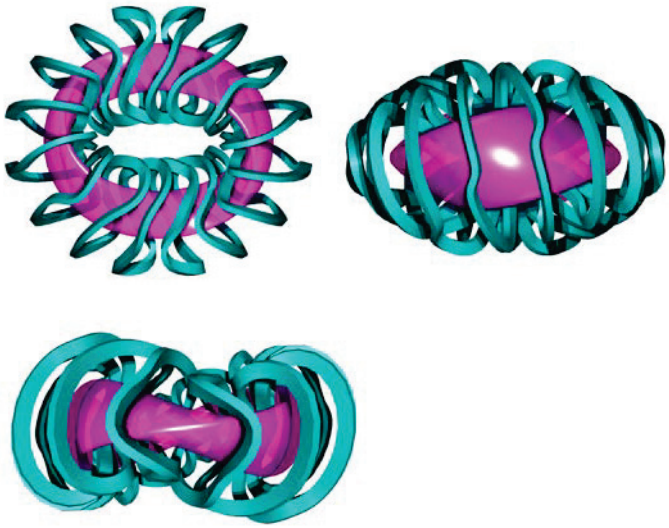

Fig. 3 Modular coil system of CFQS.

3. Bootstrap current and its effect on the configuration

The neoclassical properties of the QAS resemble those of tokamaks. Therefore, similarly to the CHS-qa [13], a large bootstrap current is expected in the QAS. The magnitude of the neoclassical bootstrap current was estimated by the BOOTSJ code, which uses a semi-analytic formula in the collision-less limit [14]. The temperature and density profiles were assumed as $T = T_0 (1 - \rho^2)$ and $n_e = n_{e0} (1 - 0.8\rho^2 + 1.3\rho^4 - 1.5\rho^6)$, respectively, and T_{i0} was set to 0.75 T_{e0}. The radial profile of the bootstrap current density at $\beta = 1.19\%$ is shown in Fig. 4(a). The equilibrium was obtained by VMEC free-boundary calculation, assuming the modular coil system described in Section 2. The dependency of the total bootstrap current on $<\beta>$ is shown in Fig.4(b). The total bootstrap current in this case with $<\beta> = 1.19\%$ was evaluated as 26.1 kA.

The effect of finite beta including bootstrap current on the neoclassical transport was investigated by the NEO code [15], which can estimate the radial profile of the effective helical ripple, $\varepsilon_{\mathrm{eff}}$. The neoclassical diffusion coefficient in $1/\nu$ regime is expressed as, $D_{neo} = \nu_d^2 \, \varepsilon_{\mathrm{eff}}^{3/2} / \nu$. Here, ν and ν_d are the collision frequency and the drift velocity, respectively. The radial profiles of estimated $\varepsilon_{\mathrm{eff}}^{3/2}$ is shown in Fig. 5. This figure shows the radial profiles for the free boundary VMEC equilibrium in various $<\beta>$. The neoclassical bootstrap current effect on the equilibrium is included in this result. The $\varepsilon_{\mathrm{eff}}^{3/2}$ profile of the fixed boundary VMEC equilibrium for CHS (R_{ax} = 92.1cm, $\beta = 0.0\%$) [16] is compared with that of the CFQS. The $\varepsilon_{\mathrm{eff}}^{3/2}$ at $\rho \sim 1$ of the CFQS is about three orders less than that of CHS. Moreover, a good confinement property of the neoclassical transport is maintained although β is increased.

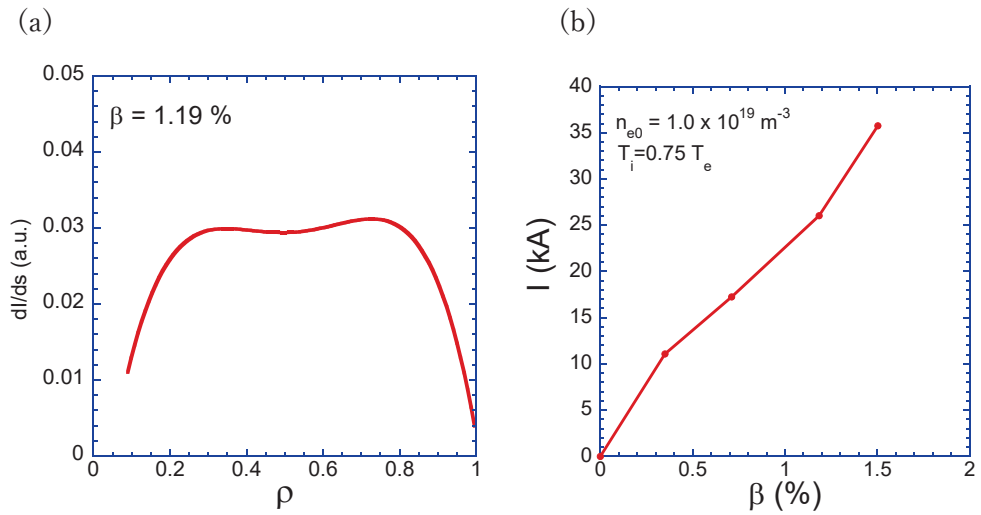

Fig. 4 (a) Radial profile of bootstrap current density of the CFQS at the $<\beta>$ of 1.19 %. (b) The bootstrap current as a function of the volume averaged β in the CFQS.

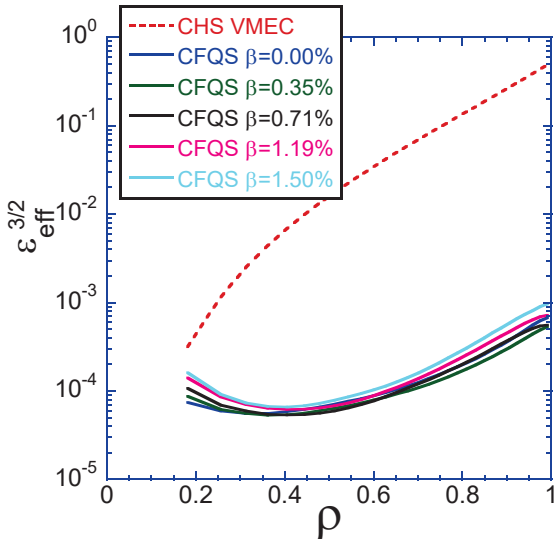

Fig. 5 Radial profiles of the effective helical ripple of the CFQS for various β with the bootstrap current.

4. Mockup coil

Engineering design of CFQS modular coils has been developed. In order to check feasibility and accuracy of manufacturing modular coil, mockup coil is now being constructed. One of modular coils, which is the most complicated shape, is chosen to construct mockup coil. The winding moulds consist of inner mould and bottom mould. The inner mould contains 12 types blocks. The 8.5 mm × 8.5 mm hollow copper conductor wrapped with fiber glass and Kapton tape was already wound on this mould. The picture of the mockup coil is shown in Fig. 6. The mould for vacuum pressure impregnation (VPI) is now being manufactured.

Fig. 6 Picture of mockup coil just after winding process of copper conductor, which was wrapped with fiber glass and Kapton tape, was completed.

5. Summary

The present CFQS equilibrium with R = 1.0 m, B_t =1.0 T, and A_p = 4.0 is shown. The neoclassical bootstrap current is estimated by the BOOTJ code in the equilibrium calculated by the VMEC code in free boundary condition. The calculation result indicates that the neoclassical bootstrap current reaches 35 kA at $<\beta>$ = 1.5 %. The effect of the bootstrap current on the quaxi-axisymmetric property and the neoclassical transport is investigated. This effect is not very large and good neoclassical transport properties are maintained up to $<\beta>$ of 1.5%, which was confirmed by the NEO code. The detailed studies of MHD stability are future issues. Mockup coil is being constructed now to check feasibility and accuracy in manufacturing.

Acknowledgements

The authors are thankful for the strong support and encouragement to the NIFS-SWJTU joint project (NSJP) from Director General Prof. Y. Takeiri of NIFS, former Vice President of SWJTU Prof. W. G. Zhang, and Vice President of SWJTU Prof. Z. Zhou. This research is supported by the NIFS general collaboration project, budget number NIFS17KBAP034, NIFS18KBAP041, NIFS budget of promotion of magnetic confinement research using helical devices in Asia, URSX 401, and the international collaboration with SWJTU, UFEX105.

Reference

[1] M. Osakabe, Y. Takeiri, T. Morisaki *et al*., Fusion Sci. Technol. **72**, 199 (2017).

[2] T. Klinger, A. Alonso, S. Bozhenkov *et al*., Plasma Phys. Control. Fusion **59**, 014018 (2017).

[3] J. Nührenberg *et al*., in Theory of Fusion Plasmas (Proc. Joint Varenna-Lausanne Int. Workshop Varenna, 1994), Editrice Compositori, Bologna 3 (1994).

[4] A. H. Boozer, Phys. Fluids **23**, 904 (1980).

[5] A. H. Boozer, Phys. Fluids **24**, 1999 (1981).

[6] H. Liu *et al*., Plasma Fusion Res. **13**, 3405067 (2018).

[7] A. Shimizu *et al*., Plasma Fusion Res. **13**, 3403123 (2018).

[8] M. Isobe *et al*., Plasma Fusion Res. **14**, 3402074 (2019).

[9] S. Okamura, K. Matsuoka, S. Nishimura, M. Isobe *et al*., Nucl. Fusion **41**, 1865 (2001).

[10] S. P. Hirshman, J. C. Whitson, Phys. Fluids **26**, 3553 (1983).

[11] M. Dravlak, Fusion Technol **33**, 106 (1998).

[12] P. Merkel, Nucl. Fusion **27**, 867 (1987).

[13] M. Isobe, S. Okamura, N. Nakajima *et al*., J. Plasma Fusion Res. SERIES **5**, 360 (2002).

[14] K. C. Shaing *et al*., Phys. Fluids B 1, 148 (1989).

[15] V. V. Nemov, S. V. Kasilov *et al*., Phys. of Plasmas **6**, 4622 (1999).

[16] K. Matsuoka *et al*., 12th Int. Conf. Plasma Phys. and Control. Nucl. Fusion Research, Nice, 1988 (IAEA, Vienna) Vol.2, p411 (1988).

Current status of engineering aspect for CFQS

Shigeyoshi Kinoshita[1], Akihiro Shimizu[1], The CQFS team[1,2,3,4]

[1] National Institute for Fusion Science (NIFS), Toki 509-5292, Japan

[2] The Graduate University for Advanced Studies (SOKENDAI), Toki 509-5292, Japan

[3] Institute of Fusion Science, School of Physical Science and Technology, Southwest Jiaotong University (SWJTU), Chengdu 610031, China

[4] Hefei Keye Electro Physical Equipment Manufacturing Co., Ltd, Hefei 230000, China

Abstract

The CFQS will be constructed on the inter-national joint project with NIFS in Japan and SWJTU in China. We are currently evaluating the technical feasibility and we have just started prototyping the main parts in China. It is being designed as a low-aspect-ratio quasi-axisymmetric stellarator with a modular coil system in a CHS-qa configuration. We are reporting the current status of the CFQS from the viewpoint of engineering design.

1. Introduction

The CFQS project began in July 2017 as a joint international nuclear fusion research project with NIFS and SWJTU[1]. The CFQS is a low-aspect-ratio quasi-axisymmetric stellarator, based on a CHS-qa configuration, which aims to improve neoclassical transport and explore high-□ configurations by combining the best features of advanced tokamaks and optimized stellarators [2]. It is expected to be stable in magneto-hydrodynamic (MHD) without a conducting structure, require no current drive at high □/□□ give good orbit confinement, and provide neoclassical confinement equivalent to that of a tokamak. In addition, achieving a low-aspect-ratio in a quasi-axisymmetric configuration is an attractive way to minimize the costs of near-term experiments and the capital costs of possible future power plants [3]. In designing the magnetic configuration, the first priority is placed on the core confinement region. However, it is well known that the concept with peripheral magnetic configuration called divertor configuration will be very important for the fusion reactor. The CFQS project also aims to confirm the effectiveness of the island bundle diverter [4].

At first, we had studied the design without coil case. In the study, it was found that too many supports were required, assembly work became very complicated and it was difficult to provide large and many measurement ports. We have proposed the improved design with the coil case and we have carried out more detailed evaluation.

2. Overall design

Table 1 gives physical data in the several stellarators. The CFQS's main parameters are as follows: toroidal periodic number $m = 2$, aspect ratio $A_p = 4$, magnetic field strength $B_t = 1$ T, and major radius $R_0 =$

1 m. The aspect ratio of the CFQS is the smallest and the modular coil shape is very complicated. They are the disadvantages that make engineering design is relatively hard. For example, the work area in the central region is very narrow and special structural idea is necessary for assembly and maintenance. Diameter of the central work area can be used for assembly is only 0.4m, that is one of the causes that make engineering design difficult, because it is not easy for workers to enter the central area. . The electromagnetic force is very large although the magnetic field in the plasma is only 1 tesla. Maximum magnetic field at coil surface is about twice that of the plasma center.

Table 1 Comparison of major physical specifications

No	Parameters	CFQS	W7-X	NCSX	HSX
1	Major Radius (m)	1.0	5.5	1.4	1.2
2	Minor radius (m)	0.25	0.5	0.33	0.15
3	Aspect ratio	4	11	4.2	8
4	Magnetic Field (T)	1	3	2.1	1
5	Toroidal Periodic Number	2	5	3	4
6	Rotational transform	0.35~0.38	0.85~1	0.4~0.65	1~1.1
7	Magnetic Well Depth	0~0.025			

Fig. 1 shows the experimental building for the CFQS which is built near Mt. Emei in China. Size of the building is about 48.7 m x 35.5m. Fig. 2 shows the major equipment in the torus hall. The CFQS body, coil power supplies, diagnostic system, heating system and so on will be installed in the torus hall. A generator and a cooling water system also required, but may be outside. The plasma heating apparatus is intended to provide for tangential neutral beam injection (NBI) of 40 kV and 1MW and electron cyclotron resonance heating of 54.5GHz and 450 kW. A Thomson scattering system, a microwave interferometer, a charge exchange system, a heavy ion beam probe, and magnetic measurements, among others will be used for plasma diagnostics,.

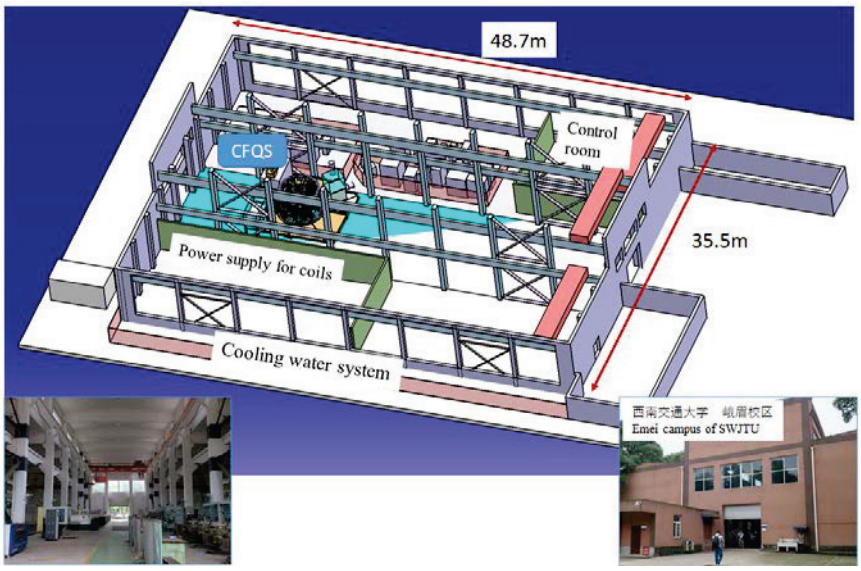

Fig. 1 CFQS experimental building

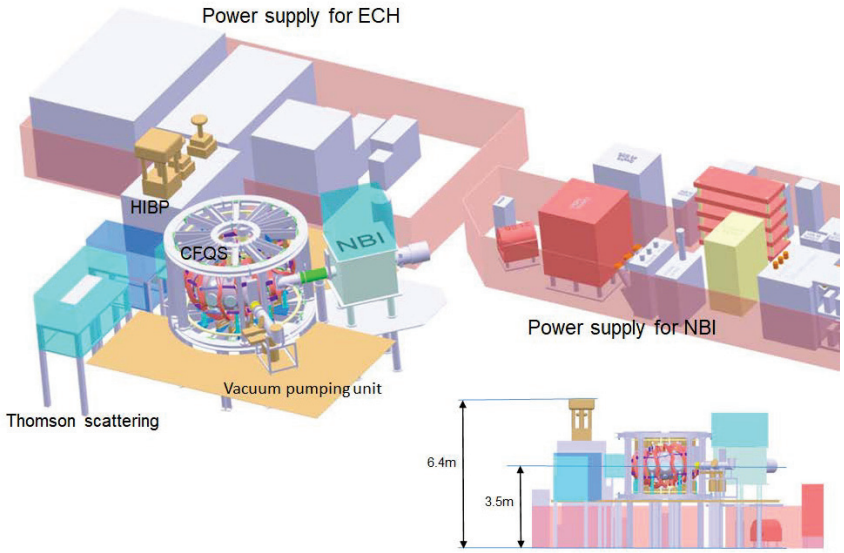

Fig. 2 Layout in the torus hall

We have designed the CFQS body according to the design targets as shown in Table 2. Fig. 3 shows a schematic of the CFQS, which is approximately 4900 mm high and has an outer diameter of 4300 mm. The electromagnetic force applied to the modular coils is supported by a cage-type support structure that was also applied for the CHS in NIFS. The top and bottom frames, and the outer pillars will be used for fixing the poloidal field coils, crossover conductors, power cables, cooling pipes and so on. Of course, they are useful to set up the measuring device.

Table 2 Design targets for the CFQS

No	Parts	Design targets
1	Assembly	Completing the vessel before installing the modular coils because it is difficult to repair defects of the vessel with coils
		Connecting four sections of the vacuum vessel by welding from the inside because there is no working space outside the vacuum vessel with coils
2	Coil	Three types of coil (MC/TF/PF) and nine power supplies will be prepared for various experiment with different configuration and to realize the island bundle
3	Vacuum vessel	Making the cross section as large as possible to increase flexibility of the experiment and to install measurement equipment in the vessel.
		Preparing large ports with an inner diameter of 300 mm or more We want to have at least three ports for ECH, tangential NBI and Thomson scattering.
		Having no one turn break to simplify the structure. The ECH will be used as a main plasma source instead of joule heating.
		Having no baking heater on the vessel to simplify the structure. Inductive high-frequency heating will be applied for 130°C baking

The schematic of the coil system is illustrated in Fig. 4. A basic quasi-axisymmetric configuration can

be produced by four types of modular coils (for a total of 16). However, in order to allow for flexible configuration, we have also installed four poloidal field coils (to move the magnetic axis horizontally) and twelve toroidal field coils (to change the rotational transform). The coil currents are driven by four power supplies for the modular coils, two for the poloidal field coils, and three for the toroidal field coils.

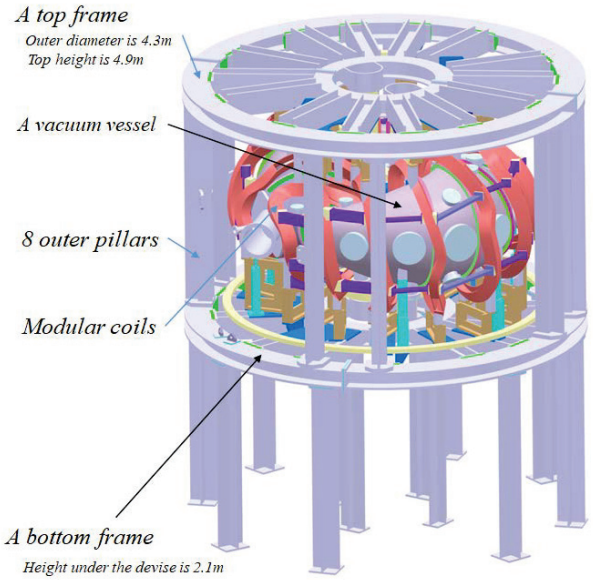

Fig. 3 Schematic of the CFQS

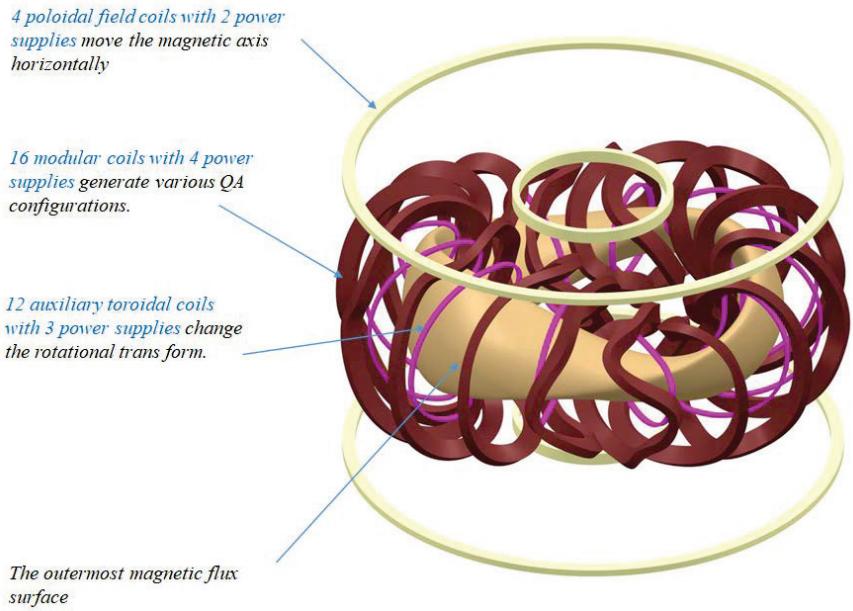

Fig. 4 Schematic of the coil system

3. Modular coil design

Shapes of the modular coils and their cross section are shown in Fig. 5. Since the current density is very high, the conductor temperature rises by about 20° per second of operation. In order to absorb this heat before the next shot, the coils are cooled by pure water. Very large magnetic forces are applied to the modular coils. The forces' magnitude and direction may be very complicated, and their characteristics are not easy to describe. They are similar to those of a tokamak's toroidal field coil, but the modular coils are more difficult to analyze and operated under more severe conditions because even the components that are negligible for tokamaks cannot be ignored. The strength of the coil conductor and insulation alone is not expected to be sufficient for large forces, it must be reinforced with a SUS case like the tokamak's toroidal field coil. In order to reduce costs, the c-shape cases are selected. The c-shape case is planned to consist of two parts, L shape plate and lid as shown in Fig. 6 and the cross section view of Fig. 5.

A number of the modular coils is 16 in 4 types as shown in Fig. 4. One modular coil is composed of 72 copper conductors with current of 4.43kA. Its current density 74 A/mm^2 is very large. The size of the rectangular cross section is 132 x 69 mm2.

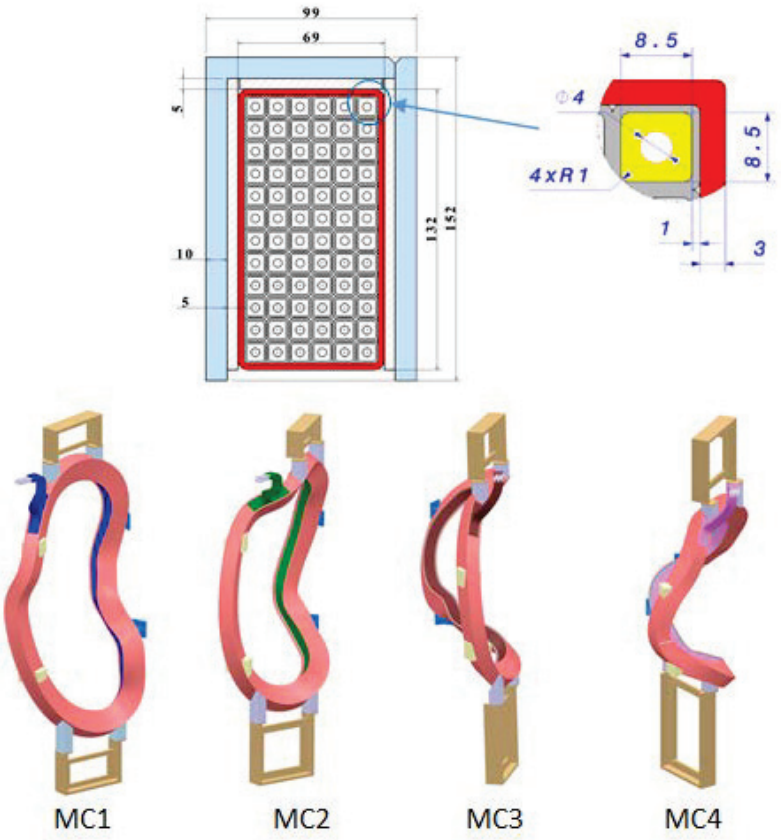

Fig. 5 Modular coil cross section and appearance

The L shape plate may interfere with the case when it is put in as shown in Fig. 6. A similar problem may occur in the process of the coil removing from winding frame. In order to solve this assembly concern, the modular coil shape is devised. Its design method is shown below.

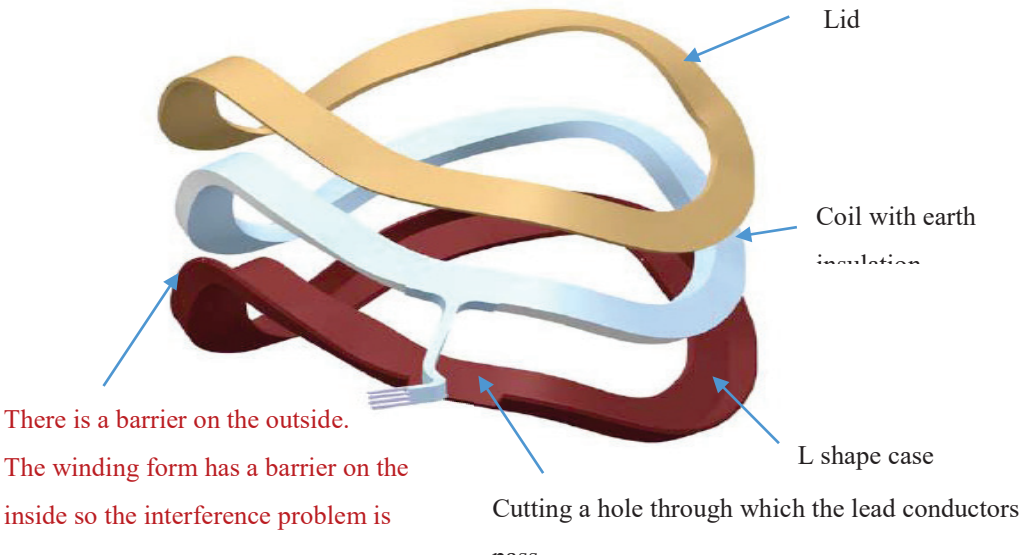

Fig. 6 Coil case and coil with insulation.

The center trajectory of the coil is calculated with the NESCOIL system. The cross-section can be determined from the engineering viewpoint. The size of coil is defined in consideration of the limit of the current density. The rotation angle for the current carrying surface (CCS) in Fig. 7 can be selected so that production or assemble is easy. We had assumed first a design that a longer axis was perpendicular to the CCS, and understood a problem in the manufacturing. We found one method to solve the problem, but it was not optimal. Fig. 8 shows the relation between the L shape winding form and the coil in the middle of the removing process. In the conventional design, two elements interfere at two places. In the improved design, the problem is certainly improved but a judgement whether or not we really removed it is not clear. We are looking for the optimal solution by some optimization technique with the angle θ adjustment.

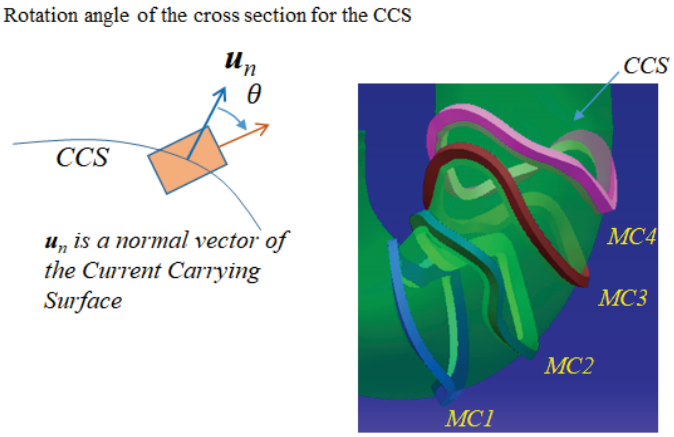

Fig. 7 The rotation angle for the current carrying surface

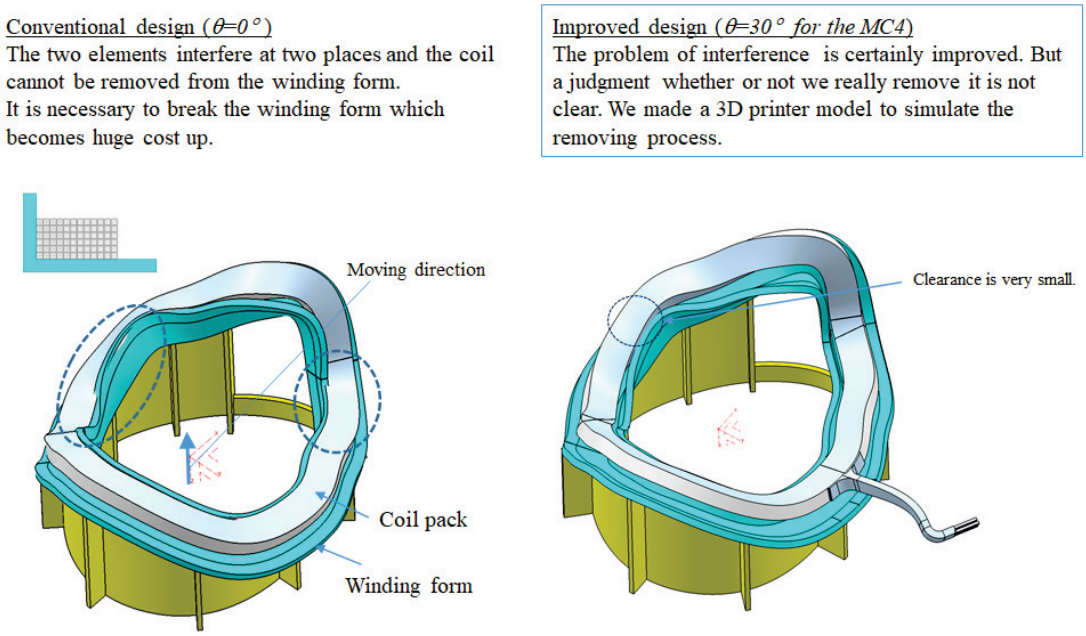

Fig. 8 Influence of the rotation angle

4. Vacuum vessel design

Fig. 9 shows a schematic of the vacuum vessel, which will be manufactured by welding together four sections in the toroidal direction. The flanges used for welding are shown. Since the electromagnetic forces on the vacuum vessel are expected to be small, it will be fabricated from SUS316L with relatively thin walls (6 mm). As a result, the one-turn resistance is roughly 0.3 m□□□which we believe to be sufficiently large while not producing significant Joule heating. The vacuum vessel is fixed to the cage-type support structure shown in Fig. 3 by eight leaf-type legs, added to allow for the vacuum vessel's thermal expansion during baking. Winding frames have also been included on the vessel in order to wind the TFCs. More than 40 large ports, with a diameter of at least 114 mm, will be provided for heating and measurement.

Fig. 10 shows a cross section of the vacuum vessel. The inner surface cross section (green) is much larger than that of the 2b32 reference surface defined for the island bundle diverter experiment , with the minimum gap between the 2b32 plane and the vacuum vessel inner surface being 30 mm. The width and height of the inner surface are both at least 450 mm, which is sufficient for people to work inside. Using such a large vacuum vessel also helps to make the experiment more flexible. Two large rectangular ports are also included, both for workers to enter and for use in NBI and Thomson scattering. Fig. 11 shows the real scale model made by 3D printer. We confirmed that a worker can put inside easily from the large rectangular port.

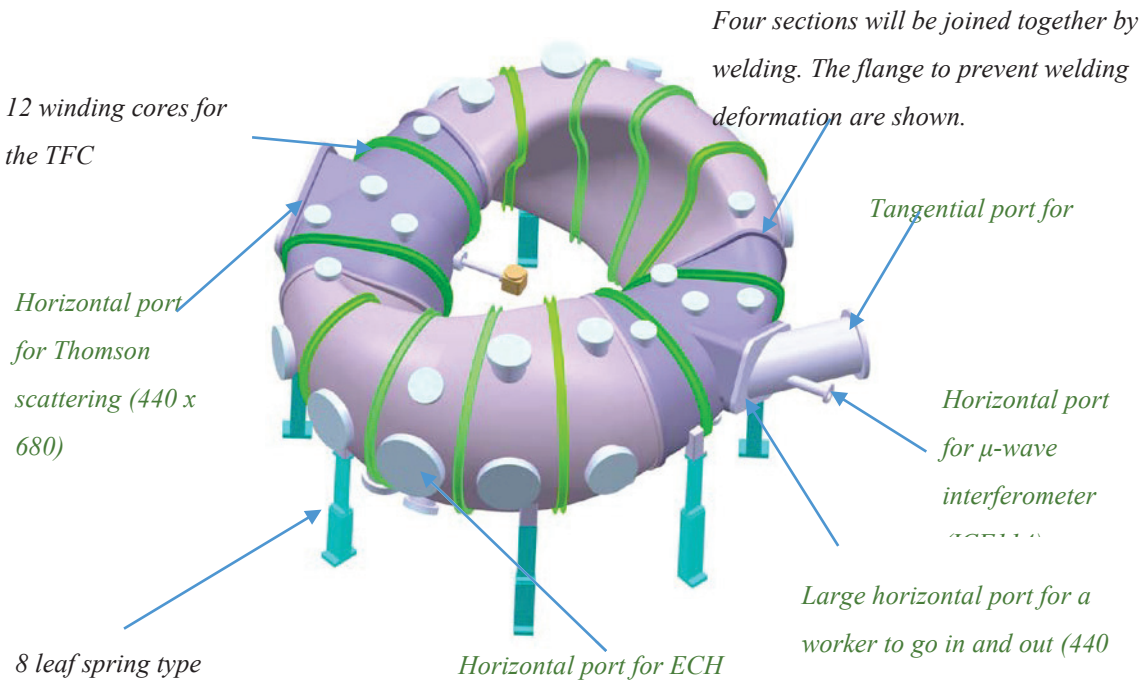

Fig. 9 Schematic of the vacuum vesse

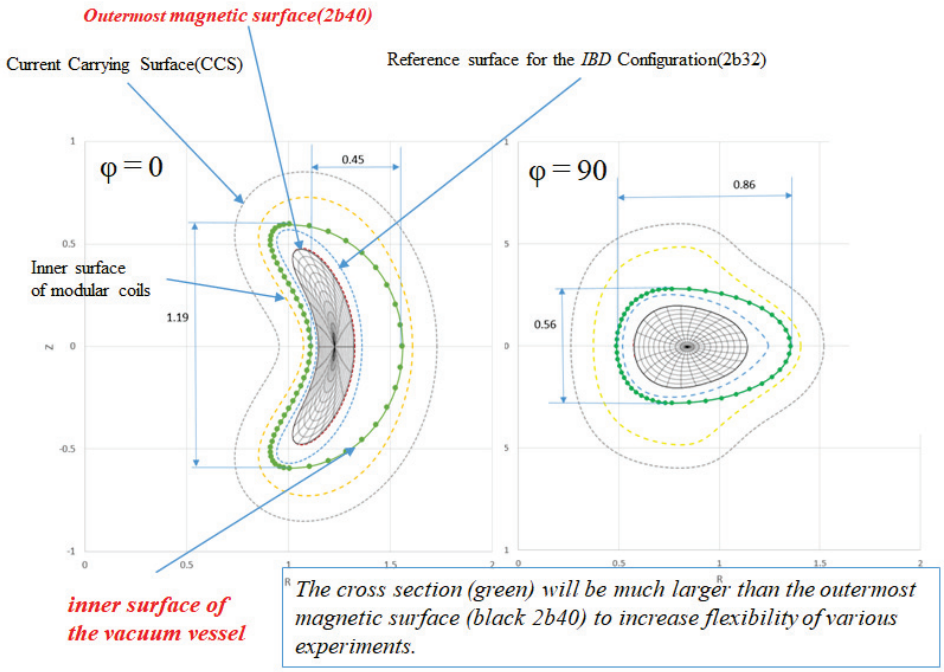

Fig. 10 Cross section of inner surface of the vacuum vessel

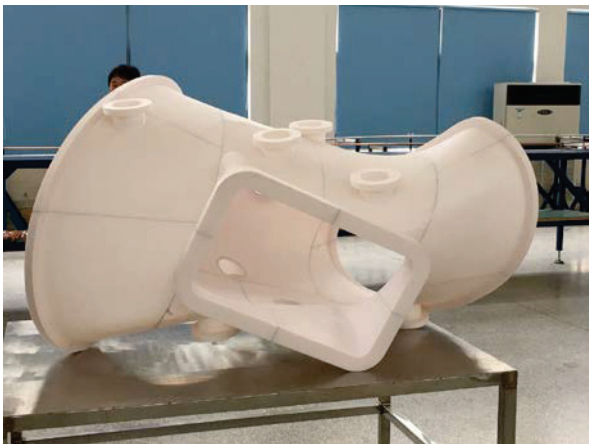

Fig. 11 Real scale vavuum vessel model made by 3D printer

5. Summary

NIFS and SWJTU are collaborating to construct the CFQS producing quasi-axisymmetric stellarator configuration in China. The engineering design processes have been completed for the modular coils (and their support structures) and the vacuum vessel. Now we are discussing the project's feasibility from an engineering viewpoint.

A design concept and a layout of torus hall was also proposed for the CFQS. In addition, One of the valid overall structure was proposed. The vacuum vessel design considering the assembly procedure and experiments with varying configuration of plasma was completed and its effectiveness was confirmed through the real scale model. The preliminary engineering design for the modular coils and its support structure was completed. It will be modified for manufacturing improvement, cost reduction and the reliability.

Acknowledgements

This work was partly supported by the Post-CUP program for Japan-China collaboration. It was also supported by NIFS budget code KEJC001.

References

[1] Haifeng Liu, A. Shimizu, M. Isobe et al., Plasma Fusion. Res. 13 (2018) 3405067.
[2] S. Okamura, K. Matsuoka et al., Nuclear Fusion 41 (2001) 1865
[3] Yuhong Xu, H. Liu et al., 27th IAEA Fusion Energy Conference (FEC 2018), Ahmedabad, India, (2018) EX/P5-23 (Poster)
[4] S. Okamura, H. Liu, et al., 45th EPS Conference on Plasma Physics, (2018), Prague, Czech Republic, Vol. 42A, P5.1034 (Poster)

Design and analysis of CFQS supporting structure

Guozhen Xiong[1)], Yuhong Xu[1)], Akihiro Shimizu[2)], Shigeyoshi Kinoshita[2)], Haifeng Liu[1)], Mitsutaka Isobe[2,3)], Shoichi Okamura[2)], Takanori Murse[2)], Sho Nakagawa[2)], Dapeng Yin[4)], Yi Wan[4)], Changjian Tang[1,5)], and CFQS team[1,2,3)]

1) *Institute of Fusion Science, School of Physical Science and Technology, Southwest Jiaotong University, Chengdu 610031, China*

2) *National Institute for Fusion Science, National Institutes of Natural Sciences, Toki 509-5292, Japan SOKENDAI (The Graduate University for Advanced Studies), Toki 509-5292, Japan*

3) *Hefei Keye Electro Physical Equipment Manufacturing Co., Ltd, Hefei 230000, China*

4) *College of Physical Science and Technology, Sichuan University, Chengdu 610041, China*

Abstract

The Chinese First Quasi-axisymmetric Stellarator (CFQS) is now under design and construction. It will be the first quasi-axisymmetric configuration device in the world. The main parameters of CFQS are as follow: the toroidal period number N_p = 2, major radius R_0=1.0 m, aspect ratio A_p=4.0 and magnetic field strength B_t =1.0 T. The low aspect ratio makes it quite difficult to design a supporting structure because of the limited space availability and strong electromagnetic (EM) load. In this paper, a cage-like supporting structure is proposed for CFQS to support the EM force and the weight of entire device. A finite element analysis is carried out for ensuring the reliability of the supporting structure. The results show that the stress on the most area of the device is in allowable range.

1. Introduction

The Chinese First Quasi-axisymmetric Stellarator (CFQS) is a quasi-axisymmetric stellarator which is designed as a joint project of Southwest Jiaotong University in China and National Institute for Fusion Science in Japan. The CFQS is a medium size device, having major radius of 1 m, average plasma minor radius of 0.25 m, and aspect ratio (A_p) of 4.0. The magnetic field strength (B_t) can be increased up to 1.0 T. The CFQS operation will be divided into the following two phases. In the initial phase, experiment will be performed at B_t of 0.09 T in order to confirm quality of the magnetic configuration. In the second phase, B_t will be increased to 1 T to perform confinement study of quasi-axisymmetric stellarator plasma.

One of main components in CFQS is its magnetic coil system, especially the 16 modular coils with four different types as depicted in Figure 1. In order to protect the device from heavy electromagnetic (EM) load, a strong support structure is required. Because it is the first time for us to design a support structure for a device with modular coils and low A_p, we need an adequate understanding of several critical issues and must carry out accurate numerical analysis for achieving a reliable design.

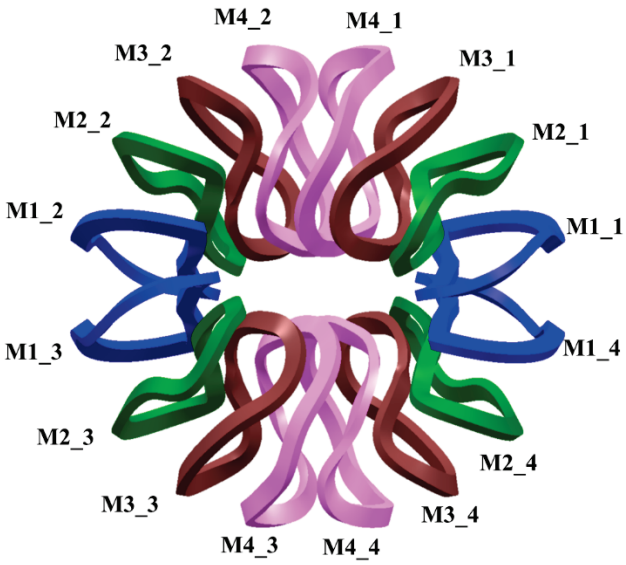

Figure 1. Top view of CFQS modular coils.

2. CFQS coil system and electromagnetic force analyses

2.1 CFQS coil system

The CFQS has three coil components, including 16 modular coils, 4 poloidal field coils (PFCs), and 12 auxiliary toroidal field coils (TFCs). These three components are used for generating helical magnetic field, changing the plasma position horizontally and/or plasma shape, and adjusting the rotational transform, respectively. The detail parameters of three coil components are listed in Table 1. The modular coils play a key role in CFQS operation. Their complicate shape can produce quasi-axisymmetric (QA) configuration.

Figure 2 shows the contour plot of magnetic field strength on each coil in the case of B_t=1 T operation. In this figure, it can be seen that the magnetic field strength on modular coils and TFCs are larger than that on PFCs.

Table 1. Different coil components in CFQS.

Coil type	Amount	Number of conductors	Coil current		Primary role
			One turn	Total	
Modular coil	16 in four groups	72 turns in series	4.34 kA	312.5 kA	Generate QA configuration
PFC	4 in two groups	32 turns in series		138.8 kA	Move plasma horizontally
Auxiliary TFC	12 in three groups	8 turns in series		34.7 kA	Change rotational transform

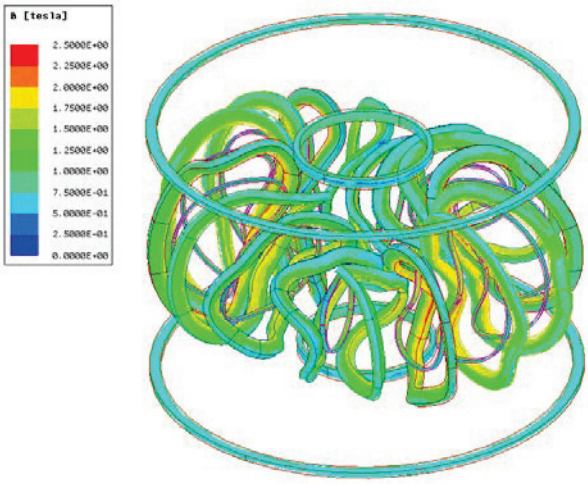

Figure 2. Distribution of magnetic field strength on the CFQS coil system.

2.2 Electromagnetic force analyses on CFQS coil system

For designing a support structure, the most important thing is the distribution of electromagnetic (EM) force on the coil system because EM force is the main load applied on our device. In this paper, EM force distributions on modular coils are evaluated by a finite element analysis software ANSYS/Maxwell™. In this calculation, the coil currents for 1 T operation state are considered and a magnetostatics solution type is set for simply getting the force distribution in discharge process. The EM force distributions on different type of modular coils are shown in Figure 3. Note that here the EM force distribution of auxiliary toroidal coils is not shown because the EM forces on them are small so they can be easily supported by winding frame on vacuum vessel. The results indicate that the EM force concentrates on high-field side of coils as expected and total forces on modular coils is larger than those on PFCs.

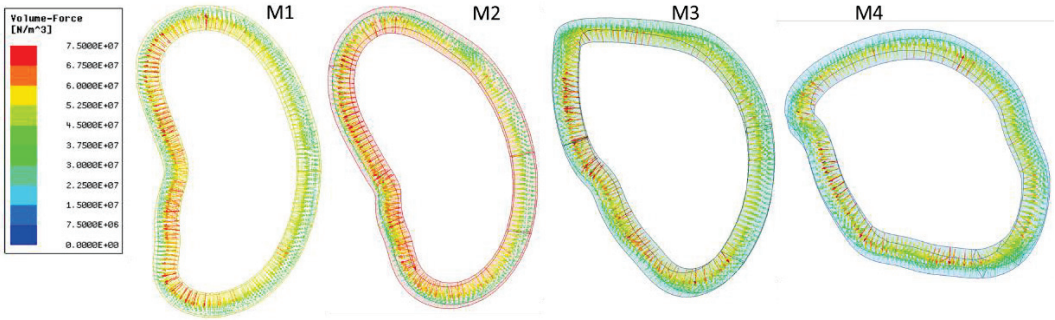

Figure 3. EM force distributions on different modular coils.

Different force components on modular coils and PFCs are summarized in Table 2. In this evaluation, EM forces on coils are roughly divided into several parts in the cylindrical coordinates to make it easier for us to predict behavior of coils. It can be seen that the centripetal component on M1, M2, and M3 coils are large, the vertical component is also large on M2 and M3 coils. Therefore, some strong supports should be set on the concerned area. Also, corresponding supports must be adopted for supporting toroidal component and overturning component.

Table 2. Different force components on modular coils and PFCs.

Force components on modular Coils				
Coil name	Centripetal force (N)	Vertical force (N)	Toroidal force (N)	Total force
M1_1	-167050	-19396	-13066	168680
M1_2	-167050	19393	13068	168680
M1_3	-167050	-19408	-13070	168680
M1_4	-167030	19401	13046	168660
M2_1	-142390	-60467	-37651	159210
M2_2	-142390	60463	37657	159210
M2_3	-142390	-60469	-37687	159230
M2_4	-142370	60470	37674	159200
M3_1	-94524	-92567	-37910	137620
M3_2	-94517	92568	37944	137630
M3_3	-94495	-92588	-37915	137620
M3_4	-94490	92559	37925	137600
M4_1	-39344	-38238	-45916	71542
M4_2	-39327	38242	45912	71532
M4_3	-39333	-38232	-45893	71518
M4_4	-39361	38243	45900	71544
Force components on PFCs				
Coil Name	Total force			
OPFC_U	14609			
IPFC_U	12006			
OPFC_L	14502			
IPFC_L	11950			

3. Design of CFQS support structure

There are several problems we need to pay attention to in our design work. First, the center area is fairly limited but robust supports against strong EM force are required. Second, the minimal gaps between the two neighboring coils, and coil and vacuum vessel are quite small. Because of this, we have to employ limited size of supports and keep space for future assembly process. Third, working space for plasma diagnostics and heating devices must be large enough. As a reference, the cross section and three-dimensional (3-D) computer-aided design (CAD) drawing of modular coils and vacuum vessel in CFQS are shown in Figure 4.

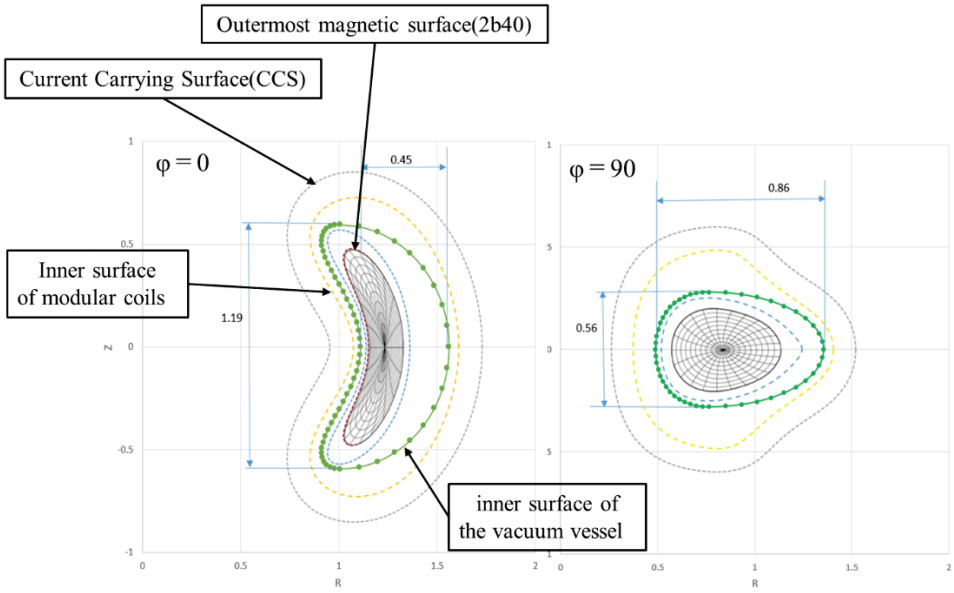

(a) CFQS vacuum vessel cross section

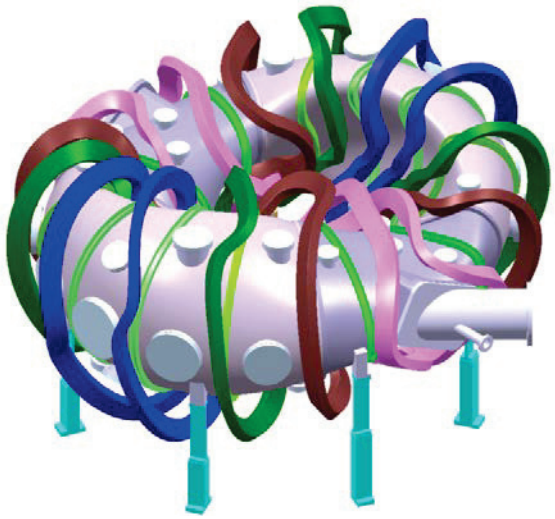

(b) 3-D CAD drawing of CFQS modular coils and vacuum vessel

Figure 4. CFQS modular coils and vacuum vessel.

Considering about issues mentioned above, a cage-like support structure has been designed with two main components, i.e., the supporting frame and coil supports. The overview of support structure of CFQS device is shown in Figure 5.

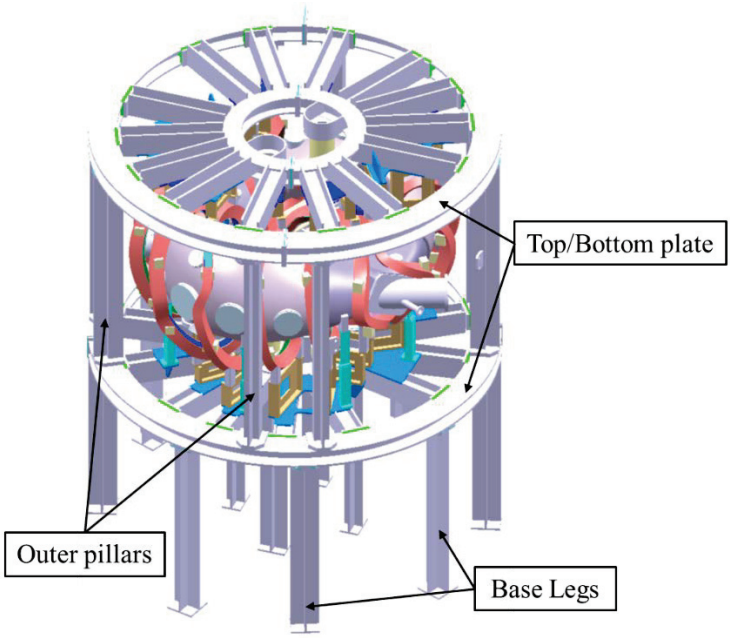

Figure 5. Overview of support structure of CFQS.

3.1 Supporting frame

The supporting frame consists of twelve base legs, top and bottom plates, eight outer pillars, and a center support. The 'cage' is formed by eight outer pillars and top/bottom plates. It is used to resist the vertical and horizontal displacement of coils and vacuum vessel. The twelve base legs will be fixed on the ground of experiment hall to support the 'cage' and leave space for vacuum pumping system and plasma diagnostics. The center support is the main part for supporting modular coils. It can also support top and bottom plates from the inside. The detail of support structure is shown in Figure 6.

In this structure, large EM load on coils will be reduced by different parts. The vertical EM force components and the weight of vacuum vessel are supported by top and bottom plates which are reinforced by 14 radial beams with cover plates. Large centripetal components will be supported by two strong columns with 210 mm in diameter and 32 mm in thickness. To partly cancel the large resultant force applied on those two columns and strengthen them, two H-shape stainless steel beams are set between the columns. Two additional link bars are set between M4 coils for canceling centripetal components because the shape of M4 coils is too complicate to be fully supported by center column.

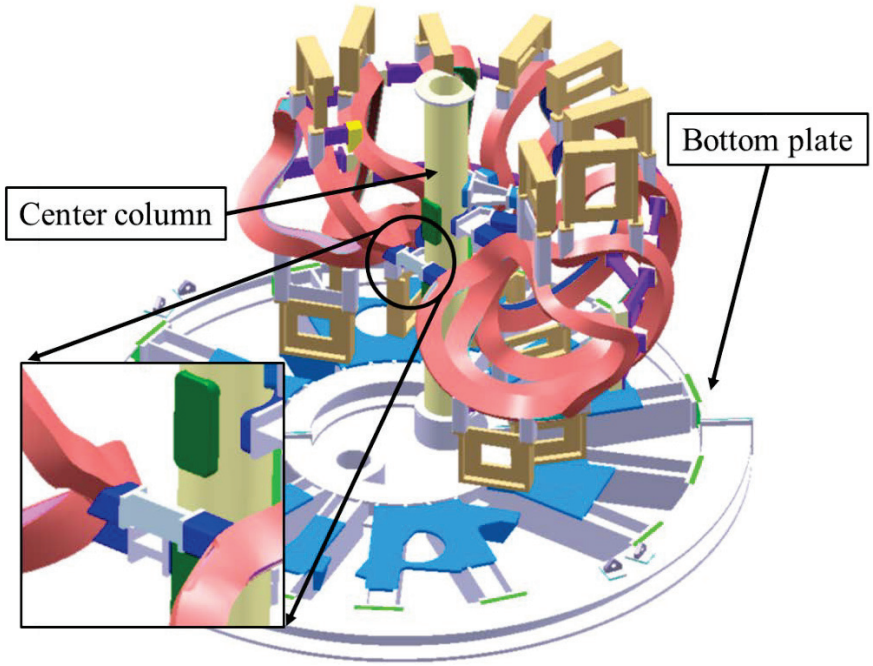

Figure 6. Center area of supporting frame.

3.2 Coil supports

Due to the complicate shape of coils and limited space in this device, we have to use coil cases and additional link bar to support the coils from deformation. A 'U' shape coil case is designed for remaining space of assembly process and simplified manufacturing process. The design of 'U' shape coil case is shown in Figure 7. Sixteen coil cases are going to be fabricated by welding one 'L' shape shell and one lid together, furthermore, some fiber reinforced plastic (FRP) spacer will be inserted into the case in assembly process to fill the gap between coils and coil cases.

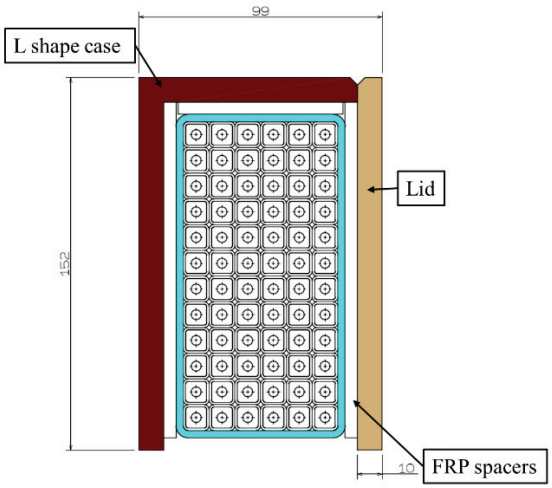

Figure 7. Design of 'U' shape coil case.

There are several additional parts located on coil cases as shown in Figure 8. One of them is the coil leg. The irregular shapes of coils require us to design legs for connecting them on top and bottom plates, and some holes are cut on coil legs for setting the cables of diagnostics. Those

protuberance located on the inboard side of coil case are used for connecting coil cases to the center support. The other protuberance located on the outboard side of coil cases are used for connecting link bars between different coils which can support the toroidal EM force components.

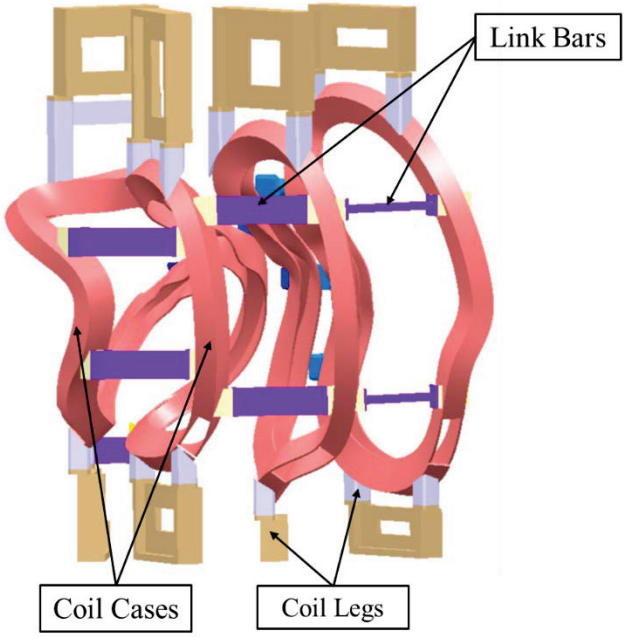

Figure 8. Coil supports for four coils, coil legs (white and khaki), link bars (purple), and protuberance (blue and yellow).

4. Finite element analysis on supporting structure

The numerical simulation is required as a reference in order to confirm the quality of support structure design and help us to make the optimization. A finite element analysis is carried out by ANSYS/Mechanical APDL™, through the evaluation result of deformation, von-Mise stress, and elastic strain we can have a clear understanding of the support structure property. The allowable stress for typical material is shown in Table 3.

Table 3. Design guideline of typical materials.

Material			SUS316	C1020 -O	C1020 -1/2H	Resin	Composite (Coil)	FRP
Young's Modulus	(GPa)	E	197	100	100	1～3	100	100
Design Stress	(MPa)	S_m	137	50	90	-	90	50
Design Strain		ε					＜0.1%	
Tensile Strength	(MPa)	σ_u	520	230	270	10～100	270	2000
Yield Strength	(MPa)	σ_y	205	80	250	-	250	500
Elongation	(%)		40	50	25	1～2	1～2	5

Poisson's ratio		ν	0.3	0.34	0.34	-	0.34	0.3
Density	(kg/m^3)	ρ	8000	8960	8960	1100	8960	1500
Thermal expansion		α	$1.73x10^{-5}$	$1.65x10^{-5}$	$1.65x10^{-5}$	$5x10^{-5}$	$1.65x10^{-5}$	$2.0x10^{-5}$
Comments			300k	OFC	OFC	after curing	OFC + isolation	Varies

- Sm = min (2/3 σ_y, 1/3 σ_u) -- ASME III criterion
- The Sm is changed according to operating temperature.
- If possible, it is desirable that strain ratio ε is less than 0.1% or 0.5% at worst for the coil

Figure 9 shows the calculation model. In this case, vacuum vessel is not included in calculation and cross section of the coil is simplified for reducing required compute resource and simulation time. In Figure. 10, the contour plot of deformation distribution on device indicates that the maximum deformation is 0.95 mm. This is an acceptable value because the misalignment caused by this deformation will not affect magnetic configuration significantly.

In consideration of large EM load applied on coils, we should check the von-Mise stress and elastic strain on modular coils for estimating the quality of support structure. In real design, coils are formed by two parts, i.e., oxygen free copper and resin insulation, but in this calculation, coils are replaced by one composite model. Therefore, both design value for von-Mise stress and elastic strain should be satisfied. We restrict that the stress on coils should be less than 90 MPa to ensure the stability of copper conductors, and restrict the strain on coils should be less than 0.1% to confirm the insulation will not be broken by EM load. The distribution of von-Mise stress and elastic stress on coils is shown in Figure 11. The results indicate that both stress and strain are in allowable range.

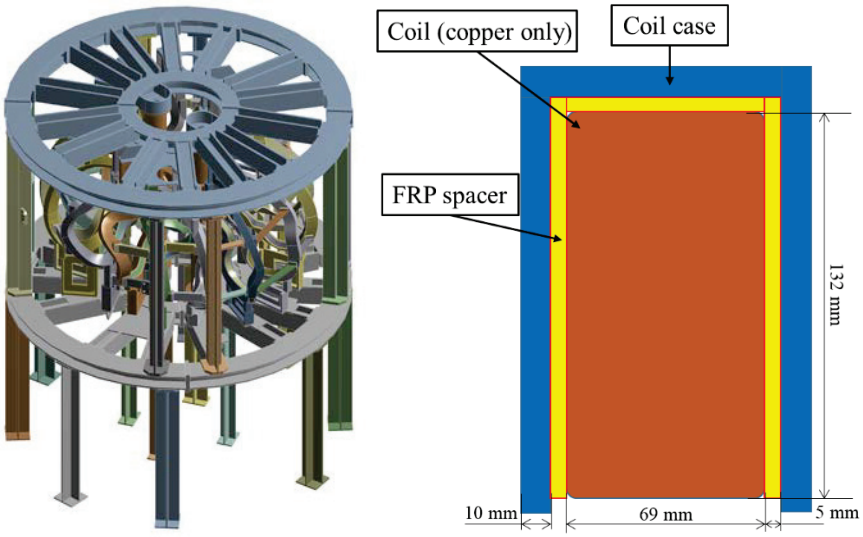

Figure 9. Simplified support structure and coil model.

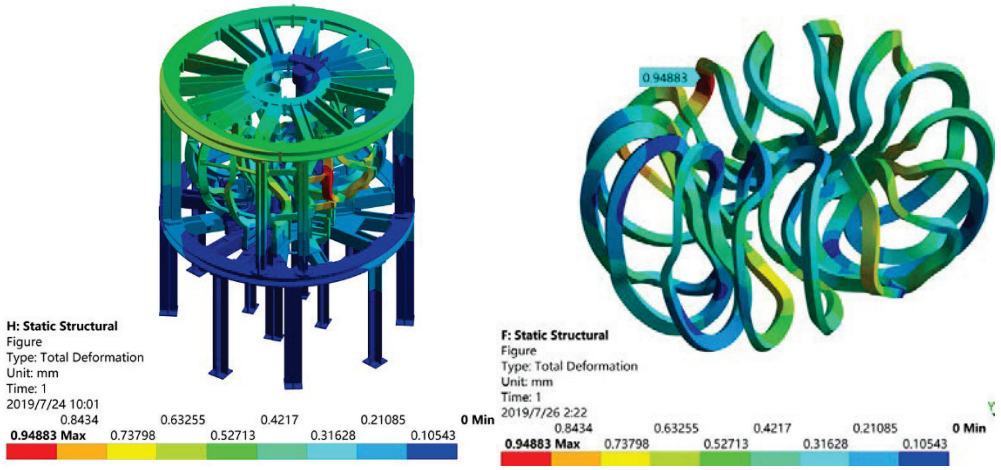

Figure 10. Deformation distribution on supports and coils.

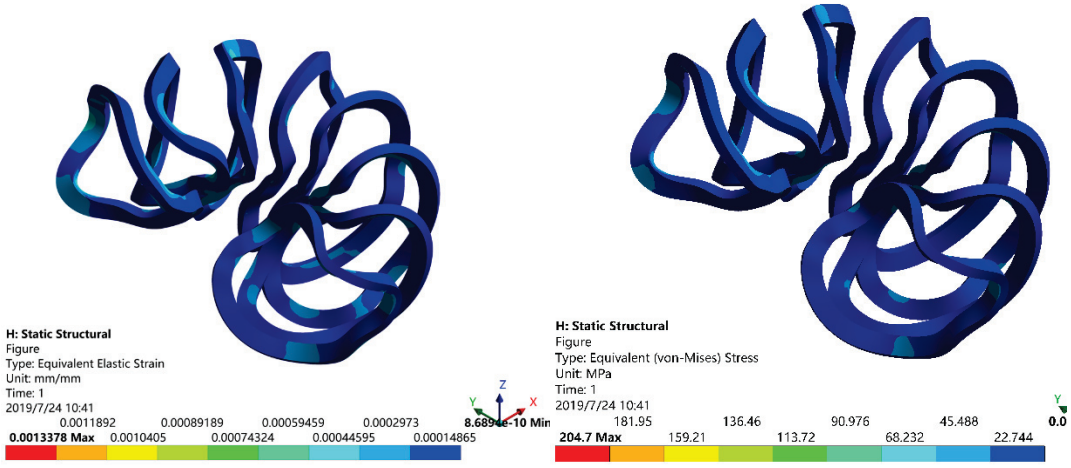

Figure 11. Stress and strain distribution on modular coils.

As for other supports in stainless steel, such as supporting frame and coil case, design stress is the only limit for ensuring stability. Figure. 12 shows the stress on supporting frame and coil cases. It is obviously that the stress on most area of the structure is less than 137 MPa, which is the design stress for stainless steel. But there still some local area on coil supports that the stress is larger than design stress and close to the yield stress of stainless steel. This situation means that the structure is not strong enough on relative place and we need a further optimization on this design.

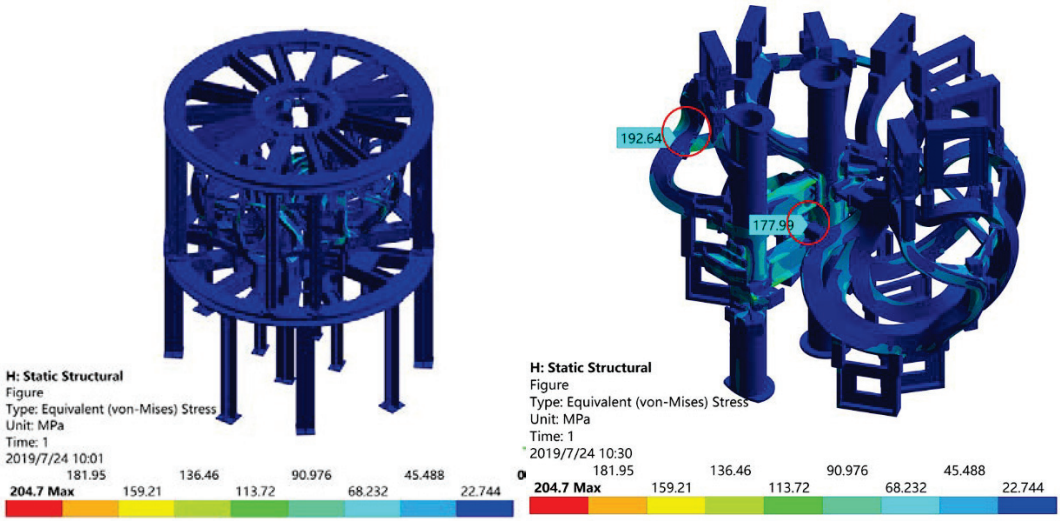

Figure 12. Stress distribution on supporting frame and coil cases.

5. Summary

In this paper, the distribution of EM force on modular coils are evaluated by finite element analysis to predict coils behavior roughly. Based on the different EM force components, a cage-like support structure design is carried out for supporting coil system and vacuum vessel. The support structure has two main parts as supporting frame and coil supports, and they are set up to prevent deformation and decrease large stress on modular coils caused by different EM force components. A finite element analysis on support structure is carried out for ensuring the strength of this design. The result indicates that in this design the coil support is strong enough to protect the modular coils, but some structures in supporting frame should be modified and decrease large stress concentrate on them.

References

[1] Mitsutaka ISOBE, Akihiro SHIMIZU, Haifeng LIU *et al*., Current Status of NIFS-SWJTU Joint Project for Quasi-Axisymmetric Stellarator CFQS, Plasma and Fusion Research, Volume **14** 3402074, 2019.

[2] Shigeyoshi KINOSHITA, Akihiro SHIMIZU *et al*. Engineering Design of the Chinese First Quasi-Axisymmetric Stellarator (CFQS), Plasma and Fusion Research, Volume **14** 3405097, 2019.

[3] Akihiro Shimizu, Haifeng Liu *et al*. Configuration Property of the Chinese First Quasi-Axisymmetric Stellarator, Plasma and Fusion Research, Volume **13** 3403123, 2018.

[4] Haifeng Liu, Akihiro Shimizu *et al*. Magnetic Configuration and Modular Coil Design for the Chinese First Quasi-Axisymmetric Stellarator, Plasma and Fusion Research, Volume **13** 3405067, 2018.

Acknowledgements

The authors would like to express their deepest gratitude to Director General Professor Yasuhiko Takeiri of National Institute for Fusion Science, former Vice President of Southwest Jiaotong University Professor Wengui Zhang for their strong support and great encouragement of the joint project for the CFQS. This work is performed with the support and under the auspices of the NIFS Collaboration Research Program (NIFS17KBAP034). Also, this work is partly supported by programs of international collaborations with overseas laboratories (UFEX105), promotion of magnetic confinement research using helical devices in Asia (URSX401), and Post-CUP program

for Japan-China collaboration.

Engineering Analysis for Vacuum Vessel of CFQS

Sho Nakagawa[1], Takanori Murase[1], Shigeyoshi Kinoshita[2], and the CQFS team[1,2,3,4]

[1]Department of Engineering and Technical Service, National Institute for Fusion Science

[2]Large Helical Device Project, National Institute for Fusion Science

[3] Institute of Fusion Science, School of Physical Science and Technology, Southwest Jiaotong University (SWJTU), Chengdu 610031, China

[4] Hefei Keye Electro Physical Equipment Manufacturing Co., Ltd, Hefei 230000, China

Abstract

The world's first quasi-axisymmetric stellarator CFQS is constructed as the joint project of National Institute for Fusion Science in Japan and Southwest Jiaotong University in China [1]. Physics design of CFQS plasma was completed[2,3], and numerous efforts are now being made to finalize engineering design of CFQS.

The CFQS vacuum vessel (VV) needs to be able to withstand several loads such as an atmospheric pressure, thermal stress during baking, and gravitational force and is fairly complicated in shape compared to tokamak fusion devices. Therefore, the structural reliability of vacuum vessel is of our great concern.

In addition, an eddy current on the VV will be induced by current changes of toroidal field coil and/or poloidal field coil. The effect of eddy current on magnetic confinement is also necessary to be investigated.

In this report, analysis have been performed to confirm the structural reliability and evaluate the influence of eddy current using finite element method software ANSYS/Mechanical™ and ANSYS/Maxwell™. The result shows that the stress on the VV is within an acceptable range and eddy current have little effect on magnetic confinement.

1. Introduction

The design of the CFQS vacuum vessel (VV) is proposed as shown in Fig.1(a). It will be made of a thin plate of stainless steel having thickness of 6 mm and has fairly complicated shape because it is designed so as to follow the convoluted shape of plasma[4].

The VV will be exposed to several loads such as atmospheric pressure, thermal stress during baking, and gravitational force. A finite element method software ANSYS/Mechanical™ is employed

to confirm structural reliability of design. Here we check a deformation and stress of the VV in order to prevent interference with modular coils and breakage of the device.

Fig.1(b) shows poloidal field coil (PFC) and toroidal field coil (TFC) of CFQS. The estimation of a time constant is crucial for evaluating the electrical property of the CFQS VV. We conducted the analysis of an eddy current induced by PFC / TFC current changes, and estimated a time constant of VV.

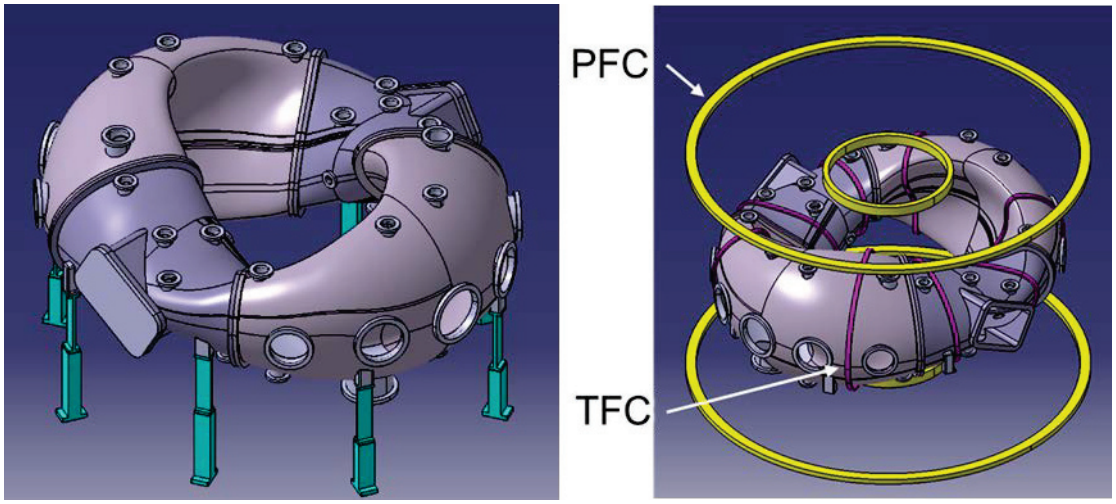

Fig. 1 Schematic view of (a) CFQS vacuum vessel and (b) poloidal and toroidal field coils.

2. Structural analysis of vacuum vessel

2.1. Case 1: Structural analysis of atmospheric pressure

In a plasma operation, compressive force due to atmospheric pressure is applied on the VV while keeping the inside in a vacuum. To clarify the effect of this force, any other load is not considered in this case. Fig. 2 shows deformation and stress, respectively. The maximum deformation is about 1 mm on the area above the rectangular port. Main component of the deformation is in vertical direction. The most stressed region is between port and VV in which the maximum stress reaches 87 MPa. The stress in similar area is tend to be high as shown in Fig. 3.

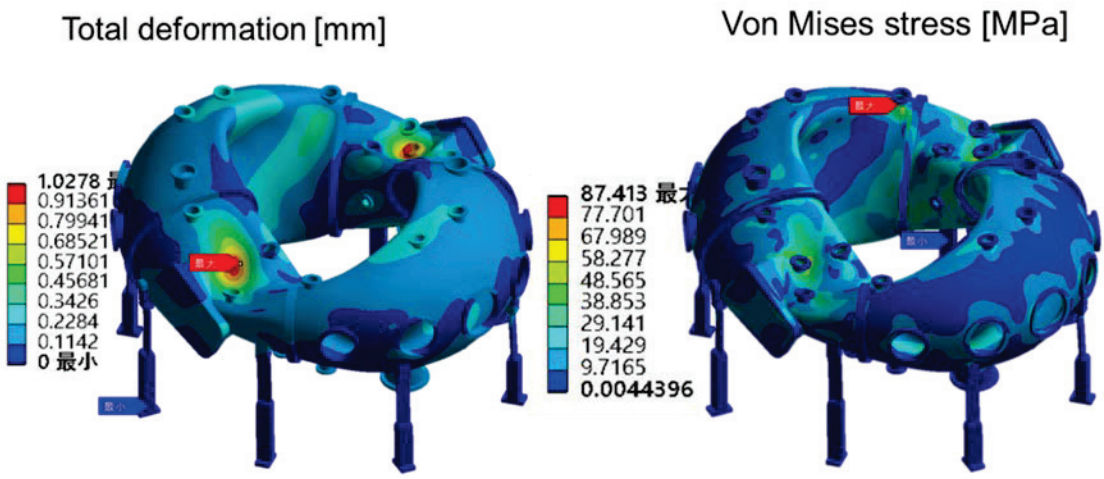

Fig. 2 Results of case 1 (a) deformation [mm], (b) stress [MPa].

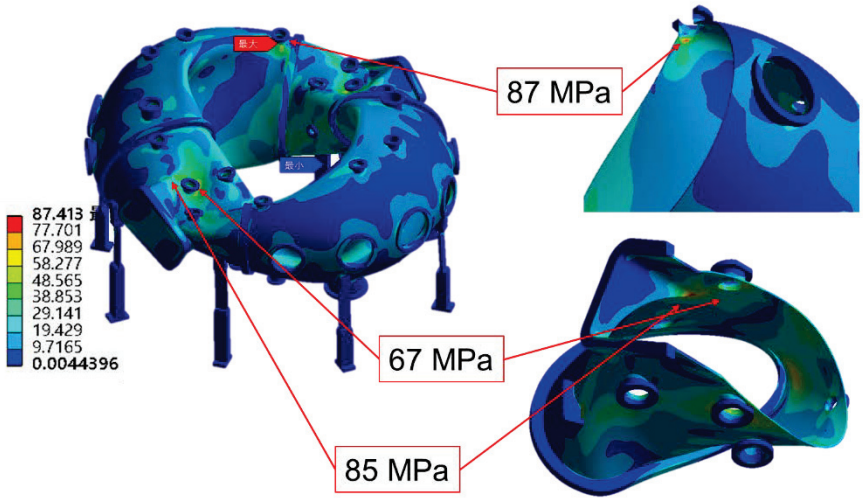

Fig. 3 High stress area in case 1.

2.2. Case 2: Structural analysis of thermal stress during baking

In case 2, only temperature rise due to baking is considered. The VV will be heated up to 130℃ in baking operation, which leads to thermal expansion of VV. The primary problem is interference with modular coils that are closely installed around the VV. As shown in Fig. 4(a), the maximum deformation is about 3 mm which appears in the outside of VV. It is tolerable value because minimum distance between modular coils and VV is about 10 mm.

Fig. 4 (b) shows stress distribution. Thermal stress is small in most region of VV, and concentrates

only in the legs because these leaf-spring type legs have flexibility in radial direction. The maximum stress is 128 MPa which appears in the area between the leg and VV.

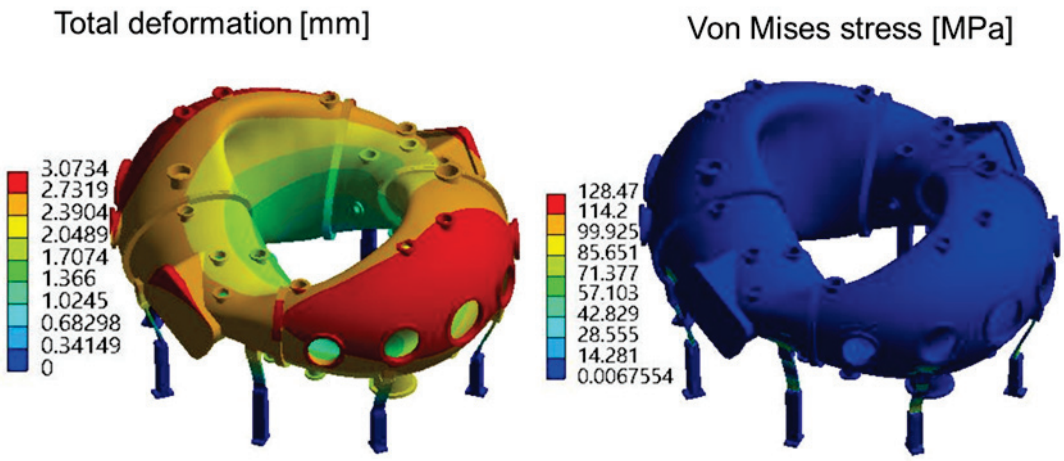

Fig. 4 Results of case 2 (a) deformation [mm], (b) stress [MPa].

2.3. Case 3 : Structural analysis considering three loads

Here we consider gravitational force in addition to above-mentioned loads. These three loads are applied at the same time on the VV. Fig. 5 shows the deformation and stress. The maximum deformation appears on the outside of VV, which is mainly caused by thermal expansion. The maximum stress is 126 MPa in area between legs and VV, which is below stress limit.

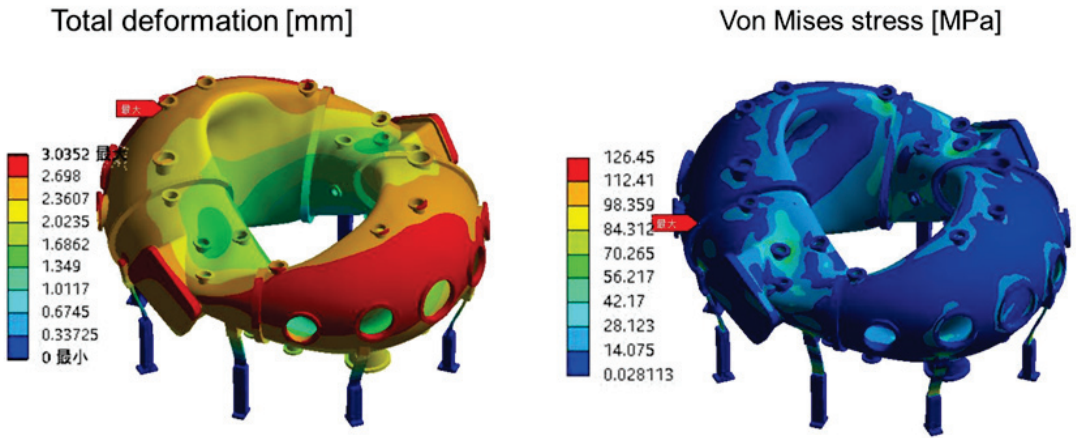

Fig. 5 Results of case 3 (a) deformation[mm], (b) stress[MPa].

3. Simulation of an eddy current induced by PFC/TFC current change

In this analysis, we calculate the time evolution of the eddy current while PFC / TFC current changing linearly. From the time evolution of eddy current, we can estimate the time constant as follows

$$I_{vv}(t) = I_0(1 - e^{-\frac{t}{\tau}})$$

$$\therefore I_{vv}(\tau) = I_0\left(1 - \frac{1}{2.71828}\right) = 0.6321 \cdot I_0,$$

where I_{vv} is eddy current on VV, τ is time constant.

If the time constant τ is sufficiently shorter than typical discharge duration of 100 ms for the CFQS, the effect of eddy current on the vacuum vessel can be neglected.

Fig. 6 and Fig. 7 show time evolution of the eddy current due to PFC / TFC current change. The eddy current is calculated by integrating the current density over across section of VV. As can be seen in Figs. 6 and 7, the time constants are estimated to be 4.4 ms for PFC and 2.4 ms for TFC.

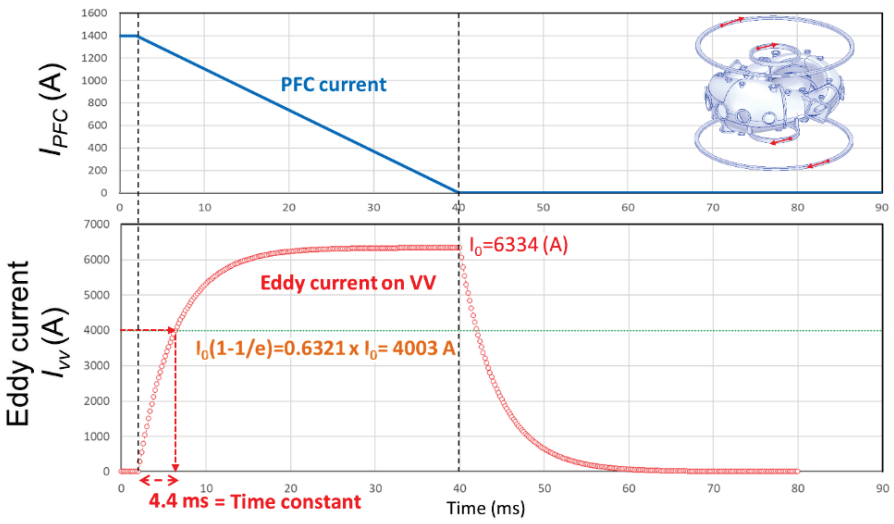

Fig. 6 Time evolution of a PFC current and an eddy current on vacuum vessel.

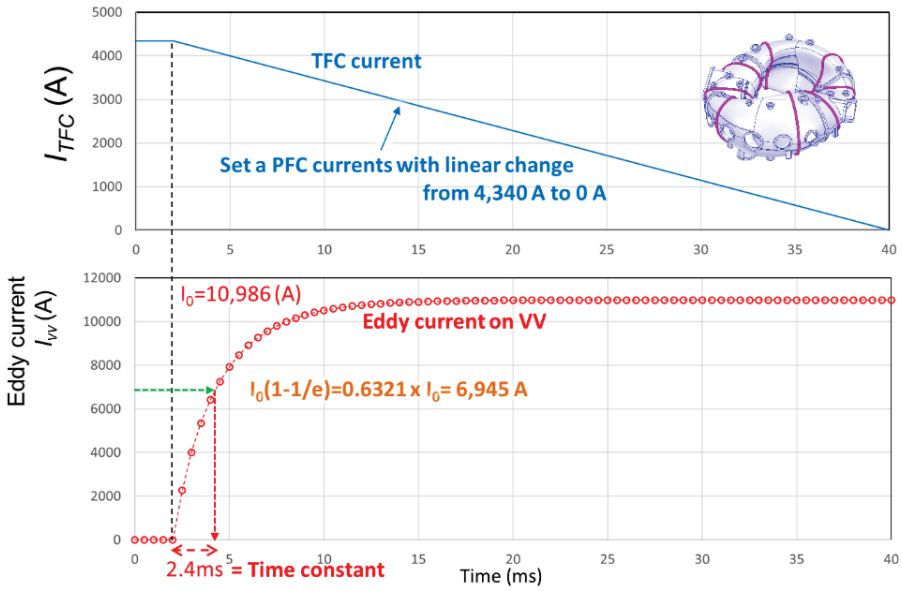

Fig. 7 Time evolution of a TFC current and an eddy current on vacuum vessel.

Summary

We evaluated structural reliability of CFQS VV and the influence of eddy current on magnetic confinement using ANSYS/Mechanical™ and ANSYS/Maxwell™.

In structural analysis, we chose three load conditions and clarified the effect of these load conditions. When we considered all three loads simultaneously, the maximum deformation is 3 mm on the outside of VV, which is lower than the minimum gap between modular coils and VV. Moreover, the maximum stress is 126 MPa which is within an allowable range.

In analysis of eddy current, the time constant of the eddy current induced by PFCs and TFCs are estimated to be 4.4 ms and 2.4 ms, respectively. These are sufficiently shorter than typical discharge duration of several hundred of ms for the CFQS. Therefore, the influence of eddy current on magnetic field configuration will not be significant.

References:

[1] M. Isobe *et al*., Plasma Fusion Res. **14** (2019) 3402074.
[2] H. Liu *et al*., Plasma Fusion Res. **13** (2018) 3405067.
[3] A. Shimizu *et al*., Plasma Fusion Res. **13** (2018) 3403123.
[4] S. Kinoshita *et al*., Plasma Fusion Res. **14** (2019) 3405097.

Micro-instabilities and turbulent transport in CFQS

M. Nakata[1,2], M. Nunami[1,2], J. Huang[3], A. Shimizu[1], M. Isobe[1,2], S. Okamura[1], H. Liu[3], Y. Xu[3], and CFQS team[1,3]

[1]National Institute for Fusion Science, National Institutes for Natural Sciences, Toki 509-5292, Gifu, Japan
[2]SOKENDAI(The Graduate University for Advanced Studies, Toki 509-5292, Gifu, Japan
[3]Institute of Fusion Science, School of Physical Science and Technology, Southwest Jiaotong University, Chengdu 610-031, People's Republic of China

Abstract

Based on the quasi-axisymmetric stellarator(QAS) equilibrium in CFQS, the linear micro-instability, turbulent transport, and zonal flow generation are investigated by means of the electromagnetic gyrokinetic Vlasov simulations. It is elucidated that QAS has more unstable ion temperature gradient(ITG) driven modes with higher growth rate in a wider range of the wavenumber space, compared with that in the case of axisymmetric limit. However, the turbulent transport level is comparable or less in the nonlinear phase. Then, relatively stronger zonal flow generation is identified in QAS for a wide range of the ion temperature gradient, which is a key driving parameter of ITG driven turbulence.

1. Introduction

The quasi-axisymmetric stellarator(QAS) concept[1] possesses combined features of tokamak and stellarator plasmas, where the vacuum magnetic field is approximately axisymmetric in the finite rotational transform of the field lines produced only from the external helical coils. Exploring the fundamental physical properties in QAS is anticipated in the Chinese First Quasi-axisymmetric Stellarator(CFQS), which is under construction in a joint project between Japan and People's Republic of China [2,3].

The neoclassical transport and the linear MHD stability are mainly optimized in QAS, but the electrostatic/electromagnetic micro-instabilities, turbulent transport, zonal flow characteristics have not fully been clarified yet. In several earlier works, electrostatic and electromagnetic ITG modes in NCSX(QAS with the field period N=3) have been investigated by the linear gyrokinetic analysis[4,5]. However, the understanding of turbulent transport and zonal flow dynamics are still limited. In this study, the linear and nonlinear simulation studies by means of electromagnetic gyrokinetic code GKV[6, 7] are carried out for the ITG turbulence and zonal flows in the CFQS equilibrium with N=2, where the comparison with the axisymmetric limit is of particular interest here.

The rest of the paper is organized as follows. The geometric features of the CFQS vacuum equilibrium and the comparison with the axisymmetric limit are presented in Sec. 2. Then, the results of gyrokinetic micro-instability analysis for the ITG modes are shown in Sec. 3. In Sec. 4, the nonlinear ITG simulations results on the turbulent heat flux and zonal flow generation, including the ion temperature gradient parameter scan, are discussed.

2. Geometric properties

In this section, the geometric properties in CFQS is briefly described. In the following analysis, mid-minor radius of ρ=0.5 in the vacuum equilibrium is considered. The profiles of the magnetic field intensity and the squared perpendicular wavenumber along the fluxtube coordinate z are shown in Fig. 1(a) and 1(b), where the axisymmetric limit (labeled by "Equiv. Tokamak") with the same rotational transform profile is also plotted for comparisons. One finds a significant difference on the perpendicular wavenumber profile, rather than the field intensity, and this can lead the different stabilization of ITG modes through the finite gyro radius effects. Also, the dependence on the magnetic field line label is shown in Fig. 1(c) and 1(d), where each field-line label is represented by the reference toroidal angle ϕ of the fluxtube considered here. The field-line-label dependence of the field intensity is relatively weaker than that of the perpendicular wavenumber. Note that the profiles are symmetric for z=0 due to the stellarator symmetry.

3. Linear ITG instability

Linear ITG instability is examined by means of GKV, where kinetic equations for the hydrogen ions and real-mass electrons including their finite collisions are solved numerically. More details of the numerical model of GKV is given in, e.g., Ref. 7. Figure 2(a) shows a comparison of ITG growth rate, which is a function of the poloidal wavenumber, between CFQS and the axisymmetric limit, where the several cases with different ion temperature gradients R_{ax}/L_{Ti} are plotted. It is found that, in CFQS cases, the ITG modes are destabilized for wider range of the poloidal wavenumber, and higher growth rate is confirmed in comparison to the axisymmetric limit. The geometric difference of the perpendicular wavenumber (see Fig. 1) is responsible for the different ITG instability properties.

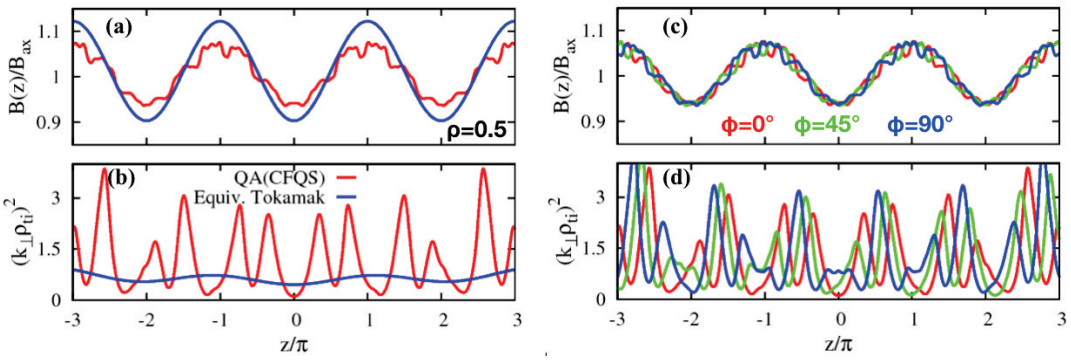

Fig. 1: Profiles of (a)the field intensity and (b)the perpendicular wavenumber in CFQS and the axisymmetric limit, where the field-line-dependence in CFQS is plotted in (c) and (d).

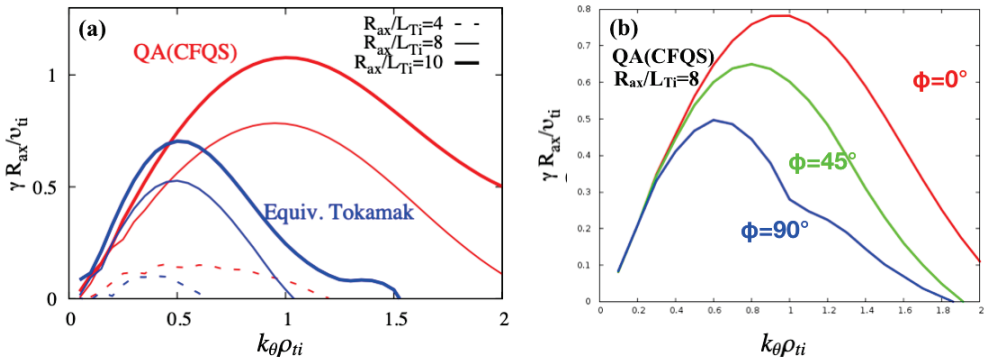

Fig. 2: ITG growth rate in comparisons with (a)axisymmetric limit and (b)field line labels.

In Fig. 2(b), a significant field-line dependence of the ITG growth rate is observed. One finds that the case with $\phi=0^{\circ}$ indicates the highest growth rate.

4. Nonlinear ITG turbulence simulations

Nonlinear gyrokinetic turbulence simulations with GKV are presented in this section, where the adiabatic electron approximation is used in the nonlinear simulations. Figures 3(a) and 3(b) show the time evolution of the turbulent ion heat flux(Qi) and the zonal flow generation defined by the ratio of the zonal flow energy and the total energy, where the axisymmetric limit is also plotted. It is observed that the nonlinear saturation levels of the ion heat flux are comparable between CFQS and the axisymmetric limit, despite more unstable ITG property in CFQS. Relatively stronger zonal flow generation is well correlated with the reduced transport in CFQS. This implies a significant impact of the non-axisymmetric field structures on the zonal flow dynamics.

As shown in Figs. 4, robustness of the reduced turbulent transport with stronger zonal flow generation in CFQS is confirmed from the nonlinear simulation scan for the ion temperature gradient parameter. For the wide range of R_{ax}/L_{Ti} , efficient suppression of turbulent transport by the zonal flow is observed in CFQS.

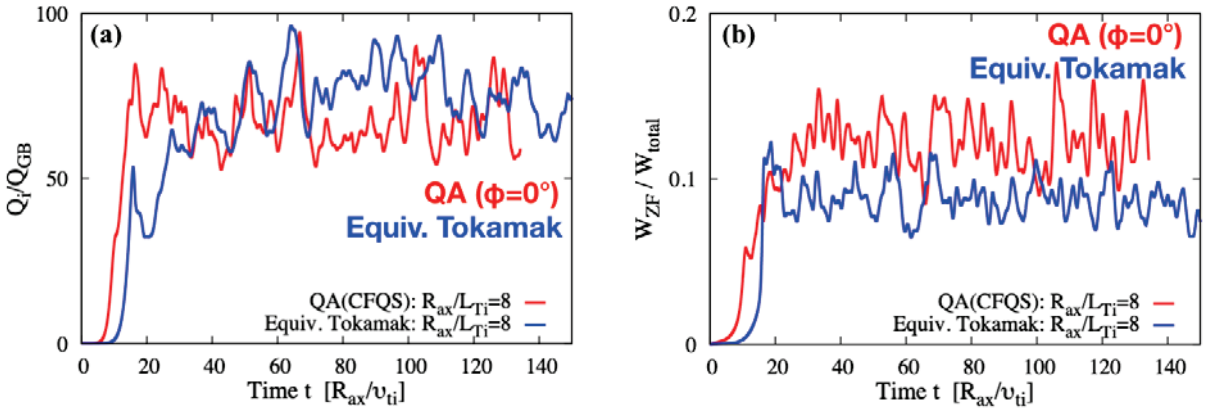

Fig. 3: (a)Turbulent ion heat flux(Qi) and (b)zonal flow generation(W_{ZF}/W_{total}) calculated from the nonlinear ITG turbulence simulation with the adiabatic electron approximation.

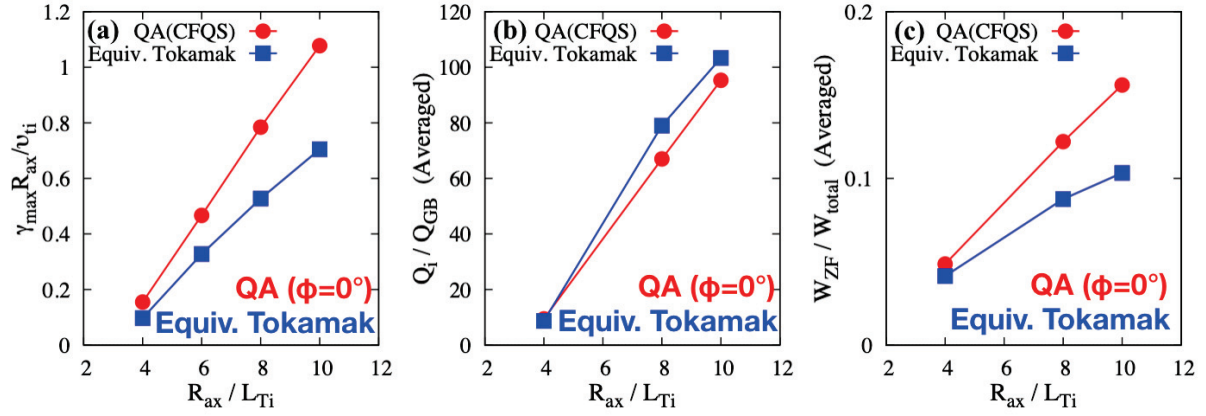

Fig. 4: Numerical scan with the ion temperature gradient parameter for (a)linear instability, (b)turbulent heat flux, and (c)zonal flow generation in CFQS and the axisymmetric limit.

In summary, linear ITG instability and nonlinear turbulent transport is investigated by means of gyrokinetic simulations with GKV, and reduced transport nature is found in CFQS. It should be pointed out that one still needs further investigations of the detailed turbulence spectrum in order to clarify the critical mechanism of zonal flow enhancement. In particular, the impact of the field-line-label dependence, which is inherent properties in stellarator plasmas, is still open. Also, the electromagnetic turbulence in QAS is another important issue, which will be addressed in future works.

Acknowledgements

This work was partly supported by the Post-CUP program. It was also supported by NIFS budget code NIFS19KUHL096, NIFS19KNST148, and was also partially supported by the Ministry of Education, Science, Sports and Culture Grant-in-Aid for Scientific Research 17K14899.

References

[1] P. R. Garabedian, Physics of Plasmas 3, 2483 (1996)
[2] Haifeng Liu et al., Plasma and Fusion Research 13 3405067 (2018)
[3] M. Isobe et al., Plasma and Fusion Research 14 3402074 (2019)
[4] J. A. Baumgaertel et al., Physics of Plasmas 18, 122301 (2011)
[5] J. A. Baumgaertel et al., Physics of Plasmas 19, 122306 (2012)
[6] T. -H. Watanabe et al., Nuclear Fusion 46, 24 (2006)
[7] M. Nakata et al., Plasma Physics and Controlled Fusion 58, 074008 (2016)

Publication List of NIFS-PROC. Series

NIFS-PROC-101 Edited by Shigeru MORITA, Liqun HU and Yeong-Kook OH
Proceeding of A3 Foresight Program Seminar on Critical Physics Issues Specific to Steady State Sustainment of High-Performance Plasmas 1-4 December, 2015, Gotemba, Japan
Sep. 09. 2016

NIFS-PROC-102 Edited by Liqun HU, Shigeru MORITA and Yeong-Kook OH
Proceeding of A3 Foresight Program Seminar on Critical Physics Issues Specific to Steady State Sustainment of High-Performance Plasmas May 17-20, 2016, Yinchuan, China
Jan. 23. 2017

NIFS-PROC-103 Edited by Daiji Kato, Zhengying Cui and Chenzhong Dong
JSPS-NRF-NSFC A3 Foresight Program Seminar Proceedings of Japan-China-Korea Joint Seminar on Atomic and Molecular Processes in Plasma Jul. 26 - 28, 2016, Chengdu, China
Mar. 17, 2017

NIFS-PROC-104 Atsuo Iiyoshi
Fusion for Sustainable World Development
Mar. 27, 2017

NIFS-PROC-105 Edited by Weihua Jiang
Frontiers of Applied Pulse Power Technology
Aug. 28. 2017

NIFS-PROC-106 Edited by Keiichi Kamada and Tetsuo Ozaki
Evolution of Pulse Power and its Peripheral Technology
Nov. 01, 2017

NIFS-PROC-107 Edited by Hiroaki Ito and Tetsuo Ozaki
Recent Progress of Pulsed Power Technology and its Application to High Energy Density Plasma
Nov. 27, 2017

NIFS-PROC-108 Edited by Yeong-Kook OH, Shigeru MORITA and Liqun HU
Proceeding of A3 Foresight Program Seminar on Critical Physics Issues Specific to Steady State Sustainment of High-Performance Plasmas November 22-25, 2016, Jeju, Korea
Jan. 11,. 2018

NIFS-PROC-109 Edited by Shigeru MORITA, Liqun HU and Yeong-Kook OH
Proceeding of A3 Foresight Program Seminar on Critical Physics Issues Specific to Steady State Sustainment of High-Performance Plasmas 11-14 July, 2017, Sapporo, Japan
Jan. 12, 2018

NIFS-PROC-110 Edited by Jun Hasegawa and Tetsuo Ozaki
Resent Developments of Pulsed Power Technology and Plasma Application Research
Jan. 12, 2018

NIFS-PROC-111 Edited by Liqun HU, Shigeru MORITA and Yeong-Kook OH
Proceeding of A3 Foresight Program Seminar on Critical Physics Issues Specific to Steady State Sustainment of High-Performance Plasmas 12 - 15 December, 2017, Chongqing, China
Jun. 11, 2018

NIFS-PROC-112 Edited by E. Kikutani (KEK) and S. Kubo (NIFS)
Proceedings of the meeting on Archives in Fields of Natural Sciences in FY 2017
Oct. 18, 2018

NIFS-PROC-113 Pulsed Power and High-Density Plasma and its Applications
Edited by Koichi Takaki and Tetsuo Ozaki
Feb. 6, 2019

NIFS-PROC-114 The 7th Japan-China-Korea Joint Seminar on Atomic and Molecular Processes in Plasma (AMPP2018)
Edited by Daiji Kato, Ling Zhang, and Xiaobin Ding
May 10, 2019

NIFS-PROC-115 CFQS TEAM
NIFS-SWJTU JOINT PROJECT FOR CFQS -PHYSICS AND ENGINEERING DESIGN-
VER. 2.1 2019. SEP.
Nov. 8, 2019

NIFS-PROC-116 Satoshi Ohdachi, Editor of the Post-CUP Workshop proceeding
Collected papers at the 2019 Post-CUP Workshop & JSPS-CAS Bilateral Joint Research Projects Workshop, 24th-26th July, 2019, Nagoya, Japan
Feb. 21, 2020